A STUDY ON SUPPORTED METAL CATALYSTS PREPARED FROM COLLOIDAL PRECURSORS

THE UNIVERSITY OF
WAIKATO
Te Whare Wānanga o Waikato

A thesis
submitted in fulfilment
of the requirements for the degree
of

Doctor of Philosophy in Chemistry

at

The University of Waikato

by

JACOB E. JAINE

———————

The University of Waikato
2016

Abstract

When metal nanoparticles are supported on the surface of an inert carrier, the resulting materials can become powerful heterogeneous catalysts capable of accelerating a diverse range of chemical reactions. Though there are a wide variety of synthetic routes by which these materials can be prepared, many offer little control over the textural properties of the resulting catalyst. Conversely, methods using pre-formed colloidal nanoparticles as a metal source offer the potential for precise control of properties like particle size and shape. This is both a topical class of syntheses, and the subject of the current body of work. Three different types of colloids were therefore prepared using different stabilising agents, and subsequently used to produce an array of different catalysts.

As support materials for the catalysts, a series of four commercially available materials were obtained, including silica, alumina, hydroxyapatite, and microcrystalline cellulose. Four novel analogues were also obtained, including halloysite, perlite, bioapatite, and macrofibrillar cellulose. In order to understand their physicochemical properties, they were characterised by a combination of Fourier transform infrared microspectroscopy, solid-state ^{1}H, ^{13}C, ^{27}Al, ^{29}Si, and ^{31}P nuclear magnetic resonance spectroscopy, x-ray diffraction, x-ray fluorescence spectroscopy, scanning and transmission electron microscopy, laser diffraction analysis, and zeta potential measurements. Additional experiments were performed to investigate the wetting properties of the materials using the Washburn capillary rise method, which was shown to be a valuable method for rationalising solvent choice for reactions involving these materials.

An initial batch of catalysts was produced by immobilising electrostatically-stabilised rhodium, palladium, and platinum colloids onto these support materials. Instrumental characterisation of the catalysts showed no major perturbation to the chemistry of the materials following the immobilisation, though some subtle surface effects were observed. These catalysts were tested in the hydrogenation of several olefins, and were found to have excellent catalytic activity, up to 64,400 hr^{-1}, under standard conditions.

A second batch of catalysts was produced by immobilising polymer-stabilised metal colloids onto the supports. Characterisation of the materials showed the

polymers and the nanoparticles they contained were associated strongly with the support materials, though the spatial distribution varied significantly between systems. Activation of the catalysts by calcination was shown to initiate their thermal decomposition and oxidation, which in turn affected their catalytic activity. The catalysts containing supported rhodium or platinum were inactive, while those containing supported palladium showed good activity, up to 41,900 hr^{-1}.

A third batch of catalysts was produced by immobilising solvent-stabilised metal colloids onto the supports. Amide-type solvents were shown to be the most effective for this purpose, though spectroscopic evidence suggested the samples contained residual solvent and related decomposition products. These catalysts displayed modest activities of up to 8,100 hr^{-1}.

Finally, a method was developed for quantifying the amount of metal in the catalysts using laser-induced breakdown spectroscopy. A series of matrix-matched standards were prepared, and their elemental compositions measured accurately using neutron activation analysis. The method was shown to be rapid and inexpensive to implement, with linearity up to 2.0 wt% metal and a precision of over 95%.

Acknowledgements

First and foremost, I would like to express my sincere gratitude to my chief supervisor, Dr. Michael Mucalo, whose support throughout this odyssey has been unwavering and whose guidance has been invaluable. Additional thanks go to my co-supervisor, Associate Professor Graham Saunders, who has always been readily available when called upon.

The contributions of an array of technical staff are also appreciated, especially Wendy Jackson, Pat Gread, Jenny Stockdill, and Annie Barker. The contributions of Helen Turner for electron microscopy, Steve Newcombe for glassblowing, and Dr. Barry O'Brien for photomicroscopy are also much appreciated.

Help provided with photoelectron spectroscopy is also valued, notably from Colin Doyle for his expert instrumental operation, and Neal Fairley for his training in spectral deconvolution and peak fitting.

Acknowledgement is made of several organisations, firstly AINSE (Australian Institute of Nuclear Science and Engineering) for their provision of a grant to fund the neutron activation work described herein. Thanks also go to John Bennett for assisting with the grant application, and to Attila Stopic for the counting and data analysis portions of the work.

Secondly, acknowledgement is made of ESCOM (Ecole Supérieure de Chimie Organique et Minérale) for providing an intern to assist with experimental work, and to Gwenaelle LeBlanc for being said intern.

Thirdly, acknowledgement is made of the University of Waikato for the provision of a doctoral scholarship for the candidate over the course of this work, making the insufferable task of being a professional student more bearable.

Lastly I must thank my friends, my family, and others dear to me. Their support through the last four years has been immensely valued, and I couldn't have done it without them.

Table of Contents

List of Figures

List of Tables

List of Abbreviations

β	Diffraction peak breadth
ΔG	Change in Gibbs free energy
$\Delta G^{\ddagger}$	Gibbs free energy of activation
ΔH_H	Heat of hydrogenation
ΔV	Change in volume
n	Refractive index
ζ	Zeta potential
η	Dynamic viscosity
γ	Surface tension
φ	(Co)solvent fraction
θ	Contact angle
θ	Diffraction angle
ARG	Arabinogalactan
AU	Arbitrary units
BAp	Bioapatite
^{n}BuOH	1-butanol
^{t}BuOH	Tertiary butanol (2-methyl-2-propanol)
C	Washburn material constant
CPMAS	Cross polarisation magic angle spinning
COD	Cyclooctadiene
D	Dispersion
D	Diameter

d	Diameter
d	Distance
DMF	N,N-dimethylformamide
DMPU	1,3-dimethyltetrahydropyrimidin-2(1*H*)-one
DMSO	Dimethylsulfoxide
DPMAS	Direct polarisation magic angle spinning
E_a	Activation energy
ELS	Electrophoretic light scattering
EDS	Energy-dispersive (x-ray) spectroscopy
EtOH	Ethanol
EtOAc	Ethyl acetate
FTIR	Fourier transform infrared
FWHM	Full-with at half-maximum
GC-MS	Gas ghromatography-mass spectrometry
HAp	Hydroxyapatite
HMPA	Hexamethylphosphoramide
HNC	Halloysite nanoclay
HPDEC	High-power ^{1}H decoupling
ICDD	International centre for diffraction data
ICP-MS	Inductively coupled plasma-mass spectrometry
K	Shape factor
LA	Laser ablation
LIBS	Laser-induced breakdown spectroscopy

LDA	Laser diffraction analysis
LOD	Limit of detection
LOL	Limits of linearity
LOQ	Limit of quantification
LRM	Laboratory reference material
MCC	Microcrystalline cellulose
MeCN	Acetonitrile
MeOH	Methanol
MSD	Mass-selective detector
NAA	Neutron activation analysis
NIST	National Institute of Standards and Technology
NMR	Nuclear magnetic resonance
NMP	N-methyl-2-pyrrolidone
NPs	Nanoparticles
PBR	Peak to background ratio
PGE	Platinum-group elements
PCS	Photon correlation spectroscopy
PDF	Powder diffraction file
ppm	Parts per million
^{i}PrOH	Isopropanol (2-propanol)
^{n}PrOH	Propanol (1-propanol)
PSD	Particle size distribution
PAA	Poly(acrylic acid)

PAM	Poly(acrylamide)
PCL	Poly(caprolactone)
PEG	Poly(ethylene glycol)
PEI	Poly(ethylenimine)
PMO	Precious Metals Online
^{n}PnOH	1-pentanol
PRL	Perlite
PVA	Poly(vinyl alcohol)
PVP	Poly(vinyl pyrrolidone)
RSD	Relative standard deviation
SAXS	Small-angle x-ray scattering
SNR	Signal to noise ratio
SBR	Signal to background ratio
SISR	Signal to internal standard ratio
SEM	Scanning electron microscopy
SMC	Supported metal catalyst
SRM	Standard reference material
SS	Solid-state
t	Time
TEM	Transmission electron microscopy
TIC	Total ion chromatogram
THF	Tetrahydrofuran
THT	Tetrahydrothiophene

TOF	Turnover frequency
TOSS	Total sideband suppression
tpa	Tonnes per annum
UV/Vis	Ultraviolet/visible spectroscopy
WAXS	Wide-angle x-ray scattering
XPS	X-ray photoelectron spectroscopy
XRD	X-ray diffraction
XRF	X-ray fluorescence

Chapter 1: Introduction

1.1 Introduction to Catalysis

In the early 19th century a flurry of research was underway across the globe on a group of combustion and decomposition reactions related by a common, but then unknown, theme [1-9]. In 1835, Berzelius realised the link between the otherwise disparate studies [10], noting that the reactions were all *catalytic* in nature. These early investigations were the genesis of what we now know as the field of catalysis [11], one which underpins many of the chemical processes conducted in the modern world [12].

Nowadays we have a somewhat greater understanding of catalysis, and clearer definitions on what a catalyst is. Any material which accelerates a chemical reaction without being consumed is called a catalyst, and the process of converting substrate molecules to products using a catalyst is called catalysis [13]. The increase in reaction rate for a catalysed process is due to the presence of an alternate reaction pathway provided by the catalyst, the activation energy for which is lower than the corresponding uncatalysed pathway. This is illustrated in **Figure 1**. The relationship between the rate constant for a reaction and the activation energy is given by the Arrhenius equation, which shows that all other factors being equal, the rate of a reaction goes up as the activation energy goes down.

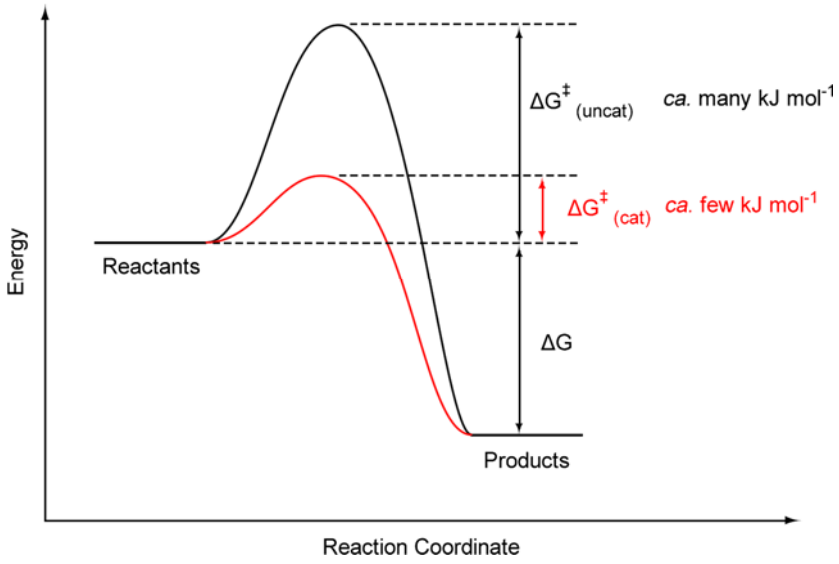

Figure 1: Diagram comparing the energy changes between an arbitrary catalysed and uncatalysed reaction.

Accelerating the rate of chemical reactions has obvious utility, especially for large-scale synthetic applications. Indeed, the vast majority of materials we encounter in our day-to-day lives have been produced, at least in part, using catalytic processes [14]. Catalysts are currently used for the production of petrochemicals, agrichemicals, pharmaceuticals, foodstuffs, fine chemicals, environmental protection, and much more. Without the use of catalytic technologies, the chemical transformations required to produce these products would be either prohibitively slow or excessively environmentally unfriendly [12, 15].

Catalysts can be grouped into two broad classes based on how they are used. *Homogeneous catalysts* are typically inorganic or organometallic complexes with a single active site at which the reaction occurs, which are dissolved into a solvent along with the substrates. Conversely, *heterogeneous catalysts* are typically solid inorganic materials over which liquid or gaseous reactants are flowed. This thesis describes work undertaken on a sub-class of heterogeneous catalysts called *supported metal catalysts*, described further in the following section.

1.2 Supported Metal Catalysts

Supported metal catalysts are a common class of biphasic heterogeneous catalyst composed of metal nanoparticles dispersed across the surface of an inert support material. This is illustrated schematically in **Figure 2**. Catalytic reactions occur on the surface of the nanoparticles, which have a high specific surface area due to their small size. The relative proportion of active phase within a catalyst is called the loading, given in weight percent, and varies widely across different catalysts depending on their application.

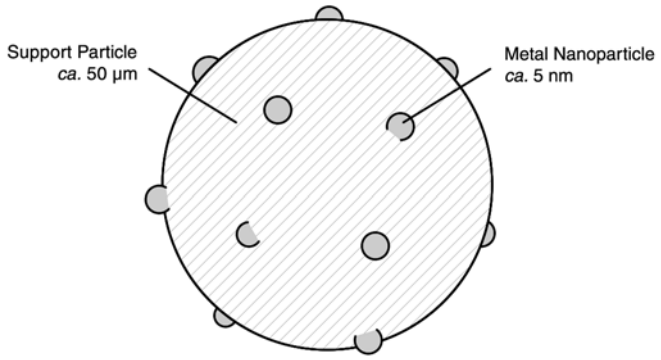

Figure 2: Schematic of a supported metal catalyst with approximate dimensions.

Since heterogeneous catalysis is a surface phenomenon, the activity of a supported metal catalyst is generally proportional to the surface area of the active phase, which depends in turn on the particle size. Smaller particles have a higher proportion of their atoms at the surface, while larger particles have a smaller proportion. The ratio of surface atoms to bulk atoms in the active phase is termed the *dispersion* or *fraction exposed*, and is given as a number between zero and one.

There are two primary advantages to using metal nanoparticles in a supported, rather than unsupported, form. Firstly, they have an increased resistance to a deactivation process called *sintering*. When two particles collide with sufficient energy, they will coalesce with one another, reducing their surface area, and consequently their surface free energy. This reduces the number of active sites at which reactions can occur, which results in a loss of catalytic activity. When the particles are immobilised on the surface of a support material their mobility is significantly reduced, and so too is the rate of sintering.

The second advantage of using metal nanoparticles in a supported form is that they are much easier to recover. Because of their small sizes they cannot be collected by ordinary filtration methods, as they pass through the pores of most common filtration devices. Furthermore, they cannot be collected by centrifugation because their sedimentation rates too low. Supporting 5 nm nanoparticles on 50 μm support particles makes both of these processes feasible, which dramatically increases the convenience of reaction workup.

Though generalisations may be made of all supported metal catalysts, no two systems behave identically. Catalysts with vastly different activities can be created depending on the specific combinations of support material and active phase, and so a discussion of their general influence is germane.

1.2.1 The Active Phase

The active phase, composed of metal nanoparticles, is the part of the catalyst upon which catalytic reactions occur. Not all of the transition metals are equal in their catalytic abilities, and in most applications some perform markedly better than the rest. The Haber-Bosch process uses iron as a catalyst, for example, while the Fischer-Tropsch process uses cobalt and the Contact process uses platinum or

vanadium [16]. The frequency with which the transition metals are mentioned in the literature is illustrated in **Figure 3**.

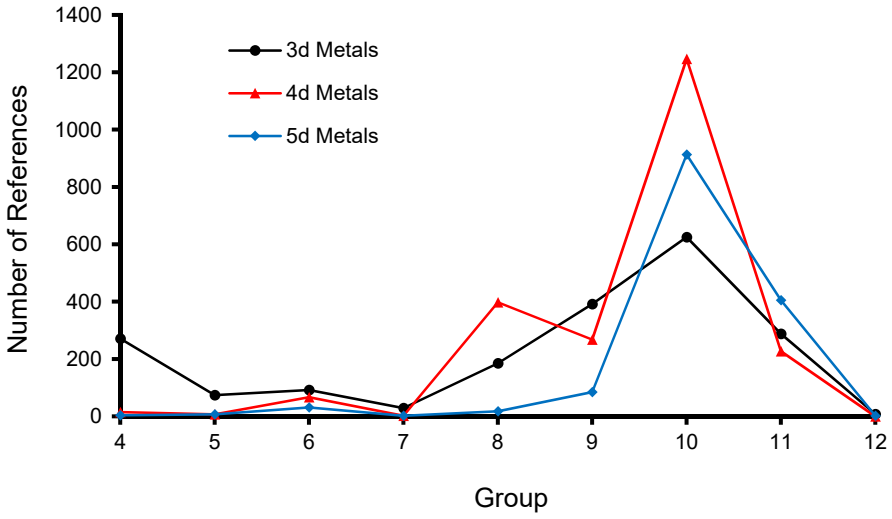

Figure 3: A visual representation of the popularity of each of the transition metals as the active phase in supported metal catalysts. The three series represent the three rows of transition metals, while the abscissa position represents the group, and the ordinate position represents the number of search results obtained on SciFinder Scholar when searching for, for example, "supported palladium catalyst". The group 10 metals, comprising nickel, palladium, and platinum, are clearly the most popular.

In spite of these marked preferences, one group of metals which performs with unparalleled versatility is the platinum-group elements. Their favourable electrochemical properties allow their salts to be reduced easily to form metallic particles, and moreover, the electronic properties of the resulting particles enable the adsorption and activation of many otherwise unreactive molecules (see section 1.4).

1.2.2 The Support Material

A wide variety of different materials can be used as catalysts supports, though the most commonly used materials share several characteristics. They are typically refractory ceramic materials with excellent chemical resistance, as well as favourable morphological properties. Often they are microporous or mesoporous, giving them specific surface areas in excess of 100 $m^2 g^{-1}$. Examples of materials satisfying these criteria include alumina (Al_2O_3), silica (SiO_2), titania (TiO_2), ceria (CeO_2), activated carbons, and zeolites.

For many years it was presumed that the support material was simply an inert carrier, though an increasing number of studies show that this is not the case [17,

18]. When a nanoparticle is immobilised onto a support its morphology changes due to the energy of adhesion [19], its electronic properties change due to charge transfer effects [20], and both of these properties can impact on the activity of a supported metal catalyst. Furthermore, the nature of the support influences the rate at which supported particles sinter, and therefore affects the lifetime of a catalyst [21, 22]. If they are not sufficiently stabilised, supported metal particles will grow with use, either by movement of entire particles or diffusion of single metal atoms across the support [23, 24]. Sintering can be reduced by increasing the surface area of the catalyst, but this can also affect the size and reactivity of the supported particles [25]. The presence of surface hydroxyl groups, though useful for facilitating interaction with metal complexes [26], can also reduce the interaction energy with supported nanoparticles [27].

It is clear from these studies that both the active phase and the support contribute to the properties of a supported metal catalyst. In order to achieve the maximum possible activity from a catalyst though, an appropriate synthetic method must be used to prepare it. Analogous catalysts prepared by different methods can have different activities [28], and so common methods are discussed in the following sections.

1.3 Synthetic Approaches

There are a wide variety of different techniques which can be used to prepare supported metal catalysts, ranging from trivial to complex. These have been categorised by the IUPAC subcommittee on catalyst characterization [29, 30] into several overlapping groups, though only a handful of these are applicable to the synthesis of supported metal catalysts. Relevant methods are described hereafter, along with selected examples of their use.

1.3.1 Impregnation

Impregnation is a broad class of methods where a solution of metal nanoparticles or their relevant precursor compounds are immobilised onto a support material by direct contact between the two. The interaction between the two is mediated by a variety of forces, including coulombic attraction, hydrogen bonding, and dipole-dipole attractions. The residual solvent is then removed, and the resulting solid is dried and treated to produce a catalyst.

One of the most commonly used variations of this method is pore volume impregnation. In this technique, the pores of a solid are filled with a solution of a metal complex, and the solvent is subsequently removed by evaporation. The previously dissolved species are left deposited in the pores, and the resulting material is activated to produce the final catalyst [31]. This type of method was used to generate Pt/SiO_2 catalysts by Dorling, Lynch and Moss, who impregnated SiO_2 with a solution of H_2PtCl_6, boiled off the water, and then reduced the H_2PtCl_6 to Pt in flowing hydrogen at high temperature to produce the final catalyst [32]. Methods of this type are experimentally simple, can be applied to a wide range of different materials, and successive impregnations can be used to generate catalysts with high metal loadings. It can be highly controllable and reproducible, but the size and distribution of the particles are extremely sensitive to the conditions of drying, reducing, and calcination. Furthermore, thermally sensitive support materials like activated carbons are less appropriate for this technique than refractory ceramics like alumina or silica.

Another commonly used method is excess solution impregnation, where the support material is soaked in a solution containing species which adsorb to its surface. The solvent is drained by filtration or a similar process, and the resulting solid is dried and activated. The adsorption mechanism depends on the nature of species involved, and could be an ion-exchange type process for charged species, or a hydrogen-bond mechanism for uncharged polar species. Pd/SiO_2 catalysts have been prepared in this way by Benesi, Curtis, and Studer, who adsorbed $[Pd(NH_3)_4]^{2+}$ onto SiO_2 from aqueous solution, taking advantage of the opposite charges of the two species, followed by filtration, drying, and activation in hydrogen at high temperature [33]. The main advantage to using solution-phase adsorption methods such as these is that a very homogeneous distribution of particles can be obtained, though the loading is limited by the number of adsorption sites on the support material. This in turn depends on the pH of the system, since the surface charge of a protic solid material depends on its isoelectric point [28].

1.3.2 Precipitation

The second class of methods is precipitation, which is common in the synthesis of large-scale commercial catalysts such as Ni/Al_2O_3. Two solutions are combined, one containing precursors to the support, and one containing the precursors to the

active phase, the combination of which results in their mutual precipitation. This ordinarily produces a slurry of finely divided material where the active and support phases are intimately mixed with one another. Laboratory catalysts may be made in this way, too; Au/TiO_2 catalysts were produced by Sakurai and Haruta by combining aqueous solutions of $HAuCl_4$ and $Ti(NO_3)_4$ with Na_2CO_3, followed by filtration, washing, and calcination of the precipitate [34, 35]. The advantage of such a technique is that very large amounts of a catalyst can be produced at once (indeed this is how Raney nickel is produced), but much of the active material may be occluded within the bulk of the support material. It also depends on the solubility of the species, and their ability to be precipitated by one another, or another common reagent.

1.3.3 Deposition

The final group of methods is deposition, which involves the vaporisation of a metal or a metal complex, followed by its subsequent condensation onto the surface of a support material. Physical vapour deposition techniques such as sputtering can be used to directly condense metal onto the surface of a support, while chemical vapour deposition techniques can be used to coat a support material with a metal complex which can be reduced in a later stage. Techniques like these are commonly used in model or theoretical studies when a single planar surface is to be coated in nanoparticles, and they work quite well for this purpose. Many complicated experimental setups can be used to perform this task, though a 'simple' method was demonstrated by Serp *et al.*, who prepared Rh/SiO_2 catalysts by chemical vapour deposition of $Rh_2Cl_2(CO)_4$ onto silica in a fluidised bed reactor, followed by activation in hydrogen [36]. Difficulty is encountered, however, when attempting to use such techniques to immobilise nanoparticles on a three-dimensional surface, especially ones with irregular morphologies or pore systems, which can make this technique difficult to use practically.

1.4 Reactivity

There are a diverse range of chemical transformations which supported metals can catalyse, and different systems are used across a wide range of industries for different purposes. These include oxidations [34, 37, 38], combustions [39-43], hydroformylations [44], dehalogenations [45], dehydrations [46], hydrocarbon

reformations [47-50], carbon-carbon coupling [51], hydrogen production [52], and hydrogenations [53].

Of these processes, the catalytic hydrogenation of molecules is one of the most versatile synthetic techniques available to chemists. Formally the process involves the addition of hydrogen across an unsaturated bond such as an olefin, carbonyl, or nitrile, resulting in the corresponding saturated analogue. A wide range of organic functionalities can be hydrogenated quickly and efficiently, and often with good stereo or regioselectivity [53]. It is precisely these characteristics which make catalytic hydrogenation so useful, a fact which is evident in the technique's ubiquity. It is performed on scales ranging from micrograms in synthetic organic chemistry laboratories, all the way to industrial chemical processes which produce hundreds of millions of tonnes of products per annum. Some common industrial applications of hydrogenation are given in **Table 1**.

1.5 Mechanisms

Regardless of the nature of the substrate, the vast majority of metal-catalysed reactions proceed *via* five simple steps, which are described by the Langmuir-Hinshelwood mechanism [54]. These are illustrated schematically in **Figure 4**. Firstly, both reactants diffuse toward the catalyst and adsorb on its surface. The two adsorbed reactants migrate across the catalyst surface toward one another, and undergo a reaction. After this point they desorb, and finally diffuse away. If only a single reactant adsorbs to the catalyst and the other reacts with it directly from the gas phase, this is known as the Eley-Rideal mechanism, which typically has lower activation energies [55].

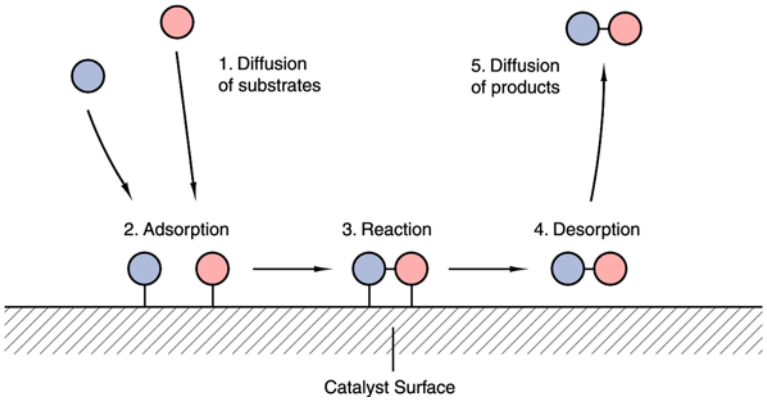

Figure 4: Illustration of the five fundamental steps in a heterogeneous catalytic reaction.

Table 1: A selection of commonly-hydrogenated substrates and their resulting products. Production given in TPA.

Substrate	Product	Example	Production (tpa)	Refs
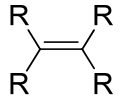 Alkene	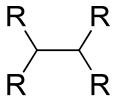 Alkane	• Partial hydrogenation of vegetable oils • Cyclohexane from benzene	1.0×10^7 2.0×10^7	[56, 57] [58]
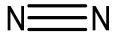 Nitrogen	 Ammonia	• Haber-Bosch process for the synthesis of ammonia	2.0×10^8	[59]
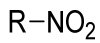 Nitro	 Amine	• Aniline from nitrobenzene for polyurethane synthesis	3.1×10^6	[58]
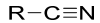 Nitrile	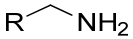 Amine	• Production of Nylon 6-6 from adiponitrile	1.4×10^6	[58]
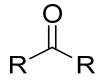 Ketone	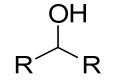 2° Alcohol	• Hoechst-Celanese process for ibuprofen	8.0×10^3	[60]
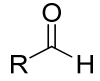 Aldehyde	 1° Alcohol	• Sorbitol from d-glucose	6.3×10^5	[61, 62]

The exact nature of the bonding between an adsorbate and the surface of a supported metal particle is complex. Because supported metals contain a range of active sites with varying geometric and electronic configurations, studies are often conducted on model single-crystal surfaces. It is shown that the adsorption of many gaseous reactants such as H_2 and O_2 proceed *via* a process called 'dissociative adsorption'. In this process the molecules are not adsorbed molecularly, but dissociate into their individual atomic constituents. This is also called 'activation'. Heats of adsorption are negative; for example *ca.* -100 kJ mol^{-1} for H_2 on Pd(110) or *ca.* -130 kJ mol^{-1} on Pt(111) [63, 64]. The barrier to chemisorption is low in these metals due to both geometric and electronic factors [65]. Larger reactants such as substrate molecules can adsorb in varying ways, depending mostly on what functional groups they possess. Olefins, for example, can be adsorbed as di-σ or π-bonded species [66] while alcohols adsorb forming a metal-alkoxide bond [67] and ketones adsorb by forming η^2 di-σ species [68].

Many reactions can be modelled effectively using kinetics based on the Langmuir-Hinshelwood mechanism. These include oxidation of CO on Rh [69] or Pt [70, 71], photocatalytic H_2O_2 decomposition over TiO_2 [72], combustion of methane over Pt [39], and a diverse range of hydrogenations. [73-77]. Refinements to this mechanism specific to hydrogenations were made in 1939, and the result has since been called the Horiuti-Polanyi mechanism [78].

1.6 Quantifying Catalytic Activity

Perhaps the most interesting aspect of a supported metal catalyst is how active it is, which is reflected in how frequently the catalytic cycle is repeated. Though this information can be gleaned from complete derivation of the mechanism and the corresponding rate law for a given system, such analyses are non-trivial. Multiple active sites may exist within a catalyst, at which there may be differences in reactant orders, rate constants, and even the nature of the rate-limiting step itself. Moreover, the relative proportions of each type of active site may change throughout the course of a reaction. These types of analyses are therefore restricted to model catalysts, using single-crystals of metals under tightly controlled ultrahigh vacuum conditions.

To simplify kinetic analyses, a number of assumptions can be made. For any given reaction, and in the absence of any mass transfer limits, (pseudo) zero order kinetics can be assumed. This means the rate limiting step observed is the actual catalytic step, and thus the observed reaction rate is reflective solely of the activity of the catalyst under those particular conditions. These data can then be used to calculate the *turnover frequency*, or TOF, which is defined as the number of revolutions of the catalytic cycle per unit time [79]. More explicitly, the TOF represents the number of moles of product generated per mole of active site per unit time, and therefore has units of inverse time, commonly given in inverse seconds (s^{-1}) or hours (hr^{-1}).

Expressing catalytic activity as a turnover frequency has a number of benefits. When a properly measured turnover frequency is supplied along with the conditions under which it was collected, it becomes a powerful metric for comparing the activity of different catalysts, both within and between individual laboratories. It can be used to reveal whether or not the rate of a reaction depends on the size of the supported particles, and it can be used for the screening of novel catalysts [79-81].

In order to calculate a turnover frequency, two pieces of information are required. The first of these is the reaction rate, in moles per unit time. For reactions conducted in a batch-type reactor this is a trivial task; small aliquots of the reaction mixture can be withdrawn at various points throughout a reaction and analysed chromatographically. A plot can then be constructed showing the conversion as a function of time, the slope of which gives the reaction rate. It is important that the data are collected under conditions where the kinetics are not controlled by mass transfer, as this leads to the generation of erroneous data. Various experimental methods are available to check this [82-84].

The second piece of data required is the number of active sites at which a reaction is occurring. This presents several problems, because as discussed previously, the task of elucidating what constitutes the 'active site' in a collection of supported metal particles is non-trivial [80]. In 1925, Taylor postulated that the active sites in supported metal particles may be specific arrangements of atoms on the surface of the catalyst known as 'ensembles' [85]. To date there have been numerous studies investigating this concept, and many are in good agreement with it. Often the active sites are shown to be crystallographic defects, such as adatoms, kinks, or step sites at the particle surface. For example Zambelli *et al* showed by STM that the active sites

for the dissociation of NO on Ru(0001) are the edges of the stepped sites [86], while Mohr *et al* showed that both the selectivity and activity of the hydrogenation of acrolein on gold varied depending on whether the (111) or (100) faces were primarily exposed [87]. While it may be of interest to elucidate the nature of the active site for every metal catalysed reaction, it is not always a practical endeavour. The assumption is therefore made that all surface atoms in a supported metal particle contribute equally to the observed reaction rate. If the amount of catalyst used in the reaction is known, and the amount of metal the catalyst contains is known, then the number of moles of active sites can be easily calculated.

Using these two pieces of data, the turnover frequency can be obtained by dividing the reaction rate by the number of active sites. Measured turnover frequencies vary by many orders of magnitude depending on the catalyst, the reaction, and the conditions under which it is performed. Highly active nickel electrocatalysts have been reported for H_2 production with activities greater than 10^5 s^{-1} [88], while an Au/Fe_2O_3 catalyst for CO oxidation may be called highly active with a turnover frequency of 'only' *ca.* 1 s^{-1}, and unsupported Au used for the same reaction may have an activity of 10^{-4} s^{-1} [89].

1.7 Aims of the Current Research

Many factors have been shown to affect the activity of a supported metal catalyst, one being the nature of the support material. While many of the common support materials are refractory oxides of aluminium and silicon, there is increasing interest in the literature in using alternative support materials such as hydroxyapatite or cellulose. Many of these materials have structural analogues which appear within nature, many of which have also proven to be effective catalyst support materials [90-115]. Preparing catalysts from a range of different support materials and comparing their properties was therefore one of the major goals of the current research.

To achieve this aim, a series of commercially-available 'model' support materials were sourced, as well as four novel structural analogues. These were extensively characterised by a suite of instrumental methods, with the goal of gaining a complete understanding of their physicochemical properties, especially those relevant to their use as catalyst supports. This forms the basis of the work described in Chapter 2. As

part of this characterisation, the wetting properties of the support materials were investigated using the Washburn capillary rise method, which forms the basis of the work detailed in Chapter 3. Once thoroughly characterised, the support materials were used to prepare a variety of different catalysts.

While the nature of the support was anticipated to be important, the choice of synthetic method was also expected to contribute significantly to the properties of the resulting catalysts. Though a diverse range of methods already exist, control of the size and distribution of the supported particles is often difficult. These are problems which have been dealt with extensively by the colloid science community, where the synthesis of well-defined monodisperse colloidal dispersions of nanoparticles is routine [116-118]. It was considered of interest therefore to investigate the use of colloidal metals as a precursor for the synthesis of supported metal catalysts, as these may confer some advantages over conventional preparative methods. Though this is a route which has already been shown to be effective [119], there are few systematic investigations of the topic. This was a second major aim of the current study.

The problem with using colloidal metal nanoparticles is that they are not thermodynamically stable, so a suspension of particles will gradually aggregate over time. This process can be prevented if a stabilising agent is added, of which three types have been investigated in this work. Colloids stabilised by intrinsic electrostatic forces have been used to produce catalysts in Chapter 5, while colloids stabilised by adsorbed polymers have been used in Chapter 6, and colloids stabilised by adsorbed solvent molecules in Chapter 7. All three methods were anticipated to produce catalysts with a unique combination of properties, and so each batch of catalysts was extensively characterised by a range of methods, and their activities tested in selected hydrogenation reactions.

In order to calculate the activities of the catalysts, an accurate method was required to measure their loadings. Traditionally this is done by digesting the catalyst and measuring the amount of metal in the resulting solutions, however this can be time-consuming and difficult, and for some metals extreme digestion conditions are required. Given the increasing availability of laser ablation-based elemental analysis methods, an investigation of their fitness for purpose was deemed an appropriate final aim for the current work. Two methods were investigated, namely laser induced

breakdown spectroscopy (LIBS) and laser ablation inductively coupled plasma mass spectrometry (LA-ICP-MS), and this forms the basis of the work described in Chapter 4.

Chapter 2: Catalyst Support Materials

2.1 Introduction

There are many factors which have been shown to contribute to the physical and chemical properties of a supported metal catalyst, but one of the most important is the nature of the support material itself. Textural properties such as surface area and porosity can affect the thermal stability of the catalyst [120, 121], while the surface chemistry can control the strength of adhesion [122] which can consequently affect the electronic structure of the supported particles [123]. These are among the many reasons why catalysts prepared with different support materials can have different activities, and illustrates the importance of having a firm understanding of the properties of a material in order to rationalise its performance.

In this research, a series of eight materials were investigated as potential catalyst supports. Four of these were commercially available 'model' support materials, including alumina, silica, hydroxyapatite, and microcrystalline cellulose. Alongside these, four novel analogues were tested, including halloysite, perlite, bioapatite, and macrofibrillar cellulose. A general review of the properties of these materials is given in the following section, after which the results of a thorough instrumental characterisation of the materials are described.

A suite of instrumental analysis methods have been used for characterising the support materials, providing a comprehensive understanding of their physicochemical properties, and thereby facilitating rational catalyst design in subsequent chapters. The size and morphology of the dry particles have been measured by scanning electron microscopy (SEM) and transmission electron microscopy (TEM), as well as when dispersed in solution by laser diffraction analysis (LDA). Elemental compositions have been measured by x-ray fluorescence spectroscopy (XRF). Information about the chemical structure has been obtained by Fourier transform infrared spectroscopy (FTIR) and solid-state nuclear magnetic resonance spectroscopy (SS-NMR), while phase purity was assessed by x-ray diffraction, (XRD) and surface properties *via* zeta potential measurements.

2.1.1 Alumina, Silica, and Analogues

Alumina, which has the formula Al_2O_3, is perhaps the most widely used catalyst support of all. It is a hard, white, refractory ceramic material, with excellent thermal and chemical stability. All aluminas have the empirical formula Al_2O_3, although different polymorphs have different crystal structures. The so-called γ-alumina is the most widely used as a catalyst support, which consists structurally of a face-centred cubic oxygen lattice with a disordered distribution of aluminium ions occupying both octahedral and tetrahedral interstitial sites [124]. Also commonly used is α-alumina, consisting of a hexagonal lattice of oxygen atoms with aluminium atoms exclusively occupying the octahedral sites. The crystal structure of an alumina has a strong effect on its surface chemistry, affecting its porosity, water content, and acidity [125]. From early on the significance of alumina as a catalyst support was recognised, prompting a series of more than 30 articles on its various properties from Pines *et al.* [126, 127].

Silica is one of the most common support materials used in heterogeneous catalysis, second only to alumina. There are a great number of polymorphs and morphologies of silica known, many of which are commercially available, and many of which can be easily synthesised. All share the basic molecular formula $SiO_2.xH_2O$, and are composed of corner-sharing SiO_4 tetrahedra stacked in varying ways. The surface of silica is usually hydroxyl-bearing, through which it can be functionalised with various functional groups [128]. Many have high specific surface areas, rendering them useful for the adsorption of a wide variety of chemical entities; indeed this is the basis for their use as substrates in column chromatography and catalyst supports [129]. Many model catalysts are based on silica, including the renowned EUROPT-1 6% Pt/SiO_2 model catalyst and its subsequent derivatives [130-135].

Halloysite is a naturally-occurring aluminosilicate clay with a unique and predominantly nanotubular morphology. There are a number of halloysite mines located throughout the world, and one of the most important is the Matauri Bay mine located in Northland, New Zealand [136]. It is assigned the chemical formula $Al_2Si_2O_5(OH)_4.xH_2O$, where the level of hydration influences the cation exchange properties of the material. The interlayer spacings, in addition to accommodating water, can also intercalate a variety of polar organic molecules [137]. The absorption

of formamide, for example, can be used to distinguish halloysite from a similar clay, kaolinite [138, 139].

Structurally speaking, halloysite is composed of alternate layers of octahedral alumina and tetrahedral silica sheets, which due to a natural 'lateral misfit', have a tendency to roll around one another in order to relieve the resulting stress. This results in the formation of nano-sized tubules, the interiors of which are rich in alumina and the exteriors rich in silica. The morphology of the tubules is further affected by the structural iron content; when Al^{3+} is substituted for Fe^{3+} the octahedral sheets are enlarged, relieving the stress, and producing halloysite with a flatter morphology [140]. Halloysites have surface areas varying from 30 $m^2 g^{-1}$ to 170 $m^2 g^{-1}$ depending on the proportion of nanotubes, which account for the majority of the surface area [141].

Recently halloysite has been investigated for a range of applications, including a potential vector for controlled release drug delivery [142], as a biomimetic reactor [143], and as an additive to improve the thermal resistivity of plastics [144]. Despite such a range of uses, its application as a catalyst support material has so far been extremely limited. It has been used to support Pt for some addition reactions [145], Au for the oxidation of cyclohexene [146], and Ag for the reduction of nitrophenol [147]. As yet there are no reports in the literature of the use of halloysite-supported platinum group nanoparticles as hydrogenation catalysts for olefins, or any other organic functionalities.

Perlite is another aluminosilicate, a pyroclastic glass formed from the hydration of obsidian [148]. It contains small deposits of water occluded within its structure, which account for 2-5% of the material's mass. Upon heating, the glass softens and the water vaporises, the rapid expansion of which causes the material to foam, expanding to 10-15 times its original volume [149]. The resulting product is known as 'expanded perlite'. Like silica, the surface of perlite is hydroxylated to form silanols, and like silica, perlite exhibits no isoelectric point. Its surface remains negatively charged within the pH range 2-11 as measured using electrophoresis [150] or potentiometry [151], whether it is expanded or not. When suspended with background electrolytes containing divalent or trivalent cations, however, the surface charge is reversed [152].

Because of perlite's highly vesicular structure, numerous studies have been conducted on its adsorption properties. It has been found adept at adsorbing organic dyes such as methyl violet [153, 154] or methylene blue [155, 156], as well as heavy metals such as Cd [157], Cu [158], and Pb [159]. Despite these desirable characteristics, few studies have investigated its use as a catalyst support material. Several studies have illustrated it can be an effective support material for titania nanoparticles as a photooxidation catalyst for molecules like phenol [160], but none have employed the platinum group elements, and none have investigated reduction reactions such as hydrogenation.

2.1.2 Apatites

Hydroxyapatite (HAp) is a crystalline calcium phosphate material, representing the hydroxyl endmember of the apatite family. It is the major inorganic component of animal bone, representing up to 50% of total mammalian bone mass. Stoichiometric HAp has a Ca:P ratio of 1.67, and is represented by the chemical formula $Ca_5(PO_4)_3OH$. This is often doubled to $Ca_{10}(PO_4)_6(OH)_2$ as a more accurate representation of the unit cell, which crystallises with a monoclinic structure in the $P2_1/b$ space group [161, 162]. Each of the ions in the HAp lattice are labile to some degree, giving HAp a significant ion-exchange capacity. The consequence of these properties is that there is a great deal of interest in the development of HAp chemistry, especially in the field of biomedical materials [163-168], wastewater remediation [169-172] , and more recently as a support material for heterogeneous catalysts.

The use of HAp as a catalyst support material is not entirely new, however the vast majority of its uses have been reported within the last decade. While it has not gained widespread use as a catalyst support, it has been reported to be effective for a wide range of niche reactions. Among others, it has been used for Suzuki cross-coupling reactions [173, 174], allylic cross-coupling reactions [175], Diels-Alder cycloadditions [176, 177], dehalogenations [178, 179], as well as a variety of petrochemical applications [180-182]. By far the major use of hydroxyapatite in catalysis, however, is as a support for the oxidation of organic molecules. It has been used to oxidise siliceous molecules using either Au [183] or Ag [184], CO using Au [185], or Ni in the oxidation of aromatics [186]. Dehydrogenations have been performed using Au [187], and oxidative cleavage has been observed with Ru [188],

and the oxidation of amines to oximes and imines using Au [189]. As a subset of oxidation reactions, it has been used frequently as a support material in the oxidation of alcohols, where Ru [190, 191], Pd [38] and Au [192] have all been studied. Curiously there are only two accounts of formal hydrogenation reactions, where Pd has been used to hydrogenate phenol [193] and Ru has been used to hydrogenate quinoline [194], both with good success.

In all of these reports, the apatites used are entirely synthetic. They are often highly purified, crystalline, and stoichiometric, with similar microstructures and chemical properties to one another. Conversely, biological apatites ("bioapatites") can possess greatly different physicochemical properties, which are expected to influence their chemistry [195]. They are often partially carbonated by substitution of PO_4^{3-} groups for CO_3^{2-} during their formation, leading to the so-called B-type carbonated hydroxyapatite. They have only 20% as many hydroxyls as stoichiometric apatites [196], and possess unique mesoporous and microporous structures. Bioapatite has never been reported as a catalyst support materials, and so its use as such herein is entirely novel.

2.1.3 Cellulose

Cellulose is the most abundant biopolymer, comprising the majority of the structural mass of most plants. Structurally it consists of thousands of β(1→4) linked D-glucose units, each with equatorial hydroxyls in the $^4C_1$ chair conformation. The degree of polymerisation is shown to vary depending on the source. Wood cellulose, for example, contains approximately 10,000 glucose units per cellulose chain, while cotton contains 15,000. The cellulose chains can be crystallised into one of six polymorphs. Naturally-occurring ("native") cellulose is composed of either cellulose Iα or Iβ, while the other polymorphs are formed by either solubilisation and precipitation ("regeneration") or by swelling and de-swelling ("mercerisation") of native cellulose. The crystal structure of cellulose I is complex, and has eluded unambiguous elucidation for some time. It is generally considered that the unit cell is monoclinic, belonging to the $P2_{1/c}$ space group; that it contains two cellulose chains, each containing two ring portions per chain; and has a length of 1.034 nm [197].

As with several of the previously-discussed materials, cellulose is available in both "natural" and "synthetic" forms. One of the most common forms of synthetic

cellulose is microcrystalline cellulose. This is natural cellulose which has been partially hydrolysed to dissolve the amorphous regions, leaving only the crystalline regions, and then mechanically disintegrated, usually in a high-shear wet ("blunging") process. Many brands of microcrystalline cellulose exist, although perhaps the most common are the "Avicel" range. Cellulose can be obtained in many less processed and rawer forms, however, including cotton fibres. These have a unique microstructure, composed of large hollow fibres ("macrofibrils") assembled from bundles of nano-sized fibrils ("nanofibrils"). The high natural crystallinity of cotton cellulose makes it interesting as a catalyst support, which has been explored by a relatively small number of groups. Cellulose in varying forms has supported different metals, including Ag, Au [198], Pt, [199] Pd for Sonogashira [200] or Heck coupling [201], Cu for Michael addition [202], or Fe for dechlorination [203]. There are few reports on the efficacy of cellulose as a support in highly oxidising or reducing environments, however, and so its use has been further explored in the current research.

2.2 Experimental

2.2.1 Material Processing Methods

Many of the eight support materials investigated were used as received. Three of the materials, however, were deemed to require further processing to convert them to a useful form. These are described in the following sections.

2.2.1.1 Perlite

Expanded perlite, in its ordinary form, consists of small "pebbles" of a foamed glass. Not only do these float on water, but much of their surface area is internal and inaccessible. To make the perlite amenable to the immobilisation of metal particles, it was acid-leached, crushed, and wet-sieved. After initial oven-drying (100 °C for 48 hours), small portions were crushed in a ceramic mortar and pestle, reducing the volume nearly ten-fold. Organic material and non-structural metallic components like iron oxides deposits were removed by stirring the powder for 48 hours in an acid solution containing 3:1:1 HCl, HNO_3 and H_2SO_4. The dispersion was gravity-filtered through 500 mL Pyrex G2 fritted glass filter funnels, and washed with 0.5 M $NaHCO_3$ until the filtrate was neutral to pH indicator paper. The filtrand was further washed with 1 L of Type 1 water, and filtered through an Endecott laboratory test

sieve with 250 μm apertures. This process retained the naturally-occurring sand and other impurities on the sieve, and allowed *ca.* 95% of the perlite suspension to pass through. The filtrate was then gravity filtered using Whatman Type 1 filter paper, and dried in air at 100 °C for 48 hours. This sample of perlite was used for all further experiments reported in the current thesis.

2.2.1.2 Bioapatite

The bioapatite used for the current study was extracted from bovine femurs. The methods used to process the bovine bone used in this study were largely based on those employed by Mucalo, Laird, and Foster with some modifications [164, 166, 204, 205]. Bovine femurs were initially cut transversely half-way between opposing condyles. In order to remove the majority of the organic components from the bone, they were repeatedly pressure cooked. Each half was placed in a separate 7 L Hawkins domestic pressure cooker and filled with 60 °C tap water such that the bones were covered by water to a depth of 2 cm. The pressure cookers were placed on a domestic hob, and heated at full power until they began to vigorously vent steam, a process which took approximately 20 minutes. The heat was then decreased, and the bones were allowed to 'cook' for approximately 2 hours. After this period of time the cookers were removed from the hob, the pressure was vented, the fluid was drained, and the bones were rinsed and scrubbed free from any loosened organic material. This process was repeated a total of 5 times, after which the majority of the organic constituents appeared to have been removed. This repeated cooking process caused the bones to fracture and split into 3 - 5 individual pieces per femur half.

After completion of the pressure cooking process, the bones were calcined in a Tetlow muffle furnace to pyrolyse any residual organic matter within their pores. Because the pieces of bone were somewhat large (*ca.* 50 to 200 g each), it was necessary to use a temperature programme to control the production of smoke and unpleasant odours. Bones were initially placed in the furnace and heated at 150 °C for 10 minutes to evaporate any water and to allow organic matter such as fats to leach out from within the pores of the bones. The temperature was then increased to 250 °C, 350 °C and 500 °C, with holds of sufficient time to allow controlled pyrolysis to occur. At 500 °C there was generally very little smoke produced, so the temperature was increased to 1000 °C where it was held for 2 hours. The furnace

power was turned off, and allowed to cool overnight. A plot showing the temperature programme used is given in **Figure 5**.

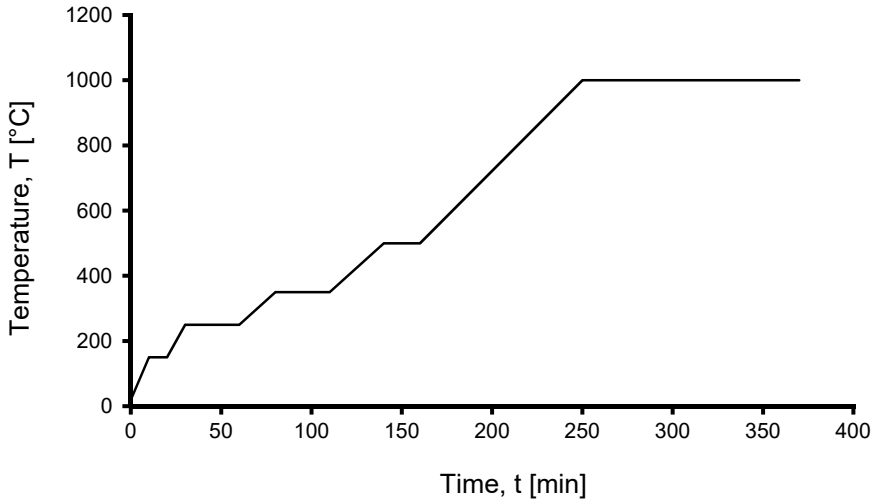

Figure 5: Temperature programme used for the calcination of bovine bones.

Once all of the individual pieces of an individual femur had been calcined, the remaining pristine white bone material was placed into a ceramic mortar, pulverised with a pestle, and then ground into a fine powder. The resulting powder was sieved to obtain the fraction ≤ 250 μm, and that which did not pass was re-ground until it did. The passing fraction was washed with distilled water until the filtrate had a pH of 7 in order to remove any calcium oxide formed during the calcination. It was then filtered, and dried at 100 °C for 48 hours. All of the bioapatite used in the current study derived from this single original batch.

2.2.1.3 Macrofibrillar Cellulose

Macrofibrils of cellulose were extracted from calico *via* acid attack. The textile was chopped into small squares, approximately 10 mm x 10 mm in size, and 50 g was placed in a 2 L conical flask with a magnetic flea. The sample was stirred vigorously with 500 mL of 0.5 M HCl and heated to 70 °C, where it was held for 1 hour. This treatment caused the fibres to separate from one another, forming a viscous suspension. The mixture was Buchner filtered through standard Whatman filter paper, followed by washing with 2 L of distilled water and 1 L of acetone and drying under vacuum. All of the macrofibrillar cellulose used in the current study derived from this single batch.

2.2.2 Instrumental Methods

Solid-state NMR spectra were collected using a Bruker Avance-III FT-NMR 300 MHz spectrometer, using a Bruker 4 mm H/X CP-MAS solids probe. Samples were packed into 4.0 mm (outer-diameter) ZrO_2 rotors and stoppered with "Kel-f" caps. All spectra were collected at 300 K. Parameter sets were fine-tuned by systematically altering the acquisition variables to maximise signal intensity and minimise observed linewidths. The optimised parameters are summarised in **Table 2**. Proton spectra were referenced to adamantane, carbon spectra to glycine, aluminium spectra to yttrium aluminium garnet, silicon spectra to 3-(trimethylsilyl)-1-propanesulfonic acid sodium salt, and phosphorus to Na_2HPO_4.

Table 2: Acquisition and data processing parameters for solid-state NMR experiments.

Parameter	**$^{1}H^{*}$**	**$^{1}H \rightarrow ^{13}C^{\dagger}$**	**$^{27}Al^{*}$**	**$^{29}Si^{*}$**	**$^{31}P^{*}$**	**$^{1}H \rightarrow ^{31}P^{\dagger}$**
Pulse length (μs)	4.00	3.50	1.00	3.50	4.00	4.00
Acquisition time (ms)	134	44.1	34.6	43.0	42.1	34.2
Contact time (ms)	-	-	-	-	-	-
MAS rate (Hz)	15000	4000	15000	15000	15000	8000
Transients	100	3000	2000	10000	500	1000
Data points	4096	2048	2048	1024	1024	2048
Gaussian broadening	0.05	0.05	0.05	0.05	0.05	0.05
Line broadening	20	25	50	40	0	5

* Direct-polarisation (Bloch decay). † Cross-polarisation from ^{1}H.

FTIR spectra obtained from samples prepared as KBr discs were recorded using a Perkin Elmer Spectrum 200 FT-IR spectrometer with 4 cm^{-1} resolution between the ranges of 4000 cm^{-1} to 500 cm^{-1}. Typically 10 scans were recorded per spectrum. Samples were prepared by grinding with oven-dried KBr and pressing at 10 tonnes in a Specac die set. The ratio of sample to KBr was varied depending on the sample measured. MicroFTIR spectra were recorded using a PerkinElmer Spectrum Spotlight 200 FT-IR microscope at 2 cm^{-1} resolution using a 1 mm^2 aperture between the ranges of 4000 cm^{-1} to 500 cm^{-1}. The number of scans was varied between 10 and 500 per sample to obtained spectra with acceptable signal to noise ratios. Spectra were digitally smoothed where necessary using a Savitzky-Golay filter, ensuring minimal loss of detail.

SEM micrographs were recorded on a Hitachi S4700 FE-SEM, using accelerating voltages between 2 kV to 10 kV depending on the sensitivity of the sample to the beam. EDS spectra were recorded at 20 kV using the NORAN System Six software. All elements were quantified from their Kα emission lines using a standardless method. Samples were prepared by placing double-sided carbon tape onto the surface of a 15 mm aluminium stub, and spreading a thin layer of the material to be analysed upon it. Samples were sputter-coated with a thin layer of platinum prior to analysis.

TEM micrographs were collected using a Philips CM-30 Transmission Electron Microscope operated with an accelerating voltage of 250 kV. An Advanced Microscopy Techniques (AMT) digital camera was used for the collection of digital micrographs, and operated using AMT Advantage 6.00 software. Samples were prepared by mixing *ca.* 10 mg of the solid powder in 20 mL of Type I distilled water in a test-tube and sonicating for up to 15 seconds. The resulting suspension was allowed to settle until the supernatant retained only the faintest turbidity observable with the naked eye, a drop of which was placed onto a 400-mesh copper grid coated with collodion. The grid was placed in an oven at 25 °C for a period of between 24 and 48 hours.

XRF analyses were performed using a Spectro X-Lab 2000 with a Pd anode using a 4000-channel Si(Li) detector with an energy resolution of <154 eV measured at the Mn kα line. The certified reference materials BHVO-2 (a Hawaiian lava) and BX-N (a French bauxite) were used as comparators to ensure the accuracy of the analysis. Samples were prepared as 40 mm pressed pellets. Approximately 5 grams of each sample were placed into wax-coated paper cups, and a 20 wv% solution of poly(vinyl alcohol) was added dropwise with stirring until a tacky consistency was reached. The mixtures were transferred into aluminium sample cups and pressed at 80 bar for 1 minute, followed by drying overnight at 70 °C in air.

Laser diffraction particle size analyses were performed using a Malvern Mastersizer 2000 with the 'Hydro 2000G' accessory. Powders were dispersed in distilled water without the addition of dispersants. Refractive indices were obtained from the literature. Particle size distributions were calculated from the scattering data assuming spherical morphology, and are therefore only indicative for materials with non-spherical morphologies.

All diffractograms were recorded on a PANalytical Empyrean multi-purpose x-ray diffractometer using Ni-filtered Cu Kα radiation and PIXcel^{3D} detector operated in 1D mode. Incident optics included a programmed divergence slit set to illuminate 20 mm, 0.04 rad soller slits, a 20 mm beam mask, and a 2° antiscatter slit. Samples were prepared by grinding in a mortar and pestle and back-filling a 30 mm sample holder, which was spun at 1 Hz. Diffracted beam optics included a 7.5 mm receiving slit and 0.04 rad soller slits and a Ni filter. No further monochromation was used. Diffractograms were recorded over the 2θ range 10° - 90° in 0.035° steps over a period of 8 hours.

Zeta potential measurements were carried by preparing aqueous suspensions of the analyte support material. Samples were prepared by charging a 250 mL beaker with 0.1 g of the solid support material, 100 mL of Type-1 distilled water, and a magnetic stirbar. No background electrolytes were used. The suspensions were stirred as fast as possible without entraining the atmosphere into the solution, resulting in the formation of bubbles. The pH of the suspensions were then adjusted to, and maintained at, the desired value using a Radiometer ABU901 pH stat controlled by a Radiometer PHM290 with a combination glass pH electrode and a Radiometer thermocouple, using solutions of either 0.01 mol L^{-1} HCl or NaOH. The typical range pH range studied spanned from 4 to 12. Once the pH had stabilised and drifted by no more than 0.02 min^{-1}, a quartz fluorescence cuvette was washed and filled with 0.5 mL of the suspension, and analysed by electrophoretic light scattering. Analyses were carried out using a Malvern Zetasizer 3000HS_A with a 535 nm He-Ne laser, equipped with the Malvern DTS5001 aqueous dip-cell. Analyses were performed 20 times per sample in automatic mode, with zero-field correction applied to subtract the effect of Brownian motion, and analysis of the correlograms performed in the ranges of -200 mV to +200 mV.

2.2.3 Materials

Supports. SiO_2 (silica gel, >99.9%) was obtained from Merck. Al_2O_3 (>99.5%, "AnalaR" analytical reagent, calcined) was obtained from BDH Chemicals Ltd. Hydroxyapatite (≥99%, sold as "tricalcium phosphate") and Microcrystalline cellulose (Avicel® PH-101) were both obtained from Fluka Chemika. Halloysite (premium grade) was generously donated by Imerys. Perlite (Australian, purities not

stated) was obtained from Egmont Commercial Ltd. Bioapatite was extracted from Hereford cattle femurs sourced at a local butchery. Bleached calico was obtained from a local textile shop and used as the source for the macrofibrillar cellulose.

Reagents. HCl (37%, ACS ISO Reagent) was obtained from Merck. H_2SO_4 (>95%, "Univar" analytical reagent) and HNO_3 (70%) were obtained from Ajax Finechem Pty. Ltd. $NaHCO_3$ (laboratory chemical, >99%) was obtained from May & Baker Ltd. NaOH "mini pearls" (>97.0%, "Univar" analytical reagent) were obtained from Ajax Finechem Pty. Ltd. Ethanol ("Unilab" laboratory reagent, >99%) was obtained from Ajax Finechem Pty Ltd. Polyvinyl alcohol (M_W ~22,000) was obtained from BDH Chemicals Ltd.

NMR Standards. Yttrium aluminium garnet (99%) and 3-(trimethylsilyl)-1-propanesulfonic acid sodium salt (97%) were obtained from Aldrich chemicals. Na_2HPO_4 was obtained from BDH Chemicals Ltd. Adamantane and glycine standards were used as received from Bruker, pre-packed in ZrO_2 rotors with KelF caps.

2.3 Results and Discussion

2.3.1 Silica

The silica used in this study was a free-flowing white powder with a granular texture. Analysis of the powder by SEM showed it was composed of faceted primary particles with no evidence of agglomeration, and with a mean particle of 94 μm ± 40 μm. An example micrograph is shown in **Figure 6**. LDA showed the volume-surface average size was 147.9 μm ± 62.8 μm, consistent with the electron microscopy data. Analysis of individual granules by TEM revealed the primary particles were composed of a random but closely packed array of nanoparticles fused to one another, producing a series of random and irregular interpenetrating pores 1-5 nm in size. This morphology is typical of sol-gel derived silicas, and presumably gives rise to the high surface area (550 m^2 g^{-1}) specified by the manufacturer. BET studies by Ek *et al.* of a similar silica gel from the same manufacturer yielded a similar surface area of 495 m^2 g^{-1} [206].

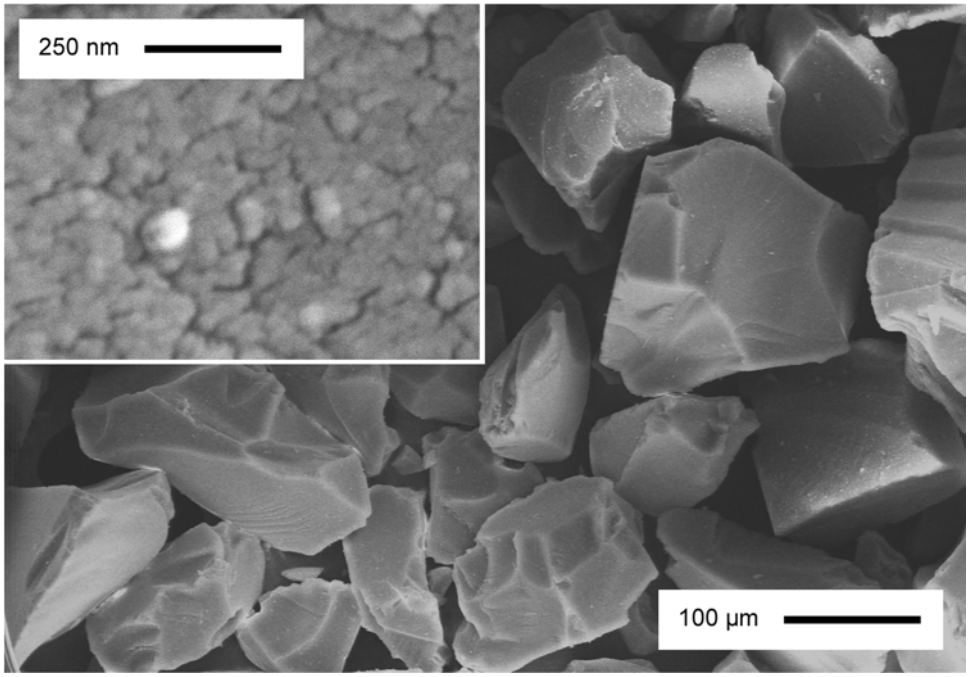

Figure 6: SEM micrographs of commercial silica gel. Inset: high-magnification image showing the surface of the particles, with some degree of porosity evident.

Elemental analysis of the sample by EDS gave an approximate composition of 53 wt% oxygen and 47 wt% silicon, which is consistent within 0.3% of the empirical formula SiO_2. Analysis by XRF gave similar results, but also showed the presence of a number of trace elements, the largest of which being 2250 ppm of sodium. This could exist as an impurity from the synthesis of the silica gel, if for example it was prepared by precipitation from a sodium-containing silicon source, such as sodium silicate [207].

The ^{29}Si solid-state NMR spectra, shown in **Figure 7**, displayed three major resonances within the spectral region studied. The chemical shifts of these resonances are consistent with their origins from one of three different silicon environments within the sample: the so-called "Q^2" environments, from silicon atoms bearing two (geminal) silanols; the "Q^3" environments, from silicon atoms bearing only a single silanol, or from the "Q^4" environments, which are silicon atoms bearing no silanols [208]. All three resonances were observed regardless of which polarisation method was used, however the relative intensities of the Q^2 and Q^3 peaks were significantly higher in the cross-polarised spectrum, which is consistent with a high concentration of silanols within the sample. Since these occur primarily

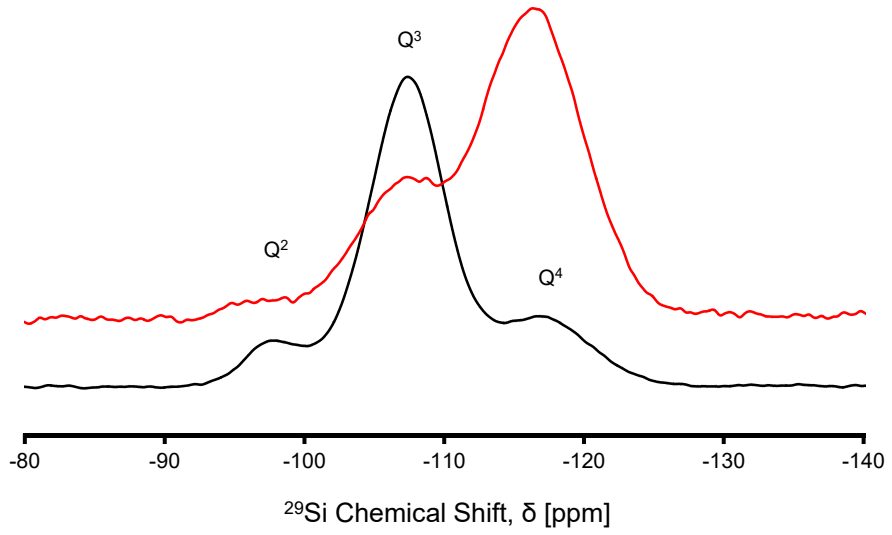

Figure 7: ^{29}Si DPMAS and ^{1}H-^{29}Si CPMAS NMR spectra of commercial silica gel.

at the surface, this is in turn consistent with the high surface area observed by TEM and specified by the manufacturer.

The ^{1}H solid-state NMR spectrum, shown in **Figure 8**, also displayed three major resonances. The chemical shifts of these correspond to hydrogen-bonded silanols, physisorbed water, and isolated silanols [209], which is further consistent with the structural and chemical properties observed thus far. Similar spectra were obtained by Trébosc for MCM-41 ("Mobil Composition of Matter") mesoporous silica nanoparticles, though their spectra exhibit two additional environments [210], since MCM-41 has slightly different structure.

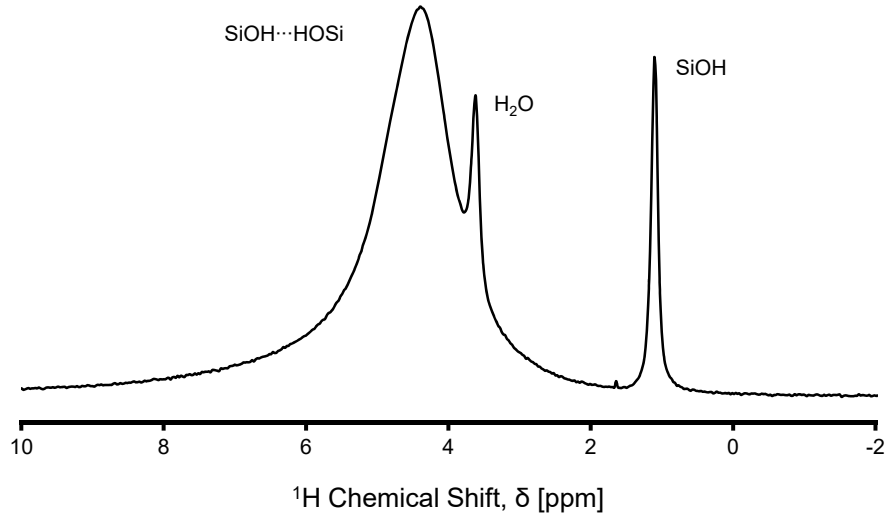

Figure 8: ^{1}H DPMAS NMR spectrum of commercial silica gel.

Infrared spectra of the sample, shown in **Figure 9**, generally support the observations made by NMR. They are dominated by a broad absorption at 3500 cm^{-1}, corresponding to the silanol O-H stretching vibration [211]. This indicates a high degree of hydration of the silica gel, as well as the presence of multiple hydroxyl environments [212]. The small band at 1646 cm^{-1} is identified as a superposition of the H-O-H bending mode for adsorbed water which occurs at 1635 cm^{-1} and the Si-O stretch overtone, commonly observed at 1640 cm^{-1}. The large peak at 1100 cm^{-1} cannot be assigned unequivocally, as there is significant controversy over the identity of many of the high-energy vibrational modes of silicas in region of 1000-1300 cm^{-1} [213, 214]. The weak peaks at 1996 cm^{-1}, 1870 cm^{-1} are assigned as the SiO combination, and the peak at 826 cm^{-1} as the SiO stretch [215].

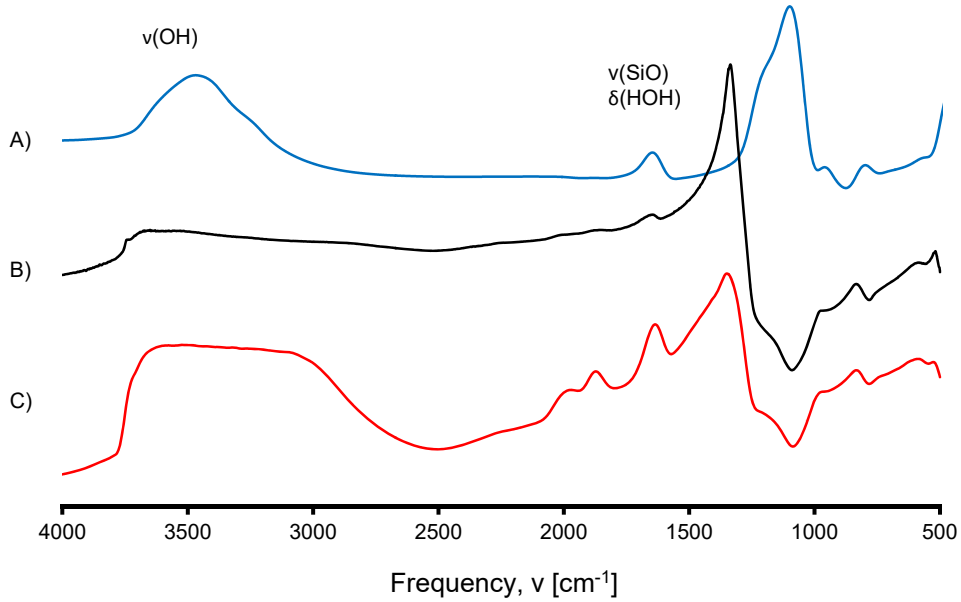

Figure 9: FTIR spectra of commercial silica gel. The different plots correspond to spectra recorded in different ways: A) transmission mode, KBr disc; B) MicroIR of a pressed pellet of the powder; C) MicroIR of the loose powder.

The powder diffraction pattern of the sample, shown in **Figure 10**, displayed a single broad peak at 21° superimposed on a relatively flat background, sloping downward toward higher angles. The lack of any sharp diffraction peaks at moderate to high angles necessarily indicates there is no long-range periodicity present within the sample, which means it is non-crystalline. This implies the sample is not composed of any of the crystalline polymorphs of silica like quartz or cristobalite, leaving amorphous silica as the only option for the structure of the sample. It may be argued that the presence of the 21° peak necessarily means the sample contains some

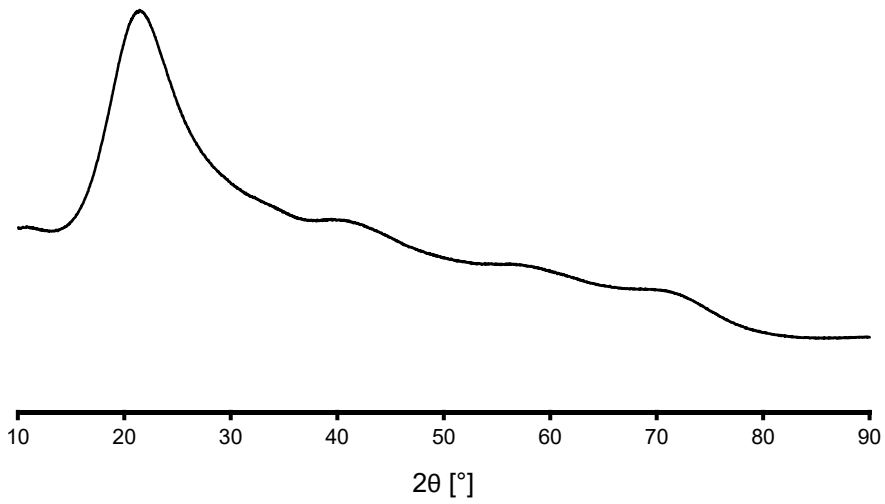

Figure 10: XRD pattern of commercial silica gel.

degree of order and is therefore not amorphous, however this 'first sharp diffraction peak' has been explained by Himmel and others as originating from medium-range order in the siloxane ring structure of silica gels [216-218]. Calling the sample amorphous is therefore somewhat of an arbitrary decision, since the degree of crystallinity is a continuous property, and no such material may exist which is completely crystalline or completely amorphous. The structures of all materials are geometrically restricted by the chemical bonds their constituent atoms can form, and thus a truly random structure cannot exist. It is convention, however, to refer to materials which give diffraction patterns such as this as 'amorphous'.

Zeta potential measurements of a 1.0 g L^{-1} slurry of the silica showed the surface charge of the particles was strongly dependent on the pH of the solution. Data from these measurements are displayed in **Figure 11**. At all pHs the zeta potential was negative, developing the greatest charge of -34 mV at pH 8.5, but returning to nearly 0 mV at pH 3.5. The pH of the slurry prior to pH adjustment was *ca.* 5, consistent with very mild Brønsted surface acidity, which is a known property of silica-water interfaces [219]. These results are generally consistent with other reports of the surface properties of silica gels [220-227], making the sample very typical in this respect.

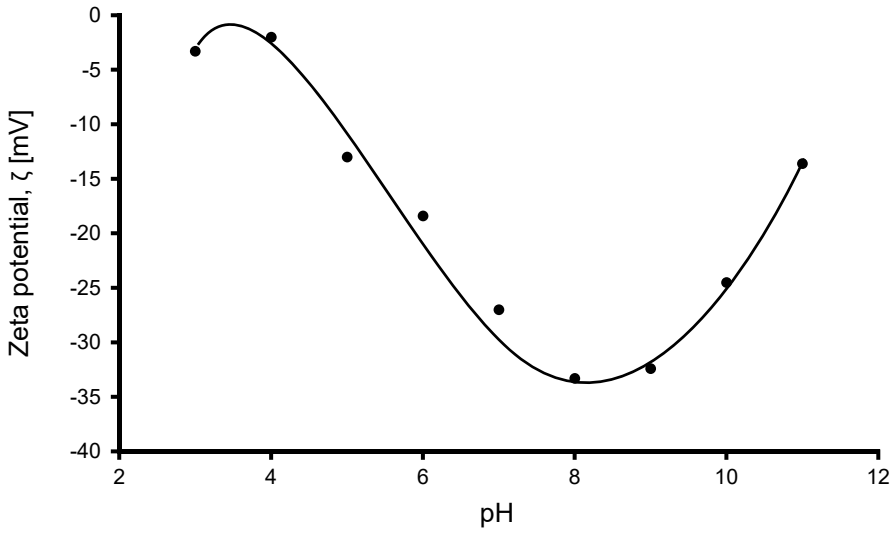

Figure 11: Zeta potential of an aqueous suspension of commercial silica gel as a function of pH.

2.3.2 Alumina

The alumina used in this study was a free-flowing white powder with a gritty texture. Analysis by SEM revealed that it was composed of spherical aggregates 63 μm ± 31 μm in size, each consisting of hundreds of smaller plate-like particles fused perpendicularly to one another, as shown in **Figure 12**. LDA gave similar results, showing a gaussian particle size distribution with a mean of 82.8 μm ± 29.7 μm. The similarity between the two measurements is consistent with the aggregates remaining intact during the dispersion process, at least for periods of time in the order of the experiment length.

Elemental analysis of the powder by EDS, performed concurrently with SEM imaging, detected Al and O as the only elements present in the sample, at concentrations of 46 wt% and 54 wt% respectively. Independent analysis by XRF showed the only major detectable element in the powder was aluminium, with a concentration of 47.61% by mass. A small amount of silicon was detected (0.8 %), although this may have been introduced during the sample grinding procedure. The only significant trace elements detected were sodium (0.46%) and sulphur (193 ppm). The results, both being similar, were consistent with the empirical formula Al_2O_3.

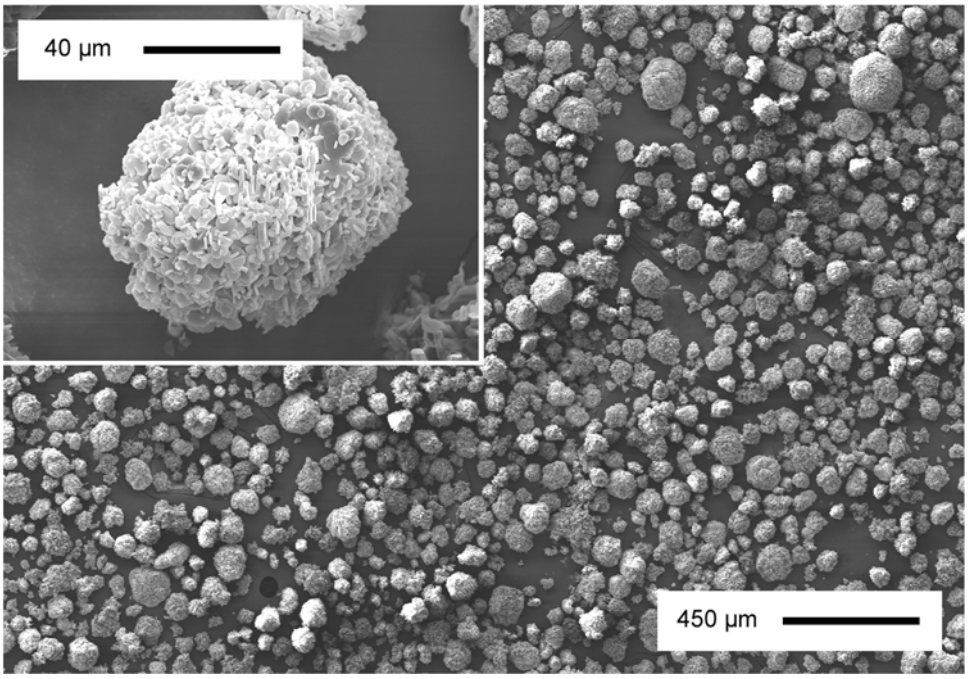

Figure 12: SEM micrograph of the commercial alumina. Inset: an individual particle.

With the empirical formula of the alumina sample determined, the phase purity and identity were investigated by both solid-state NMR and XRD. The ^{27}Al DPMAS NMR spectrum, shown in **Figure 13**, exhibited two resonances; one at 15 ppm, corresponding to the resonances of octahedrally-coordinated AlO_6 centres, and a second, much smaller resonance at *ca.* 71 ppm, corresponding in position to AlO_4 centres. This was not a spinning sideband, since it did not shift with changes to the MAS rate. No known pure phases of alumina have a composition which would give rise to this pattern, suggesting the sample may be predominantly composed of a phase containing only octahedral alumina, probably α-alumina [228], but may possess a small portion of another alumina phase as an impurity, responsible for the tetrahedral peak. Attempts at collecting ^{27}Al spectra cross-polarised from ^{1}H were unsuccessful, as were regular ^{1}H spectra. This suggested that the sample contained relatively few hydroxyl groups, if any, and also that tetrahedral the impurity was probably not an aluminium hydroxide, since these give characteristic peaks in the ^{1}H spectrum [229].

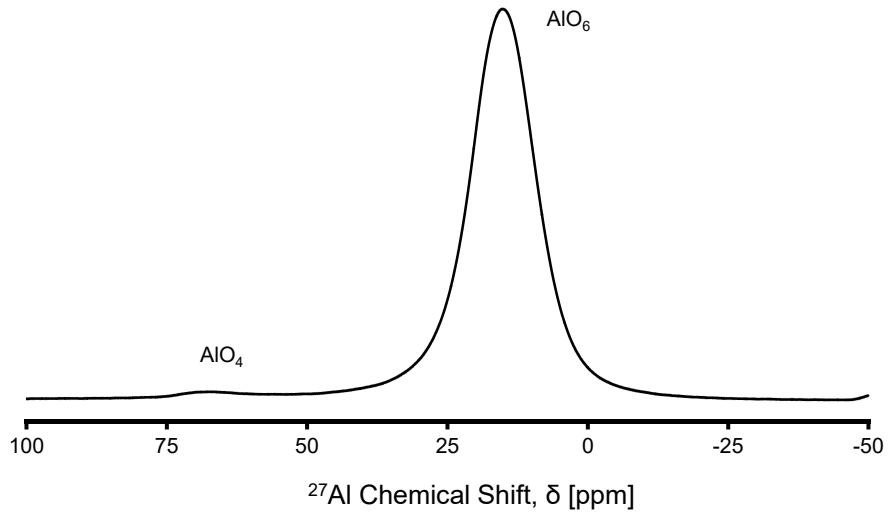

Figure 13: ^{27}Al DPMAS NMR spectrum of commercial alumina. Octahedral and tetrahedral environments are both clearly visible.

The hypothesis that the sample was comprised predominantly of α-alumina was confirmed by x-ray powder diffraction, the pattern from which is shown in **Figure 14**. The pattern contained a series of sharp peaks with full widths at half maximum (FWHMs) of *ca.* 0.1°, matching previously reported α-alumina patterns such as the International Centre for Diffraction Data Powder Diffraction File (ICDD PDF) 01-077-2135.

Anticipating that the diffraction pattern may also contain some clues as to the identity of the impurity peak observed in the NMR, pattern matching of the minor diffraction peaks was also attempted. This itself gave no strong evidence for the

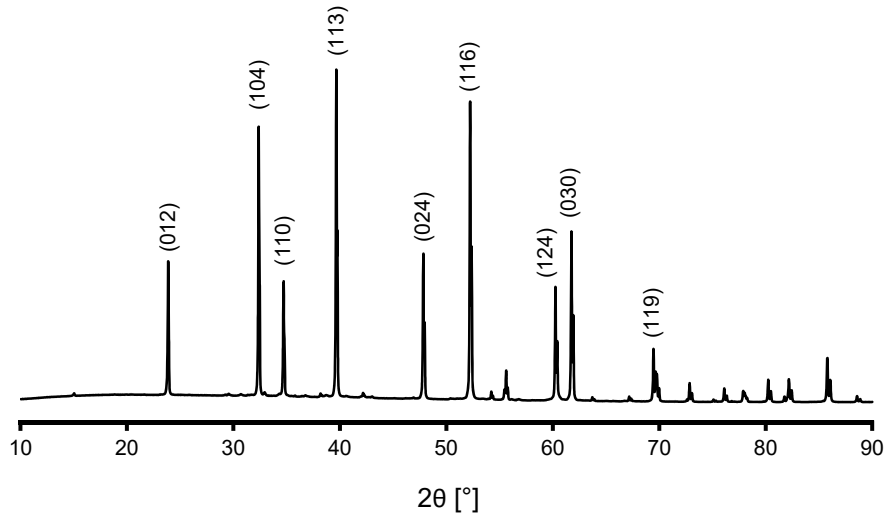

Figure 14: XRD pattern of commercial alumina with major reflections labelled. Noteworthy is the very subtle but non-flat background.

identity of the impurity, however, as almost all high-temperature phases of alumina contain varying proportions of other polymorphs with similar diffraction patterns. Though these can vary depending on the nature of the precursor material [230, 231], it seems generally agreed that calcination at 1000 °C produces samples containing mixtures of the α, γ, and θ phases [232, 233]. Both the γ and θ phases contain a portion of tetrahedral aluminium, however, and so the impurity was expected to be one of these two phases.

Infrared spectroscopy of the powder gave simple spectra, devoid of features at all but the low energy end. These are shown in **Figure 15**. The bands were broad and poorly resolved, which is consistent with a strained lattice possessing multiple phases, and consequently having many possible vibrational modes. While the bands observed in these spectra compare favourably with previously reported spectra of α-alumina, unequivocal assignment is hampered by ambiguity surrounding some of their origins [233]. The lowest-energy bands at 427 cm^{-1} and 457 cm^{-1} originate from Al-O vibrations within the AlO_6 subunits, while the peak in the valley at 506 cm^{-1} most likely originates from Al-O bends within the same. [231]. The features spanning 600 cm^{-1} through 800 cm^{-1} are variously assigned as originating from the surface of the material, either from adsorbed water or combination Al-O modes of some type.

The weak shoulder at 1068 cm^{-1} may correspond to a surface aluminol bend, especially given the observation of an equally weak absorption at *ca.* 3300 cm^{-1}, corresponding to the equivalent ν(Al-OH) mode. Though it has been said that the

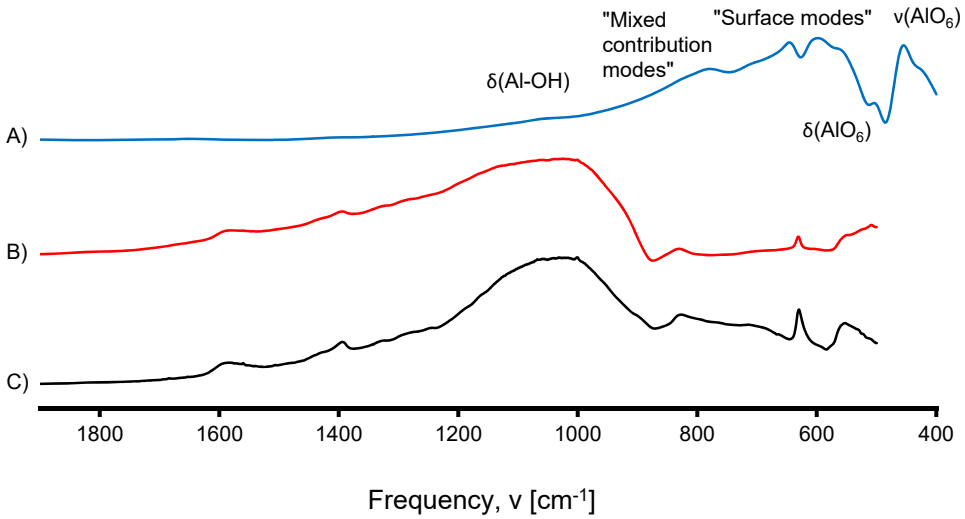

Figure 15: FTIR spectra of commercial alumina. The three plots correspond to spectra recorded in different ways, A) transmission/KBr, B) MicroIR of loose powder, C) MicroIR of a pressed pellet of the powder.

sample is "devoid" of hydroxyl groups, infrared microscopy performed in reflectance mode is more surface-sensitive than traditional instrumental configurations. Vibrational modes with high molar absorptivities such as hydroxyl stretches and bends are therefore expected to be unusually strong, and can be seen when using reflectance methods [234]. Spectra of the current sample exhibit a broad, weak, absorption spanning the ranges 2900 cm^{-1} to 3700 cm^{-1}, probably corresponding to adsorbed water, with a sharper peak superimposed atop it at 3270 cm^{-1}. A summary of the types of surface hydroxyls in calcined aluminas by Ballinger and Yates [235] suggests that the frequency of this sharp mode probably corresponds to hydrogen-bonded aluminols. Though the sample was calcined at high temperature by the manufacturer which may be expected to induce thermal dehydroxylation, aluminas treated in this way have been known since very early on to possess a low concentration of surface hydroxyls, less than a monolayer [236], and this may be an example of such.

Zeta potential measurements showed the surface charge of the alumina powder depended strongly on pH, even more so than for silica. Data is shown in **Figure 16**. The maximum observed charge was *ca.* +60 mV at pH 3.0, decreasing to a minimum value of *ca.* -40 mV at pH 8.0, and with an isoelectric point of 7-8. The results are consistent with many previously reported electrokinetic studies on alumina [225, 237-241]. The pH of a 1 g L^{-1} aqueous suspension, without adjustment, was *ca.* 8.5, indicating low-level Brønsted basicity. These results are conflicting, however, because a material which increases the alkalinity of a solution is basic, and basic materials are those which increase the concentration of hydroxyl ions in solution. Regardless of whether this occurs by abstraction of protons from water molecules or by dissociation of a surface bond to release hydroxide ions, the surface charge should be positive, which the zeta potential data indicates is not the case at pH 8.5. The data thus represents a charge reversal from what could be expected *a priori*, suggesting there are unusual surface phenomena occurring, or that the measurements are erroneous.

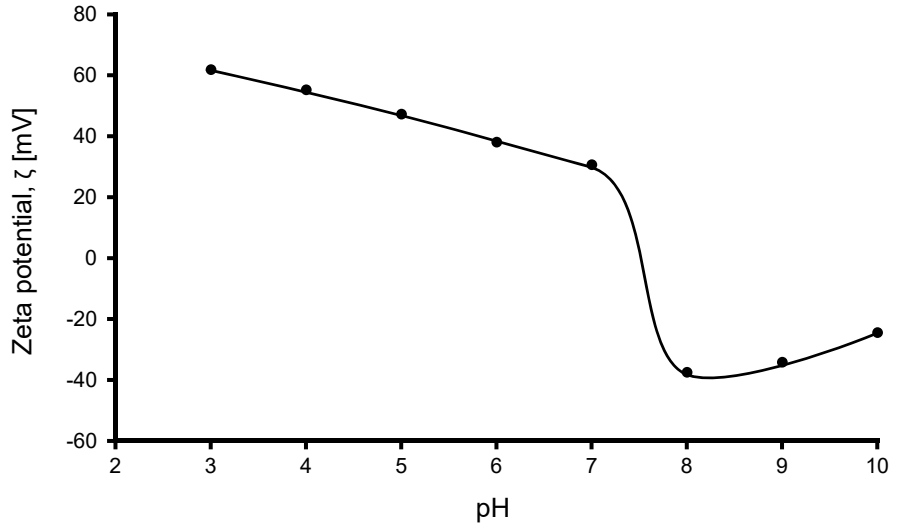

Figure 16: Zeta potential of an aqueous suspension of commercial alumina as a function of pH.

2.3.3 Hydroxyapatite

The hydroxyapatite used in this study was a white powder composed of soft, cohesive, polydisperse grains. Analysis by SEM showed the grains were predominantly round and oblate, with an average particle size of 12 μm ± 8 μm. A typical micrograph is shown in **Figure 17**. Their rough surfaces suggested that they were aggregates of many smaller particles, but at increased magnifications it became evident that they were not, and the roughness was due to high concentrations of macropores interpenetrating throughout the particles. Analysis by TEM, however, suggested a morphology somewhat like that of the silica, where the pores are just the interstitial spaces formed by the growth and sintering of smaller HAp grains as is typical of solids grown by solution methods. The porosity observed is consistent with the colour, since HAp single crystals are clear and colourless, thus introducing pores to a sample, which scatter light, would cause it to appear white.

The laser diffraction data indicated that the particle size distribution in water was bimodal, composed of a small portion by volume of 2 μm sized particles, and a much larger fraction of particles around 1 mm in size. The average was 520 μm ± 410 μm. This is consistent with the visual properties of the sample, which indicated there were a small portion of large grains but predominantly small ones. Importantly, this also shows that the HAp grains do not disintegrate readily in water, which could have potential implications on the accessible surface area available for the immobilisation of nanoparticles.

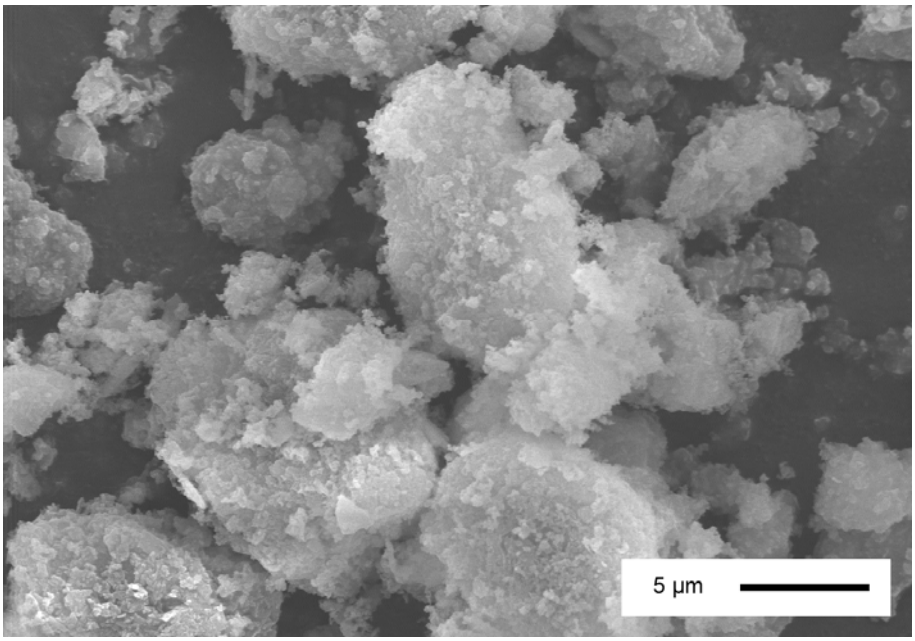

Figure 17: SEM micrograph of commercial hydroxyapatite.

Elemental analysis by XRF showed the sample was composed of 20.0% P and 39.2% Ca, corresponding to a Ca:P ratio of 1.51. This is significantly less than the value of 1.67 for stoichiometric HAp, suggesting that either the sample was either significantly calcium-deficient, or the analysis was wrong. A secondary analysis by ICP-MS of the digested sample gave an average Ca:P ratio of 1.76 ± 0.10, which is significantly closer to the stoichiometric value, but indicated, conversely, that the sample was calcium-rich. Which one of these values is more accurate is unknown, and so no reliable inferences could be made from this data other than that the sample was 'probably close to stoichiometric'.

The infrared spectra, shown in **Figure 18**, were typical of a highly crystalline, stoichiometric hydroxyapatite. The KBr spectrum was dominated by the phosphate vibrational modes; the ν_1 symmetric stretch at 967 cm^{-1}, and the ν_3 antisymmetric stretches 1094 cm^{-1} and 1046 cm^{-1}. The strength of these absorptions gives rise to a sharp change in the refractive index of the sample at this wavelength, leading to a strong derivative-like band in the MicroFTIR reflectance spectrum, which was especially pronounced when measured as a pellet. These are designated '*restrahlen bands*' (or restrstrahlen), which arise due to changes in the refractive index of a medium concurrent with a strong absorption band This is shown especially to occur in solids composed of fine particles, which is consistent with the observations made by TEM [242]. The ν_2 mode was not observed in the reflectance spectra as it is

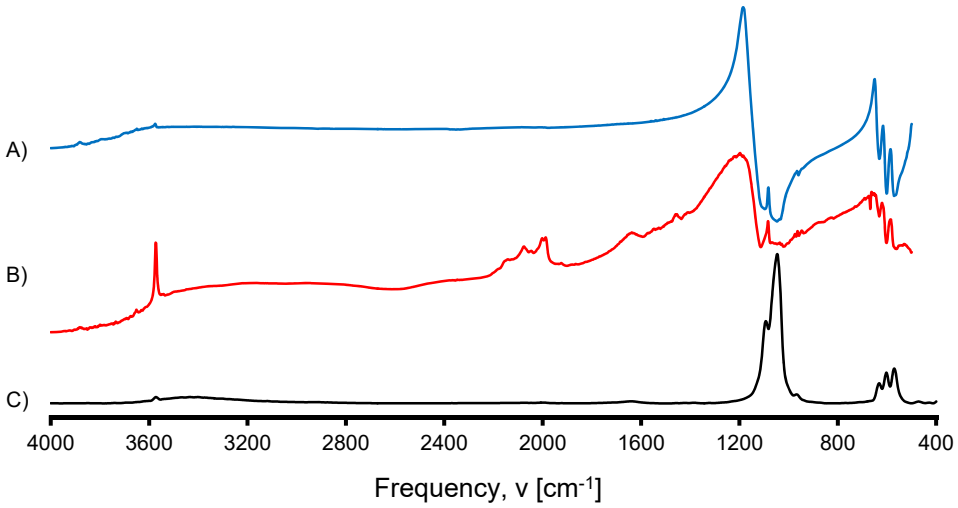

Figure 18: FTIR spectra of commercial hydroxyapatite. The three different plots correspond to spectra recorded in different ways; A) microIR of a pressed pellet, B) microIR of a loose powder, C) transmission though KBr.

outside the operable range of the MCT detector used, but was observed in the transmission spectra at 470 cm^{-1}. The three smaller peaks at 571, 604 and 632 cm^{-1} are attributed to the ν_4 antisymmetric phosphate bending modes. The sharpness of these peaks suggests that the sample is highly crystalline [243]. The hydroxyl stretch at 3570 cm^{-1} was observable in the KBr spectrum but extremely weak, while it was more dramatic in the reflectance spectra [243-245]. A broad absorption at slightly lower frequencies suggests that the sample bears a small portion of adsorbed water. No evidence of carbonate substitution was observed. The presence of hydrogen phosphate groups was also not observed.

The solid-state NMR spectra generally supported the observations made by infrared spectroscopy, but contained some additional information suggesting the presence of a significant impurity in the sample. The ^{1}H spectrum, shown in **Figure 19**, exhibited two major features. A sharp and intense resonance was observed at -0.11 ppm corresponding to the structural hydroxyl groups, and a broad, weak water peak at 5.8 ppm, corresponding to adsorbed water. Lack of any features at lower field precluded the presence of any significant concentration of hydrogen phosphate ions, supporting the observations made by FTIR.

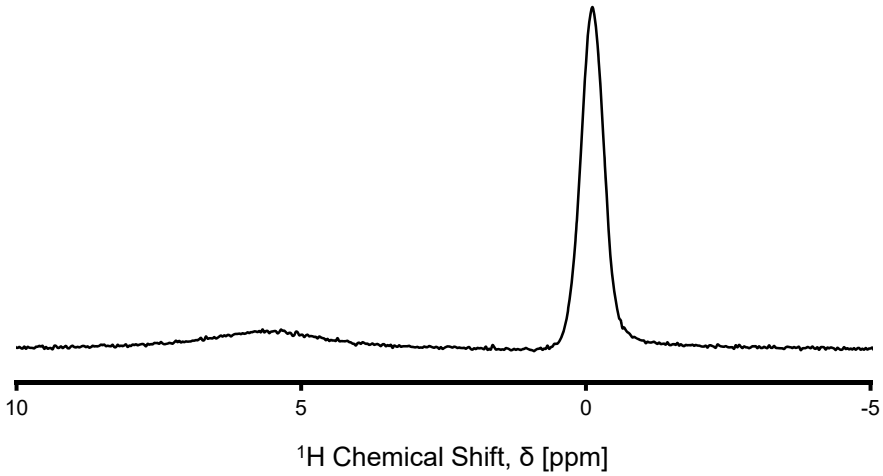

Figure 19: ^{1}H DPMAS NMR spectrum of commercial hydroxyapatite.

The ^{1}H→^{31}P CP spectrum, shown in **Figure 20**, exhibited a single narrow resonance at 2.57 ppm corresponding to resonance of the structural phosphate phosphorus atoms, which is typical of crystalline samples with 'large' particle sizes, as opposed to nano-sized hydroxyapatite particles [246]. Interestingly, however, the direct-polarised ^{31}P spectrum exhibited a manifold of smaller peaks, which are obviously a non-apatitic phase. The chemical shift range covered by this manifold includes many of the common calcium phosphates [247], although many of these can be excluded from the current sample because they contain hydrogen atoms, which would give rise to a third environment in the ^{1}H spectrum. Additionally they are not observed in the cross-polarised spectrum ^{31}P spectrum, so it was concluded that they arise from an amorphous proton-deficient phase like tricalcium phosphate.

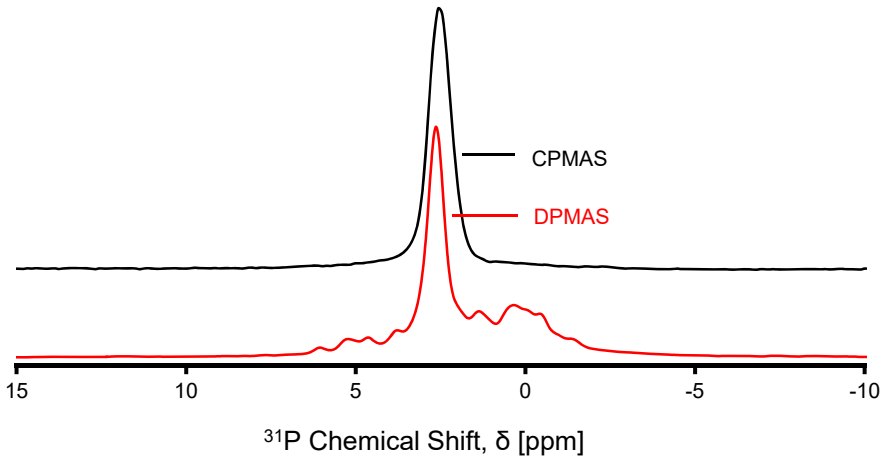

Figure 20: ^{31}P DPMAS NMR spectrum of commercial hydroxyapatite.

The powder diffraction pattern of the sample, shown in **Figure 21**, displayed more than 50 peaks in the 2θ region 10-90°, reflective of the large number of atoms in the HAp unit cell. The width of the peaks ranged from 0.2° to 1° FWHM, which again suggested the sample was highly crystalline, with large domain sizes and little residual stress, consistent with both the IR and NMR analyses presented earlier. The pattern was generally consistent with the sample being composed predominantly of HAp, however there were several peaks in the pattern which do not arise from this phase, for example the 29.2° peak directly adjacent to the HAp (211) reflection. Database searches suggested the bulk of the peaks were explained by HAp, ICDD PDF 01-074-4172, as well as a small fraction of β-TCP (tri calcium phosphate), ICDD PDF 01-070-2065, in an approximate 4:1 ratio. In order to explain the multiple additional environments in the NMR spectra, however, there must be multiple additional phases in the sample which have diffraction patterns similar to HAp or TCP, or a an amorphous x-ray invisible component.

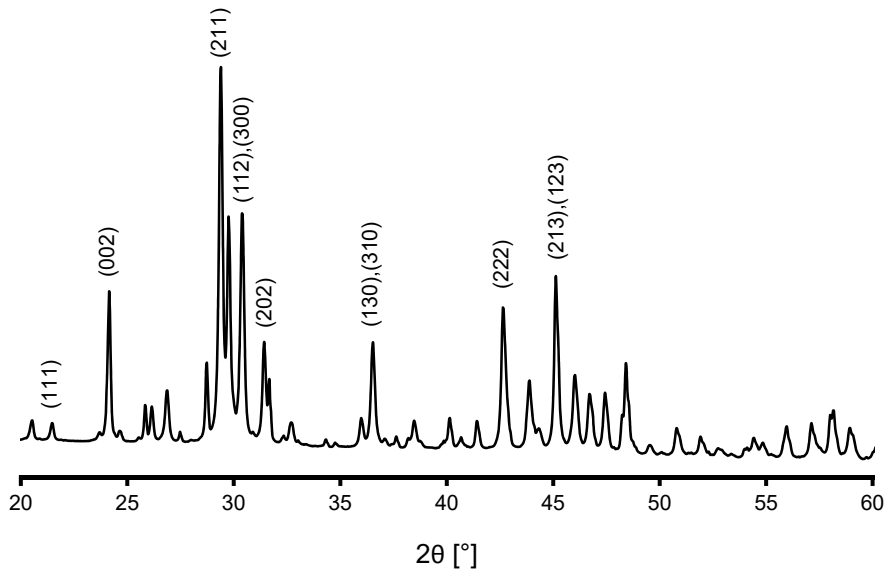

Figure 21: XRD pattern of commercial hydroxyapatite. Selected major reflections are labelled with the corresponding Miller indices from which they originate.

When the powder was dispersed in water at a concentration of 1 g L^{-1} the pH was 7.1, which indicates the sample has very mild Brønsted basicity. The surface charge of the suspended particles varied mildly as a function of pH as shown in **Figure 22**, which is similar in profile to previously reported hydroxyapatite samples [248]. The maximum charge of -17.3 mV was observed at pH 11, which increased steadily toward zero as the pH was decreased to 5. Below this pH the sample began to dissolve and could no longer be analysed. This is important, however, as dissolution

of the sample will release calcium ions into solution, which are shown to specifically adsorb on apatite surfaces and reverse the sign of the surface charge. This has wide-reaching implications for the adsorption of species such as metal salts, since those which are negatively charged will be repelled by the apatite surface unless they are sufficiently acidic to dissolve it, in which case calcium ions may be released, the charge may be reversed, and adsorption may proceed. Conversely, cationic species may be attracted to the apatite surface unless they are too acidic, in which case they will be repelled.

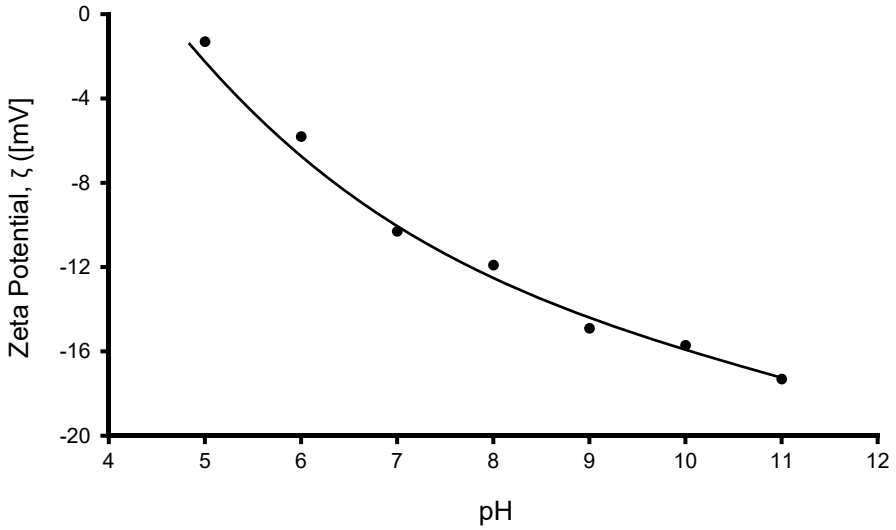

Figure 22: Zeta potential of an aqueous suspension of commercial hydroxyapatite in aqueous suspension as a function of pH.

2.3.4 Microcrystalline Cellulose

The commercial microcrystalline cellulose used in this study, as received, was a fluffy low-density powder which appeared white and optically homogeneous. Analysis by SEM showed the sample was composed of agglomerates of 5-50 primary particles, whose shapes were predominantly cylindrical and sub-rounded with low sphericity. Their aspect ratios ranged from approximately 1 to 10, and their average lengths were 61.5 μm ± 31.1 μm. An example micrograph is shown in **Figure 23**. No porosity was evident in the primary particles by either SEM or TEM. Analysis by LDA gave a volume moment mean of 72.3 μm ± 44.7 μm with a long tail down to 0.5 μm. This indicated significant polydispersity within the sample, likely a result of partial breakdown of the agglomerates present in the solid upon their dispersal in water.

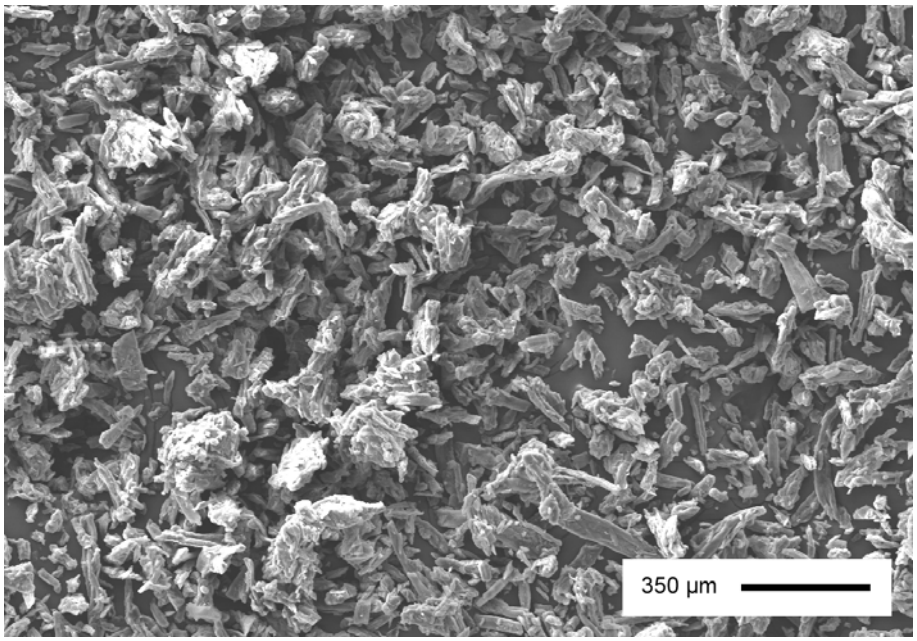

Figure 23: SEM micrograph of commercial microcrystalline cellulose.

Elemental analysis of the sample by EDS indicated it was composed exclusively of carbon and oxygen, while XRF analysis was unsuccessful because no x-ray emission was detected. This indicated, at least, that the sample was composed entirely of organic matter, with no inorganic contaminants.

The infrared spectra showed a large number of bands convoluted upon one another, typical of highly complex organic molecules. These are shown in **Figure 24**. The 'fingerprint' region of the spectrum was especially complicated, but the positions and intensities of the bands suggested the sample was composed predominantly of the cellulose I polymorph [249], which is the polymorph produced naturally by biological organisms. Assignment of the bands is difficult, however, because many represent the simultaneous collective vibration of multiple structural motifs within the molecule [250], which is exacerbated by incomplete understanding of the macromolecular structure of the material [251-253]. What can be said with somewhat more certainty, however, is that the strong broad band centred at 3400 cm^{-1} suggests that the sample contains quite a high concentration of water, either adsorbed on its surface, or absorbed within the microstructure.

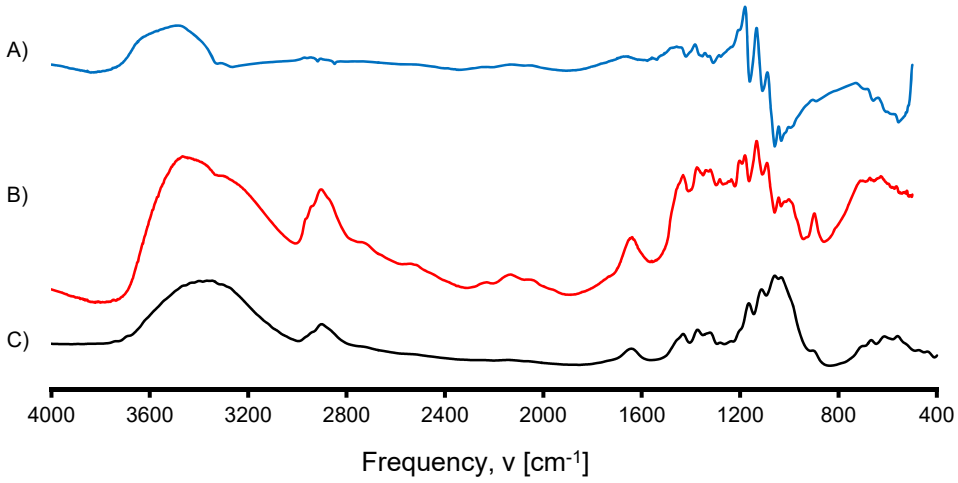

Figure 24: FTIR spectra of commercial microcrystalline cellulose. Different plots correspond to spectra collected in different ways, A) microIR of a pressed pellet, B) microIR of loose powder, C) transmission KBr.

The NMR spectra of the sample confirm the inferences made by IR, namely the bulk structure of the material and the water content. The $^{1}H \rightarrow ^{13}C$ CPMAS spectrum, shown in **Figure 25**, exhibited 7 resonances between 60 ppm and 110 ppm, the arrangements and intensities of which suggested that the sample was composed predominantly of cellulose polymorph I [254, 255]. The singlet at 105 ppm corresponds to the C1 carbons, while the C4 and C6 carbons each have two peaks at *ca.* 85 and ca. 60 ppm respectively. The C2, C3 and C5 carbons have resonances at *ca.* 72 ppm, but are not resolved from one another [256, 257]. Changing the MAS rate shifted none of the observed resonances, therefore none were spinning sidebands. The splitting of the C4 and C6 peaks is due to the presence of multiple domains within the sample, with the narrow downfield peaks corresponding to crystalline domains and the broader upfield peaks corresponding to amorphous domains. Using the ratio between the peak areas of these two domains for the C4 peak following the method of Ek *et al.* gave a crystallinity index of 59.8%, which indicates the sample is composed predominantly of almost two-thirds crystalline cellulose. This is further corroborated by the ^{1}H spectrum, shown in **Figure 26**, which shows a relatively narrow central line at 4.4 ppm, and a very broad 'hump' centred slightly at slightly lower field, corresponding to the mobile amorphous and rigid crystalline domains, respectively.

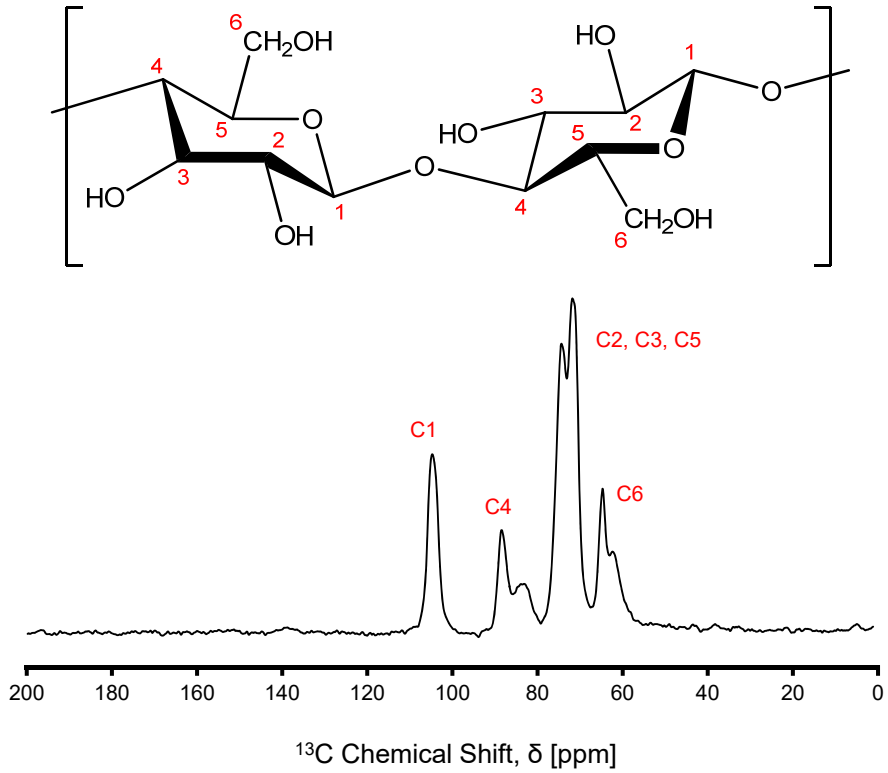

Figure 25: ^{1}H-^{13}C CPMAS NMR spectrum of microcrystalline cellulose. Peaks are labelled according to their corresponding ring positions. Splitting of the C4 and C6 peaks is due to the different environments present in amorphous and crystalline domains within the sample.

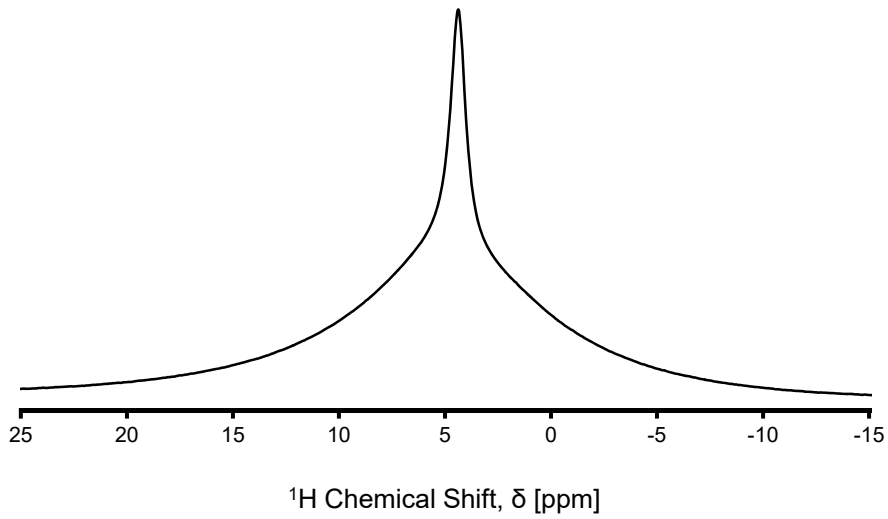

Figure 26: ^{1}H DPMAS NMR spectrum of commercial microcrystalline cellulose.

To further investigate the crystallinity of the sample, an x-ray diffractogram was recorded of the sample. It showed a small selection of broad peaks in the range 10° < 2θ < 40° typical of microcrystalline cellulose, and little outside these ranges. A diffractogram is shown in **Figure 27**. The broad and weak nature of these diffraction peaks is typical of poorly crystalline samples, and can be used to calculate a crystallinity index from the ratio of the height of the (002) peak to the height of the trough between the (101) and the (021) peaks. The result, 72.3%, agrees well with the crystallinity index calculated from the NMR data.

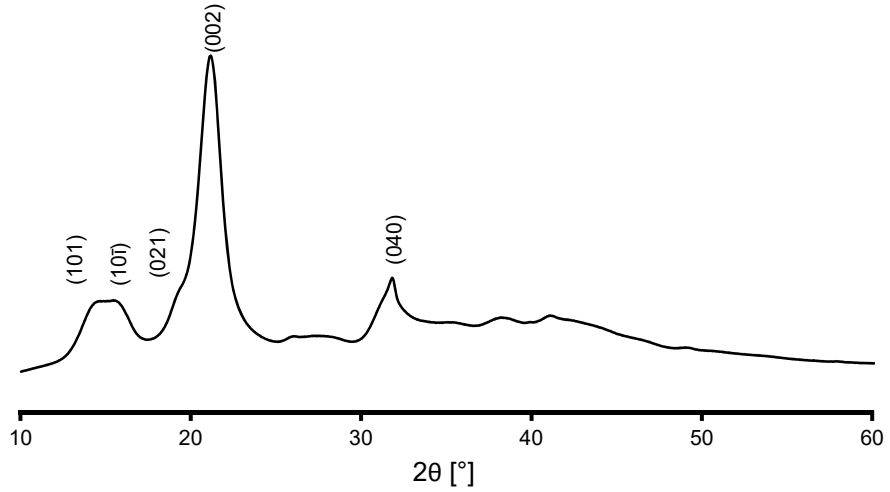

Figure 27: XRD pattern of commercial microcrystalline cellulose with major reflections labelled according to their Miller index.

An aqueous slurry with a concentration of 1 g L^{-1} gave a pH of 5.3 at equilibrium, which suggests the sample may have a very weakly acidic surface, though this is very close to the pH of CO_2 in water, and thus the meaningfulness of the result is questionable. Since the cellulose surface is mainly covered in hydroxyl groups the surface acidity seems unlikely, since most alcohols are not appreciably acidic, having pKa values similar to water. It may be that there is a small number of surface residues such as carboxylic acids which give rise to this effect instead, and although there is no direct experimental evidence for this provided by this research, it is an effect that has been noted by others [258]. Any such moieties would have to be present at such low concentrations that their detection would be extremely difficult. Regardless of the origin of the acidity, the surface charge of the particles was determined to be weakly negative over the pH range 3-12, although the spread in the data is very large. This is a known issue with measuring very weak surface charges *via*

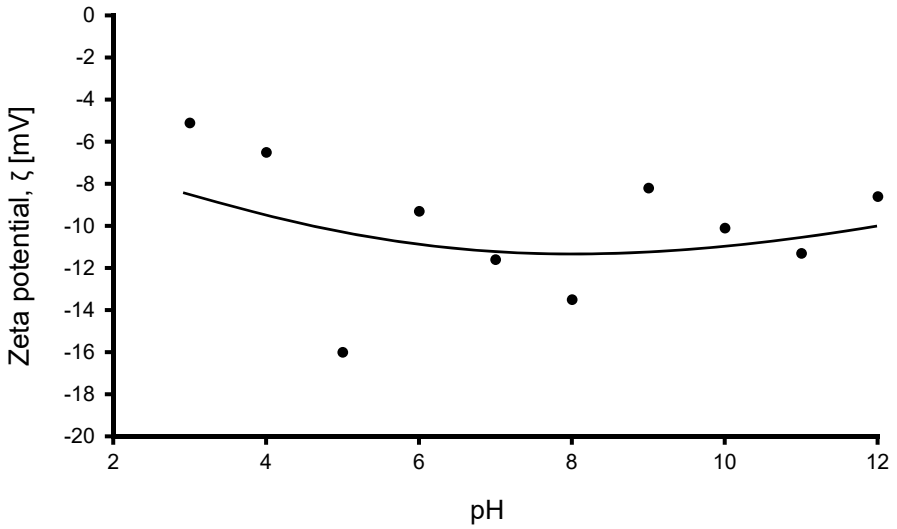

Figure 28: Zeta potential of an aqueous suspension of commercial microcrystalline cellulose as a function of pH.

the technique used. Because the charge is weak and probably sparsely populates the cellulose surface, it may be that either positive or negative metal compounds or particles could potentially adsorb to it.

2.3.5 Halloysite

The halloysite used in this study was a fine cohesive powder, off-white in colour, and with moderate density. Examination by SEM showed it was composed of rounded aggregates 12.7 μm ± 7.6 μm in size, each composed predominantly of rounded but irregularly shaped platelets, with a small amount (< 10%) of fibrous material. Conversely, examination by TEM showed equal amounts of platelet and fibrous material, with a small amount of nanoparticulate material. The platelets and the nanoparticulates showed no visible pore structure or crystallinity, while the fibres were tubular with hollow interiors. An example TEM micrograph is shown in **Figure 29**. These morphologies are typical of halloysite clays, even with multiple morphologies appearing within samples from the same source [259].

The discrepancy in the relative amounts of platelets and tubules observed *via* the two microscopy methods may be a fractionation effect resulting from differential sedimentation rates of the two, as a result of the differences in the preparative methods used. While the SEM samples are analysed 'whole' with little sample preparation, the TEM samples are suspended in water and the contents of the supernatant analysed. Differences in the surface charges of the particles could then

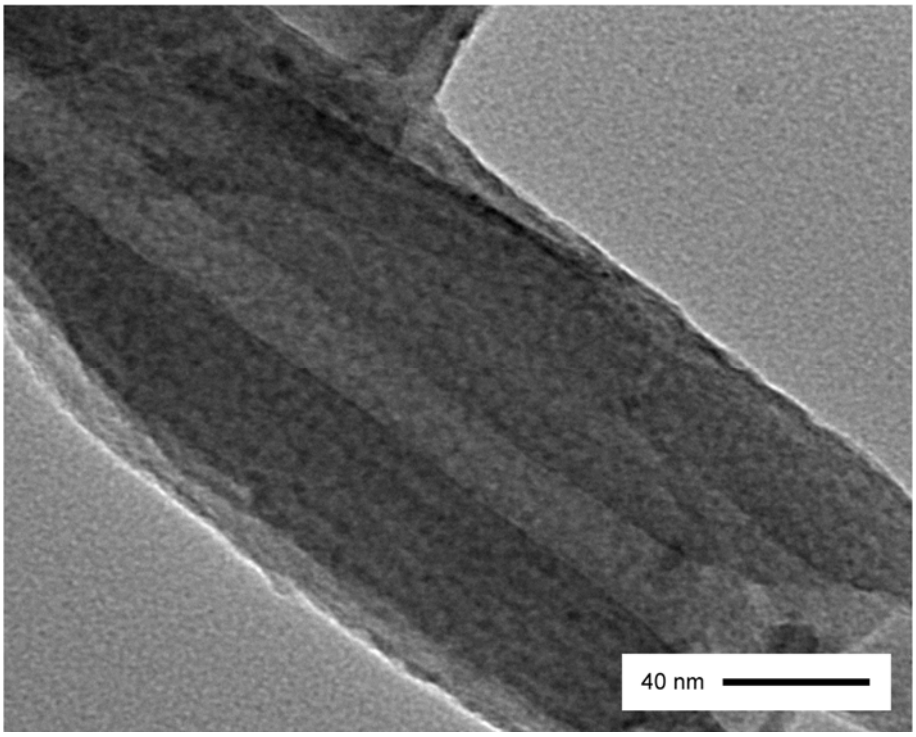

Figure 29: TEM micrograph of a halloysite nanotube, clearly showing the internal pore structure and walls of the tube.

affect the sedimentation rates, leaving the supernatant artificially enriched in tubules compared to platelets.

Laser diffraction analysis revealed that the volume mean particle size was 84.8 ± 74.6 μm. The distribution was trimodal, with peaks evident at 0.17 μm, 15 μm and 105 μm in a 1:8:10 ratio. The central peak was consistent with the size of the aggregates observed by SEM, suggesting that only a small portion of aggregates dissociated or agglomerated further when dispersed in solution.

X-ray fluorescence showed the only detectable major elements in the sample were silicon (26.0%) and aluminium (18.5%), with the remainder presumably being mostly oxygen. Traces were detected of other elements, including iron (2260 ppm), sodium (1600 ppm), sulphur (570 ppm), chlorine (370 ppm), and calcium and potassium (100 ppm each). This is consistent with the sample being extremely pure, which is a well-known characteristic of New Zealand's northern halloysites. The presence of iron may be in part responsible for the 'flat' morphology of the sample, since Fe^{3+} substitutes for Al^{3+} in halloysites, enlarging the outer octahedral sheets, relieving the stress, and producing halloysite with a flatter morphology [140]. Given stoichiometric halloysites are equimolar in silicon and aluminium, this indicated the sample was

either aluminium-deficient, or contaminated with a small portion of a silicon-rich species. Since the total mass of impurities was less than the deficit of aluminium, this indicated that contamination with a secondary silicon-based species was more likely.

The powder diffraction pattern of the sample, shown in **Figure 30**, was consistent with previously reported halloysites, specifically those of New Zealand specimens. The strong reflection at 12° and the lack of reflections below this indicated it was composed wholly of the 10 Å hydrated form [142]. This essentially confirms the sample was largely phase-pure, and the two major morphologies observed *via* electron microscopy had the essentially the same crystal structure. Pattern matching using HighScore showed the bulk of the peaks were explained by "kaolinite", ICDD PDF 00-058-2030, which has a very similar crystal structure to halloysite. The remainder of the peaks were explained by the presence of a small amount of quartz, ICDD PDF 01-070-3755, which confirms the inferences made by XRF and the observations made by TEM.

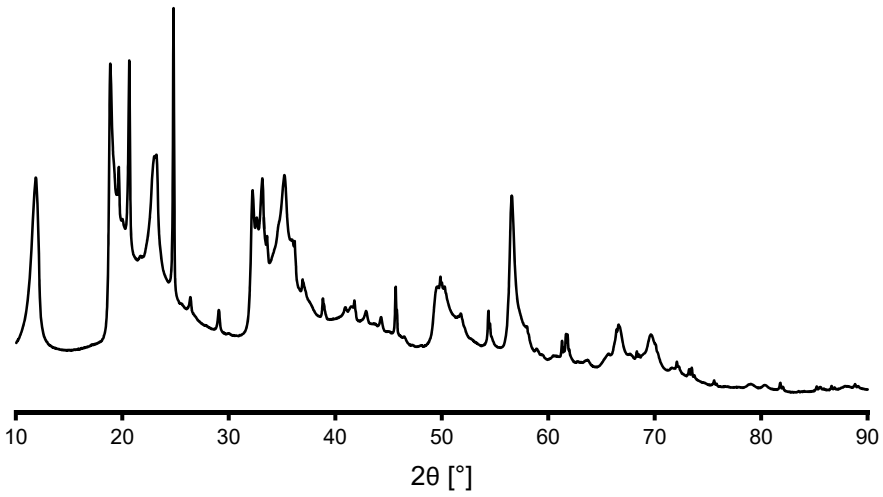

Figure 30: XRD pattern of halloysite.

The infrared spectra, shown in **Figure 31**, were as expected from a sample composed of equal portions of silica and alumina sheets. From low frequency, octahedral alumina Al-O stretches are visible, followed by broad band at 560 cm^{-1} which is possibly a convolution of the two Si-O-Al deformations. The peaks at evident at around 1000 cm^{-1} are mixed contributions from the silica, the inner-surface hydroxyl deformation, and AlOH librational modes. The far end of the spectrum showed two sharp peaks at 3600 cm^{-1} corresponding to the silanols and aluminols

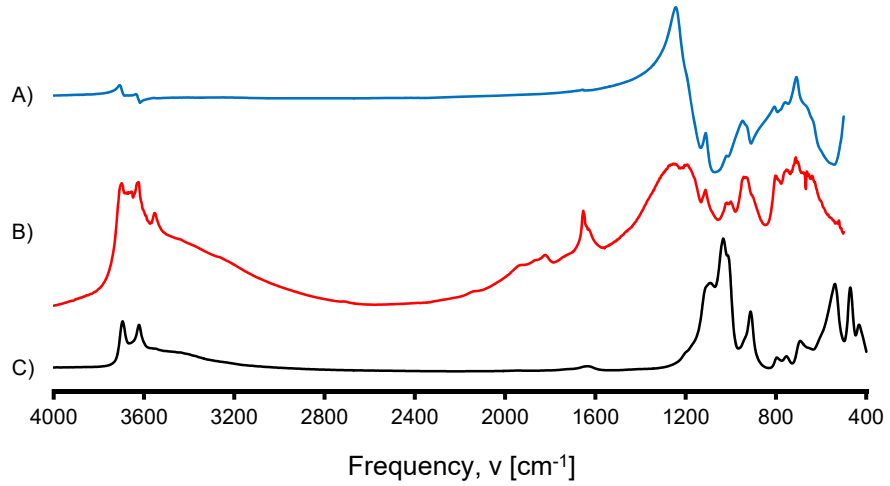

Figure 31: FTIR spectra of halloysite. The three different plots correspond to spectra recorded in three different ways, A) MicroIR of a pressed pellet, B) MicroIR of looser powder, C) Transmission KBr.

stretches, with a broad absorption underneath corresponding to adsorbed water, further corroborating the phase assignment made by XRD [260]. No features were evident which could be assigned to oxides of any of the minor elements detected by XRF, indicating that they are probably either structural or adsorbed ionic species, rather than discrete deposits of the element oxide mixed throughout the structure of the material.

The solid-state NMR spectra further confirmed the data obtained by other techniques. The proton spectrum, shown in **Figure 32**, displayed two unresolved peaks at 2.66 ppm and 4.31 ppm, corresponding to the aluminol and silanol protons. No other features were evident in the spectrum, indicating these are the only proton environments present.

The ^{29}Si spectra, shown in **Figure 33**, displayed a single major peak at -92.5 ppm, which is within the shift range expected for tetrahedrally-coordinated silicon dioxide, which is consistent with the known crystal structure of halloysite. An additional small peak at -108 ppm is evident in the direct-polarised spectrum, which could either be from proton-deficient Q^4 Si-based impurities in the sample, or from the Si(1Al) environments present in the halloysite crystal structure.

The ^{27}Al spectrum, shown in **Figure 34**, displayed a single asymmetric broad peak at 0 ppm, which is in the shift range of octahedrally coordinated alumina, but its

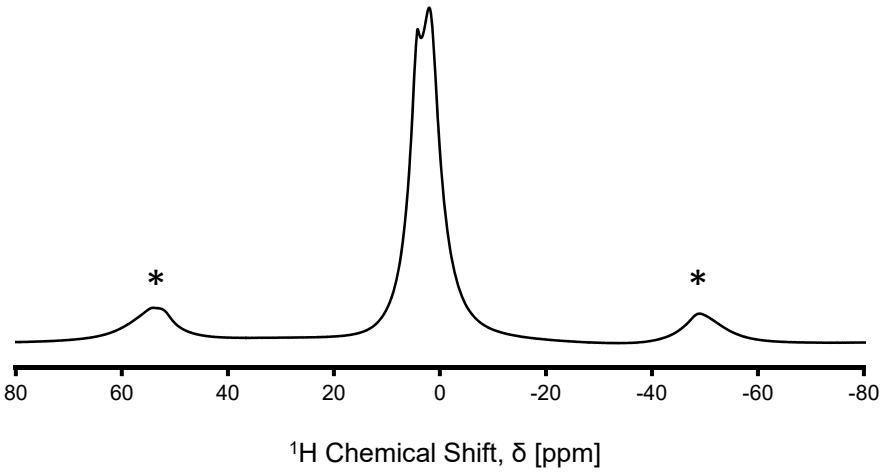

Figure 32: ^{1}H DPMAS NMR spectrum of halloysite. Spinning sidebands are marked with asterisks.

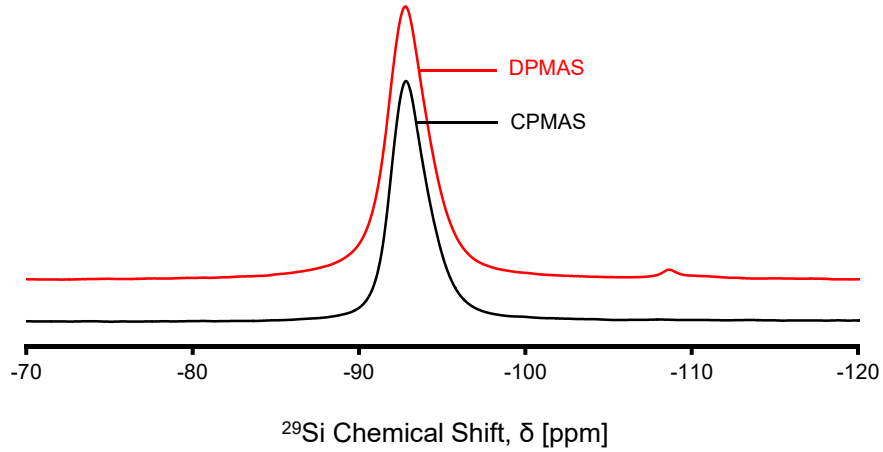

Figure 33: ^{1}H-^{29}Si CPMAS and ^{29}Si DPMAS NMR spectra of halloysite.

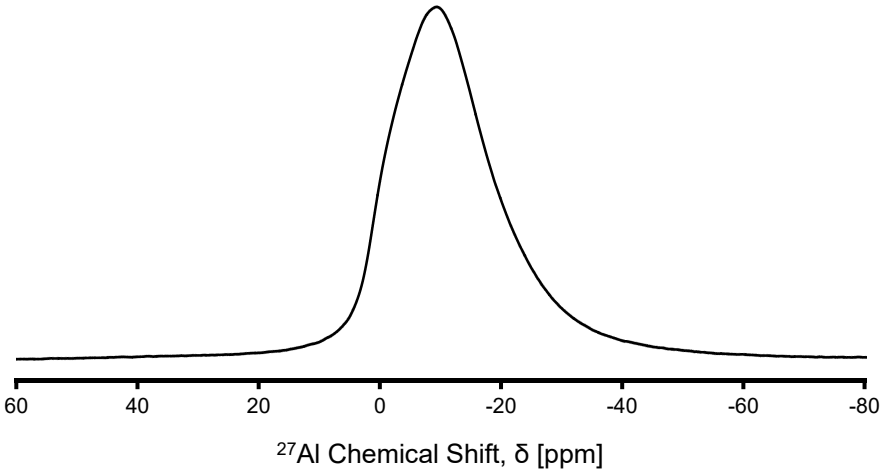

Figure 34: ^{27}Al DPMAS NMR spectrum of halloysite

unusual asymmetry suggested that it is a convolution of two or more individual aluminium sites. It may simply be the case that these arise from crystallographic distortions in the lattice, and indeed this is the explanation offered by Newman *et al.*, who propose that the size of this tail relates inversely to the crystallinity of the sample [261].

A dispersion of the halloysite in water gave pH values of 5-7, indicating the sample was less acidic than silica but more so than alumina, unsurprising given that halloysite particles have exposed surfaces of both. This situation, though expected *a priori*, is indistinguishable from a sample which does not alter solution pH at all, since the observed pH is similar to CO_2 saturated water. The zeta potential data, shown in **Figure 35**, were negative over the entire pH range studied, with a profile strongly reminiscent of the silica gel discussed earlier in this chapter. Again this is unsurprising, since it is known the outer surfaces of halloysite are predominantly silica, which effectively gives rise to the electrical double layer. The implications of this are that like silica, the halloysite will probably interact favourably with cations by electrostatic attractions, but may repel anions.

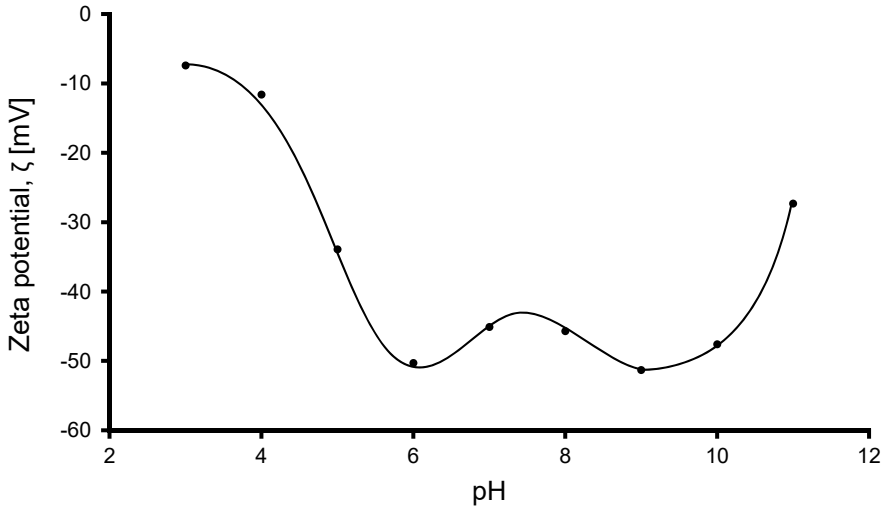

Figure 35: Plot of the zeta potential of an aqueous suspension of halloysite as a function of pH.

2.3.6 Perlite

The perlite used in this study was a homogeneous white powder, soft and fluffy in texture, and with a very low density. Examination by SEM revealed it was composed of thin jagged sheets, as shown in **Figure 36**. This unusual morphology precluded the measurement of individual particles by microscopy, however laser diffraction analysis gave a volume-surface particle size of 58.4 ± 50.3 μm.

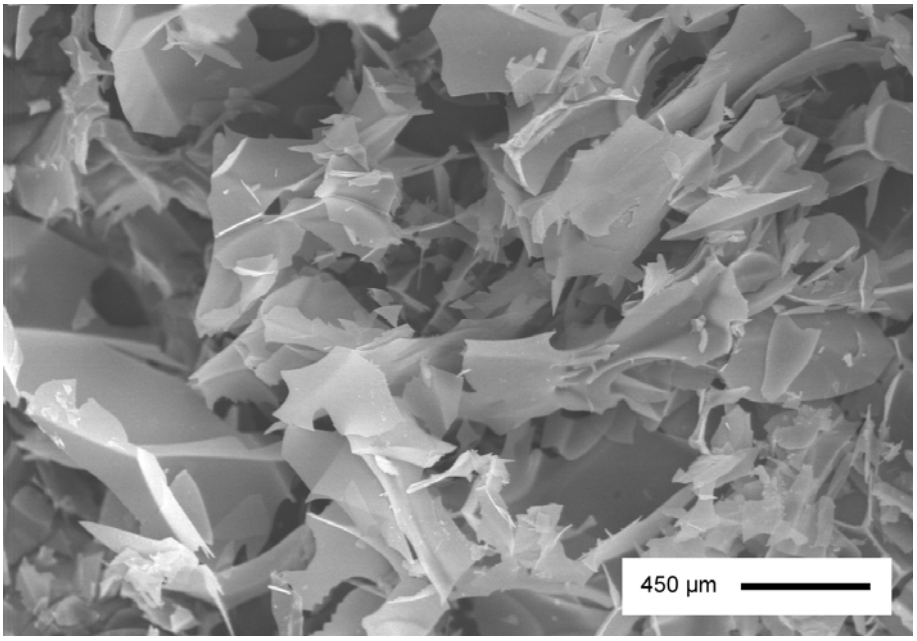

Figure 36: SEM micrograph of perlite.

Energy dispersive spectroscopy performed concurrently with electron microscopy showed the perlite was composed predominantly of silicon and oxygen. Quantitation by XRF showed it was 39.25% Si by mass, corresponding to an oxide mass of 84.1% SiO_2. The remainder was mainly aluminium (7.4% as Al; 14.0% as Al_2O_3), with small amounts of sodium (4.3% as Na), potassium (2.7% as K), calcium (0.8% as Ca), and iron (0.8% as Fe). This composition is similar to other previously reported perlites [152]. The aluminium and silicon in the sample were assumed to be present as their oxides, since this is the most common speciation for these elements in clay minerals, though the speciation of the alkali metals was at this point unknown.

The solid-state NMR spectra gave valuable insight into the connectivity of the aluminium and silicon atoms within the sample. The ^{29}Si spectrum, shown in **Figure 37**, showed only a single broad peak at -105 ppm, indicative of a system composed of tetrahedrally coordinated silicon atoms with a distribution of chemical

environments, such as in amorphous glasses [262]. The ^{27}Al spectrum, shown in **Figure 38**, showed a single broad resonance at 50 ppm, corresponding to tetrahedrally coordinated aluminium atoms coordinated through oxygen to four silicon atoms [208]. The possibility that the peak represented discrete deposits of an aluminium oxide phase was deemed unlikely, since amorphous aluminium oxide is difficult to form [263], and crystalline species would give a unique signature in the powder diffraction pattern (discussed later), which was not observed.

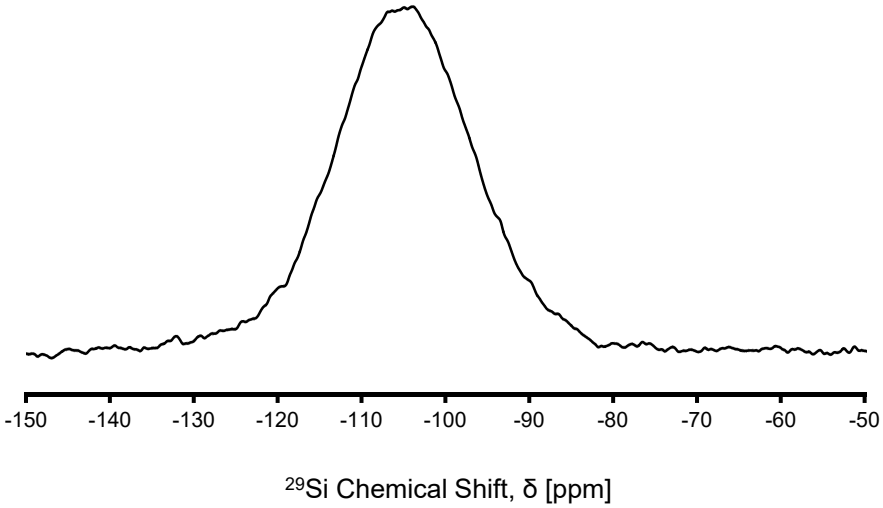

Figure 37: ^{29}Si DPMAS NMR spectrum of perlite.

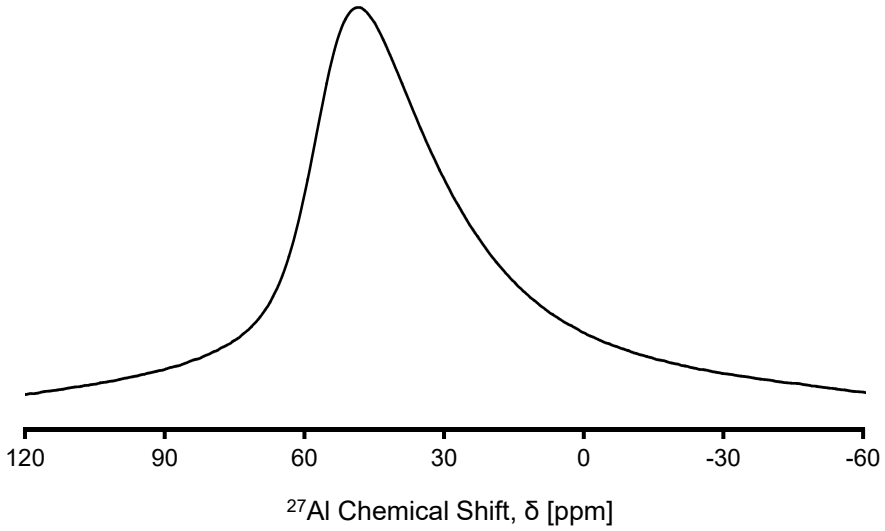

Figure 38: ^{27}Al DPMAS NMR spectrum of perlite.

The ^{1}H spectrum, shown in **Figure 39**, exhibited a broad distribution of environments tailing toward high field. The lineshape, however, was not smooth, suggesting the presence of multiple different proton environments within the sample. Though perlite has not previously been studied by ^{1}H NMR, other aluminosilicate glasses have; for example, Zeng, Nekvasil and Grey studied sodium aluminium silicates using the "TRAPDOR" pulse sequence (transfer of populations in double resonance), finding two types of molecular water, and three distinct hydroxyl environments [264]. Similar glasses were studied by Kaekawa, Saito, and Yokokawa, who also found molecular water and silanol groups [265]. *Ab initio* molecular orbital calculations performed by Xue and Kanzaki on silicate glasses also predicted various types of hydroxyls and molecular water [266]. It seems likely, therefore, that multiple environments observed for the current sample represent similar features. This has implications for the immobilisation of nanoparticles, since different hydroxyl groups might interact with particles in different ways, leading to a preferential or biased placement of nanoparticles on certain areas of the perlite surface.

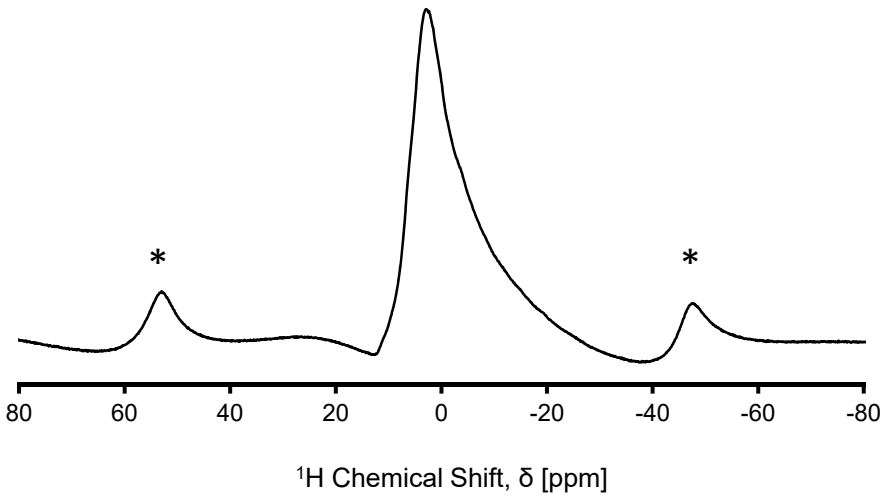

Figure 39: ^{1}H DPMAS NMR spectrum of perlite.

The inferences made by NMR that the sample is amorphous were strengthened by the powder diffraction pattern, shown in **Figure 40**, which is remarkably similar to the commercial silica gel. This confirms the bulk of the structure is an amorphous glass, but the presence of a number of small sharp peaks in the 20° region suggest the presence of a very small portion of crystalline phases. Peak matching using HighScore suggested these may originate from traces of a crystalline aluminosilicate

component, for example makatite exposed to concentrated mineral acids to yield $H_2Si_2O_5$ (ICDD PDF 00-050-0439), or the generically named "sodium aluminium silicate" (ICDD PDF 00-055-0071). While both of these are consistent with previously presented information, the same peaks have been assigned by Roulia *et al.* as originating from biotite, feldspar, and quartz [149]. Given the relative intensities of the peaks they were likely to be trace phases, however, and so their unambiguous and conclusive identification was deemed unnecessary.

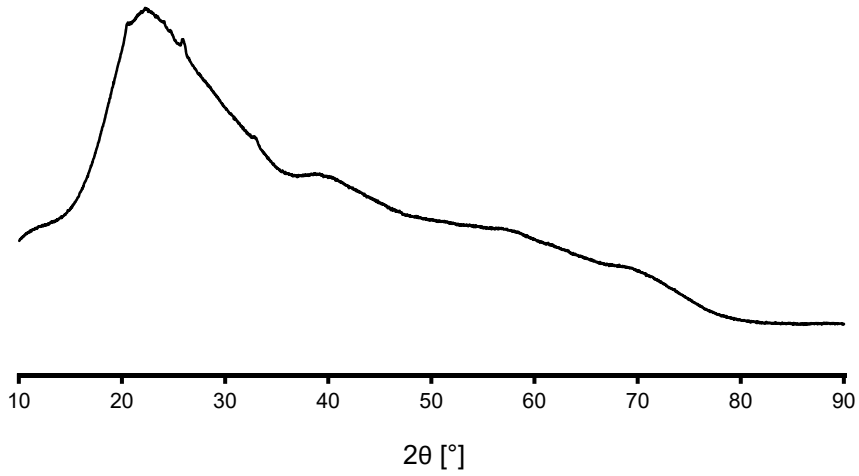

Figure 40: XRD pattern of perlite.

The infrared spectra of the sample, shown in **Figure 41**, confirmed all of the inferences made about the sample *via* other techniques. The spectra contain all the bands associated with aluminium and silicon oxides, and also show the presence of a number of different hydroxyl environments. The KBr disc spectrum shows a broad peak with two sharp but weak peaks atop it, suggesting there are a large number of hydrogen-bonded hydroxyls present, as well as at least two types of non-bonded hydroxyls. This effect is further pronounced in the MicroFTIR reflectance spectrum of the powder, which shows three distinct oscillations in the hydroxyl region. This is consistent with observations made in of the ^{1}H NMR spectrum of the sample, which suggests the same thing. There are no complete assignments of the entire vibrational spectrum of halloysite reported in the literature, which is perhaps unsurprising given that there are difficulties in the assignment for apparently simple species like Al_2O_3.

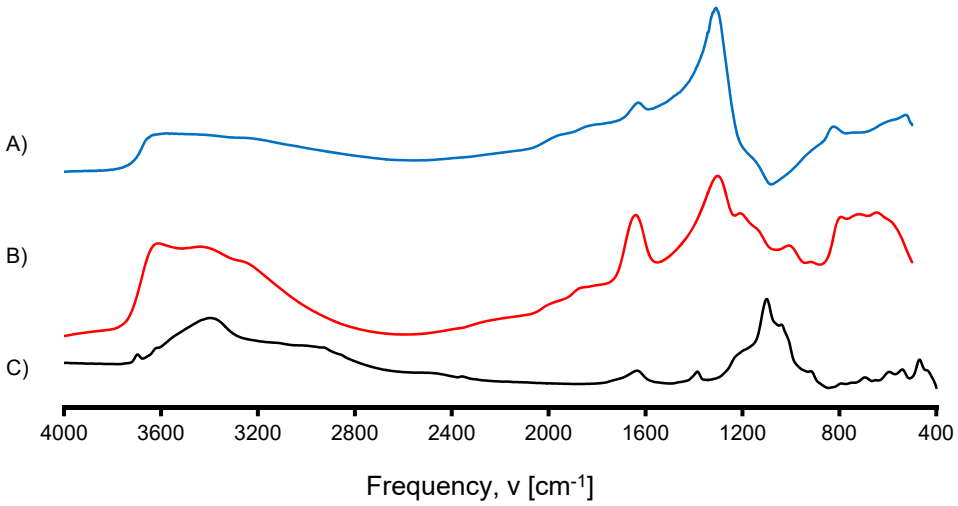

Figure 41: FTIR spectra of perlite. The three different plots correspond to three different measurement methods, A) microIR of a pressed pellet, B) microIR of a loose powder, C) transmission KBr.

Zeta potential measurements showed that in aqueous suspension the particles acquire a strong negative charge, having a maximum of -60.6 mV at pH 9. Data is shown in **Figure 42**. No isoelectric point was observed over the experimentally accessible pH range of 3-11, although the plot of zeta potential as a function of pH indicates that one may potentially exist at very low pH values. The profile of the plot is strongly reminiscent of that of silica, which is unsurprising given the elemental composition of the sample, but indicates that the aluminium in the sample is not concentrated near the surface, since this would produce a profile more similar to alumina than silica. The potential was much more negative than pure silica at all pHs, however, which suggests that the surface is somewhat different in its composition to

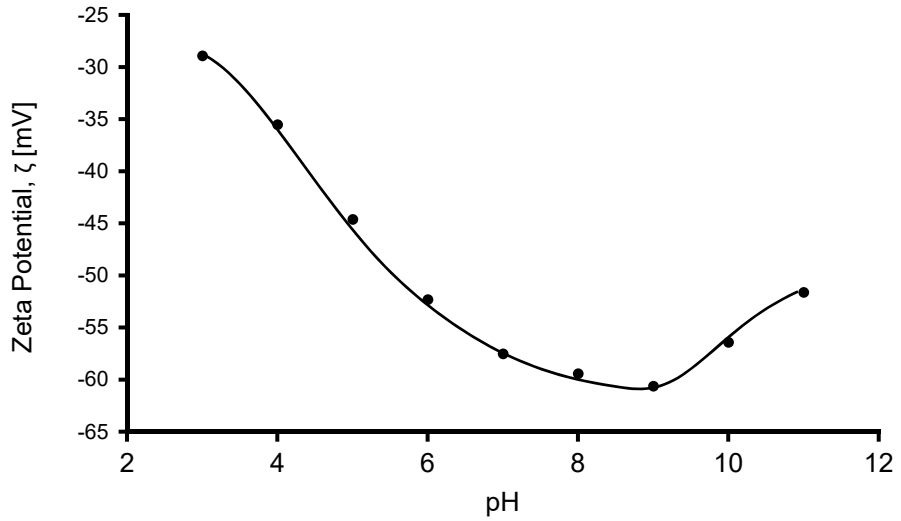

Figure 42: Plot of zeta potential of perlite as a function of pH.

this model material. These results are similar to those obtained by Doğan, Alkan, and Cakir [150, 152], who suggest the electrokinetic properties are primarily due the properties of surface silanols of varying types.

2.3.7 Bioapatitite

The calcined bovine bone produced in this study, referred to herein as "bioapatite", was in many respects remarkably similar to the synthetic hydroxyapatite. In terms of its physical properties it was a brilliant white powder, coarse in texture, and with a high apparent density. Analysis by SEM showed it was composed of rounded particles *ca.* 100 μm in size with globular microstructures, the interstices of which formed an extensive macropore system. A micrograph illustrating this morphology is shown in **Figure 43**. The size of these particles is nearly an order of

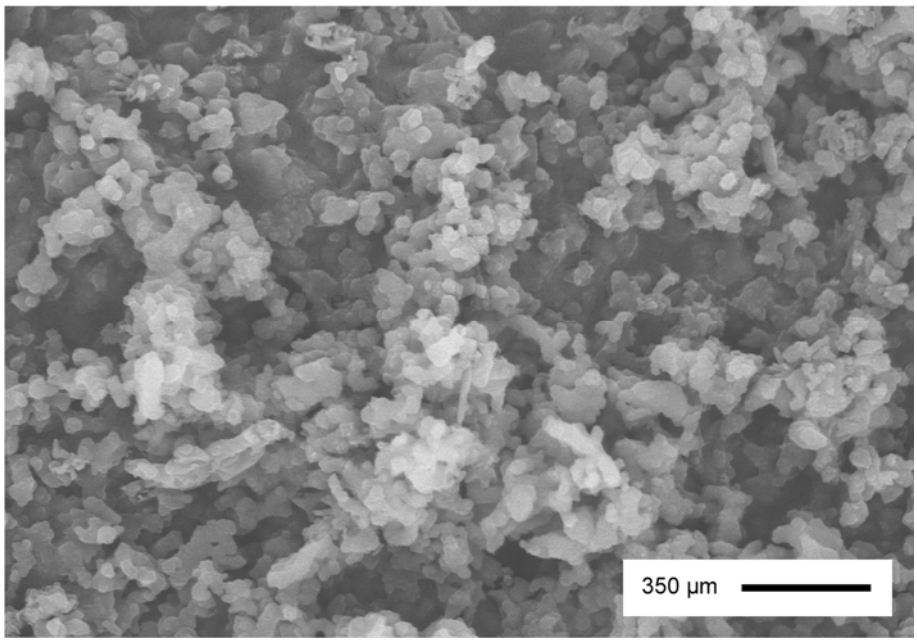

Figure 43: SEM micrograph of bioapatite.

magnitude greater than the commercial hydroxyapatite, suggesting the sample probably has a lower accessible surface area. This effect could be mitigated by more extensive grinding of the samples during preparation.

Analysis by LDA gave similar results to those obtained by SEM, yielding a volume mean of 150 μm ± 130 μm, but also showed the particle size distribution was bimodal, with 10% of the particles having a much smaller size, around 1 μm in diameter. These smaller particles are mostly likely the individual 'globules' from

which the primary particles are composed, which have broken free during the grinding process.

Elemental analysis by XRF showed the apatite was composed predominantly of calcium (29.2%) and phosphorus (19.5%), with a small amount of magnesium (0.68%) and sodium (0.54%). The Ca:P ratio of 1.53 suggests that the material is calcium-deficient relative to stoichiometric hydroxyapatite, although to a lesser extent than the commercial apatite described in the previous section. The presence of magnesium in the sample is typical of animal bone.

The infrared spectra, shown in **Figure 44**, bore many similarities to the commercial material. Once again the transmission spectrum is dominated by the phosphate $\nu_{1\text{-}4}$ modes, although the band shapes are somewhat widened, especially near their bases. The hydroxyl stretch is evident, atop a more pronounced 'hump' corresponding to adsorbed water. Several weak bands are observed in the 1300 cm^{-1} – 1800 cm^{-1} region which are not observed in the commercial sample, which correspond to the ν_3 carbonate modes present in apatites which have phosphate substituted for carbonate. This suggests the sample is a mixed Na-bearing (given the XRF results) AB-type carbonate-substituted hydroxyapatite [267], which again, is typical of animal bone [268]. Additional to this structural carbonate, the reflectance spectra showed peaks in the region of 1900 cm^{-1} to 2300 cm^{-1}, which by virtue of their increased surface selectivity, suggest the sample also contains trace portions of surface-adsorbed carbonate.

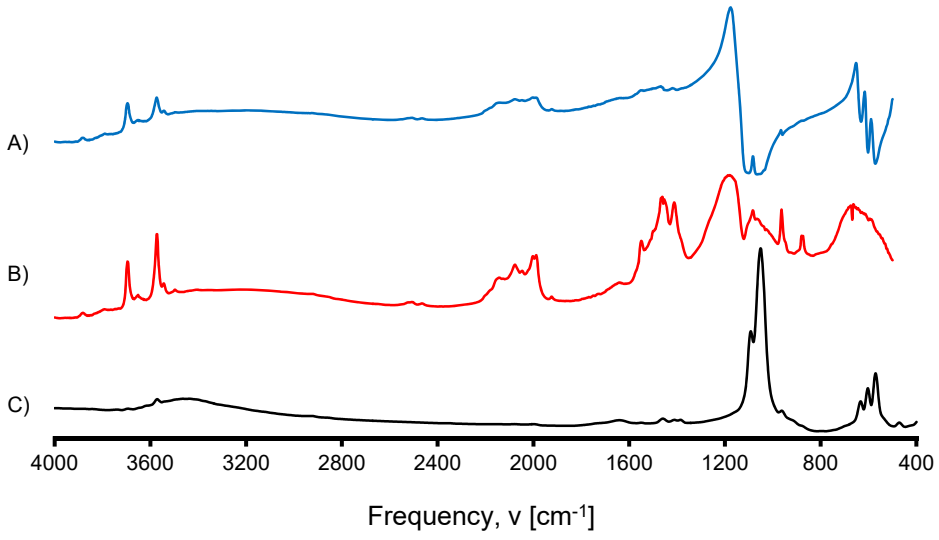

Figure 44: FTIR spectra of bioapatite. The three plots represent spectra collected in different ways, A) microIR of a pressed pellet, B) microIR of loose powder, C) transmission KBr.

The same spectra also contain an additional peak at 3696 cm^{-1} which was not observed in the transmission spectra of the commercial sample, along with five other very small peaks. Since vibrations in this region are typical of hydroxyl groups, this suggests the sample has a number of different surface hydroxyls, and since hydroxyapatite contains only one type, the surface must therefore be composed of multiple different phases. Analysis of pure and carbonated hydroxyapatites by Rey *et al.* identify the structural OH mode observed here at 3574 cm^{-1}, but make no mention of the other band [269, 270].

As calcination of bone minerals generates CaO which is hydrolysed to $Ca(OH)_2$ in water, an infrared spectrum was recorded of a pure sample of this species. A sharp band was observed at 3640 cm^{-1}, which does not agree with the currently reported value. The second most abundant species capable of forming similar species was Mg as shown by XRF, and so a spectrum was recorded of $Mg(OH)_2$. Again a sharp band was observed, but at 3700 cm^{-1}, which agrees well with the currently reported value, and so this band was assigned as originating from $Mg(OH)_2$ produced by hydrolysis of MgO produced during calcination of the samples.

The NMR spectra yielded little extra information. The ^{31}P spectra, shown in **Figure 45**, exhibited a single resonance at 2.45 ppm, equivalent in chemical shift to the commercial sample but twice the width. Similarly, the ^{1}H spectrum, shown in **Figure 46**, displayed a broad water peak at 5.8 ppm, and a broadened structural OH

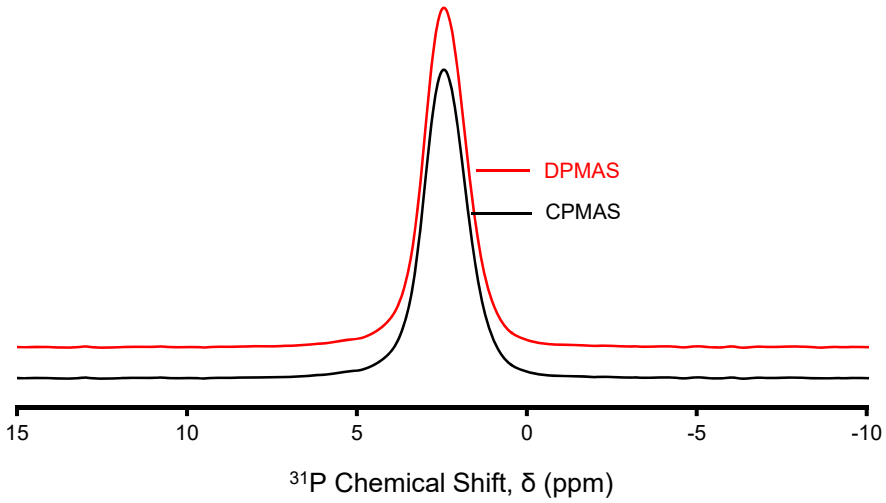

Figure 45: ^{31}P DPMAS and ^{1}H-^{31}P CPMAS NMR spectra of bioapatite.

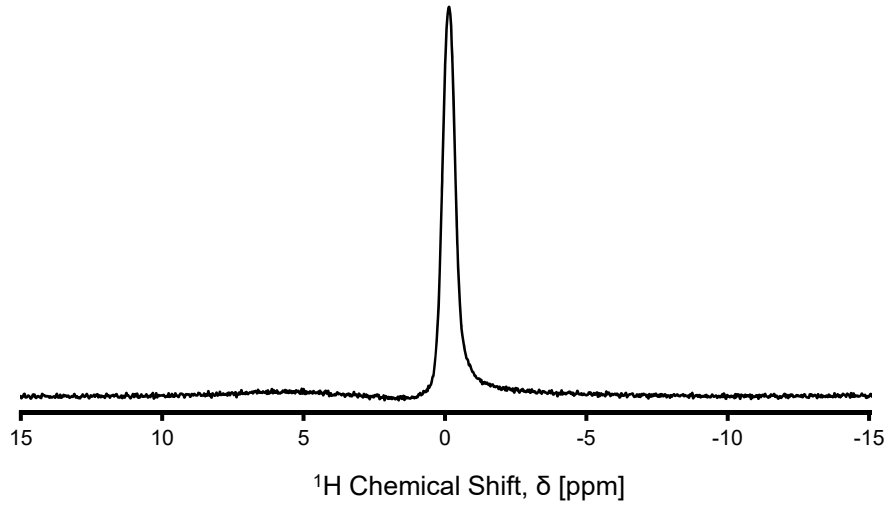

Figure 46: ^{1}H DPMAS NMR spectrum of bioapatite.

peak at -0.12 ppm. The lack of manifold bands in the ^{31}P spectrum immediately suggested the sample was more phase-pure than the commercial sample, which was confirmed by powder diffraction discussed in the next section, however the increased width of the structural phosphate peak suggested that the HAp phase which is present in the current sample possesses a greater number of chemical environments. The powder diffraction pattern ruled out a decrease in bulk crystallinity as the origin of the band broadening, and so it may be that this effect originates from spin-spin interactions with adjacent nuclei of other elements present in the sample. Regardless, the evidence suggested that the sample as a whole was more phase-pure than the commercial sample.

The powder diffraction pattern of the bioapatite, shown in **Figure 47**, exhibited a number of interesting features. Compared to the powder pattern of the commercial sample, the bioapatite had narrower peaks and fewer of them, as well as a significantly reduced background. Since the two patterns were recorded with the same optical configuration, this suggests the differences in the background arise due to the sample itself. The lower background suggests a lower amorphous content in the bioapatite sample, while the decreased peak widths categorically show the bioapatite is more crystalline than the commercial hydroxyapatite.

When the powder was dispersed in water the pH increased rapidly to 9.27 at a concentration 1 g L^{-1}. Since the powder diffraction pattern did not show evidence for the presence of CaO and the FTIR data did not show evidence for $Ca(OH)_2$, it may be this originates from dissolution of the $Mg(OH)_2$ present in the sample. The zeta

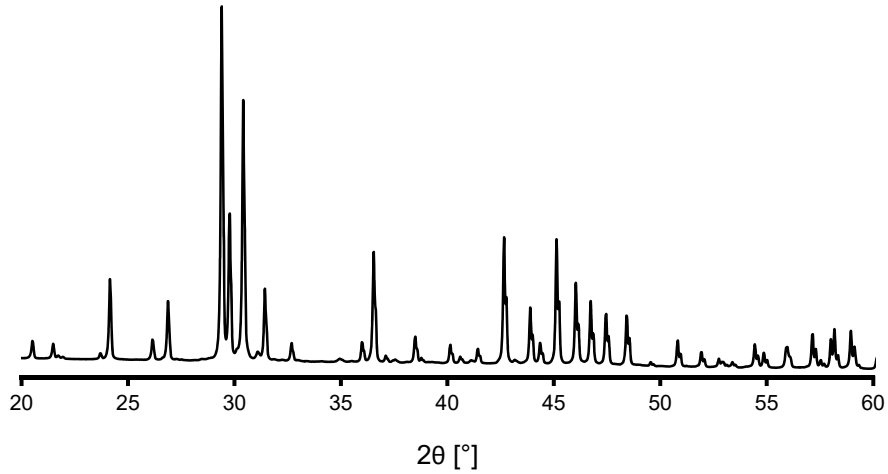

Figure 47: XRD pattern of bioapatite.

potential of the dispersion was similar to the commercial hydroxyapatite but contained an inflection point at pH 9 where the potential reached its minimum of -20 mV, before rising toward more positive values at higher or lower pHs. The data is shown in **Figure 48**. No isoelectric point was observed over the pH range studied. This is similar to the data reported by Doostmohammadi *et al.* for bone-derived HAp particles, and though their data does not contain an inflection as described here, their methodology was slightly different [271].

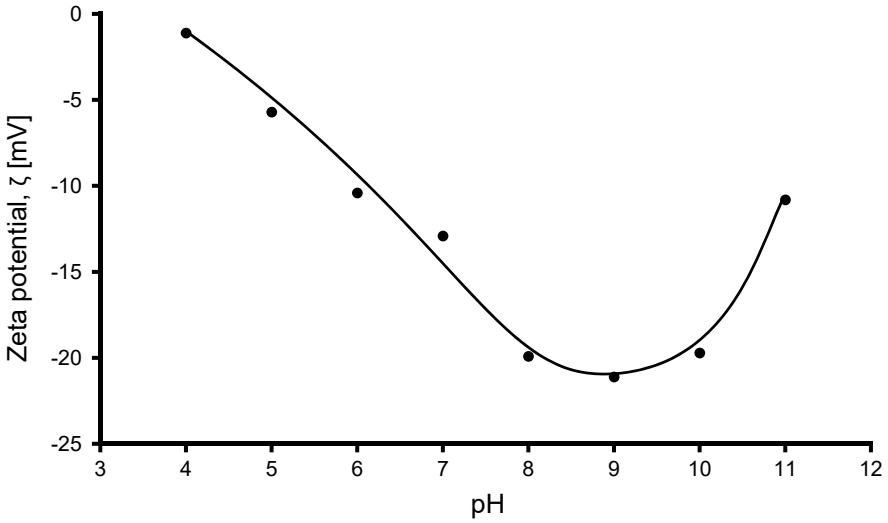

Figure 48: Zeta potential of bioapatite as a function of pH.

2.3.8 Macrofibrillar Cellulose

Macrofibrillar cellulose, extracted from calico, was used as an analogue of the commercially available microcrystalline cellulose. After the preparation procedure described earlier it was obtained as a fluffy, fibrous, slightly off-white powder, with little cohesiveness compared to the commercial cellulose. Analysis by SEM indicated that it was indeed composed of fibres of nearly uniform 20 μm diameters, but with a broad range of lengths, averaging 90 μm ± 50 μm. The fibres had hollow interiors, making them tubular, with the tube walls composed of parallel-aligned whiskers around 200 nm in length. Examples of these structures are shown in **Figure 49**. Laser diffraction analysis showed the sample had a multi-modal particle size

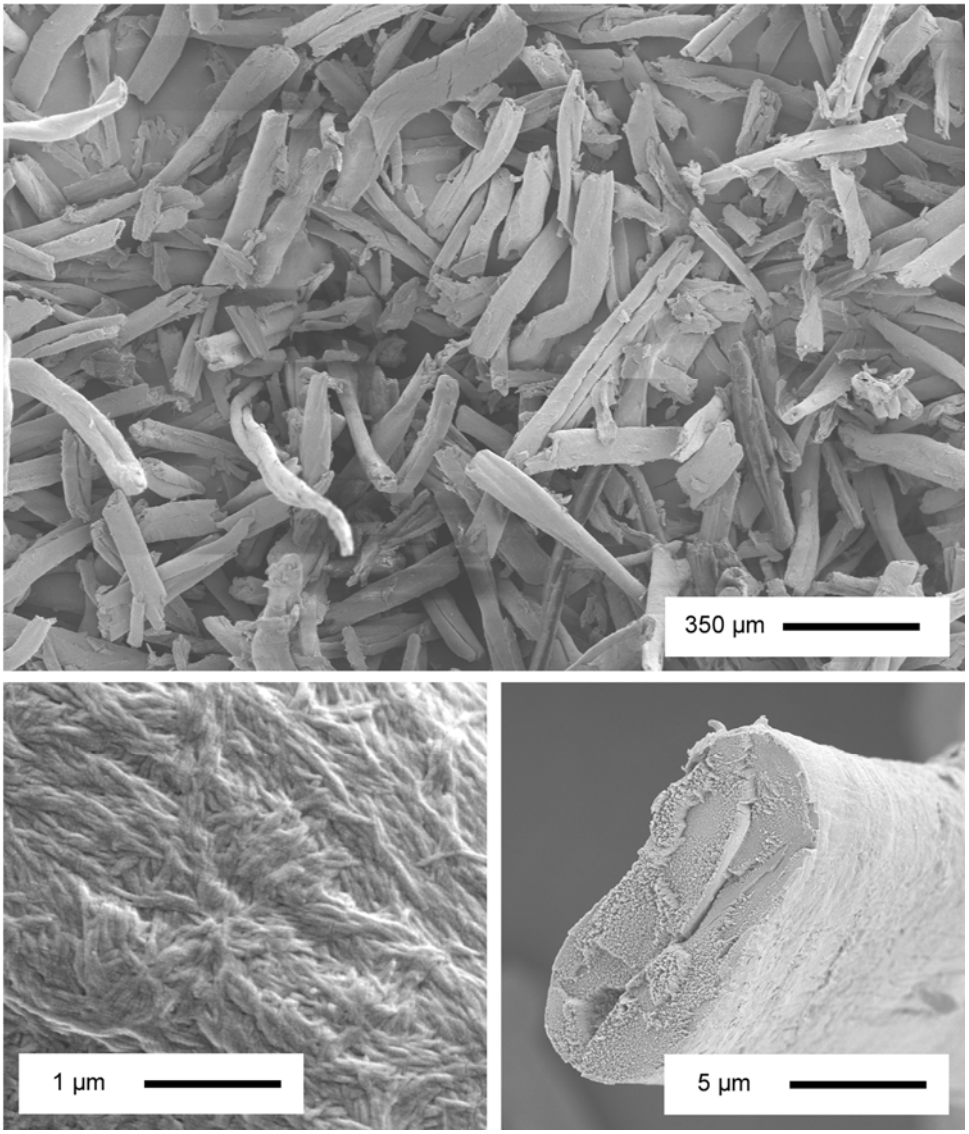

Figure 49: SEM micrographs of macrofibrillar cellulose. Top: A selection of fibres. Bottom right: The end of one of a compressed fibre. Bottom left: The surface of a fibre.

distribution extending from 500 nm up to 800 µm, with a volume mean particle size of 75 µm ± 100 µm. The multiple peaks in the size distribution probably correspond to aggregates of varying sizes resulting from poor dispersion of the sample in water, which suggests it is probably somewhat more hydrophobic than the commercial microcrystalline cellulose.

Elemental analysis by EDS showed the sample was composed predominantly of carbon and oxygen, unsurprisingly, with 0.4% Mg and 0.4% Si, 0.1% Ti also detected by XRF. These metals are probably present as a result of uptake of minerals from the soil in which the sample grew. Presumably they are not present as soluble species otherwise they would be washed out during the sample preparation procedure, thus they are more likely present as their oxides or some similar form.

The infrared spectra of the sample, shown in **Figure 50**, were remarkably similar to those of the commercial cellulose, with the same bands present in the same positions. Their increased sharpness relative to the commercial sample suggested this material was more crystalline, as may be expected from cotton-derived cellulose. If this is indeed the case then the surface of this particular sample will have fewer

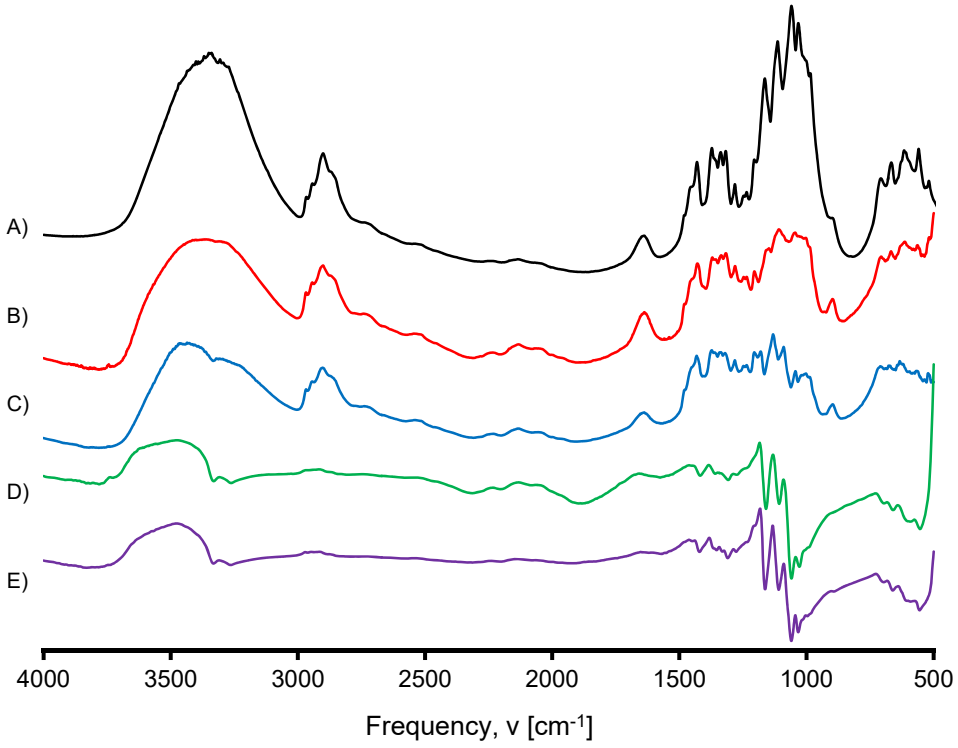

Figure 50: FTIR spectra of macrofibrillar cellulose. Different plots correspond to spectra recorded in different ways; A) KBr transmission, B) microIR of KBr-diluted loose powder, C) microIR of pristine loose powder, D) microIR of pressed KBr-diluted pellet, E) microIR of neat pellet.

accessible hydroxyl groups than the microcrystalline cellulose and would consequently be more hydrophobic, which is consistent with the observations made *via* laser diffraction. As with all the other infrared spectra collected in this study, the reflectance spectra had essentially the same bands as the transmission spectra, but were highly distorted in the regions of high absorbance.

Given the inferences about crystallinity made by the infrared data, a powder diffraction pattern was recorded to confirm the hypothesis, and is shown in **Figure 51**. The background was significantly lower and the peaks significantly sharper in comparison to the commercial cellulose sample, and the crystallinity index was calculated to be 89%, essentially confirming the increased relative crystallinity. The pattern was similar to previously reported diffractograms of raw cotton [272].

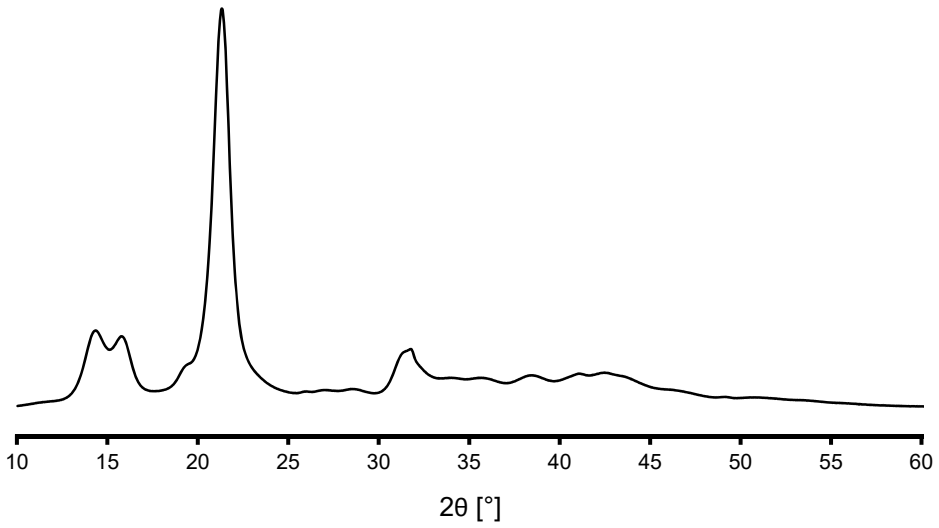

Figure 51: XRD pattern of macrofibrillar cellulose.

Zeta potential measurements, shown in **Figure 52**, indicated the sample had similar properties to the commercial sample, but with nearly double the surface charge. It is unclear whether the observed charge is associated predominantly with the surface of the cellulose itself or whatever impurities it may contain – the rapid decrease in charge toward low pHs is characteristic of silica samples, which this particular cellulose sample was suggested by XRF to contain. It may be then that the surface of the sample is selectively enhanced with impurities of some type which contribute to its altered electrokinetic properties.

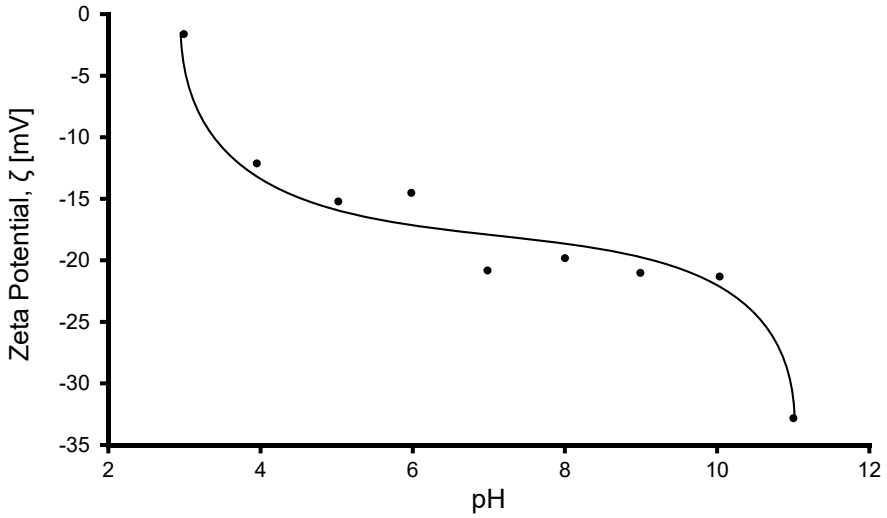

Figure 52: Zeta potential of macrofibrillar cellulose as a function of pH.

2.4 Summary

One of the major goals for this body of research was to investigate the efficacy of a range of different support materials and some novel analogues thereof. The materials chosen have been thoroughly characterised using a range of instrumental methods, results of which are reported here. Electron microscopic analysis was employed to analyse the morphology of the support materials and measure their particle size distributions, in combination with laser diffraction analysis to give information about their dispersion in water. X-ray fluorescence was used to determine the empirical formulae of the materials, and phase identification and analysis was performed using a combination of solid-state NMR, x-ray diffraction, and microFTIR. Inferences were made about the surface chemistry of the materials based on electrokinetic measurements used to obtain their zeta potentials.

The information derived from these techniques was anticipated to fulfil two main roles. Primarily, it provides a comprehensive understanding of the structure and properties of the support materials used to prepare catalysts in subsequent chapters, so that their physicochemical properties may be exploited, and the properties of resulting catalysts rationalised. Secondly, the data acts as a 'control' against which catalysts prepared from these materials can be compared, so that conclusions can be drawn reliably regarding the changes to their structures.

The silica used in this study was shown to be typical of silica gels, with an amorphous mesoporous structure and high surface area. Its surface is heavily

hydroxylated, with silanols present in a diverse range of chemical environments. In aqueous solution it displays mild Brønsted acidity, disperses readily, and its surface carries a negative charge at all but very low pHs.

The alumina was shown to be similar to other reported aluminas, composed predominantly of the highly crystalline α polymorph, but with possible low-level contamination from the γ, θ, or δ phases. The primary particles were relatively large with no detectable porosity, thus have a low surface area. The surface was coated with a thin layer of hydrogen-bonded aluminols, was highly charged, had an isoelectric point at around pH 7.5, and good dispersability in water.

The halloysite was composed of a mixture of sub-micron sized platelets and tubules, with a small portion of nanoparticulate quartz. These assembled into aggregates which did not readily redisperse in water. Although it was aluminium deficient it contained negligible amounts of substituent elements. Its surface chemistry was similar to that of silica, with a variety of surface silanols which dissociate in solution providing a negative charge.

The perlite had an unusual morphology, composed of thin, jagged, curved sheets. Its structure was deduced to be that of an amorphous silica glass substituted with a small portion of aluminium, and traces of sodium, potassium, calcium, and iron. It dispersed easily in water, and had a strong negative surface charge across all pHs.

The hydroxyapatite, sold as '*tri calcium phosphate*', was shown to be composed of irregular semicrystalline micron-sized pieces with an extensive macropore system. It did not appear to have any significant portion of surface hydroxyls, and had only a mild propensity to adsorb water. It dispersed readily in water, despite having only a mild negative surface charge. It was also shown to be contaminated with a substantial portion of non-apatitic calcium phosphate phases, most likely tri-calcium phosphate.

The bioapatite was similar in structure to the commercial sample, but with a wide variety of minor impurities to complicate it. It was less calcium deficient, but was sodium-bearing and AB-type carbonate substituted. It had a larger particle size and consequently a less portion of amorphous CaP, making it more crystalline overall. It is more basic when dispersed in water than the commercial sample, but had similar electrokinetic properties.

The microcrystalline cellulose was of high purity, containing only cellulose I, with a crystallinity of approximately 60%. It had no apparent porosity, did not disperse particularly well in water, and only had a weak surface charge.

The macrofibrillar cellulose, in comparison to the commercial sample, was much more crystalline, had a greater surface charge, and dispersed even more poorly in water. It too was composed predominantly of cellulose I. It contained a small portion of mineral impurities which are expected to influence its adsorption properties. It also had an entirely different microstructure.

2.5 Recommendations for Further Research

Future research into these materials could pursue two main routes. Firstly, extra characterisation methods could be investigated, as these would give further insight into the nature of the materials. Especially of interest would be elucidating the pore size distributions in the materials as well as their surface areas, which could be investigated by BET (Brunauer-Emmett-Teller) analysis of adsorption isotherms, intrusion porosimetry, or small-angle x-ray scattering. Surface properties such as Lewis acidity are also considered of interest, which could be investigated through spectroscopic detection of adsorbed probe molecules, for example ^{31}P NMR detection of adsorbed phosphines, or FTIR detection of adsorbed pyridine. The thermal stability of the materials may also be of benefit to measure, which could be done *via* TGA (thermogravimetric analysis) or DSC (dynamic scanning calorimetry).

Secondly, further processing methods could be investigated, for example to remove undesirable components of the samples and enhance their existing properties. Fractionation of materials like halloysite could be performed to selectively enhance the relative proportion of tubules compare to platelet particles. Acid leaching could subsequently be used to dissolve the alumina-containing portions, thus increasing the available surface area. Lastly, micronisation of the samples could be investigated by grinding the materials to increase the available surface area for subsequent immobilisation of nanoparticles.

Chapter 3: Analysis of the Wettability of Catalyst Support Materials

3.1 Introduction

Catalytic reactions using supported metals are commonly conducted in an organic solvent. In facilitating such reactions the solvent performs multiple roles, including dissolution and transport of the substrates, dissipation of heat, and potential modification of the activity of the catalyst. Catalytic reactions are therefore subject to solvent effects [273-275], which can strongly affect the outcome of an experiment. Selecting the most appropriate solvent for a reaction can thus be a difficult task, and some degree of insight is required to make a well-justified choice.

For reactions performed using a powdered catalyst suspended in a solvent in a batch reactor system, transport phenomena are especially important. If the catalyst particles are lyophobic and their surfaces cannot be effectively wetted by the reaction solvent, then they may aggregate in solution. This can inhibit the transport of the substrate to the active sites of the catalyst, thereby reducing its apparent activity. For catalysts with a low surface coverage of metal the wetting properties are expected to predominantly reflect the support material itself, and so a systematic investigation of the wetting properties of the support materials used herein was deemed necessary.

To investigate the wetting properties of the eight supports, the Washburn capillary rise method was used. This method probes the ability for a fluid to wet a powder, or in the case of this research, the ability for a range of organic solvents to wet the support materials detailed in the previous chapter. This of course depends on the both the textural properties of a support material and its surface chemistry, both of which have been extensively characterised.

The physics behind the capillary rise method are detailed in Washburn's original paper, which describes the dynamics of capillary flow as derived from Poiseuille's law [276]. It shows that when a wetting fluid contacts a capillary it is spontaneously drawn in, or imbibed, with the square of the distance travelled by the solvent front proportional to time. This is expressed mathematically by equation 1,

$$d^2 = \gamma r t \frac{cos\theta}{2\eta} \quad \ldots(1)$$

where d is the distance travelled by a solvent with contact angle θ through a capillary of radius r in time t, with a surface tension γ and viscosity η. By extension of this model, interstitial spaces between particulates in a bed of packed powder can be considered a set of tortuous capillaries in which the same phenomenon occurs. By mathematical manipulation of the previous equation [277, 278] a "modified Washburn equation" can be obtained, which describes the rate of imbibition in terms of mass. This is given by equation 2,

$$m^2 = C\left(\frac{\rho^2 \gamma cos\theta}{2\eta}\right) t \quad \ldots(2)$$

where m is the mass of solvent imbibed, ρ is its density, and C is a "material constant" representing the morphology of the capillaries. If one measures the mass of solvent imbibed by a column of powder as a function of time then several properties relating to the wettability of the system may be derived: direct comparison of the wetting rates allows inferences to be drawn regarding the penetrability of different solvents into a single powder, while comparison of the calculated contact angles allows one to compare the wettability of several different powders by the same solvent. Using this method, solvents can be chosen which will most effectively wet catalysts prepared from the support materials studied, thus reducing the potential for the introduction of mass transport limitations within these systems.

This technique has been used for measuring the wettability of a wide range of samples including soil colloids [279], quartz [280], and wood [281], although it has come under scrutiny for its occasional inability to reconcile calculated surface energy and contact angle measurements with those obtained by other techniques [282]. In spite of this, the technique is still considered a valuable tool for investigating the wetting properties of solids [283]. It has never, however, been extended to the analysis of the types of materials typically used as catalyst supports. This body of research fills this niche, representing a novel application of an existing methodology. Rather than approaching solvent selection from a trial-and-error perspective it is approached methodically and systematically herein, relating the wetting rates of different solvents to their appropriateness for use in supported metal catalysis.

3.2 Experimental

3.2.1 Methods

The traditional method for performing capillary wetting experiments using the Washburn method is using a tensiometric approach. The powder of interest is packed into a glass tube suspended from a tensiometer, which measures the increase in mass as a function of time when the tube contacts a reservoir of solvent. In lieu of a tensiometer the same experiments can be performed gravimetrically, however, using a setup similar to that of Liu *et al.* [284]. This method has been adapted for use in the current study, and is described as follows.

Powders were packed into a bespoke borosilicate sample tube, shown in **Figure 53**, and clamped with the lower 8 mm of the tube in a beaker of solvent placed atop an analytical balance, as shown in **Figure 54**. The solvent is immediately imbibed by the powder on contact of the two, and the decrease in mass of the beaker due to imbibition was measured as a function of time, giving the raw data. Losses due to solvent evaporation were measured and shown to be less than 1% of the imbibed solvent mass and were hence considered negligible, thus the mass lost from the beaker was assumed to be equal to the mass of solvent imbibed by the powder. No

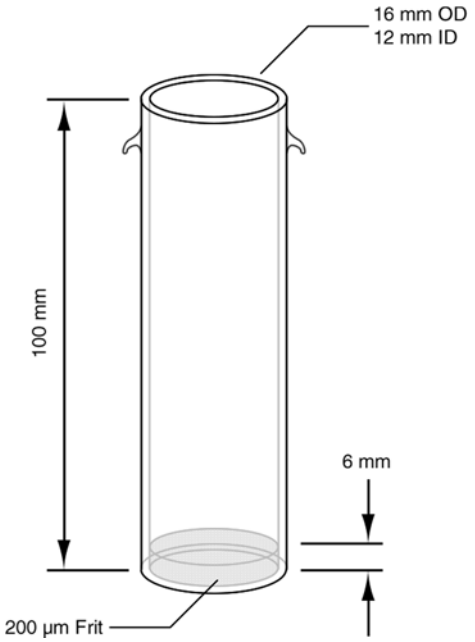

Figure 53: Schematic of the glassware constructed for the purpose of performing Washburn contact angle measurements.

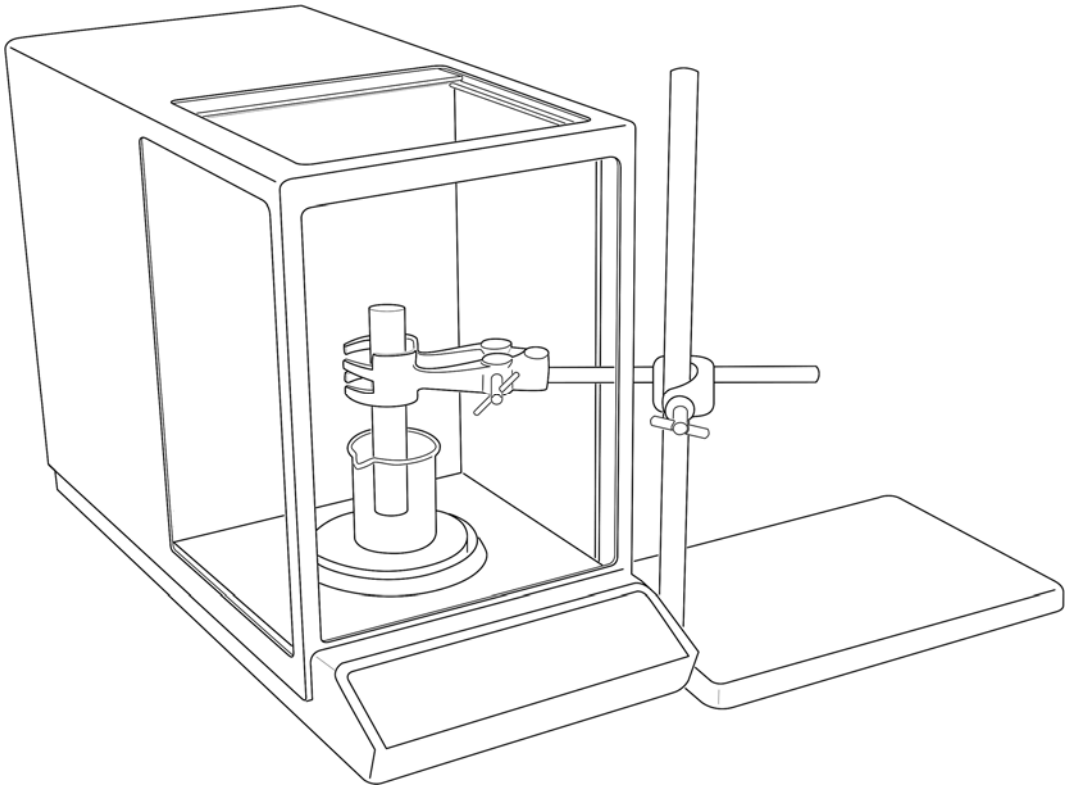

Figure 54: Schematic of the experimental setup for the Washburn contact angle measurements.

buoyancy corrections were made, since this particular sampling geometry, unlike the traditional tensiometric approach, does not significantly suffer from such issues. Additionally, the use of a relatively wide sample tube such as this reduces the potential for solvent-wall interactions which could affect results.

Wetting rates were extracted from the raw data by plotting the square of the mass of solvent imbibed as a function of time and calculating the slope of the linear portion of the graph, consistent with Equation 2. The material constant, C, was calculated for each support material by imbibing n-hexane and assuming the contact angle was equal to 0° due to its very low surface tension. This is the *de facto* method for calculating the material constant, although there are several assumptions implicit in its use [285]. Contact angles were then calculated by rearranging the Washburn equation to yield equation 3,

$$\theta = cos^{-1}\left(\frac{2\eta}{C\rho^2\gamma}\cdot\frac{\mathrm{d}m^2}{\mathrm{d}t}\right) \qquad \ldots(3)$$

where the terms of the equation are as given in the introduction section.

Two general sets of experiments were performed using this methodology. In the first experiment, a reliable method for packing the wetting tube with power was sought. The tube was packed with microcrystalline cellulose in various ways, and the imbibition of water measured as a function of time. The four most reliable methods were repeated in triplicate, and the variance in the imbibition rates calculated. Results of this workflow, along with details of the packing methods, are given in Section 3.3.1.

In the second experiment, a full wetting analysis was conducted on six of the eight support materials described in Chapter 2 using fourteen common organic solvents, resulting in a total of 84 imbibition experiments (6 supports x 14 solvents). The systems studied are given in **Table 3**. The two support materials 'perlite' and 'macrofibrillar cellulose' were not tested in the current study, because an insufficient amount was produced to allow their investigation, and re-using the materials was deemed too risky in case of surface contamination. Results of this experiment are given in Section 3.3.2.

Table 3: Support materials and solvents used for the Washburn capillary rise experiments.

Solvent	**Abbrev.**	**Support**	**Abbrev.**
Methanol	MeOH	Alumina	Al_2O_3
Ethanol	EtOH	Silica	SiO_2
Propanol	^{n}PrOH	Hydroxyapatite	HAp
Isopropanol	^{i}PrOH	Microcryst. Cellulose	MCC
Butanol	^{n}BuOH	Halloysite	HNC
Pentanol	^{n}PnOH	Bioapatite	BAp
Hexane	-		
Heptane	-		
Tetrahydrofuran	THF		
Ethyl acetate	EtOAc		
Acetone	-		
Acetonitrile	MeCN		
Dimethylformamide	DMF		
Dimethylsulfoxide	DMSO		

Two of the supports (SiO_2 and Al_2O_3) were also measured after drying to constant weight to determine if sorption of atmospheric moisture, either on their surfaces of by their bulk, may significantly impact their wettabilities. This data is also described in Section 3.3.2.

3.2.2 Materials

Support materials: All support materials used were as described in Chapter 2.

Solvents: n-hexane (>98.5%), n-heptane (>99.0%), methanol (>99%), ethanol (>99%), 1-propanol (>99%), 2-propanol (>99.5%), 1-butanol (>99.4%), tetrahydrofuran (>99%), and acetonitrile (>99%) were all supplied by Ajax Finechem, while 1-pentanol (>99%) was supplied by May & Baker, DMSO (>99.5%) was supplied by Scharlau, DMF (>99.8%) was supplied by Merck, and p-dioxane (>99%) was supplied by BDH Chemicals. All support materials used are described in Chapter 2.

3.3 Results and Discussion

3.3.1 Packing Methods

Four packing methods were found to produce beds of cellulose suitable for the imbibition of water. These were described as follows:

- Method A, the "tapped method": The tube was filled loosely with powder and then tapped vertically against a hard surface until no further settling of the particles was evident;
- Method B, the "compressed method": The tube was filled loosely and the contents compressed by hand using a plunger until the bed could be compressed no further;
- Method C, the "weighted method" The tube was filled loosely and the contents compressed for 1 minute using a plunger with a fixed 2 kg mass on top of it;
- Method D, the "loose method": The tube was filled loosely and the contents were not compressed at all.

In all four cases, the imbibitions proceeded spontaneously, with the solvent front moving up the column of powder at a decreasing rate. Different rates were observed for the four different methods, along with differences in their relative reproducibility. Methods A and B exhibited poor reproducibility, with RSDs (relative standard deviations) of 17% 10% respectively in their imbibition rates. Method D proved to be problematic because the weight of absorbed water would cause the column of powder to collapse, creating voids in the tube which prevented further imbibition. The RSD was found to be an acceptable 5.0% on the occasions when the powder column did not collapse, however these occasions were too infrequent for method D to be considered reliable. Method C proved to be the most reliable, with the RSD in the imbibition rates measured at 4.2%, and no unusual problems encountered. These results are summarised in **Table 4**.

Table 4: Summary of the imbibition rates for beds of microcrystalline cellulose prepared four different ways.

	Imbibition Rate [$mg^2\ s^{-1}$]			
	Method A	**Method B**	**Method C**	**Method D**
1	0.1594	0.1180	0.2450	0.3432
2	0.1306	0.0966	0.2360	0.3407
3	0.1131	0.1076	0.2251	0.3130
$\bar{x}$	0.1343	0.1074	0.2353	0.3323
σ	0.0233	0.0107	0.0099	0.0167
RSD [%]	17.39	9.96	4.23	5.04

The variances in the imbibition rates are easily explainable on mechanical considerations. Because the rate of imbibition depends on the size of the capillary through which it is occurring, those which are packed more tightly are likely to have smaller capillaries and a lower rate, and those which are packed the most consistently should have the lowest variance in the rates. This is consistent with the data: the powders from method B were compressed the hardest and those from method D the lightest, but A and B both rely on human judgement and so are less consistent, consequently having higher RSDs.

3.3.2 Full Wetting Analysis

Using the previously chosen packing method, the imbibition of fifteen organic solvents by beds of the four support materials were measured. In all cases the solvents were imbibed spontaneously, obeying approximately the same absorption profiles as those previously. During many of the imbibitions an evolution of heat was observed, possibilities for the origin of which are postulated later. Examples of the raw imbibition data are shown in **Figure 55**.

Processing of the data using Equation 2 showed that the imbibition rates were usually linear during the middle portion of the absorptions, with deviations from linearity occurring during the first and last fifths of the data. Examples of the linearised data are shown in **Figure 56**. The experimentally determined imbibition rates for each solvent and each support material are given in **Table 5**. The imbibition rates were fastest, on average, through beds of alumina and microcrystalline cellulose, followed by silica, halloysite, then the two apatites. Since the raw imbibition rates are proportional to the size of the capillaries in a material, this suggests that when the six materials are compressed into a column they behave very differently from one another. This reflects the differences in their textural properties noted in Chapter 2, as well as their different mechanical properties. For example, alumina is hard and lacks any internal porosity, thus when it is compressed the particles remain intact, and the only pores through which a solvent can be imbibed are the wide interparticulate pores formed from direct contact of the alumina granules with one another. Conversely, the apatite samples are much softer and contain significant microporosity, so when they are compressed the granules collapse onto one another, leaving only very fine tortuous capillaries for solvents to be imbibed slowly through.

Within a given support material, the trends in the relative imbibition rates of different solvents are harder to generalise. The imbibition rates of the alcohols were generally inversely proportional to their chain lengths, with methanol imbibed the fastest and pentanol imbibed the slowest. They generally showed good imbibition rates through many of the supports except the apatites, where the ketonic and ethereal solvents (acetone, THF, EtOAc) displayed markedly better behaviour. The polar aprotic solvents displayed mixed behaviour, rapidly wetting some supports but sluggishly wetting others. The alkanes on the other hand, being quintessentially non-polar, displayed moderate wetting rates on all of the materials studied.

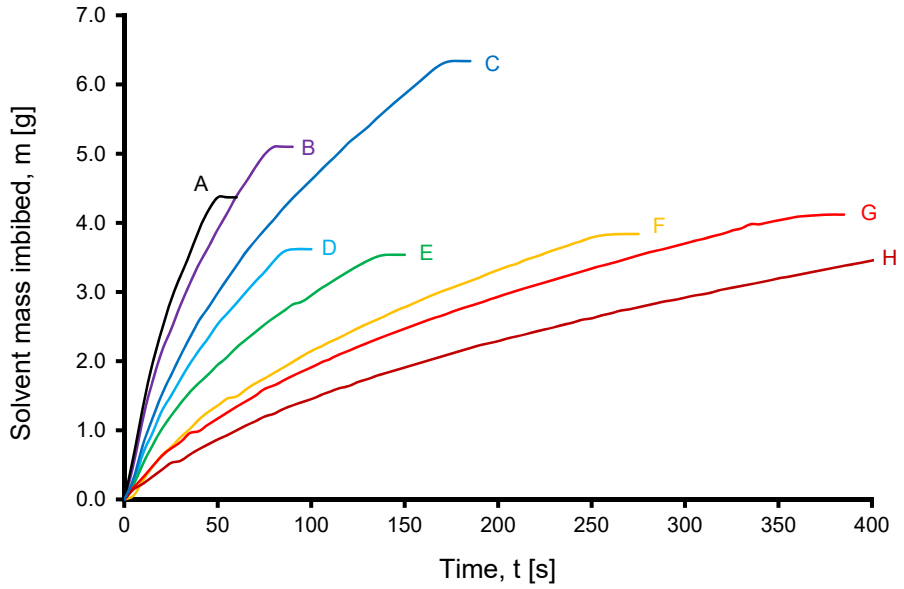

Figure 55: Raw Washburn capillary rise data for the wetting of alumina by selected solvents. The eight different traces correspond to eight different solvents; a) MeCN, b) EtOAc, c) DMSO, d) MeOH, e) EtOH, f) ^{n}PrOH, g) ^{n}BuOH, and h) ^{n}PnOH.

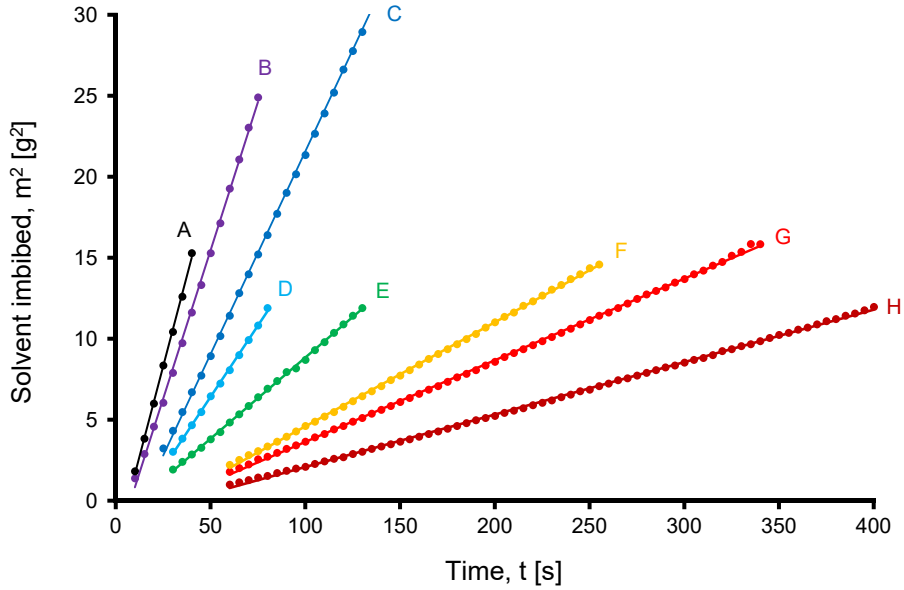

Figure 56: Linearised version of the data shown in the previous figure. The eight different traces correspond to eight different solvents; a) MeCN, b) EtOAc, c) DMSO, d) MeOH, e) EtOH, f) ^{n}PrOH, g) ^{n}BuOH, and h) ^{n}PnOH.

Table 5: Wetting rates [$mg^2\ s^{-1}$] for fifteen different organic solvents on six different powders. Parenthesised numbers correspond to the wetting rates for dried powders.

Imbibed Solvent	Imbibing Powder					
	SiO_2	**Al_2O_3**	**HNC**	**HAp**	**BAp**	**MCC**
MeOH	124.0 (161.4)	180.9 (175.9)	49.27	1.190	16.83	150.5
EtOH	64.19 (62.77)	93.34 (100.1)	22.76	1.072	12.73	82.11
nPrOH	37.21 (36.38)	57.09 (64.22)	13.91	1.056	8.813	47.09
^{i}PrOH	31.23 (30.61)	44.23 (52.08)	11.57	1.508	6.585	36.49
^{n}BuOH	33.67 (29.46)	40.77 (50.38)	7.100	1.145	4.215	36.49
^{n}PnOH	23.11 (20.19)	27.56 (33.25)	6.810	0.885	3.132	23.63
hexane	98.83 (72.83)	213.9 (195.0)	36.79	7.872	44.35	183.3
heptane	62.06 (72.81)	188.5 (196.0)	26.45	10.41	40.86	179.6
acetone	178.0 (217.9)	376.1 (361.5)	65.05	8.096	70.60	261.1
1,4-DXN	147.6 (162.6)	241.5 (250.1)	47.03	5.740	39.33	162.8
EtOAc	145.6 (137.4)	325.1 (370.4)	43.75	9.680	76.37	236.5
THF	178.3 (141.9)	369.3 (364.9)	65.24	7.892	70.44	271.2
MeCN	191.5 (182.4)	445.7 (449.2)	76.72	11.28	29.63	283.4
DMF	232.1 (220.2)	392.2 (336.0)	9.007	7.041	25.30	207.8
DMSO	159.4 (170.4)	229.6 (250.3)	0.8530	1.161	11.12	24.91

The contact angles calculated from this data, displayed in **Table 6**, also showed mixed trends. Most solvents imbibed by silica exhibited contact angles of zero, as did many for alumina, while hydroxyapatite and microcrystalline cellulose showed much greater variation, up to 89.1°, and 81.7° respectively. Halloysite behaved most similarly to silica, with contact angles of zero in most instances, with the notable exception of dimethylformamide and dimethylsulfoxide where the contact angles were high in both cases. The bioapatite sample was also wet similarly to the hydroxyapatite, although generally with lower contact angles.

Based on the surface energies of the powders [286-289] one may expect from Young's equation that molecular solids like cellulose would have the highest contact angles while crystalline covalent solids like alumina would have the lowest; however this is not completely consistent with the observations made in this study. Contact angles were observed to descend in the order HAp > HNC > BAP > MCC > Al_2O_3 > SiO_2, indicating there may be specific solvent-support interactions for some

Table 6: Contact angles [deg., °] for fifteen different organic solvents on six different powders. Parenthesised numbers correspond to contact angles on dried powders.

Imbibed Solvent	Imbibing Powder					
	SiO_2	**Al_2O_3**	**HNC**	**HAp**	**BAp**	**MCC**
MeOH	0.00 (0.00)	25.6 (18.8)	0.00	89.1	66.6	28.9
EtOH	0.00 (0.00)	21.0 (0.00)	0.00	73.1	52.8	16.6
nPrOH	0.00 (0.00)	9.12 (0.00)	0.00	60.2	43.7	18.1
^{i}PrOH	0.00 (0.00)	18.0 (0.00)	0.00	28.2	47.8	23.7
^{n}BuOH	0.00 (0.00)	30.0 (0.00)	28.7	48.6	64.9	25.2
^{n}PnOH	0.00 (0.00)	39.0 (0.00)	0.00	47.3	65.2	39.0
heptane	44.4 (0.00)	0.00 (0.00)	35.1	0.00	0.00	0.00
acetone	0.00 (0.00)	4.93 (0.00)	0.00	54.3	27.5	36.2
1,4-DXN	0.00 (0.00)	0.00 (0.00)	0.00	44.8	32.0	30.3
EtOAc	28.1 (0.00)	24.4 (0.00)	29.0	42.6	0.00	39.4
THF	0.00 (0.00)	0.00 (0.00)	0.00	52.7	21.2	28.0
MeCN	0.00 (0.00)	0.00 (0.00)	0.00	41.3	69.8	35.8
DMF	0.00 (0.00)	0.00 (0.00)	79.5	48.3	65.3	32.6
DMSO	0.00 (0.00)	0.00 (0.00)	88.6	83.4	74.8	81.7

systems which affect the wetting properties. This is supported by Zisman plots of the data, where the surface tensions of imbibed liquids are plotted on the abscissa against the cosines of their contact angles on the ordinate axis. For non-interacting liquids the data should form a straight line intercepting $\cos\theta=1$ at the position on the ordinate axis corresponding to the surface energy of the solid [290]. The data obtained in this study, however, follow no such trend, suggesting there are extraneous effects occurring which modify the wetting properties.

If it is supposed that wetting is enhanced by a favourable interaction between the solvent and the support then many of these observations can be easily rationalised. Silica for example has a very high concentration of surface silanols as shown by ^{1}H NMR, and is thus capable of hydrogen bonding with the alcohol hydroxyls. Conversely, the alumina had few detectable aluminols and cannot engage as readily in such an interaction. Cellulose is an intermediate case, possessing a large number of hydroxyls but the accessibility of which are low in crystalline samples [291, 292]. Hydroxyapatite interacts with alcohols *via* the hydroxyl moiety [293] which could

leave the hydrocarbon tails protruding outward from the apatite surface, leading to a surfactant-like hydrophobisation. This would effectively modify the HAp surface making it less polar, reducing the ability for polar alcohols to interact with it. While this may partially explain the anomalously poor wetting behaviour of the alcohols on this material, it would still make alcohols a poor choice for heterogeneous reactions involving this material.

The two alkanes, hexane and heptane, displayed similar wetting rates to the lower alcohols, but showed the opposite trends with respect to their contact angles. In the Washburn method, hexane is assumed to have a contact angle of 0° on all materials because of its exceptionally low surface tension, while heptane displayed a contact angle of 0° on all support materials except silica. Drying the supports produced no significant changes in the imbibition rates through beds of alumina, and mixed effects on beds of silica. Since the alcohols are highly polar while the alkanes are not, it is sensible that they display opposite trends in their wetting properties. This makes these two alkanes good solvents for catalysts prepared using support materials with nonpolar surfaces such as dehydroxylated alumina, but less so for those with polar surfaces such as silica.

The most interesting observation was the high rates exhibited during imbibition of the polar aprotic solvents. DMF penetrated beds of silica faster than all other solvents tested, while MeCN penetrated alumina, hydroxyapatite, and cellulose the fastest. DMSO showed similar penetration rates through silica and alumina, but was very slow to penetrate hydroxyapatite and cellulose. Drying the powders had no significant effect on the rates. The contact angles calculated from these data were correspondingly low; 0° on silica and alumina for all three, but moderate to high contact angles for hydroxyapatite and cellulose. Similar observations were made by Redón et al, who observed low contact angles between polar aprotic solvents and alumina surfaces when compared to other solvent types, and who found weak links between the contact angle and the solvent polarities [294]. All three solvents may therefore be good choices for use with catalysts prepared using silica or alumina, but less so for hydroxyapatite or cellulose, within the caveats stated above.

The four remaining solvents, acetone, ethyl acetate, tetrahydrofuran and dioxane, displayed wetting rates intermediate relative to the other solvents tested. Wetting rates were moderate to high in all cases, and contact angles were generally low. Once

again, oven drying produced no statistically significant differences in the wetting rates. Although none of these solvents have hydroxyls and thus cannot act as hydrogen bond *donors*, they may engage in hydrogen bonding as *acceptors* with support materials bearing surface hydroxyls [295, 296]. Additionally, the lone pairs of electrons present on the ether and ketone moieties may implicate them in Lewis acid-base interactions [297, 298], which may further enhance their interaction with the support surfaces. Their low viscosities and surface tensions make them preferable to the polar aprotics, while their consistent wetting properties make them preferable to alcohols. If considered purely in terms of their wetting properties this makes them the most versatile choice, although as discussed in the remaining paragraphs in this chapter, these are not the only considerations.

The unusual imbibition rates of the polar aprotic solvents brought about the consideration of several phenomena, which as discussed here, could bias the measured imbibition rates. Firstly, the imbibition rates may be artificially inflated due to decreases in viscosity of the imbibed solvent brought about by the heat released upon adsorption of the solvent molecules to the support material. Many of the solvents used herein are highly coordinating in nature by virtue of their structures, and this is reflected in their Lewis base properties [297]. The strength of this effect was anticipated to be different for different solvents, since not only would different solvents be expected to have different adsorption enthalpies on different supports, but also because the viscosities of solvents do not all change at the same rate as a function of temperature. This is illustrated in **Figure 57** for the n-alcohols, where the effect is clearly strongest with longer-chain alcohols. For n-pentanol, for example, a modest increase in temperature from 25 °C to 35 °C would reduce the viscosity from 3.62 cP to 2.68 cP, a decrease of over 25%. Given that the imbibition rates should depend on the viscosity of the solvent, this is anticipated to be a significant effect. The surface tensions of the solvents also decrease with temperature, although over the relevant temperature ranges in this study the decreases are approximately linear, and of a much lesser extent than the viscosity [299]. While this may also have an effect, it is expected to not be as strong.

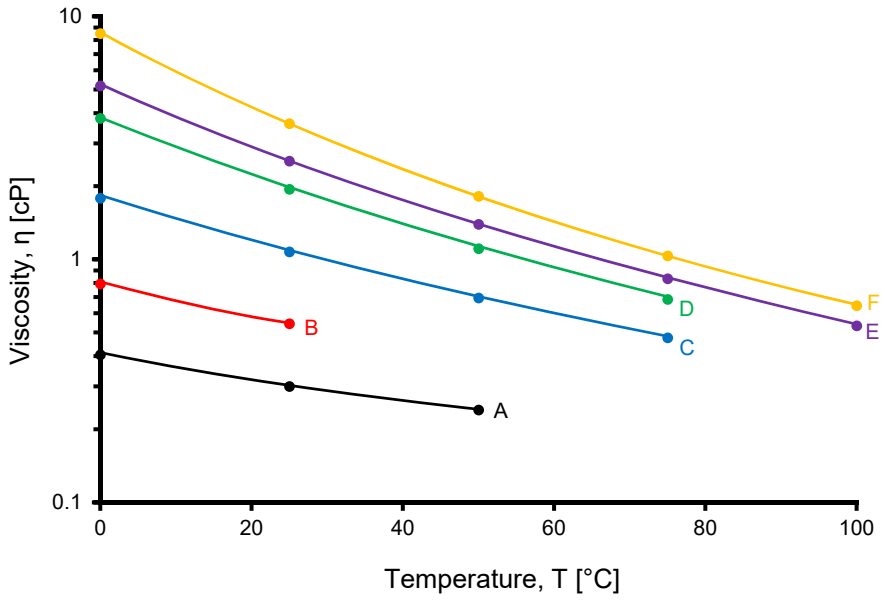

Figure 57: Plot of the viscosities of the C_1-C_5 n-alcohols and hexane as a function of temperature as obtained from the literature. Plots correspond to hexane (A), methanol (B), ethanol (C), propanol (D), butanol (E), and pentanol (F).

The approximate magnitude of the adsorption effect can be estimated by a crude calculation. The enthalpy of adsorption on silica has been reported as 25.0 kJ mol^{-1} for ethanol [300] or 60-67 kJ mol^{-1} for methanol [301], which is not insignificant. Assuming a surface hydroxyl concentration of 4.0 nm^{-2} [206] and a 1:1 stoichiometry, a 10 g sample of silica with a surface area of 550 m^2 g^{-1} can therefore bind $5.5x10^{21}$ methanol molecules, or $9.1x10^{-3}$ mol, corresponding to a net release of energy of *ca.* 550 J. Assuming a 10 cm^3 vessel with 50% porosity and that the heat is distributed primarily amongst the solvent, and given the specific heat capacity of methanol of 81.1 J K^{-1} mol^{-1}, this corresponds to a temperature rise of approximately 55 K. Though this is only a rough calculation, such a temperature rise would clearly make the imbibition vessel 'hot to the touch', and suggests the effect is possibly not insignificant.

A second possibility which could contribute to the observed imbibition rates is a change in viscosity of the solvents brought about by the release of heat due to mixing with water present in the pores of the support or physisorbed on their surfaces. On a per mole basis this effect is much weaker than for adsorption of solvent molecules, as judged by the excess enthalpy of mixing between a given solvent and water. For mixtures of DMSO and water the effect can produce a maximum of -2.8 kJ mol^{-1} [302], for DMF it is -2.15 kJ-mol^{-1} [303], for MeOH it is -

0.9 kJ mol^{-1}, and for MeCN it is +1.1 kJ mol^{-1} [304]. Making some assumptions regarding the state of hydration of the support materials we can once again calculate the approximate magnitude of this effect. For a material which contains 1% moisture, which is not unlikely for the current materials, a 10 g column of powder thus contains 0.1 g of water, or $5.6x10^{-3}$ mol. For DMSO, this corresponds to maximum exotherm of *ca.* 15 J, more than an order of magnitude smaller than the heat generated from the adsorption effect. The small size of this effect aside, the excess enthalpy of mixing for acetonitrile is endothermic, and given the sample heating observed during acetonitrile imbibition, this effect is unlikely to have contributed significantly or reliably to any significant changes in viscosity. Should either of these effects exist, however, they may be partially mitigated, by positive deviations from ideality in the viscosity of binary solvent-water mixtures observed in some systems such as DMSO-water [305].

Another issue which warrants attention in these systems is absorption of atmospheric water by *solvents*. In this study no attempts were made to pre-dry those which were used, since in many catalytic studies solvents are used 'as received', with little attention paid to pre-drying them before use. Water-miscible solvents are often appreciably hygroscopic, which can have effects on their physical properties such as viscosity and density. This may affect the results of an assay such as this, altering apparent wetting rates. Since all the supports display hydrophilic characteristics it seems unlikely that absorbed water would inhibit wetting, rather it may even enhance it in some cases. Solvents containing high concentrations of dissolved water may potentially hydrate the surfaces of previously dried support materials; indeed this is the basis of using materials such as silica or alumina to dry organic solvents [306]. Such a phenomenon may explain why there is apparently so little difference between the dried and non-dried supports in terms of their wetting rates. It would, of course, be of interest in the future to investigate exactly how the solvent water content affected the wetting properties of these materials.

Though the results of this study may be used to estimate the wetting properties of 'real' catalysts (compared to the pristine supports), caution must be exercised therein. Since the wetting properties are largely determined by the morphology and surface chemistry of the capillaries, any alteration to these properties could potential change the wetting properties and thus the trends observed in this data. This is

especially relevant to supported metal catalysts, where nanoparticles are dispersed on the surface of a support material. Having expectedly different physical properties to the support materials themselves, the nanoparticles could produce a number of unforeseen effects, especially at higher surface coverages. The surface tensions of nanoparticles are expected to be significantly higher than the support materials, since they have a significant portion of their atoms at the surface, which (by analogy to a sessile drop) Young's equation would predict an increase in the contact angle. This effect is predicted to be worse for non-coordinating solvents, since coordinating solvents tend to interact strongly with metallic surfaces of platinum group elements, which would work in opposition to the aforementioned phenomenon.

Aside from physicochemical differences caused by immobilisation of nanoparticles, there are additional textural changes to the surfaces, since nanoparticles occupy space, albeit a small amount. The immobilisation of particles could potentially have the effect of roughening the surface of the catalyst, which could potentially trap nanobubbles of gas at the catalyst surface [307]. The surfaces may then be differentially wetted depending on whether the wetting solvent can obtain a Wenzel state, where it displaces the bubbles and wets all surfaces, or a Cassie-Baxter state, where the bubbles remain in place.

Another factor to consider was the choice of reference solvent for this work. Although hexane has typically been used as the reference solvent and has been championed by Chibowski for this purpose, on more polar surfaces it may be appropriate to use a more polar solvent. Methanol, for example, maybe an appropriate choice because, although its surface tension is not appreciably higher (22.07 vs 17.89 mN m^{-1}), and though it is more than twice as viscous (0.793 vs 0.300 cP), it is still a very thin fluid. Furthermore, it is both a hydrogen bond acceptor and donor, which may be apt for polar, heavily hydroxylated, surfaces. Acetone could potentially be used, also, having a similar viscosity (0.306 vs 0.300 cP) though a slightly higher surface tension than methanol (22.72 mN m^{-1}).

A further point which warrants discussion is the solubility of hydrogen in these solvents. Although it may be possible to find a solvent which wets a catalyst extraordinarily well, if it cannot dissolve the necessary reactants it is of limited utility. It has been shown that within a homologous series of solvents the rate of a catalysed reaction depends only on the hydrogen solubility, and thus this is a critical parameter.

Hydrogen solubilities were obtained from the literature where available and are given in **Table 7**. It is evident from these values that a wide range of hydrogen solubilities are exhibited by the solvents tested, and that the solubility is generally inversely proportional to the polarity of the solvent, following the old adage '*like dissolves like*'. Gaseous hydrogen is therefore most soluble in hexane, followed closely by heptane, both of which exhibit hydrogen mole fractions at saturation of more than five times those of the polar aprotic solvents. This means that while the polar aprotics may wet some of the support materials especially well, their low hydrogen solubilities mean

Table 7: Solubility of hydrogen gas in selected solvents, given as the dissolved mole fraction, x_2, in gas-liquid equilibrium at the given temperatures and pressures. All pressures given in kPa unless otherwise stated. Some modern data is given alongside the data reported in the IUPAC-NIST solubility series.

Solvent	Solubility ($x10^4$ x_2)	Temperature (K)	Pressure (kPa)	Ref.
MeOH	1.38	278	1 MPa	[308]
	1.61	298.15	101.325	[309]
EtOH	1.95	298	101.325	[310]
	2.06	298.15	101.325	[309]
nPrOH	2.31	298.15	101.325	[309]
^{i}PrOH	2.64	298.15	101.325	[309]
^{n}BuOH	2.64	293.15	101.33	[311]
hexane	7.13	298.15	101.325	[312]
heptane	6.94	298.15	1 atm	[313]
acetone	2.87	298.15	101.325	[312]
	2.75	298	101.325	[310]
	3.01	298.15	101.325	[309]
1,4-DXN	1.84	298.15	101.325	[312]
	1.76	298.15	101.325	[309]
EtOAc	3.46	298.15	101.325	[309]
THF	2.70	298.15	101.325	[312]
	2.74	298.15	101.325	[309]
MeCN	1.84	298	101.325	[310]
DMF	1.47	298.15	101.325	[312]
DMSO	1.78	298.15	101.325	[312]
	0.76	298.15	101.325	[309]

they are probably not appropriate choices for conducting reactions in. On this basis, therefore, the alkanes possess the best compromise between their wetting properties and their hydrogen solubility, followed closely by THF and acetone.

These results are anticipated to be useful for comparing the wetting properties of the native support materials, although in many applications the materials may be decorated with metal nanoparticles, or be functionalised with some type of anchored inorganic complex. If these immobilised species are not uniformly distributed over the surface of the capillaries, it cannot necessarily be confirmed that wetting experiments such as these are filling the capillaries upon the walls of which the immobilised species reside. It would thus be beneficial to perform porosimetry experiments to determine the extent to which capillary filling is occurring, and to correlate this data with electron microscope data, for example, to confirm that the two are closely correlated, and that the accessibility of the solvents to the catalytically important structures is occurring.

3.4 Summary

The Washburn capillary rise technique was successfully applied as a novel method for rationalising solvent choice in heterogeneous reactions. The technique is experimentally simple and highly versatile, allowing users to screen a wide array of solvents for their ability to wet and subsequently penetrate powdered materials in a short period of time. No special treatment or preparation of reagents is necessary, giving results directly comparable to the open-air conditions which many catalysts and support materials are subjected to in the laboratory. Significant differences were observed in the wetting rates and contact angles of the fifteen different solvents tested in this study, providing compelling evidence for the usefulness of the technique for rational solvent selection in multiphasic chemical processes involving solid materials.

3.5 Recommendations for Further Research

Two major routes of research could be pursued in further studies. Firstly, it would be beneficial to cross-verify the contact angle data reported herein by use of a different method. This is difficult, however, since many of the other methods for calculating contact angles, such as the sessile drop or the Wilhelmy plate method, require the material to be in a flat, planar shape, which is not achievable with

powders without substantial processing. Alternatively, some other property of the materials could be measured, such as their degree of aggregation in different organic solvents. This could be probed by UV/Vis, and the absorbance, equivalent to the turbidity, given relative to the aggregation in a reference solvent.

It would also be of interest to perform some calorimetric studies to investigate the magnitude of the adsorption effect and the solvent mixing effect. Although calculations are presented in the current thesis, they are purely theoretical. Adsorption of the solvents to the support materials could also be probed spectroscopically, using FTIR or NMR, to give evidence supporting the theories proposed herein.

Chapter 4: Development of Laser Ablation-Based Methods for Quantifying Catalyst Loading

4.1 Introduction

One of the most important properties of a supported metal catalyst is its loading, that is, the amount of supported metal it contains. The loading affects both physical and chemical properties of a catalyst, and its accurate measurement is essential for calculating kinetic properties such as turnover frequencies. Measuring the loading of a catalyst is traditionally done by digesting it in mineral acid, and spectrometrically analysing the resulting solutions. While the spectrometric analysis is relatively straightforward, the effectiveness of the digestion can vary dramatically depending on the nature of the catalyst and the method used.

One of the most commonly used digestion methods is with mineral acids. While this is trivial for base metals like iron and nickel, the noble metals, as suggested by their names, can present somewhat more of a challenge. More extreme conditions must be used to solubilise these, with combinations of hot mineral acids such as HF, H_2SO_4, or $HClO_4$ often used, often at elevated pressures, and often with the assistance of microwave radiation. Even so, additional oxidising agents are sometimes required, thus H_2O_2 is often included in the reaction mixtures [314].

Another common digestion method is alkali fusion, where samples are attacked at by molten alkali salts such as NaOH, Na_2O_2, Na_2CO_3, *etc,* at temperatures in excess of 1000°C. This solubilises the metals, and once cooled, they are ensconced in a pellet of salt. The pellet can then be reconstituted in water, and its metal content assayed [314-316].

A third method, perhaps the least common though most effective, is direct chlorination. Samples are heated to several hundred degrees in an atmosphere of flowing chlorine gas and a molten chloride salt, which converts the metal particles into their corresponding chloride salts. The metal can then simply be rinsed free from the residual material, and the resulting solutions assayed spectrometrically.

Though all of these methods are applicable to the digestion of a broad range of catalysts, not all laboratories are equipped to implement them; moreover, there are obvious logistical issues associated with doing so safely. Notwithstanding, these methods are laborious or expensive, there is no guarantee that the digestions are repeatable, nor that the recovery of metal is quantitative.

Fortunately, there is an array of analysis methods which exist for measuring the elemental concentrations of solid materials without the need for any sample digestion whatsoever. Two such techniques were investigated in the current study; laser ablation-inductively coupled plasma-mass spectrometry (LA-ICP-MS), and laser-induced breakdown spectroscopy (LIBS). Neither of these methods has been widely adopted for quantifying the metal loadings in supported metal catalysts, but with increasing availability of the necessary instrumentation an assessment of their fitness for purpose was deemed a fitting project to pursue.

LIBS is a laser-based optical emission method which shares its principles with atomic emission spectroscopy. A high-powered laser is focused at the surface of a solid sample, causing ablation of a small portion of material. The heating produced by the laser ionises the plume of ablated material producing a plasma, the composition of which is proportional to the bulk of the sample. As the plasma cools, the ions loose energy as photons, producing an optical emission spectrum. Measuring the wavelengths and intensities of these emission lines allows the elemental composition of the sample to be determined. It is a mature method which has spawned numerous books [317-319] and reviews [320-324], though has been infrequently applied to the analysis of catalyst materials. Most applications focus on the analysis of spent catalytic converts from automobiles [325-328], though none report the application to accurate and precise metal quantitation in laboratory-based metal catalysts.

A second, related, technique is LA-ICP-MS. In this method a high-powered laser is used to ablate material from the surface of a solid sample, which is swept by a stream of gas into an inductively coupled plasma mass spectrometer. Within the plasma the ablated material is ionised, separated by mass to charge ratio, and the ion current measured by a detector. A small body of research has illustrated that it can be successfully applied to the analysis of the platinum-group elements in a variety of matrices, including geological materials [329-339], urban particles [340-342] and road

sediments [343, 344], reference materials [345-347], meteorites [348, 349], artefacts [350] and feathers [351]. A further handful of studies have cursorily mentioned the application of laser ablation to the study of supported metal catalysts, but give only fleeting details, if any, of the accuracy, precision, validation and procedural aspects of the technique [352-358]. No studies present a systematic investigation of the use of LA-ICP-MS for supported metal catalysts, however, making this a technique of interest to investigate further.

While these methods sound appealing, it is important to note that they are both ratio methods. This means that the concentration of the analyte in a sample is determined by comparing its instrumental response with that of a standard with a known composition. As the instrumental response in ablation methods depends heavily on the matrix, this dictates that the precisely matrix-matched standards should be used [359, 360]. This is problematic for supported metal catalysts, as no such standards are commercially available.

To solve this issue, laboratory reference materials (LRMs) must be created and their elemental compositions determine prior to analysis of real samples. Such analyses are often performed using neutron activation analysis (NAA), which is considered the 'gold standard' in elemental analysis. In this method a sample is irradiated with neutrons, the capture of which by analyte nuclides produces unstable radioisotopes. The decay of the radionuclides proceeds *via* known pathways, including the emission of gammas of known energies. This is illustrated in **Figure 58**. Performing gamma spectroscopy on an irradiated sample therefore allows calculation of its elemental composition.

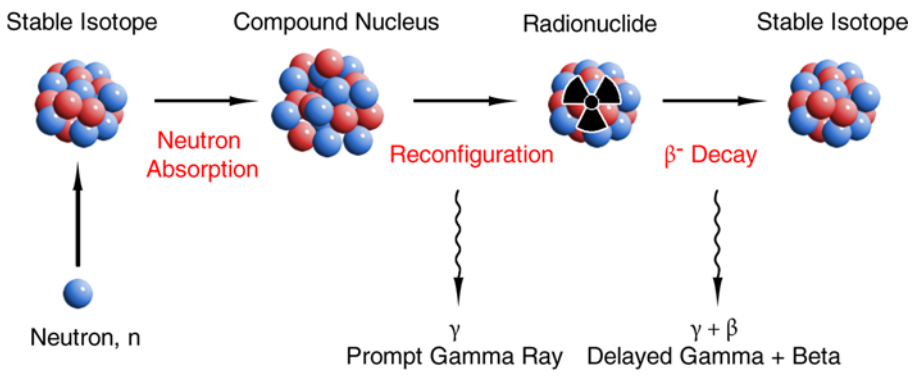

Figure 58: Schematic of the neutron activation process.

Clearly a niche exists for the development of a method for the solid-state analysis of supported metal catalysts, which is the topic of the research described in this chapter. At the outset of this work, The University of Waikato possessed only an LA-ICP-MS system. Initial development work was undertaken using this system to assess its fitness for purpose, which successfully lead to the development of a good experimental workflow. The need was identified for the creation of a series of matrix-matched LRMs, which were produced and characterised by NAA. At this point the laser was (unfortunately) decomissioned, though a LIBS instrument was subsequently acquired. Further method development was performed using only this instrument, which proved to be faster, easier, and more reliable. The resulting method was used for the quantification of metal in the catalysts prepared in all subsequent chapters, thus proving an indispensable tool for catalyst characterisation. The basic details of the experimental workflows followed are given in the following sections, with further details given in Appendix 1.

4.2 Experimental

4.2.1 Experimental Methods

4.2.1.1 LA-ICP-MS Workflow

Raw data collected by LA-ICP-MS is the form of an ion current as a function of time, as illustrated schematically in **Figure 59**. Multiple ions can be monitored simultaneously during data acquisition, each representing a specific element. For a

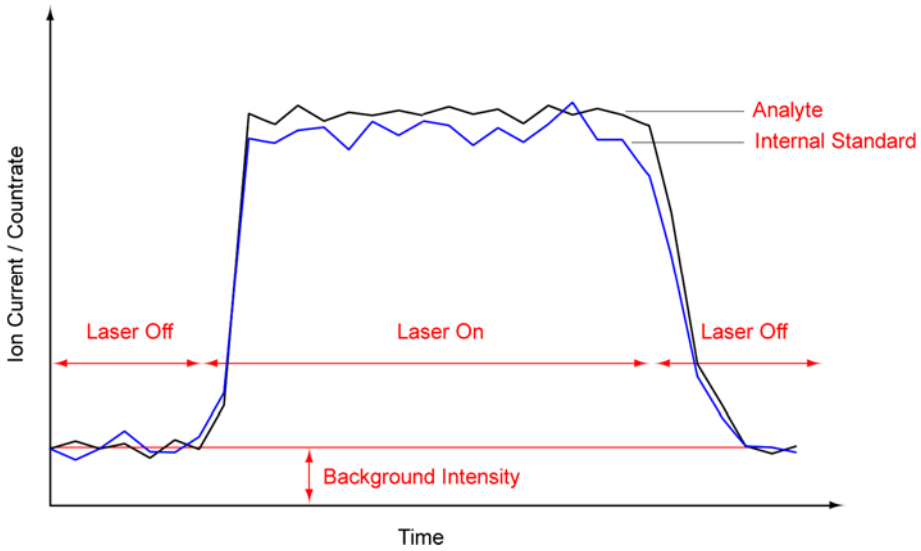

Figure 59: Schematic of an LA-ICP-MS ion profile illustrating the signal fluctuation with laser operation.

given sample the ion current is proportional to the concentration of the element, and so this data can be used, after significant optimisation and development, for quantitation of elements of interest.

As with many analytical techniques an internal standard is often used in the analysis, and so a minimum of two ions/elements are monitored. Normalisation of the ion current of the analyte element using the ion current of an internal standard element therefore allows an unknown sample to be compared to a standard sample, from which the amount of the analyte can be quantitatively determined. In the current research, a series of experiments were performed in order to optimise the quantitation conditions by systematically varying different experimental parameters and assessing their effects on the data. Three main parameters of the data were investigated:

- **Ion current intensity**. Since quantitation is performed using the ion current intensity, it was considered of interest to set the experimental parameters to achieve the greatest possible current without saturating the detector, thus maximising the dynamic range of the assay.

- **Analyte to internal standard ratio.** As quantitation requires the normalisation of the analyte's ion current to that of an internal standard, it was considered of interest to investigate the effect of different experimental parameters on the ratio between the two.

- **Intrasample and intersample variability.** For reliable quantitation the precision of the assay should be as high as possible, which can be achieved by maximising the within-sample homogeneity and having the least possible variance in technical replication.

A series of experiments was therefore conducted on a range of samples, systematically varying different experimental parameters and investigating their effects on the previously listed qualities. These experiments are briefly detailed as follows:

Standard Development: In the first set of experiments, an appropriate method was sought to prepare the necessary standard materials (LRMs) for subsequent analyses. Alumina was doped with rhodium, palladium, and platinum nanoparticles

by eleven different methods, and subsequently analysed by LA-ICP-MS. The details of the eleven methods are given in A1.1.1.

Linearity Testing: Once the most appropriate method for preparing the LRMs was chosen, a series of materials with linearly increasing amounts of metal were prepared. These were analysed by LA-ICP-MS to determine whether or not the instrumental response increased linearly with concentration, and therefore whether the technique would be appropriate for further development. Details of the materials are given in A1.1.2.

Standard Doping: Once a linear response was confirmed, a method was sought to dope the LRMs with a foreign element to act as an internal standard to which the data could be normalised. Cobalt was chosen as the internal standard, and was doped into the LRMs by thirteen different methods. The samples were once again analysed by LA-ICP-MS to determine which method was the most reliable. Details of the doping methods are given in A1.1.3.

Data Processing: After the most reliable standard doping method was chosen, one of the LRMs was prepared and analysed in triplicate by LA-ICP-MS. The data were mathematically manipulated in six different ways, and the resulting between-sample and within-sample variability in the PGE:Co (platinum group element) ratio was investigated. Details of the data processing methods are given in A1.1.4.

Pulse Parameter Optimisation: Once the best doping method was selected, one of the LRMs prepared using this method was analysed by LA-ICP-MS and the laser properties systematically varied to investigate their effects on the data. Multiple line scans were therefore performed on the sample, with the laser power/fluence adjusted, followed by the spot size, scan speed, and repetition rate. Details of the parameters altered are given in A1.1.5.

Standard Testing: Once the technical variability was assessed, a second generation of standards were prepared using higher concentrations, up to 2.5 wt%. Line scans of the samples were performed, Co-to-PGE ratios calculated, and calibration curves constructed. Results from this trial, as detailed later in the results section, indicated that a third generation of standards needed to be produced. Further details on the standards tested are given in A1.1.6.

4.2.1.2 NAA Workflow

For the third generation of standards the best methods from the initial development were re-investigated but prepared using linearly increasing amounts of metal, *viz.*, a series of standards. The samples were split in half, with one half kept, and the other half doped with cobalt. To measure the absolute concentration of metal in the resulting standards so that they could be used quantitatively as laboratory reference materials (LRMs), samples were sent for Neutron Activation Analysis. at the Open Pool Australian Light-Water Reactor (OPAL). A grant from the Australian Institute of Nuclear Science and Technology (AINSE) was secured for this purpose. Details of this analysis are given in in the 'instrumental methods' section. Details of the synthesis of the third generation of standards are given in A1.2.1.

At this point during the method development the LA-ICP-MS laser was decommissioned, rendering the hitherto performed method development largely irrelevant, as it would have to be repeated for the new instrumental setup. As a LIBS spectrometer was acquired shortly afterward, subsequent development was therefore switched to LIBS, and a similar series of processes were investigated using the portion of the standards which had *not* been cobalt-doped.

4.2.1.3 LIBS Workflow

Data obtained from LIBS is in the form of an emission spectrum, which is a plot of emission intensity as a function of wavelength. This is illustrated schematically in **Figure 60**.

As with LA-ICP-MS, LIBS requires the use of an internal standard to which data can be normalised, which in turns allows the comparison of an unknown sample to a standard sample, from which the concentration of selected elements may be determined. In the current research, a series of experiments was therefore performed to optimise the conditions for quantitation, based on their effects on three parameters. These are described as follows.

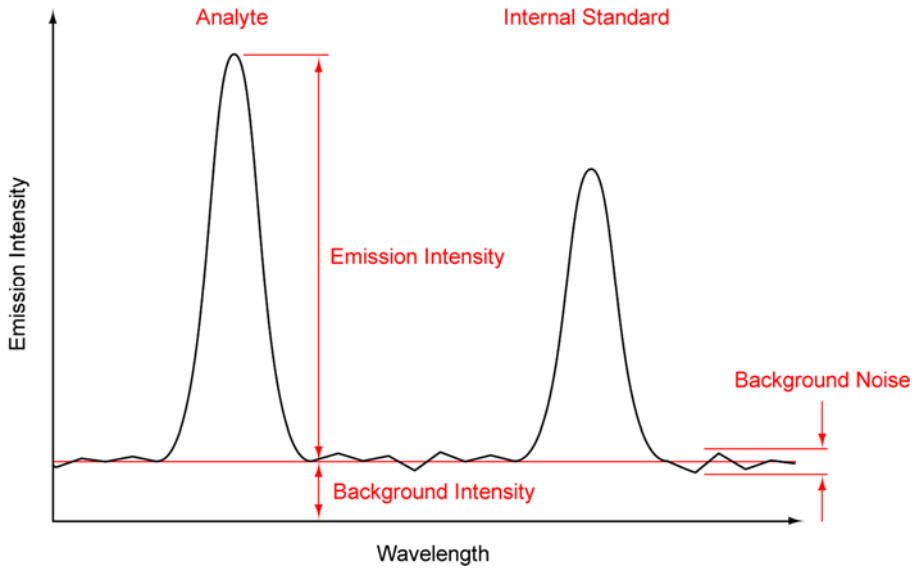

Figure 60: Schematic of a LIBS spectrum, illustrating the various parameters investigated.

The three parameters investigated, in relation to **Figure 60**, were:

- **Signal to Background Ratio (SBR).** In order to achieve the greatest dynamic range possible, it was considered desirable to acquire data having the lowest background and highest emission intensity possible. This was calculated from the intensity of the emission peak divided by the intensity of the background.

- **Signal to Noise Ratio (SNR).** In order to have the lowest detection limits possible, it was considered there should be as little variance in the background noise as possible. This is because the limit of detection (LOD) is commonly defined as three times the standard deviation in the background, while the limit of quantification (LOQ) is commonly defined as five times the standard deviation in the background. This was calculated by dividing the intensity of relevant emission lines by the standard deviation in a nearby portion of the spectrum containing no emission lines.

- **Signal to Internal Standard Ratio (SISR).** In order to normalise data so that unknown samples could be compared with standards, it was considered necessary to divide the intensity of relevant analyte emission peaks (*i.e.* Pd peaks) by relevant support material emission peaks (*i.e.* Al peaks). It was therefore of interest to determine how the signal to internal

standard ratio varied as a function of various experimental parameters, for example laser power, so that the data were as reliable as possible.

In the current research a series of experiments was therefore performed to determine how various experimental parameters could impact on these properties, in order to optimise the method for the most accurate quantitation possible. These are described as follows.

Preliminary Optimisation: The first experiments performed were to investigate whether appropriate emission signals could be obtained from the samples. Pelletised samples were analysed by LIBS in "timing mode", where the laser rasters constantly across the surface of the sample, and changes in the emission can be inspected in live time. The laser power, gate delay, and laser repeat rate were iteratively adjusted to obtain the lowest background and greatest peak intensities, and these settings were used for further developmental work. Further details of the preliminary optimisation are given in A1.3.1.

Dilution Testing: In the next experiment the effect of sample dilution was investigated, since this was shown to be an important factor in obtaining quality LA-ICP-MS data. Samples were re-prepared by diluting with microcrystalline cellulose, and analysed by LIBS using an array of 10x10 spots covering a 10 mm x 10 mm area on the sample, and ablated five times sequentially. The properties of the relevant emission lines were analysed, and these results used to select the most appropriate level of sample dilution. Further details of how the dilutions were performed and on what samples are given in A1.3.2.

Pulse Counting: In the next experiment the effect of the number of pulses was investigated. The same 10 x 10 array of spots was ablated on each sample (newly prepared), but repeated 20 times. The properties of the emission lines were investigated as a function of ablation depth in order to determine whether the greatest sensitivity was obtained at the surface of the sample, or deeper inside it. Further details of this experiment are given in A1.3.3.

Grinding Effects: In the next set of experiments the effects of sample homogenisation by grinding were investigated. The samples were re-prepared after different grinding for either 0 s, 10 s, 100 s, or 1000 s. The samples were ablated in a 10 x 10 array once again, and the most appropriate grinding time selected based on

the properties of the relevant emission peaks. Further details of the grinding experiment are given in A1.3.4.

Pulse Parameters: In the next set of experiments the effects of pulse parameters were investigated. The LIBS unit used in this study had only three adjustable parameters: laser repetition rate, laser power, and gate delay. Repetition rate was set at a fixed 1 Hz, and the other two parameters were systematically altered and their effects on the emission peaks investigated. Further details of the pulse parameters and how they are optimised are given in A1.3.4.

Calibration Curves: In the next set of experiments the linearity of the method was investigated. The NAA-measured samples from the earlier LA-ICP-MS work were pelletised and analysed using the optimised parameters selected from the previous experiments, and calibration curves constructed. The effect of line choices was investigated, as well as different normalisation options. Details of how the calibration curves were constructed and from which samples are given in A1.3.5.

4.2.2 Instrumental Methods

Laser induced breakdown spectroscopy was performed using a Laser Analysis Technologies SpectroLaser 4000 (acquired by XRF Scientific, acquired by Photon Machines, acquired by Teledyne, divested to, and currently licensed by, TSI). The unit had a New Wave Research Nd:YAG 'Tempest' laser operating at the 1064 nm fundamental, with a maximum power of 200 mJ and a fixed 500 µm spot size. The pulse length was 7 ns and the repeat rate <20 Hz. Emissions were separated by four Czerny-Turner spectrographs and detected by four CCDs, covering the wavelengths 190 nm - 950 nm with 0.09 nm resolution at 300 nm. The sample position was controlled with a precision 2-axis translation stage, and the sample chamber purged with air.

LA-ICP-MS was performed using a Perkin-Elmer SCIEX ELAN DRC II ICP-MS, operated using ELAN 3.3 software. Samples were introduced using a New Wave UP-213 laser ablation system, employing a 213 nm Nd:YAG laser operating in q-switching mode.

Neutron Activation Analysis was performed at the OPAL ("Open-Pool Australian Lightwater") reactor in Lucas Heights, Sydney. The primary purpose of this 20 MW

research reactor is for neutron transmutation doping of silicon ingots for the semiconductor industry, but also for the provision of neutrons for materials characterisation techniques such as NAA.

All sample preparation was performed by ANSTO staff in a class-6 clean room, with powders prepared and analysed as received. Small portions of each (*ca.* 50 mg) were weighed out using a microbalance into cylindrical polyethylene sample capsules. Samples were co-irradiated using a gold comparator, which subsequently allowed quantitation of the analytes of interest using the k_0 method. For short irradiations the comparator was Au on filter paper, prepared from an aqueous NIST SRM, while long irradiations used small pieces of 0.1% Au wire.

Samples were transferred by ANSTO staff from the laboratory to the reactor core using a digitally controlled pneumatic transfer system with a timing uncertainty of ±1 s. Long irradiations were performed for *ca.* 6 hours in neutron fluxes of *ca.* 2.5×10^{13} n cm^{-2} s^{-1}, while short irradiations were performed for 20-30 seconds in fluxes of *ca.* 2.2×10^{12} n cm^{-2} s^{-1}. After irradiation the samples were transferred back to the laboratory, where a "cool down" period was used allow the activity to drop to <1 μCi before gamma spectroscopy was performed.

Gamma spectroscopy was performed by ANSTO staff using an ORTEC p-type HPGe detector coupled to an 8192-channel DAC. The energy range and efficiency of the detector was calibrated using a europium standard. The counting position was selected to obtain a count rate of *ca.* 2000 cps with 10% dead time across the full energy range. Samples were counted until reaching 80,000 counts at the most intense peak. Zero dead time (ZDT) areas were obtained by subtraction of Compton background, and gaussian peaks fitted to the emission lines with either stepped or linear backgrounds fitted to minimise the fitting residual. Areas were processed using Kayzero (v3.02) for Windows to obtain the final elemental composition of the samples.

4.2.3 Materials

Support materials: All support materials used herein for preparing standard materials were as described in Chapter 2.

Metal salts: Palladium(II) chloride (laboratory reagent, 99%), and rhodium(III) chloride hydrate (laboratory reagent) were obtained from Aldrich Chemical Co., Inc. Potassium(II) tetrachloroplatinate (laboratory reagent, 99%) was obtained from BDH Chemicals Ltd and Monash University LPO, Melbourne. $Co(acac)_3$ (for synthesis, >99%) was obtained from Merck.

Reducing Agents: Sodium borohydride (reagent grade, 99%) and hydrazine hydrate (65%) were obtained from BDH Chemicals Ltd. Hydrogen gas was obtained from BOC Ltd.

Solvents: Type I water was used in the preparation of all aqueous solutions. Methanol (>99%), ethanol (>99.8%), and dichloromethane (>99.0%) were obtained from Merck. ^{t}BuOH (>98.0%) was obtained from BDH.

Miscellaneous Reagents: Polyvinyl pyrrolidone (M_W ~700,000), polyethylene glycol 4000 (M_W 3300-4000), aluminium sulphate (reagent grade, 99%) and lanthanum chloride (reagent grade, 99%) were obtained from BDH Chemicals Ltd.

4.3 Results and Discussion

4.3.1 Laser Ablation-Inductively Coupled Plasma-Mass Spectrometry

4.3.1.1 Standard Development

All of the eleven methods for producing standards successfully yielded materials containing metal nanoparticles, though significant differences were observed in the amount of aggregation they contained. While some materials were homogeneous grey-appearing powders, others could be more accurately described as coarse mixtures of metal and support material.

The least successful method, "Method I", involved dripping pre-formed colloidal nanoparticles onto a hot powder of alumina. Though this resulted in immobilisation of nanoparticles onto the alumina, it also resulted in ejection of the material from the preparative vessel followed by its deposition onto nearby laboratory items.

Conversely, the most effective methods involved suspending the alumina in a dilute aqueous solution of metal salt, followed by the addition of a reducing agent. When this was performed in glass vessels as per "Method A" a small portion of metal was found to adsorb on their interior walls, though this effect was far worse

when Nalgene vessels were used as per "Method B". No significant advantage was observed when the pH was changed as in "Method E", nor when the surface of the alumina was functionalised with thiol groups as per "Method F". The rate at which the particles became adsorbed to the support material increased rapidly when an aggregating agent was added as in "Method C" and "Method D", and so Method D was chosen as the most appropriate method for the preparation of future LRMs.

4.3.1.2 Preliminary Analysis

Preliminary analysis of the sample prepared by Method D by LA-ICP-MS showed that signals for all of the desired elements could be observed with ease, but that there were a variety of potential issues with the analyses.

Of the four readily adjustable instrumental parameters, scan rate and repeat rate appeared to have little effect on the quality of the data, and thus were left at the default setting of 3 mm min^{-1} and 10 Hz respectively. The laser power and spot size, however, significantly affected the data. Since the spot size controls the area of the material being samples, it is desirable to have this set as high as possible, especially for heterogeneous materials, so that the resulting instrumental response is representative of the sample bulk. Similarly, it is desirable to use as high a laser power as possible so that the amount of material sampled is also representative.

When a non-diluted sample was analysed, with the laser power and spot size set to their highest values, all of the analyte signals were beyond the measurable range of the detector. When the laser power was decreased to 60%, the PGEs remained within range, though the aluminium signal did not. Further decreases to the laser power resulted in an unreliable signal with too high a temporal variance. This is important, because one of the most common methods for reliably quantifying elemental compositions from LA-ICP-MS data is using an internal standard, often a major element within the sample. For supported metal catalysts this means the signal arising from the support material must be reliable, while the current parameter set indicated it was not. In the interests of using higher power to gain more stable data, the samples were diluted 1:20 with microcrystalline cellulose for further analyses, since cellulose is composed of elements too light to give a mass spectral signal.

Analysis of the diluted sample produced much better results. A satisfactory signal could be obtained for all elements using a 60 μm spot, with the laser set at 50%

power (10 J cm^{-2}). Example data is shown in **Figure 61**. These parameters were used for the remaining experiments up until the 'pulse optimisation' section.

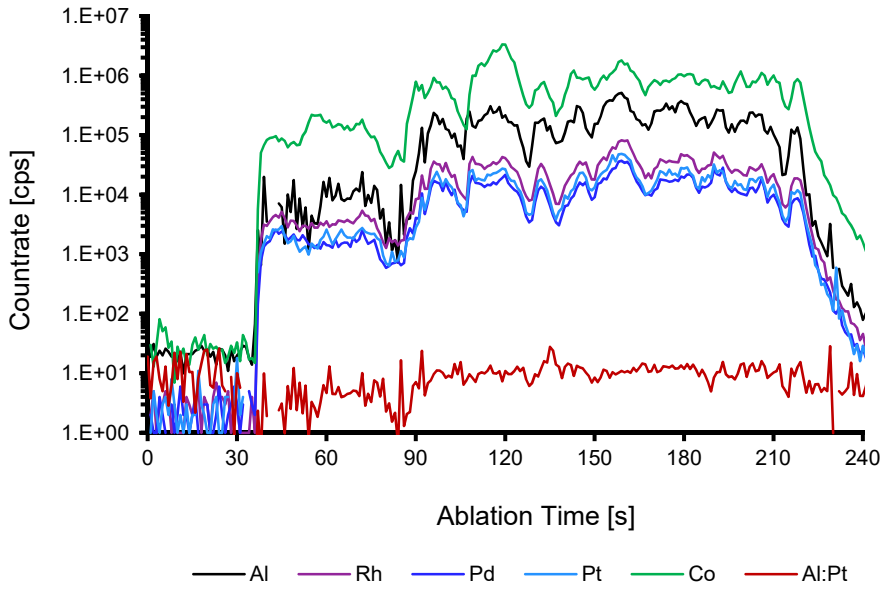

Figure 61: Ablation profile obtained during initial LA-ICP-MS experiments.

4.3.1.3 Linearity Testing

After the initial parameter optimisation, a series of standards were measured in order to construct a calibration curve, and assess whether the instrumental response increased linearly with concentration. The samples for this analysis were composed of a linearly increasing amount of PGEs doped onto the surface of alumina, *via* "Method D" described earlier. Plots of the raw PGE intensity for each sample against nominal concentration produced a linear plot, shown in **Figure 62**. This strongly suggested that LA-ICP-MS could be used for metal quantitation, since the high correlation coefficient suggests good precision and linearity, even without further optimisation. Noteworthy, however, is that the curves do not intercept the origin. This indictates that the limits of linearity (LOL) do not extend down to zero, though they do cover at least the range of concentrations spanned by the standards.

Normalisation of the PGE signal to the aluminium signal significantly reduced the quality of the calibration curves, reducing the correlation coefficients to around 0.65. Analysis of the temporal fluctuation of the aluminum signal showed it was

largely stable except for randomly dispersed spikes, which had intensities up to 3 orders of magnitude larger than that of the average aluminium signal. This was hypothesised to be due to large alumina particles being swept into the plasma after being freed from the pressed pellets by the laser. This signalled that the support material may not be appropriate as an internal standard, and suggested the need to incorporate a secondary internal standard into the samples.

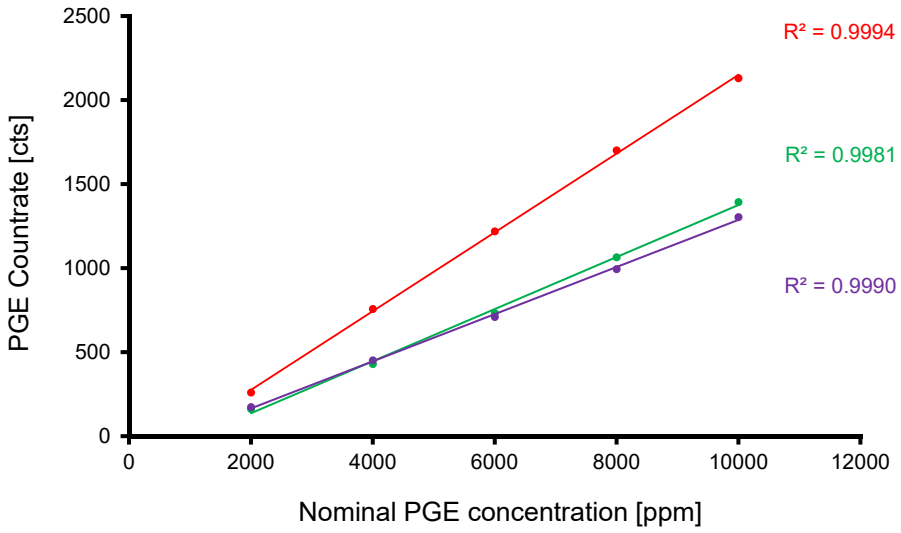

Figure 62: Calibration curves produced *via* LA-ICP-MS for a series of PGE-containing LRMs.

4.3.1.4 Standard Doping Investigations

Doping of alumina with cobalt as an internal standard was successful *via* all thirteen methods trialled. All of the samples changed from pure white, the colour of the pristine alumina, to a shade of light green, reflective of the colour of the cobalt acetylacetonate compound used for the experiment. In order to assess how homogeneously the samples were doped, they were analysed by LA-ICP-MS, and the correlation between the temporal variance in the cobalt and aluminium signals was analysed. The results of this analysis are summarised in **Figure 63**.

For data presented in this fashion, the height of each bar represents how strongly correlated the observed cobalt and aluminium signals are, while the error bars represent the standard deviation in the correlation coefficient calculated from three independent line scans on each sample. For a homogeneously doped sample the height of the bar should be close to unity and the error bars should be small;

conversely a poorly-doped sample will have a low correlation coefficient and large error bars. Using this metric, the data indicated that the most homogeneously doped samples were those prepared by "Method B", "Method E", "Method G", and "Method L".

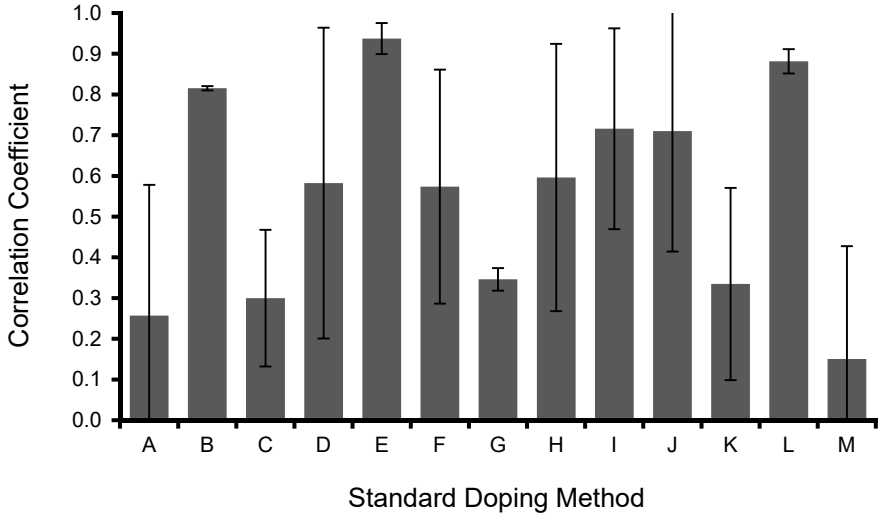

Figure 63: Plot of the correlation coefficients between the concentration of aluminium and the concentration of cobalt in alumina doped with $Co(acac)_3$ in 13 different ways as measured by LA-ICP-MS. Error bars represent the standard deviation in the correlation coefficients measured for three replicate measurements of each sample in different physical locations on the prepared pellets.

The common feature of the four most homogeneous doping methods was that they all involved the use of a polymer, polyvinylpyrrolidone, in their preparation. The advantages conferred by the presence of this polymer presumably related to its high viscosity; as the solvent containing the Co and the PVP evaporates, the Co begins to crystallise out. At the same time, the concentration of the PVP rapidly increases, and so too does the viscosity of the solution. This could inhibit transport of the $Co(acac)_3$ molecules, so preventing the growth of the crystallites, and leading to a more homogeneous coating of cobalt.

Method B, having the lowest within-sample variability, was then used to dope a PGE-containing alumina sample with Co in order to analyse its technical variability, *i.e.* the between-sample variance. The sample was analysed by LA-ICP-MS in the same way, but data was analysed by calculating the PGE:Co ratios, rather than the Al:Co ratios. The between-sample and within-sample ratios were both found to be acceptable, varying a maximum of 10% between individual samples. This is

illustrated in **Figure 64**. While this may initially seem relatively small, because of its desired use as an internal standard these could lead to too large a variation to be of use. Repeating the doping in triplicate *for each sample*, was shown to dramatically reduce this variation. All further samples, therefore, were split in three and doped individually before recombination into a single sample for analysis by LA-ICP-MS.

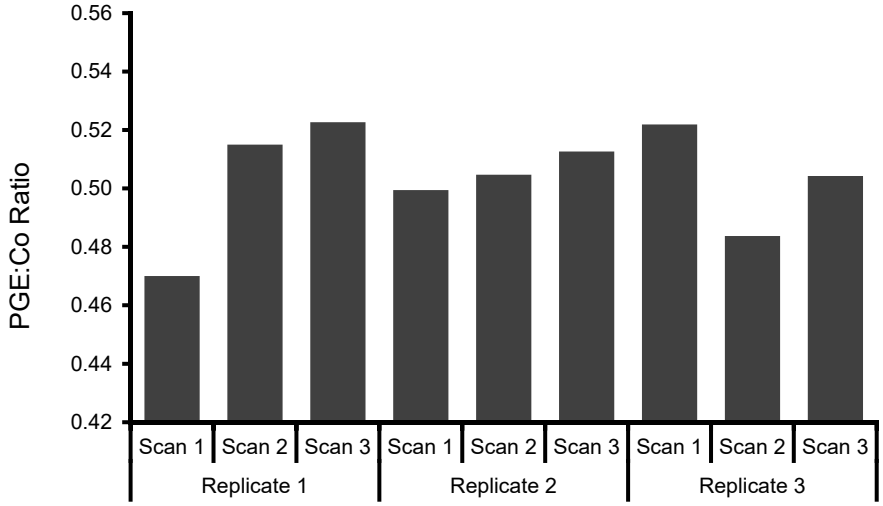

Figure 64: Technical variability in PGE:Co ratios measured by LA-ICP-MS for a 1% PGE/Al_2O_3 sample doped with $Co(acac)_3$.

4.3.1.5 Data Processing Methods

Data generated by laser ablation can be processed in many ways, as could be surmised from **Figure 61**. It may be variably smoothed, averaged, normalised, or any combination of the above, all of which can potentially affect subsequent calculations performed on the data. Until this point a simplistic analysis method was used where the property of interest, for example the PGE:Al ratio, is calculated independently at each time point, and the result averaged to obtain a final value upon which evaluation of the data is made.

The idea that a secondary internal standard may be necessary prompted an investigation into how the data could best be processed to take advantage of this. Six data analysis methods were therefore trialled, by simple mathematical manipulation of the data obtained in the previous experiment. The data were composed of three replicate scans performed on three samples prepared in an identical fashion, allowing both the intersample and intrasample variation in the instrumental response to be

assessed. Since the cobalt to aluminium ratio was of interest at this point, it was calculated for each scan in each sample by the six different methods, and is plotted in **Figure 65**. The variance in the heights of the bars for each group represents the between-sample variance in the Al:Co ratio, while the error bars represent the within-sample variance of the same quantity. The best data analysis method therefore has bars of equal heights with the smallest possible error bars.

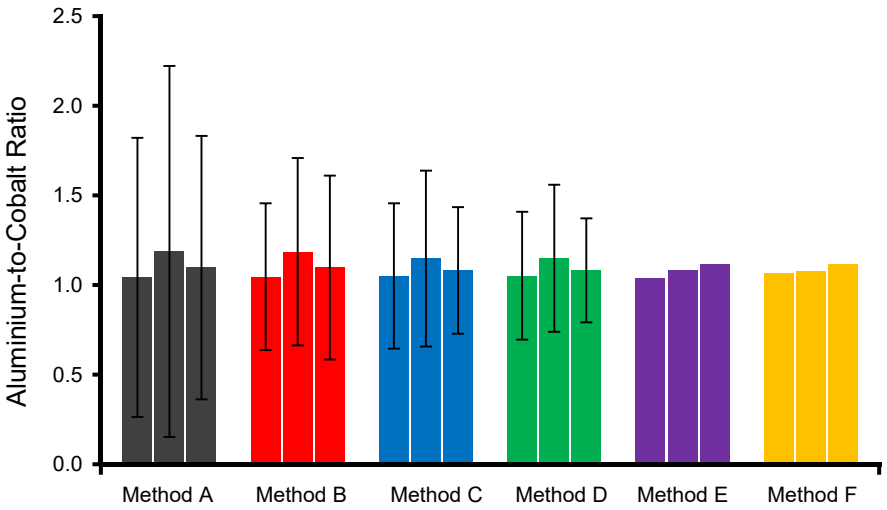

Figure 65: Plot showing the calculated aluminium to cobalt ratios in three different linescans of a sample with different data processing techniques used. Individual groups represent different data processing techniques; bars within a group represent a single linescan within the sample; error bars represent the standard deviation (not the error in the mean) in the calculated aluminium to cobalt ratio.

As indicated using the previously described metric, none of the data analysis methods trialled had any significant effect on improving the intersample variability, as indicated by the similar heights of the bars in the graphs. This suggests the variance between the scans is real, presumably resulting from slight differences in the spatial distribution of cobalt on the surface of the samples.

Conversely, all of the methods significantly altered the apparent within-sample variability, as indicated by the grossly different size of the error bars in the graph. This is perhaps unsurprising given the 'spikes' in the data, presumably resulting from the high spatial resolution of the laser (given the 60 μm spot size) picking up individual particles of aluminium or cobalt during its rastering across the sample surface. "Method D" was therefore used for all further processing of LA-ICP-MS data in the current study.

4.3.1.6 Pulse Parameters Optimisation

Once the most appropriate data processing and preparative methods were chosen, a systematic investigation was undertaken to analyse the effects of the laser parameters on the quality of the data. For this purpose cobalt was doped onto a PGE-containing alumina sample, and the variance in the PGE:Co ratios inspected as a function of the various laser parameters. Second-order polynomials were fitted to the data, and the correlation coefficient used to estimate how strongly the data was affected by the particular parameter in question. The results of this analysis are summarised in **Table 8**, and indicated the data was most strongly affected by the spot size, repetition rate, and fluence, but not by the scan speed.

Table 8: Effect of laser parameters on PGE:Co ratio in LA-ICP-MS. The parameter altered is listened in the left column, while the R^2 for a second-order polynomial fitted to the data is given in the second column as an indication of the strength of the effect of that parameter on the data.

Pulse Property	R^2	Lowest RSD
Fluence	0.7907	20 J cm^{-2}
Spot Size	0.9981	100 μm
Scan Speed	0.0302	15 μm s^{-1}
Repetition Rate	0.8791	15 Hz

By far the most important parameter was the spot size, with an extremely strong effect on the smoothness of the data. This is unsurprising, since the larger the spot size the larger the portion of the sample being sampled per unit time, which would smooth out of the effects of any spatial concentration inhomogeneities. The power and repetition rate also had moderate effects on the data smoothness, increasing with power and rate. This may arise due to the same general principle as the spot size: as the power is increased the sample is more completely ablated and ionised, leading to more representative data. The scan rate, conversely, had no detectable effect on the data, with the same ratio obtained regardless of whether the laser was rastered quickly along the sample surface, or if it was held in place to 'bore' down through it.

4.3.1.7 Standard Testing

Using the combination of the optimised parameters described in the preceding sections, a second generation of standards of increased concentration was doped with Co and analysed by LA-ICP-MS. Results indicated that the lower concentration

standards responded linearly, but that the instrumental response curved off toward the higher concentrations. This is illustrated in **Figure 66**. It was not clear whether this was an artefact of the analysis or whether the standards *actually* contained a non-linear amount of metal, so the analysis was repeated using Al as the internal standard, which produced curves of the same shape. If these standards were to be used for subsequent catalysts analyses, however, this would mean the assay would be less sensitive at higher concentrations due to the decreased gradient of the curve. This was judged as an unacceptable situation, and prompted the synthesis of the third round of standards which were sent for analysis by NAA. The details of this analysis are given in the following section.

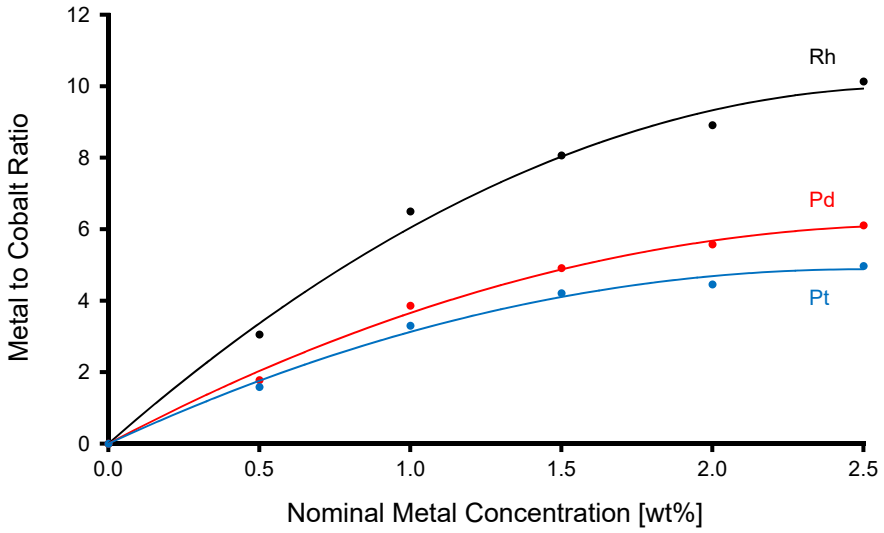

Figure 66: LA-ICP-MS calibration curves for a series of PGE/Al_2O_3 standards. Co was used as the internal standard for these curves.

4.3.2 Neutron Activation Analysis

Neutron activation analysis and subsequent gamma spectroscopy was successfully completed on the samples, allowing the accurate measurement of the concentrations of Rh, Pd, Pt, Co and Ca in the samples with a combination of long and short irradiations. An example gamma emission spectrum is shown in **Figure 67**. The results of the analyses showed that the laboratory reference materials created contained levels of the PGEs 10-30% lower than the nominal concentrations, although with good linearity. An example is shown in **Figure 68**. The decrease in metal content at higher nominal concentrations was probably due to metal particles adhering to the walls of the beakers, as well being swept into the atmosphere with

the evaporated ethanol vapour. Cobalt concentrations were approximately equal across each standard, suggesting its usefulness as an internal standard using the doping method developed earlier. Normalisation of the PGEs using the Co concentrations generally improved linearity, as shown in **Figure 69**.

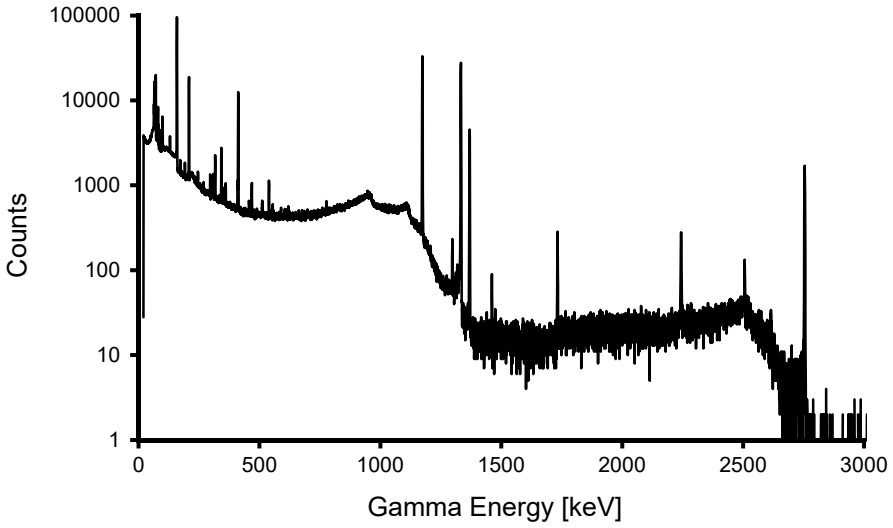

Figure 67: Gamma emission spectrum from a neutron-activated laboratory reference material composed of RhPdPt/HAp.

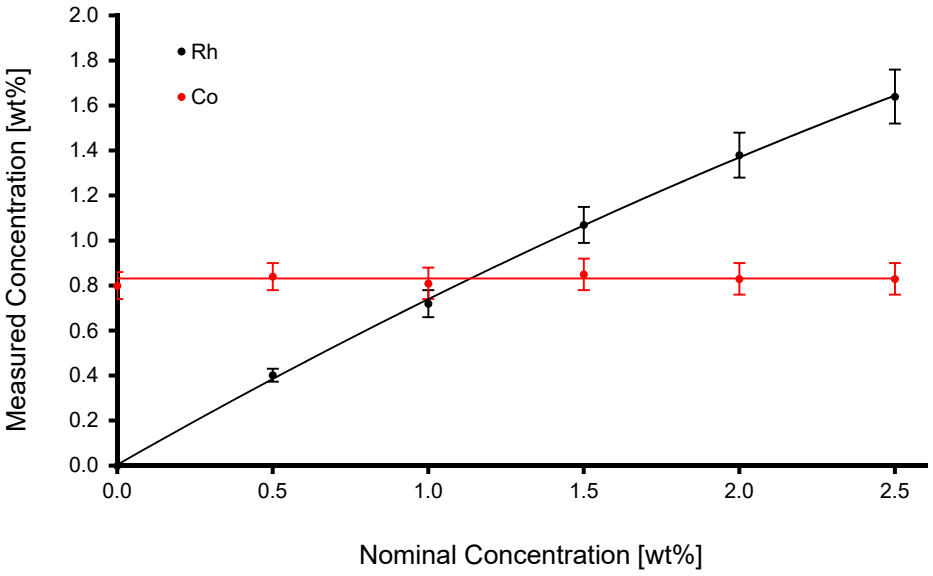

Figure 68: Concentrations of Rh and Co in the SiO_2 laboratory reference materials as measured by NAA. Error bars correspond to 2σ confidence intervals.

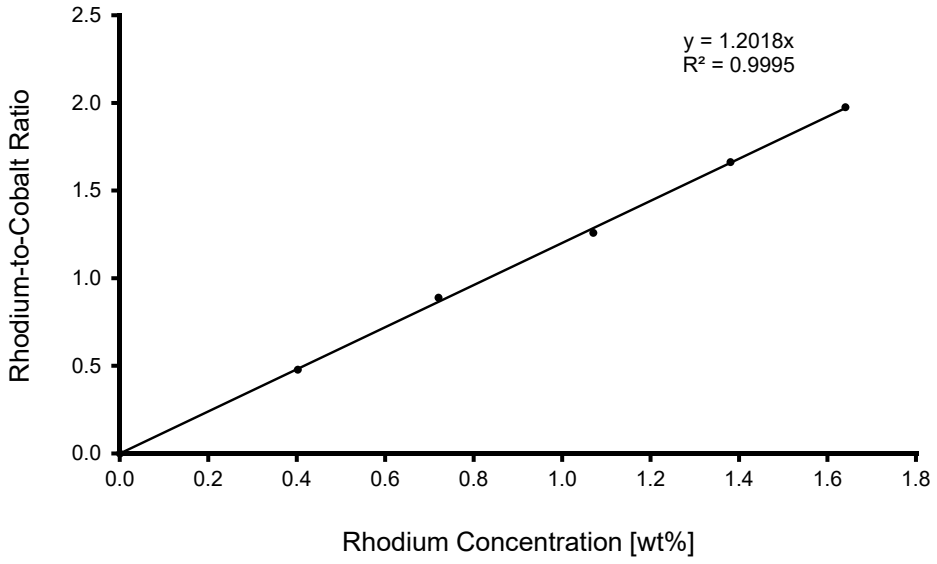

Figure 69: Rhodium-to-cobalt ratio in the SiO_2 laboratory reference materials as calculated from NAA results.

With the concentrations of metal in these LRMs accurately determined, this allowed them to be used as standards against which the concentration of unknown samples could subsequently be prepared by LA-ICP-MS. At this point in the experimental workflow the laser was decommissioned and replaced with a completely different unit, requiring the method development to be repeated from the beginning. A LIBS spectrometer was subsequently acquired, and so further method development and analysis of the LRMs was switched to this instrument.

4.3.4 Laser-Induced Breakdown Spectroscopy

4.3.4.1 Base Parameter Set

Analysis of the LRMs described previously, which are powders in their native form, required they were pressed into pellets for presentation to the spectrometer. This was achieved by filling a 13 mm Specac die set with *ca.* 200 mg of powder and pressing at 10 tonnes for 10 seconds, a pressure of *ca.* 19 MPa. A photograph of selected pellets prepared for this experiment, and others, is shown in **Figure 70**.

Ablation of the samples readily resulted in ejection of material from the surface of the pellets, as indicated by the patterns of dots which appeared on their surfaces. Systematic variation of the laser and spectrometer properties allowed observation of their emission spectra, which contained a series of several hundred sharp peaks of

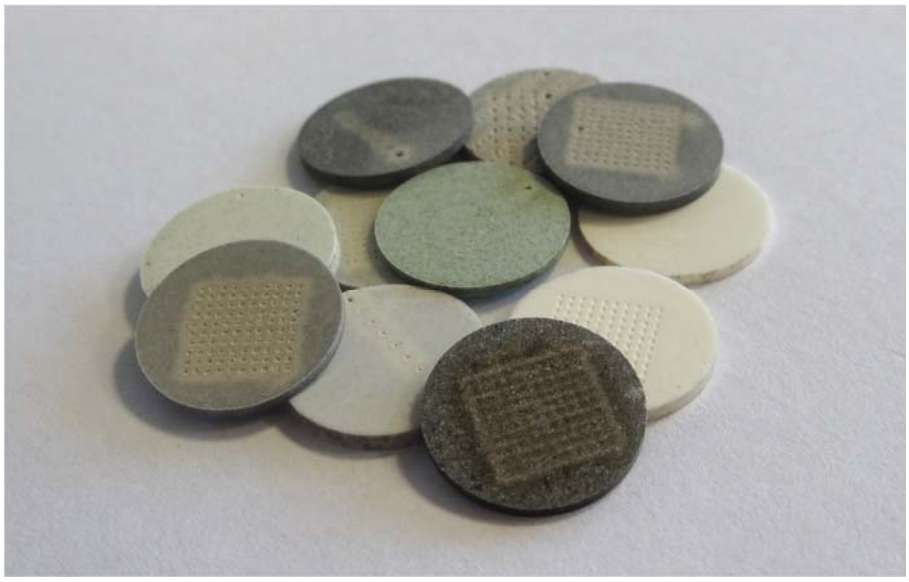

Figure 70: Photograph of pelletised samples for laser ablation. Dark pellets contain metal nanoparticles, white pellets are blanks, and green pellets are blanks doped with cobalt acetylacetonate. Note the different patterns of dots on the samples' surfaces, produced by laser-induced breakdown.

varying intensities, as shown in **Figure 71**. When very low gate delays were used the spectra had high backgrounds and weak emission peaks, which was remedied by increasing the gate delay to 1.0 μs. The relative emission intensity was further increased by increasing the laser power to its maximum value of 200 mJ at a repetition rate of 1.0 Hz. These values were consistent between samples, providing the lowest background and greatest emission intensity regardless of whether the sample analysed used Al_2O_3, SiO_2, HAp, or MCC as the support material. These parameters were subsequently used for further method development work.

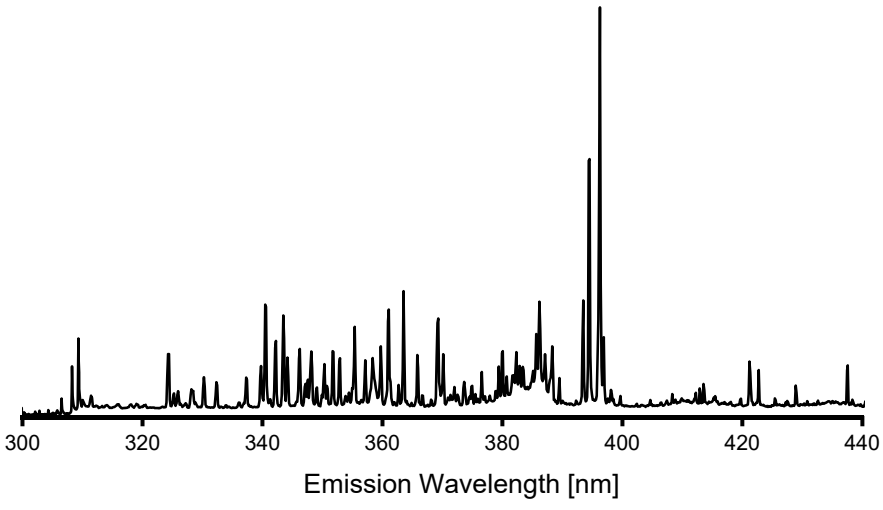

Figure 71: LIBS spectrum of a 1% Rh,Pd,Pt/Al_2O_3 standard

4.3.4.2 Sample Dilution

Since sample dilution was shown to be an important parameter in obtaining quality data for LA-ICP-MS, its effect on the LIBS data was also investigated. Four of the LRMs measured by NAA were analysed for this purpose, after dilution with microcrystalline cellulose by various factors. Results indicated that sample dilution markedly impacted the emission spectra of the samples. Generally speaking, the greatest signal intensities and the lowest backgrounds were obtained with the least possible sample dilution, while the signal to noise ratios reached a maximum at higher dilution, and the signal to internal standard ratios varied subtly across the dilution ranges studied.

The signal intensity for the analytes measured from appropriate emission lines generally decreased exponentially with dilution factor, having maximum emission intensities in their undiluted forms. The aluminium standards, for example, showed a two-fold decrease in emission intensity when diluted 10x, but only a four-fold decrease when diluted 50x. This is illustrated in **Figure 72**. Similar decreases were observed with the silica and cellulose supported standards. The hydroxyapatite standards, on the other handed, showed maximum emission intensity at 1:1 dilution. The average background intensity remained approximately equal regardless of dilution factor, and consequently the signal to background ratio followed a similar trend to the signal intensities.

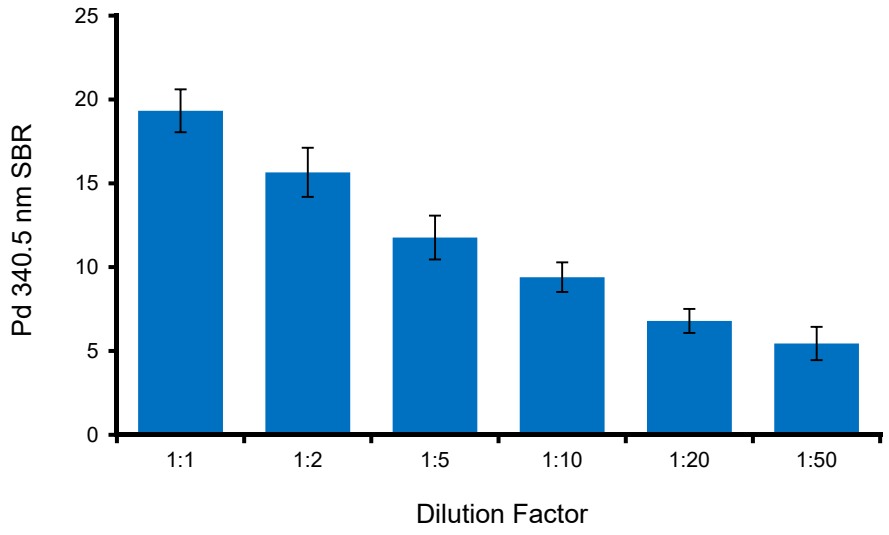

Figure 72: Effect of dilution on peak-to-background ratio of the Pd 340.6 nm emission line

The signal to noise ratios, on the other hand, generally reached their peak at greater dilutions, usually around 1:5 or 1:10. Since the signal intensity decreased toward lower dilutions this must indicated the variance in the background signal decreases at a more rapid rate in order to generate the observed increase in SNR. It may be that the background, despite appearing flat visually, contains very weak emission lines from the support material which are reduced on dilution, thus giving rise to the observed effect. This has important implications for analysing trace amounts of supported metal, however, since the ability to detect a signal (the 'limit of detection', or LOD) is generally defined as three times the standard deviation in the background signal. It may be the case, therefore, that dilution increases the sensitivity of the assay at the expense of some other property.

The signal to internal standard ratios were also shown to vary based on the dilution, although to a much lesser extent than the SNR or SBR. For the silica catalysts, normalisation to the Si 390.56 nm line showed that SISR increased with dilution, from, for example, 0.600 for platinum in undiluted samples up to 0.796 in samples diluted tenfold. Similar trends were observed for the other analytes in the silica standards. The opposite trend was observed for hydroxyapatite standards, where the SISR was greatest at lower dilutions. Cellulose standards could not be normalised to carbon, however, since no strong carbon emission lines were observed in the spectra. These variations with dilution are very important, because they indicate that the samples and the standards must be diluted equivalently, otherwise discrepancies will arise in the response factors of different analytes. For all further work, a 1:1 dilution was chosen.

4.3.4.3 Sample Grinding

Results of the grinding experiments indicated that the length of time the samples were ground for had strong effects on the data, which are analyte, matrix, and ablation depth dependent.

The emission intensity increased with grinding time for the aluminium and cellulose standards, reaching a plateau beginning at around 100 seconds. The silica and hydroxyapatite supported standards on the other hand decreased in emission intensity with any increase in grinding. The backgrounds were largely unaffected by these processes, meaning that the signal to background ratios followed the same

trends. The process was also shown to be depth-dependent for the alumina standards, with the PBR changing with ablation depth. This is illustrated in **Figure 73**. The maximum PBR can therefore be achieved *either* by the use of two cleaning pulses on an unground sample, or with no cleaning pulses on a heavily ground sample. The compromise, however, was that the variance in the PBR was slightly higher in the unground samples regardless of the number of pre cleaning pulses. The signal to noise followed more complicated trends than the SBR. In the silica supported standards it decreased constantly with grinding time, while in the hydroxyapatite and cellulose supported standards it peaked at 100 seconds.

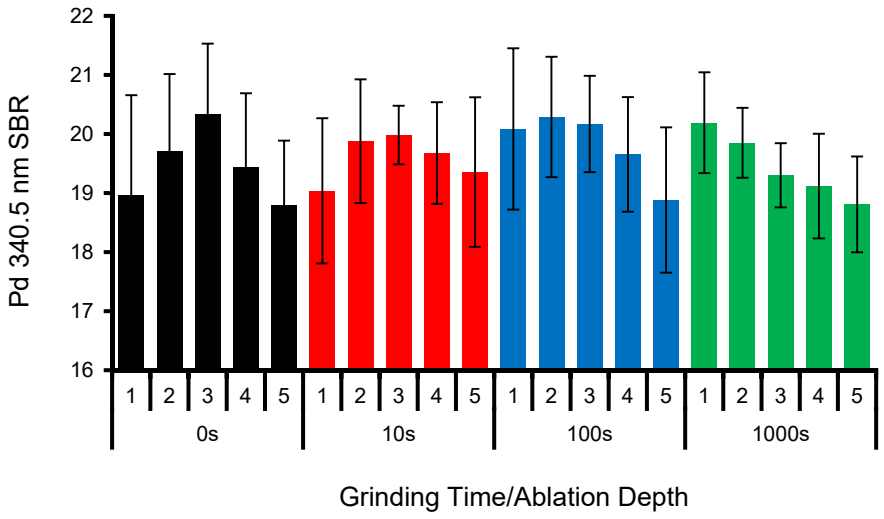

Figure 73: Effect of sample grinding time on the peak to background ratio of the Pd 340.5 nm emission line.

In the apatite standards the SISR was almost completely insensitive to grinding time for Pt and Rh, changing less than 3.2% and 10.6% respectively across the different treatments, while Pd changed by 27.8% with grinding. In the silica standards, on the other hand, the SISR decreased steadily with grind time, dropping *ca.* 30% for each analyte between 0s and 1000s. Since the nanoparticles are located at the surfaces of the silica particles, when they are ground and consequently broken apart, a higher amount of pristine silica surface would be exposed, effectively decreasing the amount of metal presented to the laser for ablation, and subsequently altering the apparent SISR. It is critically important therefore that if a standard

material is obtained in the form of a powder that it have particle sizes and a spatial metal distribution as close as possible to the analyte powder for the greatest accuracy.

4.3.4.4 Pulse Statistics

As there is intrinsic pulse-to-pulse variance in laser ablation methods, it was deemed necessary to investigate how many individual pulses were necessary before a sufficient number of results could be averaged to obtain accurate SISRs. To do this, a 10 x 10 pattern was ablated on the surface of the same pellet 20 times in a row, and the average SBR, SNR, and SISR studied as a function of ablation depth.

The results from this experiment show that there was generally a significant dependence of each of the three parameters on ablation depth. Emission intensities and consequently SBRs peaked around 3-5 ablations deep regardless of the analyte metal or support, and then fell to a constant value at around 7-8. Of critical importance, however, it was shown that the SISRs of the three metals also depended on ablation depth in the alumina and hydroxyapatite samples, but were *independent* in the silica standards. This is important because of the intrinsic heterogeneity of the sample and the variance in the LIBS method, which dictates that a relatively large number of pulses are required to obtain an accurate mean value.

Since sampling statistics dictate that for an arbitrary number of pulses we can only know the mean value of a measured property to a certain level of accuracy, if we can estimate the variance from a large number of pulses, we can then calculate the number of pulses required for the sample mean to fall within a certain percentage of the population mean with a specified degree of certainty. This was done using the SISR data, and is plotted in **Figure 74**. The calculations suggested that *within* a given matrix the three analyte metals behave similarly, but differently *between* matrices. In the silica standards, for example, 95% accuracy could be achieved to 2σ certainty after approximately 100 pulses, but 99% accuracy would require over 1000 pulses. In the alumina and apatite standards, 95% accuracy was achieved after only 50 pulses due to the lower variance in the SISR.

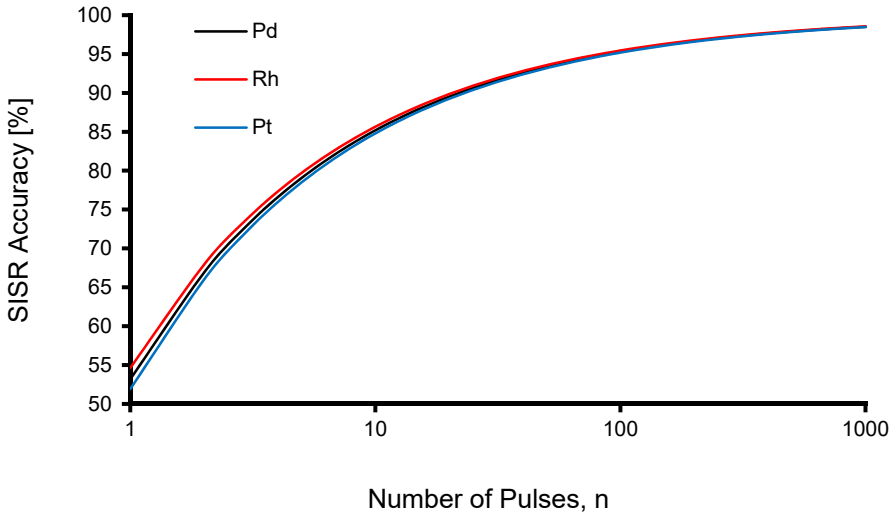

Figure 74: Plot showing the LIBS SISR accuracy for Rh, Pd, and Pt as a function of number of pulses acquired

4.3.4.5 Pulse Power

The influence of laser power on spectral quality was very clear. With no laser power no material is ablated from the surface, and consequently there is no emission observable. As the power was increased the emission intensity increases, with higher intensities obtained at higher laser powers. This had the side-effect, however, of increasing the background intensity and noise faster than the analyte peaks, leading to a diminishing return on signal to background ratio at higher powers, and better signal to noise at lower laser powers. An example is shown in **Figure 75**. The relative variance in peak intensities was also shown to be proportional to laser power,

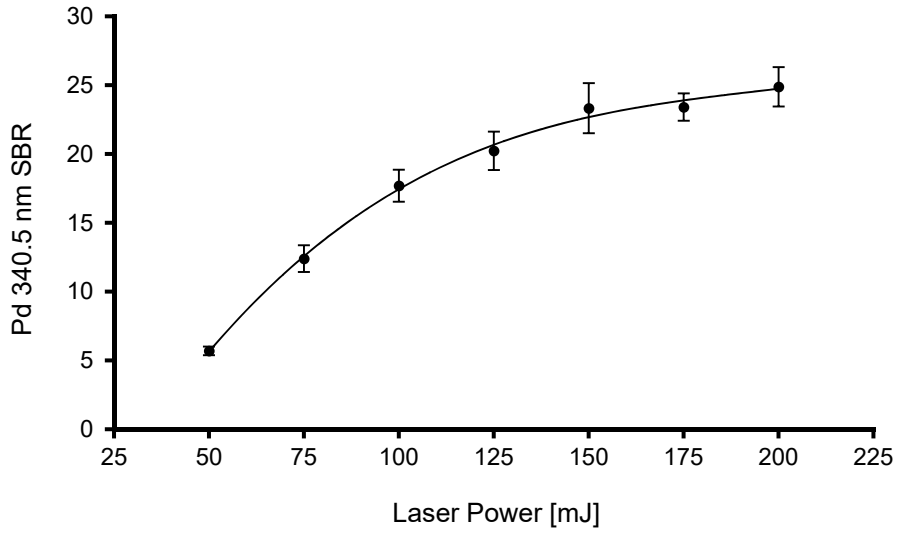

Figure 75: Effect of laser power on the Pd signal to background ratio.

meaning that lower power could produce more reliable results. The SISR was also shown to be strongly dependent on laser power in all of the systems studied, meaning that the laser power stability is important in obtaining reliable, quantitative, results.

All of the effects described above are easily rationalisable. The effect of laser power on emission intensity, for example, can be attributed to the increasing amount of material ablated at higher powers, since this represents at higher flux, and thus more energy per unit time absorbed by the sample. At higher powers the ablation process is also more 'violent', producing a deeper crater with a greater amount of 'debris' scattered around its peripheries. This dust has the potential to scatter light, and thus affect the observed emission intensities, manifesting in an increased variance at higher laser powers. The increasing variance in the background with laser power could also be attributed to the appearance of weak emission lines at higher powers, which would appear as an increased noise level.

4.3.4.6 Gate Delay

The gate delay was shown to be an especially important parameter in controlling spectral quality. Generally speaking the emission intensity dropped precipitously with gate delay, following an exponential decay curve. Short gate delays lead to the spectra were dominated by a high and broad background, with weak emission lines superimposed atop. As the delay was *increased* the background decayed rapidly while the emission lines remained, leading to an increase in PBR up to around 1 μs before slowly decaying with further time. The exception to this rule was alumina, for which the maximum was obtained at 4 μs. This is shown in **Figure 76**. The SNR followed the same trends, peaking at approximately the same delay lengths. Conversely, the SISR showed completely different trends, varying 20% over the studied range in the silica standards, but 180% over the same range in the apatite standards. This means that good control of gate delay is *critically* important in obtaining reliable quantitative results for these types of analyses.

Once again, the results above can be rationalised in terms of plasma physics. During the early phases of ablation a plasma is formed, which emits a continuous spectrum giving rise to the high background. With time the plasma cools and the emission lines become obvious. The effect on the SISR is more complicated,

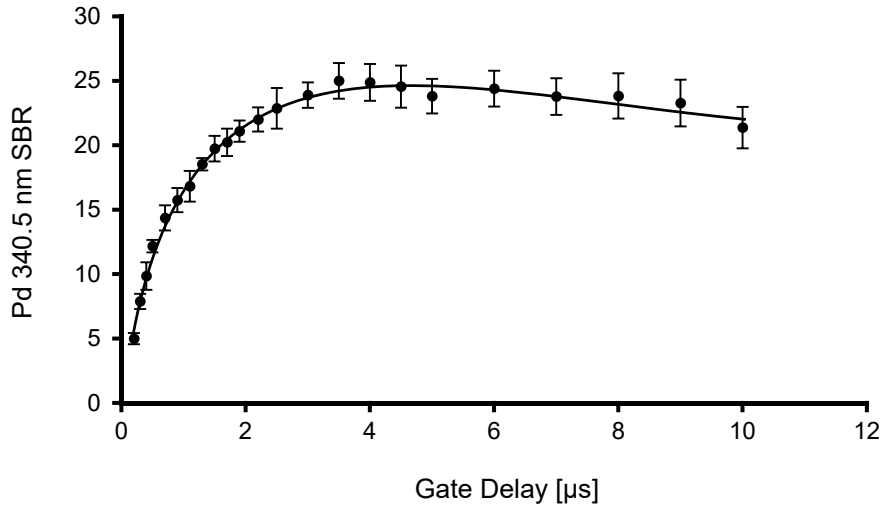

Figure 76: Effect of gate delay on the Pd signal to background ratio

however; since different emission lines have different lifetimes, the decay in their emission intensity with time will be time-dependent, and therefore the ratio of two dissimilar lines will produce values with unusual temporal dependences.

4.3.4.7 Calibration Curves

Measurement of the emission spectra of the series of LRMs irradiated for NAA showed linear relationships between the SISR measured by LIBS using the conditions developed in this chapter and their actual metal concentrations. An example is shown in **Figure 77**. For the alumina, silica, and hydroxyapatite standards correlation coefficients above 0.99 were obtained in all cases using emission lines from the support as internal standards, while Co doping using the method described earlier

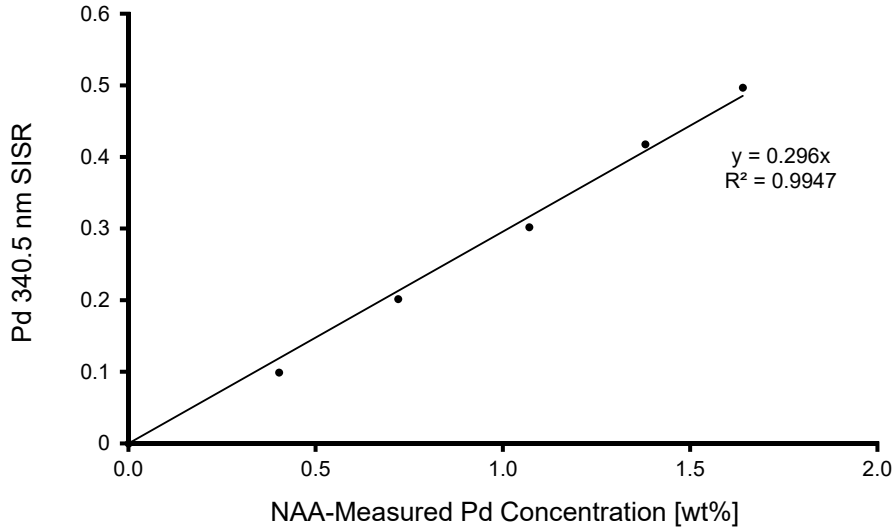

Figure 77: Example LIBS calibration curve for Pd in SiO_2.

was necessary to achieve the same level of accuracy for the cellulose supported standards, which had no observable C emission lines in the range studied.

Once the linearity of the method was confirmed, this allowed the method to be used for quantification of rhodium, palladium, or platinum in unknown samples. An unknown sample and a standard are analysed sequentially, and the signal to internal standard ratio calculated for each. The concentration of the unknown is then obtained from the ratio of two values, as given by equation 4:

$$c_m^{spl} = \frac{I_m^{std}/I_s^{std}}{I_m^{spl}/I_s^{spl}} . c_m^{std} \qquad \ldots(4)$$

where the concentration *c* is concentration of an analyte element, *I* is the intensity of an emission line from the metal *m* or the support *s*, either from the standard *std* or the sample *spl*.

4.4 Summary

A series of experiments have shown that laser ablation can be used to quantify the amount of metal in supported metal catalysts. Analysis by LA-ICP-MS is possible using the count rate of the analyte metals normalised to an element present exclusively in the support material, however the difference in abundances means that low laser powers and small spot sizes must be used, which has the effect of decreasing the accuracy of the assay for a given analysis time. Doping of cobalt into the samples as an alternate internal standard was investigated and found to produce repeatable results, but decommissioning of the laser meant that no relationship could be established between the linearity of the instrumental response to standard materials.

As an alternate method of analysis LIBS was investigated. This method was shown to produce better results than LA-ICP-MS in a shorter period of time, and with the added advantage of not consuming large quantities of argon or other consumables. Parameters anticipated to affect quantitation using this method were systematically investigated using a set of typical materials to deconvolute their effects on spectral quality. These are summarised in **Table 9**.

Table 9: Summary of optimised LIBS parameters for the laboratory reference materials produced in this study.

Parameter	Standard			
	Al_2O_3	SiO_2	HAp	MCC
Laser Power	200	200	200	200
Gate Delay	4.0	1.5	2.0	1.0
Grinding	0	0	30s	120s
Dilution	1:0	1:1	1:1	1:0
SISR Depth Sensitivity*	Stable >7	Insensitive	Stable >5	-

* The depth after multiple spatially coincident ablations at which the signal to internal standard ratio stabilises to a constant value.

After reliable results were obtained from the instrument a series of special laboratory reference materials were prepared. Their concentrations were precisely measured by NAA, which showed they contained a linear amount of metal. Analysis of the materials by LIBS gave a linear response, indicating that LIBS is an accurate method for assay metal content in metal catalysts, but only after substantial method development.

4.5 Recommendations for Further Research

There are three main areas in which the research presented in this chapter could be extended. Firstly, further method development to reduce the analytical error may be of benefit. As the main source of error was the concentration of the LRMs, these could be analysed by a secondary method to increase the confidence in the assay. Possible alternate elemental analysis methods for this task include proton induced x-ray emission (PIXE) or x-ray fluorescence (XRF).

Secondly, further experimental parameters may be investigated to determine their influence on instrumental response. It could be of interest to determine whether there are significant effects from variation in the size and distribution of the supported particles, the amount of absorbed or adsorbed moisture, as well as different pelletisation methods.

Thirdly, it could be useful to investigate alternative methods for method calibration. Rather than using a single-line calibration as used herein, multivariate methods including machine learning and statistical prediction could be investigated.

These more advanced methods may lead to increased precision in the assay, and therefore greater accuracy and a greater level of confidence in the resulting numbers.

Chapter 5: Catalysts Prepared from Electrostatically Stabilised Metal Colloids

5.1 Introduction

Supported metal catalysts can be synthesised in many different ways, ranging from trivial to remarkably complex. While many reported methods produce highly active catalysts they often require multiple reaction steps, the use of specialised equipment, or are not directly applicable to all combinations of metals and support materials. It is desirable, therefore, to develop generalised synthetic routes which can be applied to produce a wide variety of catalytically active materials.

One possible class of synthetic routes involves the use of colloidal dispersions of pre-formed metal nanoparticles as a metal source, with catalysts produced by immobilisation of these particles onto an appropriate support material. The advantage of using pre-formed nanoparticles over growing them directly on a support material is that the particle size and morphology can be tuned using solution-phase methods, allowing catalysts with a wide variety of textural properties to be created. Investigation of these routes was one of the aims of this body of research, and is the focus of the current chapter of this thesis.

One of the main problems with using colloidal nanoparticles is that they are not thermodynamically stable. Because of their small size they have a high surface to volume ratio, which in turn gives them an intrinsically high surface free energy. For particles in colloidal suspension, it is energetically favourable to agglomerate with one another, thereby minimising their surface areas and thus their free energy. This also reduces the number of active sites on a metal particle, and so if such a colloid is used to prepare a catalyst, the resulting activity can be diminished. This effect can be minimised by stabilising the colloids, and thereby preventing aggregation. Two main stabilisation methods exist: electrostatic, and steric.

Electrostatic stabilisation is the naturally-occurring stabilisation mechanism for metal colloids. Most metal surfaces have an intrinsic surface charge, and when they are submerged in water an electrical double layer forms as a consequence. This double layer consists of a shell of charge-balancing ions [361], which produce a repulsion between particles which inhibits their aggregation. The effectiveness of

this double layer depends on the surface charge of the metal, and although for some metals like platinum or gold it is sufficiently strong that they can remain colloidally stable indefinitely, for other metals like rhodium or palladium the addition of an extra protecting agent is required. These are commonly called 'capping agents', which are molecules or polymers which adsorb to the surfaces of the colloidal particles. They provide a thick steric layer which is entropically repulsive, producing a physical barrier between particles which inhibits their aggregation [362, 363].

In this thesis, colloids stabilised by both of the aforementioned mechanisms have been investigated as precursors for synthesis of supported metal catalysts, though the current chapter details only catalysts prepared from electrostatically stabilised colloids. A set of 24 catalysts has been produced using the eight support materials described in Chapter 2, each with one of three precious metals immobilised on their surfaces. The activities of the resulting catalysts have been tested in the hydrogenation of cyclohexene, 1-octene, and 1,5-cyclooctadiene, and their properties extensively investigated by a suite of instrumental methods including scanning electron microscopy (SEM), transmission electron microscopy (TEM), x-ray diffraction (XRD), infrared microspectroscopy (μFTIR), and solid-state nuclear magnetic resonance spectroscopy (SS-NMR). Relationships between the structure of the catalysts, the surface chemistry of their constituents, and their properties are also discussed.

5.2 Experimental

5.2.1 Synthetic Methods

Prior experiments detailed elsewhere [364] indicated that while colloidal platinum was stable with only the natural electrostatic stabilisation produced when the colloids were generated, colloidal rhodium and palladium were not. While the platinum colloids remained stable indefinitely, the palladium colloids dropped out of suspension after an hour, while the rhodium colloids did the same within only a few minutes. These time scales were not considered sufficient to produce a colloid and subsequently immobilise the nanoparticles it contains onto an appropriate support material, so an *in-situ* reduction method was devised as a work-around. In this method metal salts were reduced in an aqueous suspension of the relevant support material, allowing the particles to immediately adsorb onto the surface of the

supports. This method is similar to that reported by Brown and Brown [365] in the 1960s, involving a simple one-pot reduction method where metal salts are reduced in an ethanolic suspension of support material. This particular method was shown to be both trivial to implement and to produce catalysts with remarkably high activity, and is therefore useful in studies where multiple catalysts are made using support materials with vastly different chemistry.

In order to prepare this 'first generation' of catalysts, a series of metal salt stock solutions were produced. Aqueous solutions of $RhCl_3$, $PdCl_2$, and H_2PtCl_6 were prepared at concentrations of 0.05 mol L^{-1} using Type 1 water, and stored in sealed Nalgene containers until use. The insoluble $PdCl_2$ was converted to the water-soluble $PdCl_4^{2-}$ ion by addition of two mole equivalents of NaCl. A round-bottom flask was then charged with 2.97 g of support material, a PTFE stirring flea, 100 mL of Type-I water, and an aliquot of metal salt solution containing 0.0300 g of metal. The solution was stirred vigorously for 30 minutes, followed by dropwise addition of 0.05 mol L^{-1} $NaBH_4$ until no further reduction was observed. After a further thirty minutes the suspensions were gravity-filtered through Whatman 540 filter-paper and washed free of chloride by repeated rinsing with Type-I water. Removal of chloride was detected by reaction of the filtrate with 0.05 mol L^{-1} $AgNO_3$ solution, which produces a white precipitate of AgCl. The filter papers containing their respective filtercakes were places on watchglasses and dried in air at 25 °C for 24 hours, then dried for a further 24 hours under vacuum desiccation.

The activity of the resulting catalysts were tested using the hydrogenation of cyclohexene, 1-octene, and 1,5-cylcoctadiene as model reactions. A bespoke glassware reactor was designed for this purpose, composed of a water-jacketed reaction vessel connected to a gas manifold, allowing the headspace of the reactor to be evacuated, purged, or filled with nitrogen or hydrogen. A diagram of the setup and instructions for its operation are given in Appendix 2. All reactions were conducted under 1 atm H_2 at 20 °C. The reactor was charged with 45 mL of n-heptane, 5 mL of substrate, and *ca.* 200 mg of the catalyst, and its contents stirred rapidly under H_2 for a period of 1 hour. Every 10 minutes a small sample was withdrawn for analysis by gas chromatography-mass spectrometry (GC-MS) to determine the rate of conversion and the nature of the products. The sample preparation for this step is given in Section 5.2.2. Heptane was chosen as the solvent

for these reactions because of its favourable wetting properties, as discovered during the work detailed in Chapter 3. The activity of the catalysts was calculated as per section 5.2.3.

5.2.2 Instrumental Methods

To investigate the distribution of metal across the support materials within the resulting catalysts all samples were analysed SEM in both secondary electron mode and backscatter mode. All micrographs were recorded with a Hitachi S4700 FE-SEM as described in Chapter 2. Secondary electron micrographs were recorded with the same configuration, but backscatter electron (BSE) micrographs were collected using an inbuilt BSE detector.

The limited resolution of the SEM system used meant that it was not appropriate for measuring the size of the individual supported metal particles, so for this purpose TEM was used. All analyses were performed on a Philips CM30 operating at 200 – 300 kV. Sample preparation was as per Chapter 2. As quantitative particle size measurements were required, the magnification was calibrated using Catalase resolution standards (Electron Microscopy Sciences Ltd), details of which are given by Williams and Carter [366]. For each catalyst sample the contents of the grid were surveyed, then five representative micrographs were collected at high magnification from which particle size measurements were taken. Approximately 200 individual supported particles were measured in each catalyst using ImageJ 1.46, from which the average particle size and the population spread were calculated. Details of the error in these analyses are discussed in Appendix 3.

The structures of the catalysts were investigated by a variety of methods, including microFTIR. These 'transflection' spectra were recorded using a PerkinElmer Spectrum Spotlight 200 FT-IR microscope at 2 cm^{-1} resolution between the ranges of 4000 cm^{-1} to 500 cm^{-1}. 100 scans were collected per spectrum, with three spectra collected per sample in different spatial locations. Spectra were digitally smoothed where necessary using a Savitzky-Golay filter, ensuring no loss of spectral detail.

Phase purity of the samples and changes to the crystal structure were probed by XRD. All diffractograms were recorded on a PANalytical Empyrean multi-purpose x-ray diffractometer using Cu Kα radiation and a PIXcel^{3D} detector. The optical

configuration was similar to that in Chapter 2, except that a graphite monochromator was used in the diffracted beam in place of the nickel filter to improve peak shape. Diffractograms of the pristine support materials were subtracted from those of the catalysts, revealing the presence of reflections arising solely from the supported metals. The background in the subtracted data was modelled using a manually fitted cubic spline, and the peak profiles fitted with pseudo Voight profiles composed of Kα1 and Kα2 components. The fit was refined over 20 iterations by variation of the peak position, height, width, and shape. The FWHM of the Kα1 component was then used for calculation of the crystallite size of the supported metal nanoparticles (technically domain size) using the Scherrer equation, given in equation 5:

$$D = \frac{K\lambda}{\beta cos\theta} \qquad \ldots(5)$$

where D is the crystallite diameter, K is the shape factor, β is the peak breadth, and θ is the diffraction angle. All calculations were performed using the PANalytical HighScore Plus software, version 4.1. Peak widths were corrected for instrumental contributions by subtracting the peak width of a CeO_2 standard prepared according to reference [367].

Solid-state NMR experiments were also performed on the catalysts to probe their structures. The same hardware and experimental set up was used as in Chapter 2, but parameters were slightly adjusted for increased spectral quality. The adjusted parameters are detailed in **Table 10**. Special attention was paid to increasing resolution and decreasing signal to noise by reducing the spectral windows and FID acquisition lengths, as well as zero-filling before Fourier transformation.

Samples for GC-MS analysis were prepared by diluting *ca.* 100 μL of reaction mixture in 10 mL of acetone, followed by filtration into 1.5 mL silanised Agilent GC vials through a glass Pasteur pipette stuffed with a small wad of cotton to remove particulate matter, followed by capping with pre-slit PTFE/silicone vial caps. Analysis was performed on an Agilent 6890-series gas chromatograph (GC) coupled to a 5973-series mass selective detector (MSD), after introduction using a 7683-series autoinjector. Injections of 1 μL were introduced into a split injector held at 150 °C, with a split ratio of 1:25. The column was a Phenomenex Zebron™ ZB-5 capillary column. Column temperature was ramped from 50 °C to 120 °C at a rate of 25°C per minute. The carrier gas was helium, run at constant pressure. Chromatograms were

Table 10: Solid-state NMR acquisition and processing parameters used for the experiments reported in the current chapter.

Parameter	Experiment					
	^{1}H	^{27}Al	^{29}Si	^{1}H-^{29}Si	^{31}P	^{1}H-^{31}P
TD	4784	310	474	1024	1024	2000
NS	100	100-1000	10,000	10,000	500	500
DS	2	2	2	2	2	2
SW [ppm]	40-200	200-400	200	200	100	240
AQ [ms]	40	10	20	45	40	35
P1 [µs]	5	1	3.5	3.5	4.0	4.0
PL1 [dB]	-4	-3	2.0	0.5	3.0	7.0
SI	8192	512	1024	4096	4096	8192
WDW	GM	GM	GM	GM	GM	GM
LB [Hz]	-5	-5	-5	-5	-5	-1
GB	0.1	0.05	0.05	0.01	0.05	0.05
MASR [kHz]	15	8	5	5	10	8
D1 [s]	3	1	4	1.0	3.0	2
P15 [ms]	-	-	-	8	-	5
P3 [µs]	-	-	-	3.5	-	4
PL12 [dB]	-	-	-	-5	-	-2.20

integrated manually using Agilent's Chemstation software. Peak areas of the relevant substrate were normalised against the heptane peak area, and the ratio compared to that of a series of co-injected standards to determine conversion rates in moles per minute and conversion percentages. Error calculations are detailed in Appendix 2.

Liquid NMR experiments were also performed on the products from the catalytic reactions to further confirm the identity of the species observed by gas chromatography. These were performed on two different instruments, either a 300 MHz or a 400 MHz Bruker AVANCE spectrometer. Samples were prepared in standard 4mm NMR tubes using deuterochloroform as the lock solvent, and with a basic Bloch decay experiment using a 70 degree pulse and proton decoupling.

5.2.3 Activity Calculations

The activities of the catalysts tested in this chapter were expressed as turnover frequencies (TOFs), with units of inverse time (s^{-1} or hr^{-1}). These values are equivalent to the number of moles of substrate converted per mole of active site per unit time, as given by equation 6:

$$TOF = n_s/n_a/t \quad \ldots(6)$$

where t is the time taken for n_s moles of substrate to be converted by n_a moles of active sites. This can be re-arranged to a more convenient form, shown in equation 7:

$$TOF = \frac{n_s}{t}\frac{1}{n_a} \quad \ldots(7)$$

The first fractional term in the equation represents the measured conversion rate, which is obtained from plots of the conversion as a function of time obtained by GC-MS. The second fractional term in the equation is obtained *via* manipulation of TEM data using the method of Borodziński and Bonarowska [368]. This method is used to convert the number-average particle sizes into dispersion, D, which is the average fractional proportion of atoms at a particle's surface, using an empirical relationship between TEM and hydrogen chemisorption titration data. The fundamental equation used is equation 8:

$$D = \frac{5.01 d_{at} \sum_j n_j d_j^2 + 2.64 d_{at}^{0.81} \sum_k n_k d_k^{2.19}}{\sum_i n_i d_i^3} \quad \ldots(8)$$

where d_{at} is the atomic diameter, n_j is the number of particles with diameter d_j ($d_j >$ 24.0 d_{at}), n_k is the number of particles with diameter with d_k ($\leq$ 24.0 d_{at}), and n_i is the number of particles with d_i.

The number of moles of active sites in a mass of catalyst is then calculated from equation 9:

$$n_a = \frac{D.m}{M} \quad \ldots(9)$$

where D is the dispersion, m is the mass of catalyst used, and M is the atomic weight of the element from which the nanoparticles are made.

5.2.3 Materials

Support materials: All support materials used in the current study are as described in Chapter 2.

Metal Salts: $RhCl_3 \cdot 3H_2O$ (>99%) was obtained from Precious Metals Online (PMO), based at Monash University, Australia. $PdCl_2$ (>99%) was obtained from Aldrich. H_2PtCl_6 (>99%, though technically the oxonium salt, $[H_3O]_2[PtCl_6] \cdot 3H_2O$, ref. [369]) was obtained from BDH.

Miscellaneous Reagents: NaCl (99.8%) was obtained from BDH. $NaBH_4$ (99%) and $LaCl_3$ (99%) were obtained from Ajax. CeO_2 (<5 μm, <99.9%) was obtained from Sigma-Aldrich.

Solvents: n-heptane (>99.8%) was obtained from Ajax. Acetone (99%) was obtained from Merck. Type I water was used for the preparation of all stock solutions.

Hydrogenation Substrates: Cyclohexene (>99%, synthesis grade) was obtained from AppliChem. 1-octene (>99%, for synthesis) was obtained from Merck. 1,5-cyclooctadiene (99%) was obtained from Sigma Aldrich.

5.3 Results and Discussion

5.3.1 General Remarks

The preparation of all 24 catalysts generally proceeded similarly to one another, regardless of which combination of metal salt and support material was used. No obvious visual changes occurred when the support materials were dispersed in water, nor when the metal salt solutions were added to these suspensions. Addition of the aqueous sodium borohydride, used in this case as a reducing agent, caused the suspensions to rapidly darken in colour. This signalled the reduction of the precursor metal salts to their metallic states, where the particles strongly scatter light and the medium temporarily becomes a deep black colour. After stirring was ceased, the suspensions settled to the bottom of the vessels, leaving little suspended or coloured matter in the supernatant. The platinum-containing systems were an exception to this general rule, with the supernatants remaining light brown in colour for an extended period of time. A 100 μL aliquot of $LaCl_3$ was added to these catalysts to induce

aggregation of the platinum particles which remained in colloidal suspension [370] so that the maximum designed loading of 1.00% was achieved. This behaviour is partially expected, as platinum nanoparticles are colloidally stable even without additional stabilising agents, while rhodium and palladium are generally not.

The sedimented matter observed after stirring was ceased was usually a mixture of grey and black particulates, suggesting that some portion of the reduced metal had spontaneously adsorbed to the support materials, while some had formed large black aggregates of metal up to a millimetre in size, especially evident in the silica-based systems. Drying of the samples produced light grey powders speckled with black flecks, presumably arising from metal aggregates not associated with or bound to the surface of the support materials. Gentle grinding of the samples with an agate mortar and pestle progressively reduced the size of these black flecks, until the samples appeared totally homogeneous. Photographs of the catalysts illustrating the variation in colour of the final products are shown in **Figure 78**. All catalysts were various shades of grey, with the greatest variation evident between catalyst prepared using different support materials. Since the grey colour is due to scattering of light by the nanoparticles in the sample, this betokened differences in the state of aggregation of the metal across the different support materials, an idea which was confirmed later by electron microscopy.

Prior to reduction, the pH values of the solutions varied significantly between different systems as shown in **Table 11**. Most fell within the range of 2 – 4, with the exception of the two apatitic systems, the pHs of which were closer to 5 for HAp and 8 for BAp. As the metal salt solutions are appreciably acidic, especially H_2PtCl_6, it would be expected that the pH of these dispersions should be several pH units lower than reported for dispersions of the pristine support materials, as described in Chapter 2. This was not the case, however, which suggests there may have been an acid-base type neutralisation occurring between the support and the metals salts, especially for the two apatites. The significantly higher pH of the bioapatite relative to the commercial hydroxyapatite may be attributable to residual CaO or MgO in the material as a result of the calcination process through which it was prepared.

Figure 78: Photographs of the catalysts prepared from electrostatically stabilised colloids. Clear differences are evident in the colour of the different catalysts, betokening differences in the levels of aggregation of the supported metal particles.

Table 11: Solution pH values during synthesis of catalysts prepared from unprotected metal colloids. Clear differences are evident between different support materials and metals.

Support	Metal	pH	Support	Metal	pH
Al_2O_3	Rh	4.20	HNC	Rh	2.95
	Pd	3.90		Pd	3.69
	Pt	2.34		Pt	2.33
SiO_2	Rh	3.03	PRL	Rh	2.73
	Pd	3.36		Pd	3.58
	Pt	2.50		Pt	2.31
HAp	Rh	5.16	BAp	Rh	7.82
	Pd	4.74		Pd	8.42
	Pt	4.77		Pt	9.17
MCC	Rh	2.80	MFC	Rh	2.86
	Pd	3.16		Pd	2.86
	Pt	2.50		Pt	2.36

It could be expected from currently reported pH values that, in combination with the zeta potential data reported in Chapter 2, predictions could be made regarding the nature of the interaction between the metal salt and the surface of the support. At the reported pH values most of the supports displayed a negative surface charge, suggesting they could attract cations in solution *via* electrostatic forces. The only one of the metal salts which was anticipated to yield positively charged ions in solution, however, was $RhCl_3$ [371-376], suggesting this may be the only one of the metal salts attracted to the support materials, at least electrostatically. Given in the equivalent levels of aggregation in the catalysts as later shown by electron microscopy, this suggests that electrostatic interactions between the support and the precursor salt are not a predominating factor in producing supported catalysts with a low degree of metal aggregation.

5.3.2 Electron Microscopy

The combination of SEM and TEM proved to be extremely powerful for characterisation of the textural properties of the catalysts. Magnification ranges spanning five orders of magnitude were used to qualitatively assess the metal distribution, and quantitatively measure particle size distributions. Unequivocal

identifications of the metal particles were made through the use of backscatter detection in combination with EDS, which successfully allowed the elemental composition of different features within the samples to be measured with spatial resolution of *ca.* 100 nm. Clusters were evident in the micrographs which were not seen in the pristine support materials, the EDS spectra for which showed they were composed of the metals Rh, Pd, or Pt. In no cases were any Cl peaks observed in the spectra, indicating they were metallic particles and not simply crystals of the dehydrated precursor salts. Example spectra are shown in **Figure 79** for three different catalysts.

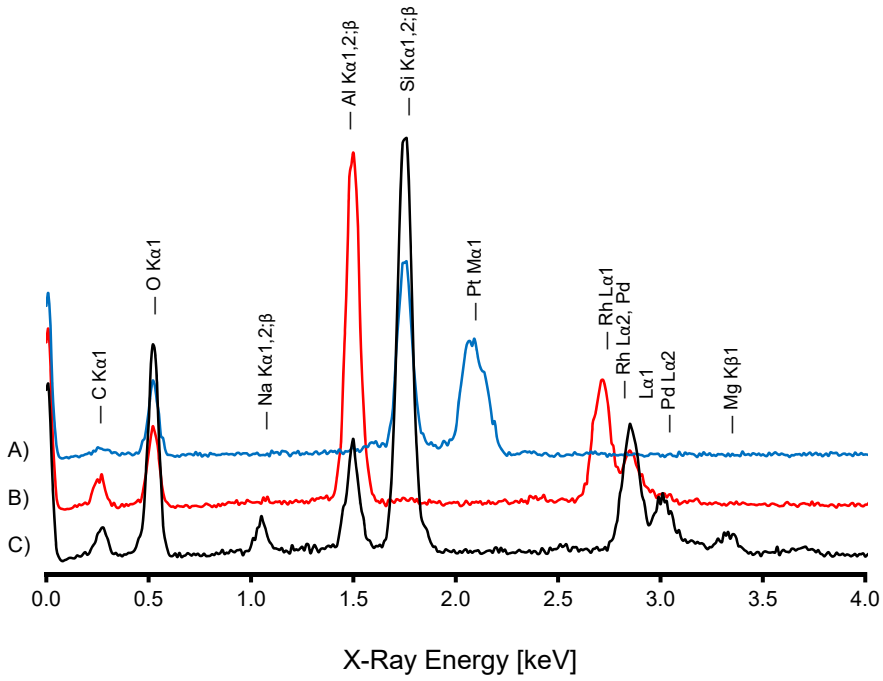

Figure 79: EDS spectra of three aluminosilicate-supported catalysts prepared from electrostatically stabilised metal colloids. The three traces correspond to spectra from: a) Pt/SiO_2, b) Rh/Al_2O_3, c) Pd/PRL.

Clusters of nanoparticles spanning five orders of magnitude in size were observed across the 24 different catalyst systems, from individual nanoparticles approximately 1 nm in diameter through to aggregates of nanoparticles spanning nearly 100 μm in diameter. Differences were also observed between the distributions of different metals on the same support materials, as suggested by the differences in colour of the different catalysts discussed in the preceding section. Example BSE-SEM micrographs are shown in **Figure 80**, and example TEM micrographs are shown in **Figure 81**.

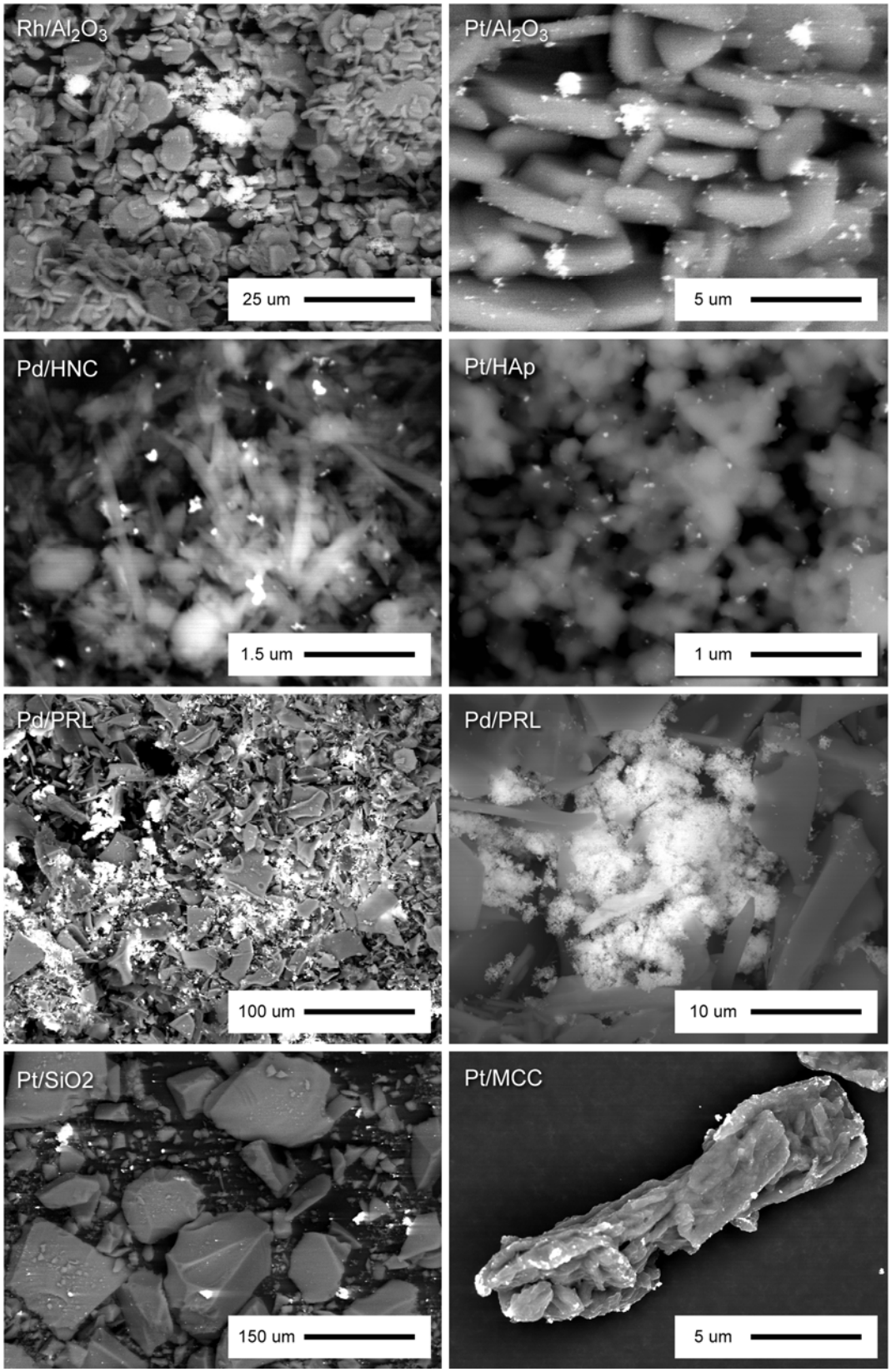

Figure 80: BSE-SEM micrographs of various catalysts prepared from electrostatically stabilised metal colloids. High-brightness white patches correspond to regions in the sample of higher atomic mass, in these cases originating from the supported metal particles. Differences in the metal dispersion are clearly evident between different systems.

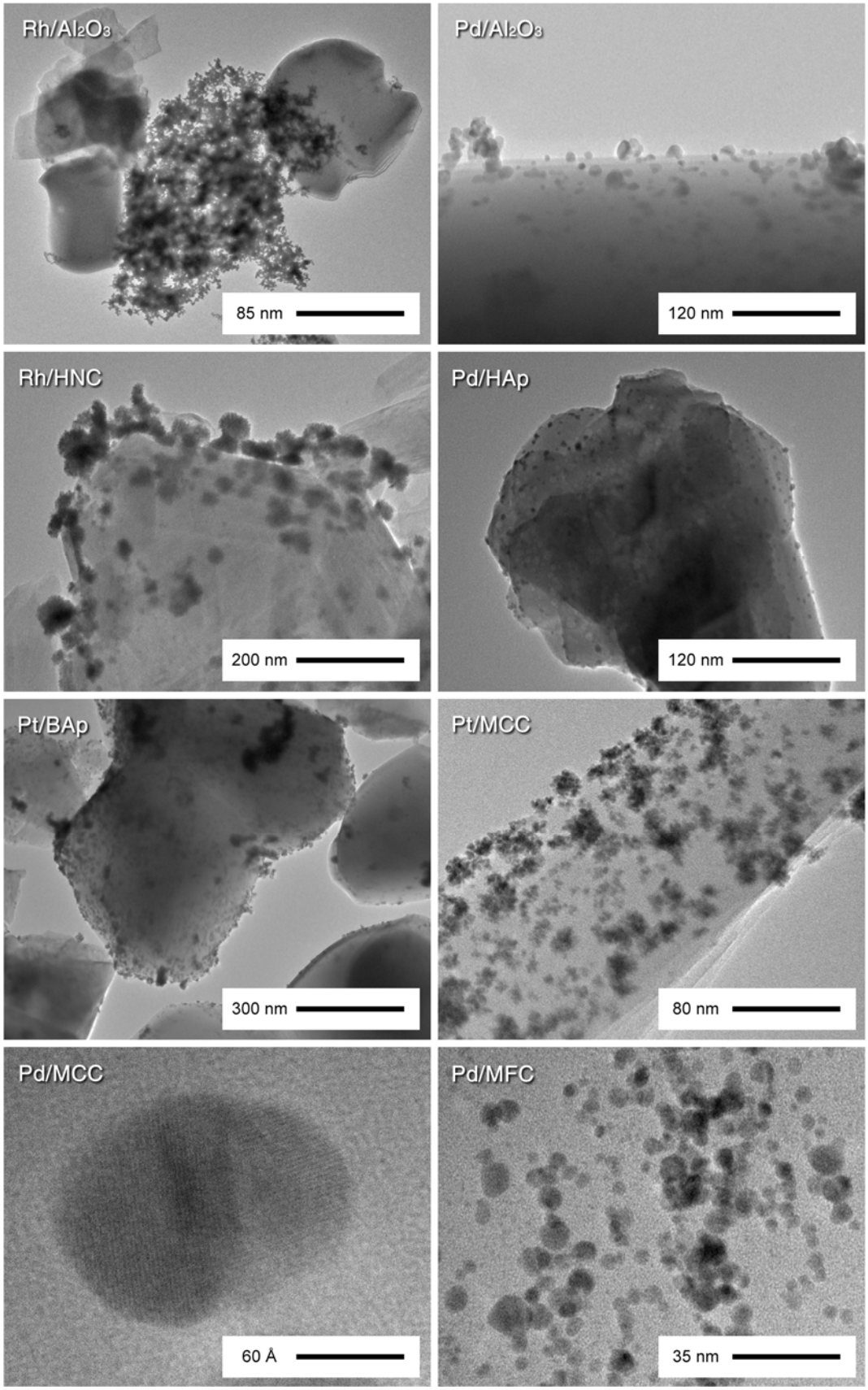

Figure 81: TEM micrographs of various catalysts prepared from electrostatically stabilised metal colloids. Dark spots correspond to supported metal particles; clear differences are evident in the particle sizes and their distribution across the various support materials.

In all cases, metals were observed immobilised on the support materials as nanoparticles with diameters ranging from 2 nm to 8 nm. The particle sizes and their standard deviations for each of the catalysts studied are listed in **Table 12**. Supported rhodium particles generally showed the smaller particle sizes of the three metals, with no sintering (the fusion of particles with one another) evident between particles. The supported palladium particles were generally the largest, although their 'lumpy' appearance suggested their larger sizes may have been a result of the sintering together of several smaller particles.

Table 12: Particle sizes of the catalysts prepared from unprotected colloids, as measured by transmission electron microscopy. Of note is the generally similar particle sizes between different catalysts, as well as the moderate monodispersity.

Catalyst	Particle Size [nm]	Catalyst	Particle Size [nm]
Rh/SiO_2	3.5 ± 0.5	Rh/PRL	2.8 ± 0.4
Pd/SiO_2	5.0 ± 0.8	Pd/PRL	9.2 ± 5.0
Pt/SiO_2	3.6 ± 0.6	Pt/PRL	4.0 ± 0.8
Rh/Al_2O_3	3.3 ± 0.6	Rh/HNC	3.7 ± 0.8
Pd/Al_2O_3	9.7 ± 4.1	Pd/HNC	8.3 ± 2.8
Pt/Al_2O_3	4.0 ± 1.0	Pt/HNC	3.2 ± 0.6
Rh/HAp	3.8 ± 0.9	Rh/BAp	2.7 ± 0.5
Pd/HAp	3.3 ± 0.5	Pd/BAp	2.8 ± 0.4
Pt/HAp	3.8 ± 0.7	Pt/BAp	3.6 ± 0.5
Rh/MCC	2.6 ± 0.5	Rh/MFC	3.3 ± 0.6
Pd/MCC	6.0 ± 2.9	Pd/MFC	4.7 ± 2.1
Pt/MCC	3.6 ± 0.7	Pt/MFC	3.5 ± 0.7

Micrographs of the silica-supported catalysts showed that the supported metals were indeed speciated as nanoparticles, ranging in average size from 3.5 nm in diameter for the Rh/SiO_2 catalyst up to 5.0 nm in diameter for the Pd/SiO_2 catalyst. Most of the particles were aggregated into large clusters ranging in size from 1 μm to 100 μm, and were not dispersed uniformly across the surface of the support as intended. Individual supported nanoparticles could not be discounted, however, because the inherent mesoporosity of the support material gave it a 'mottled' appearance which prevented their direct observation.

The alumina-supported catalysts showed much more homogeneous metal distributions than the silica-supported catalysts. The metals were once again speciated as nanoparticles, ranging in average particle size from 3.3 nm for the Rh/Al_2O_3 catalyst to 9.7 nm for the Pd/Al_2O_3 catalyst. Many of the particles were irregular in size and shape, with morphologies reminiscent of tiny "nano-potatoes" glued to a flat surface. Every surface of every alumina particle investigated was coated with nanoparticles in this way, though many large metal aggregates were observed as well. This suggests that the alumina surface had a high affinity for metal particles, but because of its low surface area it became 'saturated' at very low loadings, leading to any further incoming nanoparticles to aggregate with one another into large clusters rather than bind to the surface.

The halloysite-supported catalysts, being composed equally of alumina and silica elementally, showed distributions of metal intermediate between pure alumina and pure silica. The majority of metal existed as small clusters around 10 nm in size, associated intimately with the surface of the halloysite particles. The largest average particle size was 8.3 nm in the Pd/HNC catalyst, while the smallest average particle size was 3.2 nm in the Pt/HNC catalyst. Curiously for all three catalysts there was a strong bias observed in that the flat halloysite particles tended to have much higher loadings of metal than the tubular particles.

The perlite-supported metals existed as nanoparticles of varying sizes, with a maximum average particle size of 9.2 nm for the Pd/PRL catalyst, and a minimum average particle size of 2.8 nm in the Rh/PRL catalyst. Much like the silica-supported catalysts though, these nanoparticles were predominantly found in large aggregates, even larger in size than in the silica catalysts. Since the perlite is not mesoporous but the silica is, one may expect a greater amount of aggregation given the lower surface area. However, the surface area of the silica gel is presumably mostly internal, that is, arising from the presence of the mesopores. If these pores are inaccessible to the metal nanoparticles then the two support materials may have more similar 'accessible' surface areas. It seems likely therefore that the poorer metal distribution is a result of the greater zeta potential of perlite compared to silica, as shown in Chapter 2, which could inhibit adsorption of the metal salts and subsequently generated particles as discussed in the previous section.

The HAp-supported metals were by far the most homogeneously dispersed metals of all the systems studied, with almost all metal particles dispersed individually upon the surface of the apatite. The maximum average particle size was 3.8 nm, observed in both the Rh/HAp and Pt/HAp catalysts, while the minimum average particle size was 3.3 nm in the Pd/HAp catalyst. Not all surfaces of the apatite were equally coated, however, with some HAp particles nearly completely coated in metal, and others with none. It may be the case that the nanoparticles, once reduced, cannot penetrate into the pore structure of the apatite, and simply become lodged on the outer surface of the particles. When the resulting catalysts are sonicated the particles are cleaved, and the inner pristine surfaces are exposed.

The BAp-supported catalysts showed similar metal distributions to their model HAp counterparts, with all metal nanoparticles dispersed as small clusters evenly across the BAp surfaces. The maximum average particle size of 3.6 nm was observed in the Pt/BAp catalyst, while the minimum average particle size of 2.7 nm was observed in the Rh/BAp catalyst. These are generally smaller than the HAp supported nanoparticles, which suggests that the BAp surface may have a greater affinity for metal nanoparticles than HAp, removing them from the solution more rapidly during reduction, leading to retarded growth. Alternatively, the high pH during reduction could convert the metal salts to a hydroxide form with different reduction properties, and consequently a different particle size.

The MCC-supported metals were dispersed as small clusters similar to the halloysite-supported metals, ranging from individual particles up to clusters 100 nm in size, but with an average around 10 nm. The maximum average particle size of 6.0 nm was observed in the Pd/MCC catalyst, while the minimum average particle size of 2.6 nm was observed in Rh/MCC catalyst. The particle size distributions of the metals on this particular support were the most polydisperse of all studied, with the sizes of particles within a single catalyst ranging from 2 nm up to 20 nm. Additionally, because of the electron-transparent nature of the predominantly carbonaceous cellulose support, excellent quality transmission electron micrographs could be obtained with relative ease, with phase-contrast images of the nanoparticle lattices easily achievable, illustrating that the supported metal particles are crystalline.

The MFC-supported catalysts showed similar characteristics to the model MCC-supported catalysts. The greatest average particle size of 4.7 nm was observed in the

Pd/MFC catalyst, while the minimum average particle size of 3.3 nm was observed with the Rh/MFC catalyst. Once again the particles were quite polydisperse, though not significantly more so than the MCC-supported catalysts.

5.3.3 X-Ray Diffraction

The x-ray powder diffraction patterns of the catalysts showed various differences between the catalysts and their corresponding pristine support materials. Most notably the catalysts contained a series of broad peaks not observed in the supports, whose positions and breadths were consistent with metal nanoparticles, based on match to the International Centre for Diffraction Data's Powder Diffraction Files, as well as other reported studies from the literature. Three example powder patterns are shown in **Figure 82** for some silica-supported metals. The peaks shapes and intensities were shown to vary significantly between different catalysts, which suggested they carried information regarding the size of the nanoparticles and the strain within their lattices. For this purpose profile fitting followed by line broadening analyses were carried out

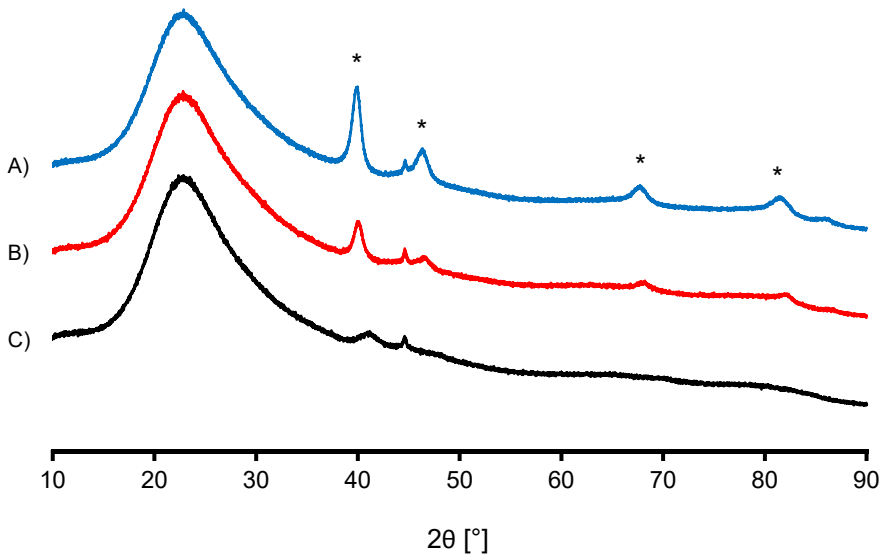

Figure 82: XRD patterns for the three silica-supported catalysts prepared from electrostatically stabilised colloidal metal nanoparticles. The three plots correspond to: a) Pt/SiO_2, b) Pd/SiO_2, and c) Rh/SiO_2. Starred peaks correspond to reflections originating from the supported metal particles.

Peak fitting using HighScore was successfully carried out using either Voight, pseudo-Voight, or Pearson VII profiles. Fitting errors (residuals) were usually not greater than the signal to noise of the patterns, indicating that the peak shapes were

accurately modelled. Asymmetry was usually not significant enough to warrant the use of split peaks, however in some cases it increased the fit accuracy. Calculation of the particle sizes from the fitted profiles gave values as high as 11.7 nm for the (222) reflection of the Pd/MCC catalyst, and as low as 3.0 nm for the (200) and (220) reflections of the Rh/MCC catalyst. Within each catalyst the measured sizes varied depending on which reflection was used, and so values were calculated for each and averaged to provide the final particle sizes, as listed in **Table 13**.

Interestingly, the rhodium-supported particles generally showed the broadest reflections, in some cases so broad that they could not be reliably modelled. This suggests that the rhodium particles are generally the smallest, which is consistent with both their TEM measurements, and with their anomalously high catalytic activities, described later. The palladium-supported particles generally showed narrower lines, and the platinum-supported particles narrower still. Again, this is consistent with the trends measured by TEM. In most cases the (111) reflections were the narrowest, suggesting that particles may adhere to their supports normal to this plane, or alternatively that the particles are simply not spherical and elongated in this direction. Given that they generally *are* spherical (or hemispherical) as seen by TEM, the former seems more likely.

On average the sizes obtained by XRD were 25% higher than those obtained by TEM, although the differences ranged from 82.5% higher for the Pt/Al_2O_3 sample through to 36.1% lower for the Pd/HNC samples. Correlation between the XRD and TEM results showed there was no obvious relationship between the two. Previous studies have found much better agreement between TEM and XRD measurements of this type – in the order of 5 to 10% – for homogeneous quasispherical particles [377], however given the morphological observations made by TEM this is obviously not an accurate model of the particle shapes present in these catalysts. They range from spherical to oblate to hemispherical, and as such it should be expected that the different crystal planes extend for different lengths within a given particle, which would complicate their measurement. It is therefore unsurprising that the two sets of measurements do not perfectly complement one another.

Table 13: Particle size measurements obtained by line-broadening analysis of powder diffraction data. Cells with dashes could not be adequately modelled due to poor signal to noise, or severe overlap with reflections from the support material.

Catalyst	Particle Size [nm]					
	(111)	(200)	(220)	(311)	(222)	Average
Rh/SiO_2	4.0	-	-	-	-	4.0
Pd/SiO_2	9.3	6.7	6.5	6.7	7.1	7.3
Pt/SiO_2	7.8	5.0	5.6	5.1	-	6.3
Rh/Al_2O_3	-	-	-	-	-	-
Pd/Al_2O_3	10.9	7.1	-	9.6	-	9.2
Pt/Al_2O_3	8.8	7.1	-	6.0		7.3
Rh/HAp	-	-	-	-	-	-
Pd/HAp	-	-	-	-	-	-
Pt/HAp	17.5	12.9	6.7	6.9	-	6.9
Rh/MCC	3.6	3.0	3.0	3.7	-	3.4
Pd/MCC	6.5	5.7	5.9	6.2	11.7	7.2
Pt/MCC	5.1	4.2	4.4	4.3	4.7	4.5
Rh/HNC	4.6	2.9	2.3	2.2	-	3.0
Pd/HNC	8.1	3.3	4.7	5.0	5.4	5.3
Pt/HNC	5.8	4.5	5.0	5.2	5.6	5.2
Rh/PRL	4.2	-	4.3	-	-	4.3
Pd/PRL	9.6	5.9	6.0	7.7	8.2	7.5
Pt/PRL	9.0	5.4	4.9	4.8	6.7	6.2
Rh/BAP	-	-	-	-	-	-
Pd/BAp	-	-	-	-	-	-
Pt/BAp	6.7	-	5.9	6.9	-	6.5
Rh/MFC	3.9	3.9	4.5	4.6	-	4.2
Pd/MFC	6.4	4.4	5.5	5.5	-	5.5
Pt/MFC	5.3	4.7	5.0	4.7	4.9	4.9

Several other complications existed which may have affected the analysis and which are therefore of interest. Firstly, it was non-trivial to recover the diffraction pattern of the supported particles separate from their support material, especially with highly crystalline materials like alumina, where reflections from the support and the nanoparticles overlap one another. Furthermore, at the low concentrations used

(1% wt NPs per catalyst) very long collection times were required to obtain acceptable counting statistics, which even then were noisy. Ultra-small particles (>2 nm) may have been partially obscured by low SNR, especially since they give rise to ultra-broad reflections in the powder pattern. Furthermore, smaller particles may be more accurately described as 'amorphous' than 'crystalline', therefore not contributing to the line breadths, and raising the apparent particle sizes. These were all expected to contribute error to the measurements, and thus the TEM measurements remain the 'gold standard' for particle size measurement in the current work.

5.3.4 Infrared Spectroscopy

The infrared spectra of the catalysts generally showed an array of subtle changes between the catalysts and their pristine supports. Interpretations of these differences were complicated by the sampling method used, however, since the 'transflection' spectra generated by the microFTIR configuration contain both absorptive and reflective spectral characteristics, sometimes producing derivative-shaped bands. The spectra for the individual catalysts, all acquired by microFTIR, are discussed in the following paragraphs.

The alumina-supported catalysts showed a clear loss of three bands on nanoparticle immobilisation, at 3295 cm^{-1}, 1584 cm^{-1}, and 1393 cm^{-1}. This is illustrated in **Figure 83**. Since the powder diffraction patterns (and the NMR spectra, see later) remained largely unchanged, both of which are 'bulk analysis' methods, this suggested these were vibrational modes associated with the surface of the sample. These have been previously assigned as originating from surface hydroxyls and adsorbed water as described in Chapter 2, which are presumably removed or severely damped by the high surface coverage of nanoparticles as observed by TEM.

The silica-supported catalysts showed an increase in intensity of the sharp 3741 cm^{-1} band, as well as a variety of distortions in the low energy region spanning 750 cm^{-1} to 1150 cm^{-1}. The former of these is consistent with the NMR evidence, discussed in a later section, suggesting partial dehydration of the sample on nanoparticle immobilisation. The low-energy changes however were less reliable, and only appeared in certain spectra. These may have arisen due to a distortion of the surface of the silica particles as a result of the presence of nanoparticles, though the

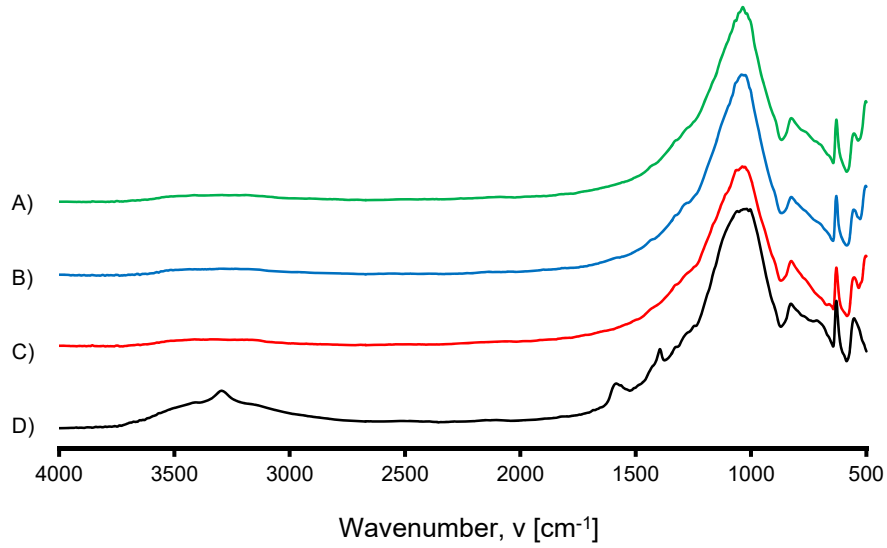

Figure 83: FTIR spectra of alumina-supported catalysts prepared from electrostatically stabilised colloids. The three plots correspond to Rh/Al_2O_3 (A), Pd/Al_2O_3 (B), Pt/Al_2O_3 (C), and pristine Al_2O_3 (D).

low surface coverage observed by TEM suggested this was probably not the case. It seems more likely therefore that the differences arose from modified optical properties of the sample due to changes in particle size and morphology due to the grinding procedure, rather than the immobilisation of nanoparticles.

The halloysite-supported catalysts showed the same effects as those supported by silica, *i.e.* a slight improvement of the definition of some of the low energy bands compared to the support. No significant changes were observed in the hydroxyl region, however. Perlite displayed the same effect as silica but to a lesser extent.

The hydroxyapatite-supported catalysts were difficult to analyse, because the observable vibrational bands were so intense that they saturated the detector and produced poor quality spectra. Pressing the samples flatter, however, produced the derivative-like '*restrahlen*' spectra typical of the infrared transflection technique, which did not suffer the same problems. No significant differences were observed between the support and the corresponding catalysts, however.

Bioapatite-supported samples showed similar to properties to those supported by hydroxyapatite. Firstly the spectra were very sensitive to the arrangement of the powder – unpressed or loosely pressed powder gave typical absorption spectra as produced by the transmission/KBr method, however with application of only minor pressure with a laboratory spatula, the spectra changed to the derivative-like

'*restrahlen*' spectra. More interesting, however, were the bands detected in the high energy end of the spectra – in the BAp-supported catalysts there were multiple absorptions in this region, the intensities of which varied depending on the supported metal. The peak at 3695 cm^{-1} appears in the native support material, but completely disappeared in the platinum-supporting catalyst. Conversely, the peak at 3575 cm^{-1} which corresponds to structural hydroxyl groups remained of equal intensity. This is illustrated in **Figure 84**. In Chapter 2 this band was assigned as originating from $Mg(OH)_2$ produced *via* hydrolysis of MgO, which is consistent with its attack and subsequent reduction by acidic metal salt species.

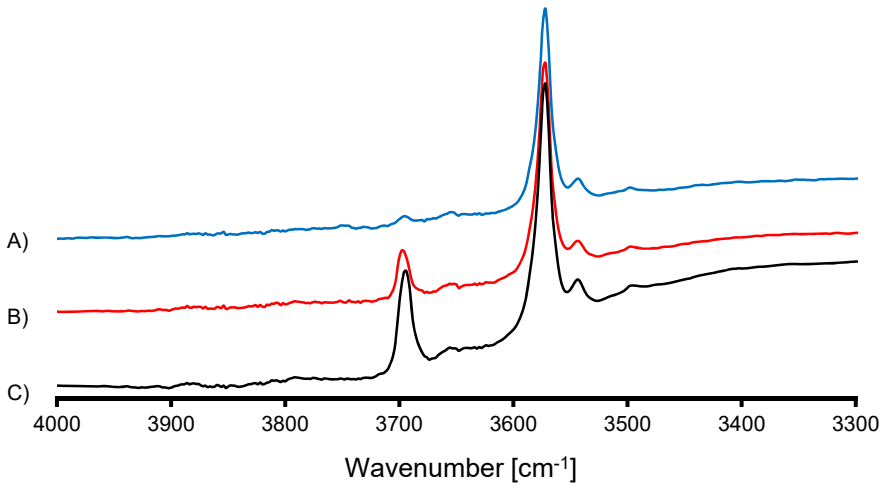

Figure 84: FTIR spectra of bioapatite-supported rhodium, palladium, and platinum catalysts prepared from unprotected colloids. The three plots correspond to A) Pt/BAp, B) Rh/BAp, C) Pd/BAp.

Microcrystalline cellulose supported catalysts showed no differences from one another, nor to their parent support materials, in terms of the infrared spectra. Macrofibrillar cellulose supported catalysts showed no differences between any of their spectra, much like those supported by microcrystalline cellulose.

In parallel to the acquisition of spectral data by microFTIR, photomicrographs of the catalysts specimens were simultaneously acquired using the inbuilt digital camera collinear with the infrared optics. When the focal plane was scanned vertically up and down through the samples the presence of randomly-distributed black flecks could be seen in the silica-supported and perlite-supported samples, as shown in **Figure 85**. These were presumed to be large aggregates of metal particles which had not

adhered to the surfaces of the support materials, just as were seen by electron microscopy.

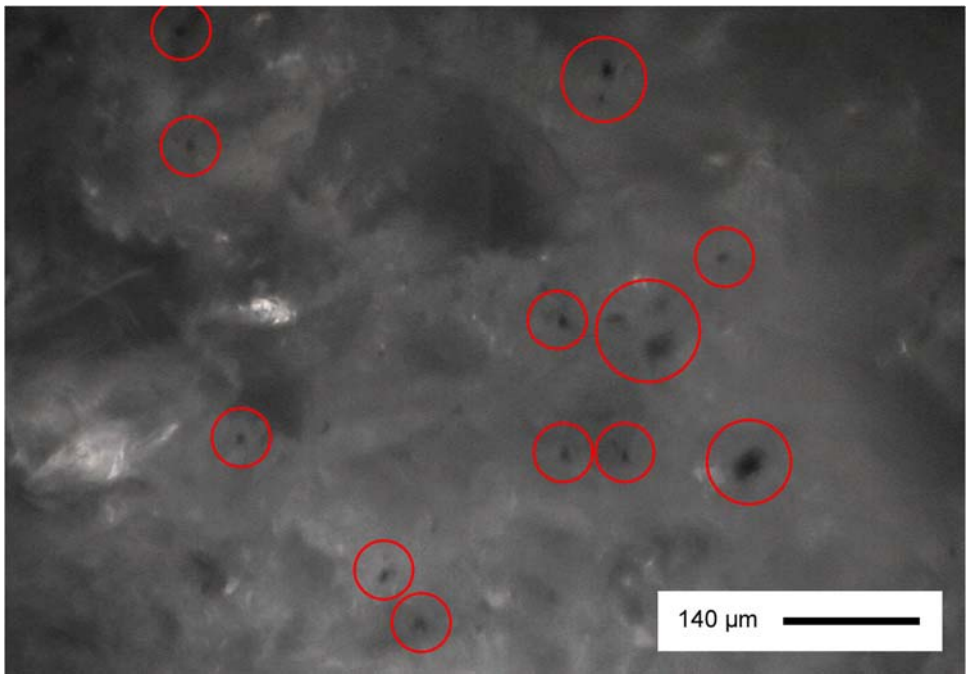

Figure 85: Photomicrograph of Rh/SiO_2 collected using the FTIR microscope prior to spectral acquisition. Regions circled red contain black patches not observed in the pristine support, corresponding to large aggregates of metal particles.

5.3.5 Solid-State NMR

Many of the solid state NMR spectra of the supported catalysts were identical to those of their pristine parent support materials, as described in Chapter 2. Some systems, however, exhibited subtle differences between the two. The alumina supported catalysts are an example of this; while the ^{27}Al spectra of the supported catalysts were remarkably similar to one another, all three were subtly different to the pristine Al_2O_3. Where the pristine support had an intense symmetrical resonance at 16 ppm corresponding to the structural AlO_6 units, in the supported catalysts this resonance developed a slight asymmetry tailing toward the low field side. The pristine support also showed a weak resonance at 65 ppm corresponding to tetrahedral AlO_4 units, while in the supported catalysts this peak was several times more intense. No differences were observed in the ^{1}H spectrum, however, which suggests the differences in the ^{27}Al spectra don't arise from a surface hydration step, but more likely originate from a subtle crystallographic distortion in the surface of the alumina as a result of the high surface coverage of metal nanoparticles.

The silica-supported catalysts also exhibited spectral differences between the catalysts and the pristine support. While the pristine support exhibits a broad bell-shaped resonance at *ca.* 5 ppm in its ^{1}H spectrum, the supported catalysts exhibit significantly distorted peak shapes with different chemical shifts, indicating a difference in the state of hydration of the sample. This is perhaps unsurprising, because the NMR spectra reported in Chapter 2 are of the support materials 'as received', while the spectra of the supported catalysts are after saturation with water, immobilisation of nanoparticles, and subsequent drying.

The halloysite-supported catalysts also showed differences in their NMR spectra, much like the SiO_2 and Al_2O_3. In the ^{1}H spectrum of the pristine support there were two resonances of equal intensity evident, one from the silanols and one from the aluminols. In the supported catalysts, however, the intensities of the aluminol resonances were diminished relative to the silanols. The ^{29}Si spectra of the same samples show no significant differences compared to the pristine supports, while the ^{27}Al spectra showed the appearance of a shoulder peak at 25 ppm much like the alumina-supported catalysts. This suggests that the nanoparticles were immobilised preferentially on the alumina-rich faces of the halloysite particles, which is consistent with observations made by electron microscopy.

The perlite-supported catalysts showed no appreciable differences in their ^{29}Si spectra relative to the pristine support. This is logical given what has been presented hitherto: the perlite is not heavily hydrated and so cannot exhibit any changes in this respect; furthermore, the perlite-supported catalysts do not have any appreciable surface coverage of nanoparticles, thus there is no interaction present which should manifest in any spectral changes. This was reflected in the ^{27}Al spectra which show no additional environments created on nanoparticle immobilisation, unlike the halloysite or alumina supported catalysts. This does, however, suggest that the aluminium present in the perlite is not concentrated at the surface of the particles, since this would produce spectral changes akin to those observed for the other aluminium-containing catalysts.

The HAp-supported catalysts showed various differences in their NMR spectra compared to the pristine support. In the ^{1}H spectrum a substantial increase in the intensity of the 5.8 ppm peak was observed for the supported catalysts relative to the pristine support, as well as a tail extending to low field. This is assigned by as Jäger *et*

al. [246] as resulting from HPO_4^{2-} substitution in the surface layers of the apatite. This is supported by the observation that the manifold of small peaks appearing at the base of the central phosphate resonance in the ^{31}P DPMAS spectrum, as described in Chapter 2, are diminished in intensity in the supported catalysts. Since the metal salt solutions are significantly acidic this suggests the apatite surface may be attacked and partially dissolved during the preparation of the catalysts, and is perhaps precipitated onto the surface of the catalysts during drying as a calcium salt of monobasic hydrogen phosphate.

The NMR spectra of the microcrystalline cellulose-supported catalysts, on the other hand, were the least interesting in terms of spectral differences. None of the catalysts showed any significant differences to their ^{13}C spectra, suggesting there is no change in the overall crystallinity of the sample, though all three catalysts showed increased peak half-widths in their ^{1}H spectra, which could be a result of disruption of surface structure due to nanoparticle adsorption. Similar changes, or lacks thereof, were observed for the macrofibrillar cellulose-supported catalysts.

5.3.6 Catalytic Activity

All of the catalysts tested displayed some degree of activity with respect to their activity in cyclohexene hydrogenation. In all cases the reaction proceeded directly from cyclohexene to cyclohexane, with no intermediate products observed. Peaks were assigned by matching their mass spectra against the NIST database, and against the retention time of known standards. Baseline resolution of the cyclohexene and cyclohexane peaks was achieved in all instances, as illustrated in **Figure 86**. Integration and processing of the data showed that rate of conversion was linear in all cases, which is consistent with the zero-order kinetics observed by Gonzo and Boudart [378]. No other products were detected by either GC-MS or NMR. No double bond migration was observed, because even if this were to occur, '1-cyclohexene' is not distinguishable from '2-cyclohexane'.

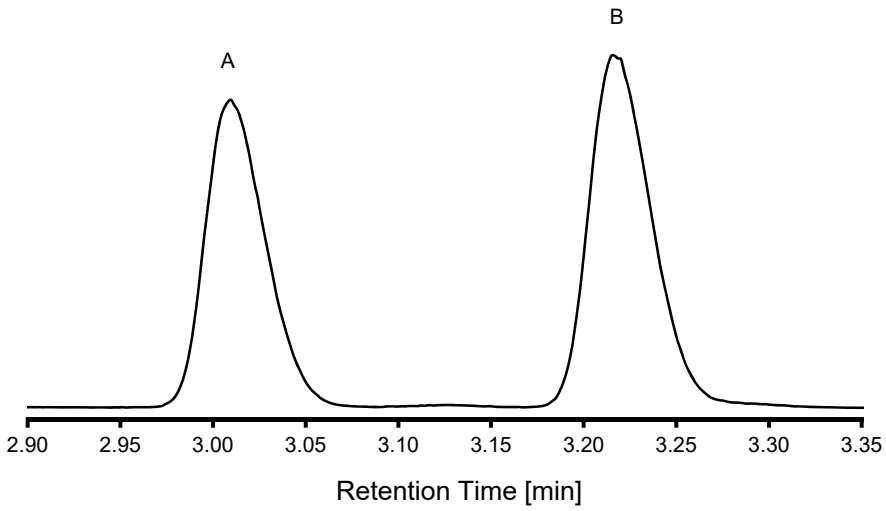

Figure 86: GC-MS TIC showing the reaction products after 20 minutes for the hydrogenation of cyclohexene by Pd/HAp. The two peaks were assigned as cyclohexene (A) and cyclohexane (B).

Calculation of the reaction rates from the GC-MS data showed the catalysts displayed a diverse range of activities. Of the three different metals used palladium was generally the most active, followed by rhodium and then platinum. The specific activities depended greatly on the material upon which they were supported; the greatest activity was observed with the Pd/MCC catalyst at 30,200 $mmol^{-1}$ g^{-1} hr^{-1} (TOF 26,400 hr^{-1}), while the activity of the Pd/SiO_2 catalyst, prepared in an equivalent fashion, produced an activity of only 3,630 $mmol^{-1}$ g^{-1} hr^{-1} (TOF 2,940 hr^{-1}). The full activity results are tabulated in **Table 14**.

The minimum activity was observed with the Rh/BAp catalyst which turned over no detectable quantity of substrate during the period of an hour. This poor activity cannot be attributed to either the metal or the support individually, however, as the Pd/BAp catalyst displayed an activity of 6,380 $mmol^{-1}$ g^{-1} hr^{-1} (TOF 3,080 hr^{-1}), while other supported rhodium catalysts displayed good activities, for example Rh/MCC, whose activity was 13,600 $mmol^{-1}$ g^{-1} hr^{-1} (TOF 9,390 hr^{-1}). Curiously however, the Rh/HAp catalyst also displayed poor activity, at 150 $mmol^{-1}$ g^{-1} hr^{-1} (TOF 145 hr^{-1}). It would seem, therefore, that the currently used method does not produce highly active Rh/apatite catalysts, at least for the hydrogenation of cyclohexene.

Table 14: Catalytic activity of catalysts prepared from unprotected metal colloids in cyclohexene hydrogenation.

Support	Metal	Specific Rate [mmol g^{-1} hr^{-1}]	Turnover Frequency [hr^{-1}]
Al_2O_3	Rh	1,240	1,030
	Pd	2,640	5,380
	Pt	1,700	1,700
SiO_2	Rh	4,440	4,390
	Pd	3,630	2,940
	Pt	5,090	4,440
HAp	Rh	150	145
	Pd	19,500	10,700
	Pt	13,300	12,100
MCC	Rh	13,600	9,390
	Pd	21,300	30,200
	Pt	29,000	26,400
HNC	Rh	6,000	5,580
	Pd	9,820	15,700
	Pt	16,600	13,500
PRL	Rh	8,500	6,160
	Pd	3,740	9,070
	Pt	4,690	4,630
BAp	Rh	0	0
	Pd	6,380	3,080
	Pt	1,310	1,170
MFC	Rh	11,900	10,100
	Pd	11,300	11,800
	Pt	9,800	8,790

In the current study, the variable most greatly influencing the catalytic activity was shown to be the support material itself. The alumina and silica supported catalysts appeared the least active of all eight, which is unusual given their place in the literature as typical catalyst support materials. The hydroxyapatite supported catalysts generally showed good activity (except Rh/HAp), while the microcrystalline cellulose supported catalysts were exceptionally active. The novel analogues of these support

materials showed different activities compared to their 'model' analogues, with the halloysite and perlite supported catalysts both more active than either the alumina or silica supported catalysts by a factor of *ca.* 3, while the bioapatite and macrofibrillar cellulose supported catalysts were less active by the same factor.

The range of the currently reported turnover frequencies is interesting, as several groups have reported studies indicating that catalytic hydrogenation of cyclohexene is "*facile"* or "*structure-insensitive*", that is, the turnover frequency does not depend on particle size nor the nature of the support [379, 380]. Curiously though, the turnover frequencies obtained in the current study, as well as many reported in the literature, vary dramatically within individual studies and between different groups. Some examples obtained from the literature are listed in **Table 15**. This shows that the activities measured in the current study compare favourably to those of other groups, and that the current synthetic method is capable of producing catalysts with activities equal in magnitude to other conventional preparative techniques.

Table 15: Turnover frequencies for catalytic hydrogenation of cyclohexene obtained from the literature.

Catalyst	TOF	Conditions	Ref
Pd/SiO_2	33,000	25 °C, 40 psi	[381]
Pd/Fe_3O_4	11,538	75 °C, 6 atm	[382]
Ir/MgO	64	25 °C, 1 atm	[383]
Rh/Al_2O_3	49,300	298 K, 101 kPa	[384]
Pd/SiO_2	29,700	35 °C, 1 atm	[378]

All of the catalysts tested also showed excellent activity in the hydrogenation of 1-octene, being several times more active than for cyclohexene hydrogenation. In the case of the rhodium and platinum supported catalysts the reactions proceeded directly from octene to octane with no other species observed, while significant isomerisation was observed with the supported palladium catalysts, usually producing internal olefins like 2-octene at the same initial rate as octane itself. Gas chromatographic analysis of the reaction mixtures was more difficult than with cyclohexene, and complete baseline separation of the three octene isomers observed could not be achieved. An example chromatogram is shown in **Figure 87**. The four peaks were integrated separately, but the three peaks corresponding to the

unsaturated olefins, A, B, and C, were quantified together assuming equivalent response factors. This allowed their quantification as 'total octenes' for calculation of the conversion rate.

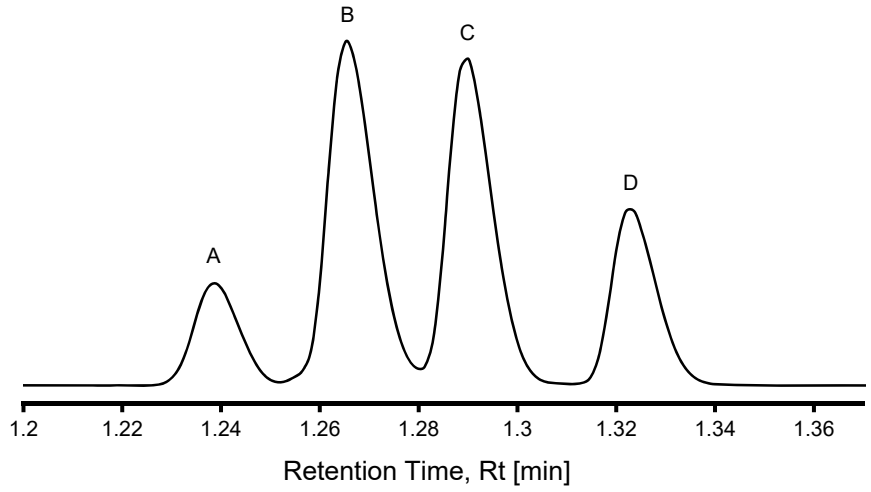

Figure 87: GC-MS TIC for the hydrogenation of 1-octene by Pd/Al_2O_3 after 60 minutes. Peak assignments are 1-octene (A), 2-octene (B), 3-octene (C), and octane (D).

Calculation of the reaction rates from the GC-MS data showed once again that the catalysts displayed a range of activities, with the supported palladium catalysts generally showing the greatest activities, followed by rhodium, and then platinum. The activities also depended strongly on the nature of the support material, as the greatest activity was observed with the Pd/HAp catalyst at 117,000 $mmol^{-1}$ g^{-1} hr^{-1} (TOF 64,400 hr^{-1}), while the equivalently prepared Pd/SiO_2 catalyst had an activity almost an order of magnitude less, at 12,600 $mmol^{-1}$ g^{-1} hr^{-1} (TOF 10,300 hr^{-1}). The full list of activities is given in **Table 16**.

The minimum activity was observed with the Pt/Al_2O_3 catalyst, with a measured reaction rate of 6,320 $mmol^{-1}$ g^{-1} hr^{-1} (TOF 6,470 hr^{-1}). The Rh/Al_2O_3 catalyst also displayed similarly low activity, though the equivalent Pd/Al_2O_3 was several times more active, with a measured rate of 19,600 $mmol^{-1}$ g^{-1} hr^{-1} (TOF 39,900 hr^{-1}). This indicates that the alumina is used in the current study is not an inherently bad support material, but that the activity of catalysts prepared from it depend markedly on the identity of the supported metal.

Table 16: Catalytic activity of catalysts prepared from unprotected metal colloids in 1-octene hydrogenation.

Support	Metal	Specific Rate [mmol g^{-1} hr^{-1}]	Turnover Frequency [hr^{-1}]
Al_2O_3	Rh	7,740	7,230
	Pd	19,600	39,900
	Pt	6,320	6,470
SiO_2	Rh	17,900	15,800
	Pd	12,600	10,300
	Pt	13,400	11,700
HAp	Rh	40,800	39,400
	Pd	117,000	64,400
	Pt	34,500	31,500
MCC	Rh	41,500	28,600
	Pd	27,900	39,500
	Pt	12,400	11,300
HNC	Rh	25,400	23,800
	Pd	34,100	54,600
	Pt	30,300	24,600
PRL	Rh	16,100	11,700
	Pd	12,000	29,100
	Pt	8,520	8,420
BAp	Rh	23,800	21,200
	Pd	30,200	14,600
	Pt	11,700	10,400
MFC	Rh	26,000	21,900
	Pd	35,600	37,200
	Pt	23,500	21,000

The activities of the current catalysts compared favourably with those in the literature, examples of which are given in **Table 17**. Only a single study by Adlim *et al.* [385] has reported faster TOFs than those reported herein, making these some of the fastest octene hydrogenation catalysts ever reported, especially considering the use of standard conditions for the reactions performed for this work. Considering

the modest activity of the same catalysts in cyclohexene hydrogenation, it would therefore be of interest to test these catalysts with other substrates in the future.

Table 17: Turnover frequencies for n-octene hydrogenation reported in the literature.

Catalyst	TOF [hr^{-1}]	Conditions	Ref
Pd/chitosan	1,490-100,000	30°C, 1 atm	[385]
Pt/chitosan	10,700		
Pd/montmorillonite	2,200-23,100	298K, 1 atm	[113]
Pd/PVP colloids	2,880	-	[386]
Ru/PEI-SiO_2	30.6-327	90°C, 5 atm	[387]
Rh/PEI-SiO_2	34.8-1,660		
Pd/PEI-SiO_2	816-1,560		
Pd/montmorillonite	7,100	298K, 1 atm	[388]
Pd/SiO_2	1,800		
Pt/C	1,600	30°C, 4 bar	[389]
Pt/SiO_2	8,880-9,600	303K, 1 atm	[390]
Rh/PVP colloids	10,000	70 °C, 1 atm	[391]

In addition to the two substrates described earlier, the alumina, silica, and halloysite-supported catalysts were also tested in the hydrogenation of 1,5-cyclooctadiene. All nine catalysts were active to varying degrees, though rather than producing predominantly the fully unsaturated alkane, cyclooctane, the major products observed in these reactions were cyclooctene, corresponding to saturation of a single bond, and other isomers of the diene, corresponding to a double bond migration. This produced four peaks in the GC-MS TICs, as shown in **Figure 88**, which were assigned by a combination of matching the mass spectra for each peak against the NIST database or with authentic standards. No standards for the 1,4- and 1,3- isomers were available, however, which meant that peak B, whose mass spectra matched both isomers, could contain either both of these species, or only one.

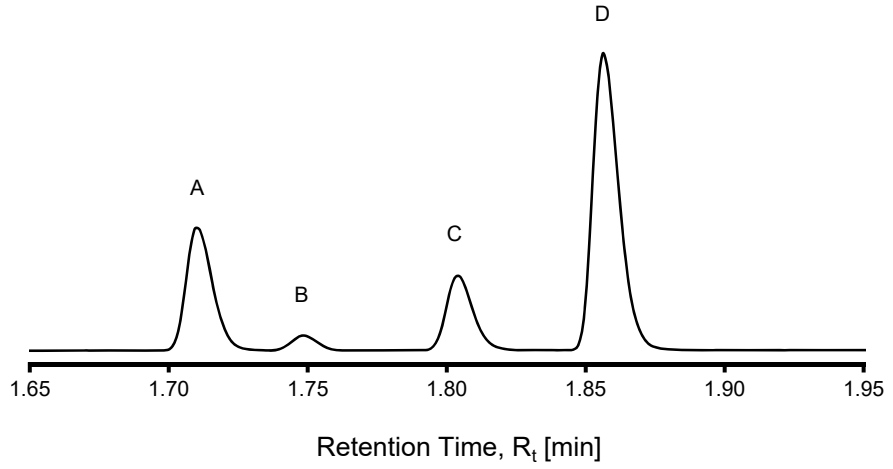

Figure 88: GC-MS TIC showing the reaction products after 60 minutes for the hydrogenation of 1,5-COD by Rh/HNC. Peak assignments are A) cyclooctene, B) isomerised 1,5-COD, C) cyclooctane, and D) 1,5-COD.

Calculation of the reaction rates from the GC-MS data showed similar trends in the catalyst activities to those observed for the previous two substrates. Palladium and rhodium generally displayed similar activities, while platinum was less active than either two. The maximum activity was observed with the Pd/HNC catalyst at 6,560 mmol g^{-1} hr^{-1} (TOF 10,500 hr^{-1}), while the equivalent Pd/Al_2O_3 and Pd/SiO_2 catalysts were only half as active. The full list of activities is given in **Table 18**.

Table 18: Catalytic activity of catalysts prepared from unprotected metal colloids in 1-octene hydrogenation.

Support	Metal	Specific Rate [mmol g^{-1} hr^{-1}]	Turnover Frequency [hr^{-1}]
Al_2O_3	Rh	1,750	1,450
	Pd	3,030	6,160
	Pt	600	613
SiO_2	Rh	3,600	3,170
	Pd	3,450	2,800
	Pt	1,400	1,220
HNC	Rh	6,560	6,140
	Pd	6,560	10,500
	Pt	2,400	1,950

While these numbers are much smaller than the activities for the hydrogenation of either cyclohexene or octene, they still compare favourably with other catalysts reported in the literature, as shown in **Table 19**. Most displayed activities of less than 2000 hr^{-1}, with the exception of the anomalously active Pd/pumice catalysts of Deganello *et al.*, who report activities in excess of $3x10^5$ hr^{-1}.

Table 19: Turnover frequencies for cyclooctene hydrogenation reported in the literature.

Catalyst	TOF [hr^{-1}]	Conditions	Ref
Pd/Pumice	232,000-328,000	25 °C, 1 atm	[101]
Pt/Pumice	3,600	25 °C, 1 atm	[102]
Cu/TiO2	360-530	433K, 3 atm	[392]
Pd/PEG	240-1400*	50-90 °C, 1 MPa	[393]
Pd/Dendrimer	40-884†‡	RT, 1 atm	[394]
Pd/Dendrimer	0-1400‡	20C, 1 atm	[395]

* Not area-normalised. † Biphasic. ‡ TOF H_2/metal/hr.

The turnover frequencies reported in this study are of course only valid under the specific conditions used, *viz.*, at 1 atm H_2 at 20 °C. Alteration of the experimental conditions can lead to dramatic changes in rate determining step, and thus to the observed turnover frequencies [80]. Considered especially important was the potential presence of mass transfer limitations, which reduce the apparent reaction rate by inhibiting the transport of substrate molecules to the active sites of the catalysts. For catalysts used in a batch reactor and where the majority of the metal nanoparticles are immobilised on the outer surface of the support particles, these issues can be partially alleviated by using a solvent which effectively wets the surface of the catalyst, as has been explored in Chapter 3 of the current thesis. Further studies, though not detailed herein, also focused on determining the sufficient agitation rates, substrate concentrations, *etc*, so that mass transfer was not limited. The turnover frequencies reported for the catalysts with relatively little aggregation are therefore probably not subject to these issues, though the same cannot necessarily be said for those where most of the metal exists in large aggregates whose interior surfaces are difficult to access. This may go some way to explaining the anomalously low activities of the alumina- and silica-supported catalysts described earlier.

5.4 Summary

The work presented in this chapter has conclusively shown that a simple 'one-pot' reduction method using electrostatically stabilised colloids as a metal source is a viable method for producing supported metal catalysts. Characterisation of the samples by electron microscopy showed they contained metal nanoparticles 2 nm to 10 nm in diameter, the distributions of which depended on the material on which they were supported. Some systems contained large aggregates of metal particles, for example those using silica as a support material, while other systems like hydroxyapatite had individual nanoparticles distributed evenly across their surfaces. Analysis by XRD showed the metals were in their metallic forms, and were not significantly oxidised. Solid-state NMR and micro-FTIR spectra showed there were no disturbances to the bulk chemistry of the supports when the nanoparticles were immobilised on their surfaces, though some subtle changes in the surface chemistry of the materials were observed through use of these characterisation techniques.

Almost all of the materials tested showed good activity in the hydrogenation of a range of olefins. The supported palladium catalysts were generally the most active, though they also produced significant double bond migration in the substrates. The specific activities of the catalysts also depended markedly on the choice of the support material, with hydroxyapatite- and microcrystalline cellulose-supported metals generally displaying the greatest activities. Conversely, the alumina- and silica-supported catalysts generally displayed relatively poor activities, though the catalysts prepared from their structural analogues, especially halloysite, performed much better.

The activity of the catalysts was generally around $1x10^4$ hr^{-1} for the hydrogenation of cyclohexene, with the maximum measured TOF of $3x10^4$ hr^{-1} obtained using the Pd/MCC catalyst. The activity of the catalysts for hydrogenation of 1-octene was significantly higher, averaging $3x10^4$ hr^{-1}, with a maximum measured TOF of $6.4x10^4$ hr^{-1} obtained using the Pd/HAp catalyst. The hydrogenation of cyclooctadiene, conversely, was much slower, with an average TOF of $2x10^3$ hr^{-1}, and a maximum TOF measured using the Pd/HNC catalyst of $1x10^4$ hr^{-1}. These activities generally compare favourably to those reported in the literature, with many exhibiting the highest conversion rates ever reported for the substrates studied under the given conditions. The high activity of the catalysts using novel support materials is

especially noteworthy, as not only are they largely untested materials, but in many instances are more active than those using the traditional alumina or silica supports.

5.5 Recommendations for Further Work

The greatest problem with the current catalysts may be considered the inconsistent distribution of metal across the surface of the supports. This was especially evident in the silica supported systems, where the support appeared to display no affinity whatsoever for the metal nanoparticles. This may be due to a repulsive force between two the two, probably electrostatic in nature. This could be prevented either by changing the pH of the reduction medium to a value where the electrical double layers have opposite signs or low charges, or by performing the reductions in an aprotic medium which would completely collapse the double layer. This would additionally have the effect of making the particles smaller [396], and thus more active unit mass. The choice of solvent should be carefully considered to maximise the penetration of the colloids into the pores of the support, for which the data from Chapter 3 may be considered.

A second route of research worth pursuing is additional catalytic reactions, for example alcohol oxidations or carbon-carbon coupling. These are potentially more valuable synthetically, but also offer the advantage of not having to be performed in air-free conditions. Using atmospheric oxygen as an oxidant would also be a 'green' method synthetically.

Additional characterisation methods could also be pursued to gain a greater understanding of the nature of the catalysts. The powder diffraction and NMR data, both essentially bulk analysis methods, suggest that any changes occurring in the catalysts are at the surface, and thus surface-sensitive methods would be of advantage. This data could be obtained simply by altering the configuration of the instruments used; grazing incidence optics for both XRD and FTIR would provide surface-enhanced spectra which may carry more valuable information than the standard configurations used in this study. Methods utilising spectroscopic probes could be of benefit also; for example infrared detection of CO adsorbed on the supported particles or pyridine for detection of the different types of acid sites on the supports, or NMR ^{31}P detection of adsorbed phosphines.

Chapter 6: Catalysts Prepared from Polymer-Stabilised Metal Colloids

6.1 Introduction

Colloidal dispersions of metal nanoparticles are an attractive precursor for the synthesis of supported metal catalysts because of their tuneable properties. Altering the synthetic conditions under which they are produced can affect the particle size, shape, and chemistry [118, 397-401], which can in turn affect the properties of the resulting catalyst. Despite these promises, interest in such synthetic routes has only recently accelerated [402-408], and is currently a topical field of research [409, 410].

One of the problems with using colloidal nanoparticles, as described in Chapter 5, is that they are metastable and have a natural tendency to agglomerate. Adsorption of polymers to the surface of colloidal metal particles protects them against this agglomeration process, imparting them with long-term stability. The most effective polymers are those containing donor moieties, such as ketones or alcohols, since these can bind to the surface of the metal particles. Some common examples of these types of polymers are shown in **Figure 89**.

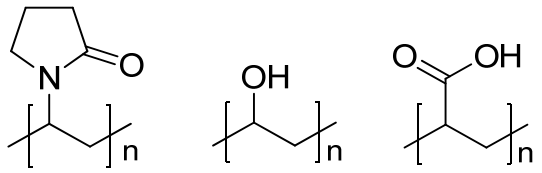

Figure 89: Structures of some polymers commonly used to stabilise colloidal dispersions of platinum-group nanoparticles. Left: poly(vinyl pyrrolidone); centre: poly(vinyl alcohol); right: poly(acrylic acid).

Immobilisation of polymer-stabilised colloidal nanoparticles onto appropriate support materials has been used to prepare supported catalysts in the recent past, especially by Somorjai *et al.* They have extensively investigated the immobilisation of PVP-stabilised Pt colloids onto various types of silica, and have shown the resulting materials to be highly active in a range of reactions, including many hydrogenations. [119, 411-424]. It was considered of interest, therefore, to extend this methodology in the current work, investigating the efficacy of alternate systems using different polymers and metals which have not been investigated hitherto.

Immobilising a polymer-protected nanoparticle on a support material may be envisaged to occur in one of two different ways. Either the polymer chains coating the nanoparticle become adsorbed to the support and so tether the nanoparticle to the support, or the nanoparticle itself binds directly to the support and the polymer plays no role. These two mechanisms are illustrated in **Figure 90**. For support materials like silica which show no intrinsic attraction to nanoparticles as observed in the previous chapter, the nature of the polymer was therefore anticipated to be crucially important, as certain polymers will only bind to certain support materials. PVP for example will bind strongly to silica but not alumina [425, 426], while PVA will adsorb on both [427, 428].

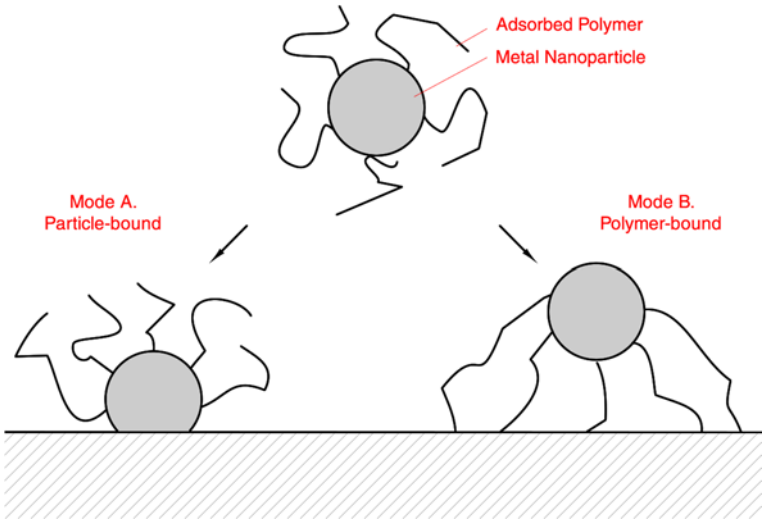

Figure 90: Schematic of two different ways a polymer-protected metal nanoparticle can bind to the surface of a support material.

In the current study, a series of experiments were therefore performed to find the optimum conditions for immobilising polymer-stabilised metal colloids onto appropriate support materials. A series of polymers were trialled for their ability to stabilise rhodium, palladium, and platinum colloids. Their size distributions and aggregation levels were probed by photon correlation spectroscopy (PCS), ultraviolet/visible spectrophotometry (UV/Vis), and transmission electron microscopy (TEM). Different methods were then trialled to immobilise these metal particles onto a range of support materials, in order to generate catalysts with the optimal textural properties. A range of catalysts were then produced and their activities tested in the hydrogenation of cyclohexene. The materials were then characterised by a suite of instrumental methods, including photomicroscopy,

transmission electron microscopy (TEM), laser-induced breakdown spectroscopy (LIBS), x-ray diffraction (XRD), Fourier transform infrared microspectroscopy (μFTIR), solid-state nuclear magnetic resonance spectroscopy (SS-NMR), and x-ray photoelectron spectroscopy (XPS).

6.2 Materials and Methods

6.2.1 Experimental Methods

In the first phase of experimental work, ten polymers were selected and screened for their ability to stabilise colloidal dispersions of rhodium, palladium and platinum nanoparticles. The rationale for this was that in order to prepare a catalyst containing a homogeneous dispersion of metal particles on its surface, the precursor colloid from which it is prepared must be as homogeneous as possible. Since the polymers may affect both the stability of a colloid and its interaction with the surfaces of other materials, it was therefore important to trial many polymers in order to find those most suitable. The polymers selected were:

- PVA: poly(vinyl alcohol), a poly-alcohol;
- PCL: poly(caprolactone), a poly-ketone;
- PVP: poly(vinyl pyrrolidone), a poly-cyclic amide;
- PAM: poly(acrylamide) a poly-amide;
- PEI: poly(ethylenimine), a poly-amine;
- PAA: poly(acrylic acid), a poly-carboxylic acid;
- PAM-co-NaPAA: poly(acrylamide)-co-sodium(polyacrylate), a poly-carboxylate/amide;
- PEG: poly(ethylene glycol), a poly-ether; and,
- MeOPEG: methoxy poly(ethylene glycol), a methoxy-terminated poly-ether.

To assess the stabilising effect of these polymers a variety of metal colloids were prepared in their presence. A scrupulously cleaned beaker was charged with a magnetic stirring flea, metal salt solution (1 mL, 0.03 mol L^{-1}, $RhCl_3$ or K_2PtCl_4 or

Na_2PdCl_4), polymer solution (1 mL, 5% w/v, any of those listed above), and distilled water (48 mL). To this solution $NaBH_4$ (2 mL, 0.03 mol L^{-1}) was added dropwise with rapid stirring. In the case of the colloids using PCL as the protective polymer, the distilled water was replaced with a 1:1 mixture of dichloromethane and methanol to facilitate dissolution. After stirring for 1 hour, *ca.* 1 g of ion-exchange resin was added to remove salt from the colloids, after a further hour they were filtered and stored for 12 hours, followed by instrumental analysis by PCS, UV/Vis and TEM.

A set of additional experiments were then performed to determine the minimum amount of polymer required to stabilise the precursor colloids while still remaining stable. The rationale for this was that the less polymer was incorporated into the catalyst the less time they would have to be calcined to remove the capping layer, and the fewer the potential negative effects from this process would be incurred. For this set of experiments a series of colloids were prepared with each of the chosen polymers present at different concentrations. Beakers were charged with a magnetic stirring flea and metal salt solution (1 mL, 0.03 mol L^{-1}), as well as a volume of polymer solution (5 wv%) of either 1000 μL, 500 μL, 250 μL, 125 μL, or 60 μL. The samples were then analysed in the same way as the colloids described previously.

Once it was determined which polymers were capable of most effectively stabilising colloidal suspensions of the chosen metals, initial trials were conducted to determine the optimal method by which they could be immobilised on the selected support materials. Four sets of colloids were created as the source material for the experiments. To each of 12 1 L beakers was added 12 mL of 0.03 mol L^{-1} metal salt solution, 12 mL of 5 wv% polymer solution and 552 mL of Type I water. 24 mL of 0.03 mol L^{-1} $NaBH_4$ was then added dropwise to each with stirring to reduce the precursors to metallic nanoparticles. Three different immobilisation methods were then investigated: adsorption from solution, precipitation, and solvent evaporation. The details of each of these three methods are given in the following paragraphs.

The adsorption method involved adding 0.30 g of support material (SiO_2, Al_2O_3, HAp or MCC) to 4 of 16 50 mL flasks along with 50 mL of one of the precursor colloids (using PVP, PVA, PAA or PAM as protecting agents) such that all 16 combinations of the four polymers and four model support materials were created. The flasks were covered with Parafilm and placed in an oscillating laboratory shaker for 120 hours at 20 °C, after which point the unadsorbed colloid was decanted and

the flask and its contents dried in air at 100 °C for 24 hours. The contents of each sample were then split in half, one portion being calcined in ceramic crucibles for 3 hours at 500 °C to remove the capping polymer layer [429]. The resulting materials were characterised by TEM, XRD, and SS-NMR.

The precipitation technique involved precipitating the colloidal matter from solution using acetone, since this is an anti-solvent for many of the polymers tested. 250 mL beakers were charged with 0.3 g of support material and 50 mL of colloid. 100 mL of acetone was added dropwise from a dripping funnel while stirring, causing the polymer and any bound nanoparticles to be precipitated, thereby encapsulating the suspended support material particles. The resulting materials were gravity-filtered through Whatman Type-1 filter paper and air-dried at 100 °C for 24 hours. As with the previous technique the samples were halved, calcined, and analysed by the same instrumental methods described previously.

The evaporation technique used rotary evaporation to remove the water from the colloids in the presence of the four support materials. 250 mL round-bottom flasks were charged with 0.3 g of support material and 50 mL of colloid, and then evaporated at 80°C under vacuum using a water aspirator. Once all water was removed, the flasks were put in a laboratory oven at 100 °C for 24 hours, and the contents were divided, calcined, and analysed as with the previous techniques.

Once the best polymers were selected, the minimum polymer concentration determined, and the optimal immobilisation method selected, a full suite of 54 catalysts were produced (3 metals x 3 polymers x 6 support materials[1]). The cellulose-based support materials were not used for the preparation of this final batch of catalysts, as the calcination step used caused them to ash and turn to gas. As with the previous chapter their properties were probed instrumentally using a combination of photomicroscopy, scanning electron microscopy (SEM), transmission electron microscopy (TEM), x-ray powder diffraction (XRD), solid-state nuclear magnetic resonance spectroscopy (SS-NMR), infrared microspectroscopy (μFTIR), and x-ray photoelectron spectroscopy (XPS). All samples were analysed pre- and post-calcination to determine the effects of this process. The activities of the resulting

[1] The cellulose-based support materials were not used for this final batch of catalysts, as the calcination step caused them to ash and volatilise as, presumably, CO_2.

catalysts were then tested using cyclohexene hydrogenation as a probe reaction to measure their relative activities.

6.2.2 Instrumental Methods

The state of aggregation in the precursor colloids was probed *in-situ* using Photon Correlation Spectroscopy (PCS), which gives a direct measurement of the hydrodynamic radius of the particles. Measurements were carried out using a Malvern Zetasizer 3000HS_A, using a 535 nm He-Ne laser. Samples were analysed in disposable polystyrene fluorescence cuvettes in triplicate with ten sub-runs per replicate. Correlation data was analysed using the CONTIN algorithm with size boundaries of 0 nm to 10000 nm, quartic weighting and a dilation of 1.20. The refractive index and viscosity of the dispersion medium were assumed to be equal to that of pure water.

The turbidity of the precursor colloids was also measured by Ultraviolet/Visible spectrophotometry (UV/Vis), which yields complimentary data to PCS [396]. Measurements were performed using a VARIAN Cary 100 Scan UV/Vis spectrophotometer using Cary WinUV Scan software, version 3.10(182), operated in double-beam mode. Matched quartz cuvettes were used in all measurements, with the reference cell filled with an aqueous polymer solution. The colloids were diluted until their absorbance at 450 nm was below unity, and the resulting value multiplied by the dilution factor to obtain the A_{450} value of the original, undiluted, colloid.

The colloids were also imaged *ex-situ* using Transmission Electron Microscopy (TEM) to obtain information about the particle size distribution of the primary particles and their aggregates. Transmission electron micrographs were all collected using a Philips CM30 operating at 250 kV using a LaB_6 filament. Measurements were calibrated against a bovine catalase standard. Samples were prepared by placing a drop of each colloid onto a carbon/formvar-coated 400 mesh Cu grid and drying in air for 24 hours. For each sample the contents of the grid were surveyed at low magnification, and then a random selection of 300 particles subjected to particle size measurements. From this data the average and standard deviation in the size distribution were calculated. For solid catalyst materials prepared from these colloids, samples were prepared in the same way as described in Chapter 5.

When the colloids were doped onto the support materials to generate supported catalysts, the distribution of polymer was probed by photomicroscopy. Analyses were performed with two different optical microscopes. As a preliminary survey, catalysts were analysed with an Olympus SZ-6045 with a variable 1.0X-6.3X objective lens and 10X eyepieces. Samples were sprinkled directly onto a petri dish and illuminated from underneath, with the resulting bright field images collected using a standard Sony digital camera. As a secondary method the samples were analysed with a Leica microscope with a variable 2-10X objective lens and 10X eyepieces. Samples were sprinkled onto glass slides, and illuminated with a combination of transmitted and oblique lighting, varied per sample to illustrate different features. Micrographs were collected using a digital camera. At higher magnifications evidence of chromatic aberration was evident, so a blue filter was placed in the beam path to filter the transmitted light.

To probe the chemical structure of the catalyst materials, solid-state NMR was used, notably ^{1}H, to investigate the interactions between the polymer and support. Because silica and alumina only have protons at their surface present as hydroxyls, the technique is essentially surface-sensitive for these nuclei. The rationale was that if there is some type of bond formed between the polymer and the surface of the support this might manifest in the appearance, disappearance, or shifting of the proton peaks. All spectra were recorded using a Bruker Avance II 300 MHz NMR with a 4 mm MAS probe as described in Chapter 5.

Samples were additionally analysed by Infrared Microspectroscopy to detect bulk changes to the materials, as well as possible interactions between the support and the polymers used. For example it has been shown that there is a shift in the stretching frequency of the carbonyl group in PVP when it is acting as a hydrogen-bond acceptor [430]. Analyses were performed with a PerkinElmer Spectrum Spotlight 200 FT-IR microscope. Samples were prepared by sprinkling onto a polished stainless steel slide and lightly compressing to produce a flat surface for analysis. A background spectrum collected from a polished gold mirror was subtracted automatically by the software. Sample spectra were collected from three random regions in each sample to assess homogeneity (2 cm^{-1} resolution, spectral range 4000 cm^{-1} to 500 cm^{-1}, 10 acquisitions each), then a final 'high resolution' spectrum (500

scans) was collected for subsequent analysis. Savitsky-Golay smooths were applied to all spectra, ensuring no significant loss of spectral information.

X-ray powder diffraction was also performed on various samples, in two different geometries. Samples prepared in small quantities (*i.e.* the initial immobilisation method trial samples) were analysed in transmission mode using a SAXS stage, referred to herein as WAXS patterns. Samples prepared in larger quantities (*i.e.* the final catalysts) were analysed in the traditional reflection mode. WAXS patterns were recorded using a PANalytical Empyrean diffractometer equipped with the open-air SAXS stage using Ni-filtered Cu Kα radiation. Incident optics included 0.04 rad soller slits, a fixed 1/8° divergence slit, a 1/8° anti-scatter slit, and a 20 mm mask. Slits on the stage were fixed in wide open positions. Diffracted optics included 0.04 rad soller slits, a 7.5 mm receiving slit, and a PIXcel3D detector operated in scanning mode. Patterns were recorded over the range $5° < 2\theta < 60°$ in 2θ geometry with a step size of 0.02° and time per step of 1000 s. The details of the collection of the regular reflection patterns are given in Chapter 5.

X-ray photoelectron spectra of selected samples were collected in order to determine details of the chemistry of the supported metal particles, specifically their oxidation states and the effects of calcination. All spectra were recorded at the University of Auckland's Department of Engineering with a Kratos AXIS Ultra DLD using a monochromated Al Kα source. Samples were pressed into pellets for shipping, and subsequently broken apart to expose fresh surfaces for analysis. Samples were mounted as powders on indium coils and analysed using a 700 μm spot. Charge neutralisation was performed using an electron flood gun on all samples. Data was processed using CasaXPS version 2.3.17. Spectral referencing was performed relative to the 284.8 eV peak corresponding to the C 1s core level of adventitious carbon, or Ca 2p core level peaks. For peak fitting of the core level spectra Shirley baselines were subtracted unless otherwise stated. All peaks were fitted with Voight profiles, with the Gaussian to Lorentzian ratio varied to obtain the best fit. Spectra displaying spin-orbit coupling were fitted with doublets constrained with respect to their relative areas, widths, and splitting energy, with the exception of the Rh 3d spectra whose areas were not constrained due to the presence of a Coster-Kronig transition [431]. These constraints are given in **Table 20**. Generally speaking,

peak models were made as simple as possible within the listed constraints, but sufficiently complex to accurately fit the data and provide structureless residuals.

Table 20: Restraints used for curve-fitting and deconvoluting XPS spectra.

Parameter	Element				
	Rh 3d	**Pd 3d**	**Pt 4f**	**Ca 2p**	**C 1s**
Position [eV]	nil	nil	nil	nil	284.8
Area	nil	2:3	3:4	1:2	nil
Splitting [eV]	4.75	5.25	3.35	3.50	nil
Width [eV]	<2.0	<2.0	<2.0	<2.0	N/A

To determine the amount of metal in the supported catalysts, laser induced breakdown spectroscopy was used. All analyses were performed with a Photon Machines Spectrolaser 4000, using the method developed in Chapter 4.

All hydrogenations were performed as stated in Chapter 5, but a different gas chromatography (GC) system was used for their analysis. These were performed on an Agilent 7890A system equipped with an HP-5 column and coupled to a 5975C mass-selective detector (MSD). Injections of 1 μl were made using a 7683B autosampler into a 150 °C inlet and split 1:50 into the column at 0.4 mL/min. The oven temperature was set initially at 50 °C, ramped at 2.5 °C/min to 60 °C totalling a 4 minute programme. The MSD was set to scan from 2-4 minutes over the range $30 < m/z < 120$ at a rate of 12.37 Hz. Samples were prepared as per the previous chapter and injected in triplicate. The instrument was controlled with Agilent ChemStation E.02.02.1431 software. The peak areas of the cyclohexene and cyclohexane peaks were integrated manually, and conversion calculated by measuring the ratio between the two peaks after accounting for their relative responses. The conversion rate was calculated from the slope of the concentration as a function of time, and the error in the slope obtained from the standard deviation in the residuals of the linear regression, quoted as $\pm 2\sigma$.

6.2.3 Materials

Metal Salts: Rhodium trichloride trihydrate and potassium tetrachloroplatinate(II) were obtained from PMO ("Precious Metals Online") based

in Monash University, Australia. Palladium(II) chloride (99%) was obtained from Sigma.

Solvents: All water used in the preparation of the current sample was Type I. Methanol (>99.8%), dichloromethane (>99.0%), and n-heptane (>99.0%) were obtained from Merck.

Hydrogenation Substrates: Cyclohexene (>99%, synthesis grade) was obtained from AppliChem. 1-octene (>99%, for synthesis) was obtained from Merck. 1,5-cyclooctadiene (99%) was obtained from Sigma Aldrich.

Polymers: Polyacrylamide (M_W >5,000,000), polyvinyl pyrrolidone (M_W ~700,000), polyethylene glycol 4000 (M_W 3300-4000), and polyvinyl alcohol (M_W ~22,000) were obtained from BDH Chemicals Ltd. Polyacrylic acid (M_W ~1,800), polycaprolactone (Mw ~14,000), polyethylenimine (M_W ~250,000), and methoxypolyethylene glycol (Mw ~2,000) were obtained from Aldrich chemicals. Polyacrylamide-acrylic acid-sodium salt ("high carboxyl", M_W ~200,000) was obtained from PolySciences, Inc.

Miscellaneous Reagents: NaCl (99.8%) was obtained from BDH. $NaBH_4$ (99%) was obtained from Ajax.

6.3 Results and Discussion

6.3.1 Polymer Trials

6.3.1.1 General Comments

Addition of the sodium borohydride solution to the metal salt solutions caused them to darken from yellow or orange to black or brown, signifying their reduction to metallic nanoparticles. In the absence of a protective polymer this process was instantaneous, but when a polymer was introduced prior to reduction the process was somewhat slower. Once stirring was ceased, it was apparent even from visual observation that the ten different polymers all had different protective abilities, relative to one another and to the colloids prepared without polymer. Those prepared in the presence of some polymers (PVP, PVA, PAM, PAA, ARG and PAM-co-NaPAA) remained optically homogeneous and colloidally stable for an extended

period of time, while those prepared in the presence of the other polymers (PEG, MeOPEG, PCL and PEI) aggregated and settled out of suspension within minutes.

When the four most stable colloids (those using PVP, PVA, PAM, or PAA) were re-prepared with variable polymer concentrations, similar effects were observed as in the previous experiment. Obvious differences could be seen in the colours of the colloids, suggesting that not only were some polymers better protecting agents for some metals than others, but also that the concentration was an important experimental factor. This assumes, however, that the precursor metal salts are completely reduced, and that the level of reduction is equivalent across the range of systems. The measurements collected from these colloids are described in the following sections.

6.3.1.2 Transmission Electron Microscopy

Analysis of the colloids by electron microscopy showed that those prepared in the presence of a protective polymer had significantly different morphological properties to those prepared in the absence of a polymer. This manifested in the size of the primary particles, their morphologies, and their states of aggregation. Particle size measurements from these micrographs are given in **Table 21**, and example micrographs are shown in **Figure 91**.

In the absence of a polymer the platinum colloids showed very little aggregation. The primary particles had an average size of 6.17 nm, though their morphologies, shown in **Figure 91**a, suggested they were composed of smaller particles which had become fused together. The use of a protective polymer dramatically reduced the particle size in all cases, with the maximum observed average particle size of 4.86 nm observed in the Pt/PAA colloids. For several of these systems the particle size was shown to independent of polymer concentration, for example the Pt/PVP systems, while for others there was a strong dependence, for example in the Pt/PAA systems. The morphological properties of the particles were also impacted by the presence of a protective polymer, though they did not depend strongly on which polymer was used.

The rhodium colloids prepared in the absence of a protective polymer were shown to be highly aggregated, reflecting their rapid aggregation and sedimentation rates during their synthesis. Most particles existed in large clusters up to 100 μm in

size, with very few existing as discrete individual particles. Where individual particles could be discerned at the edges of these large aggregates they were generally spherical in shape, and had an average particle size of 6.17 nm. When prepared in the presence of a protective polymer the size of the aggregates was drastically reduced, once again reflective of their increased stability in colloidal dispersion. The particle sizes also showed a dramatic decrease, with a maximum average particle size of 4.15 nm in the Rh/ARG system, and a minimum average particle size of 2.21 nm in the Rh/PAA system. Some of these systems also showed a concentration dependence on the particle size, for example the Rh/ARG system, while others were insensitive to it, such as the Rh/PVA system. The same general morphological properties were observed as with the Pt colloids.

Table 21: Average particle sizes for polymer-protected metal colloids as a function of polymer volume as measured by transmission electron microscopy.

System		**Average particle size [nm]**					
Polymer	**Metal**	Polymer solution volume, v [mL]					
		1.000	0.500	0.250	0.125	0.060	0.000
PVP	Rh	2.9	2.7	2.9	3.1	3.4	6.2
	Pd	-	3.4	2.8	3.3	3.6	4.1
	Pt	3.0	3.1	3.1	3.3	3.1	6.2
PVA	Rh	2.9	2.8	2.5	2.5	2.3	-
	Pd	2.5	2.6	2.5	2.5	2.2	-
	Pt	3.1	2.7	2.6	2.9	2.9	-
PAA	Rh	2.2	2.0	2.2	2.3	2.4	-
	Pd	3.0	3.2	3.8	4.2	4.9	-
	Pt	3.5	3.7	3.8	4.2	4.9	-
ARG	Rh	2.8	2.9	3.3	3.6	4.2	-
	Pd	2.7	2.9	2.9	3.5	4.4	-
	Pt	2.5	2.5	2.5	2.9	2.5	-
PAM	Rh	2.4	2.3	2.7	2.7	2.3	-
	Pd	-	-	-	-	-	-
	Pt	2.2	2.7	3.2	3.8	3.1	-

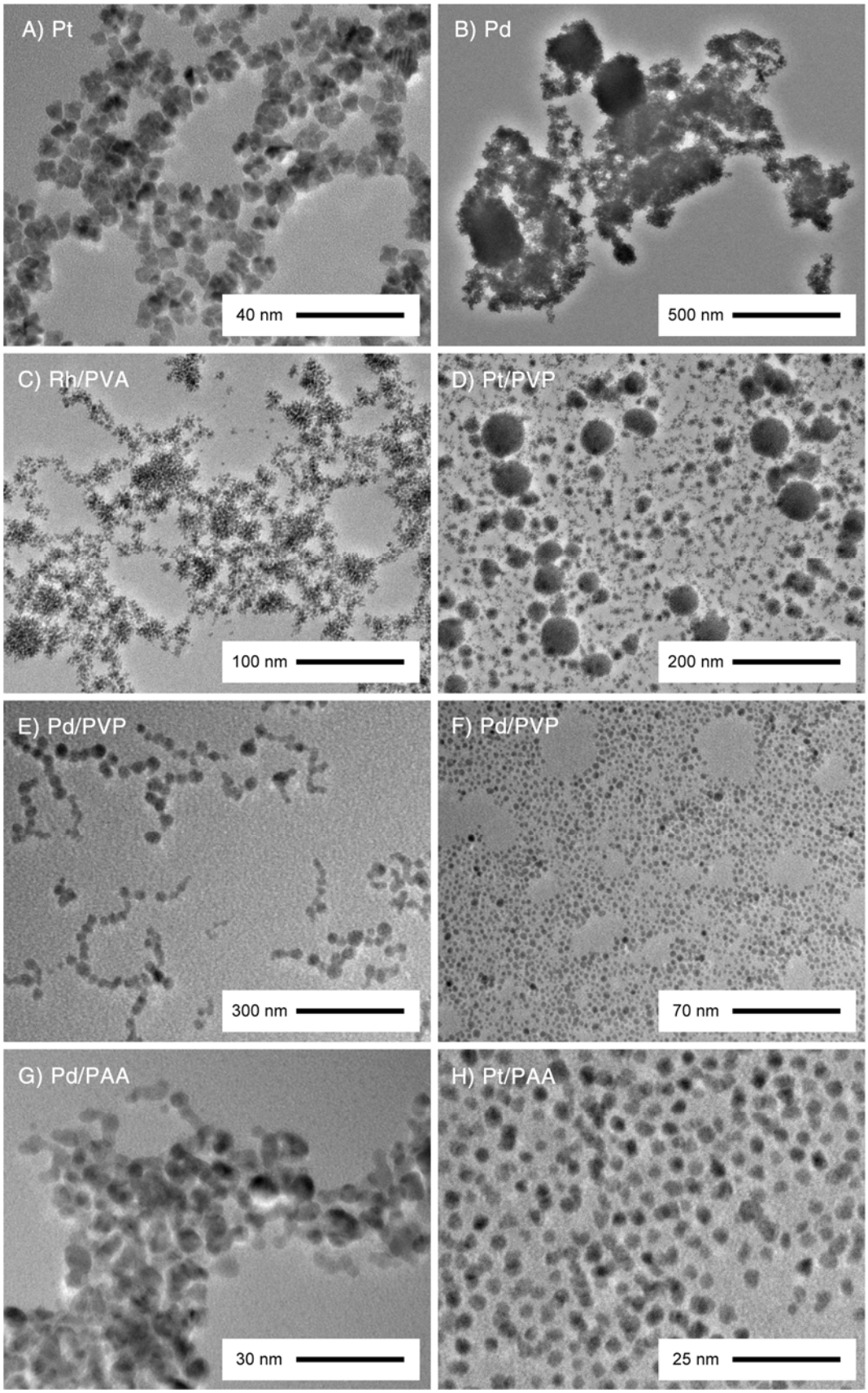

Figure 91: TEM micrographs of some polymer-protected colloids. Without polymer the particles aggregate, as in A and B, while varying levels of stabilisation are achieved with when a polymer is used, as in C-H. Samples E and F show the effect of varying the polymer concentration.

The palladium colloids displayed similar, though slightly different, behaviour to the rhodium or platinum systems. Like the unprotected rhodium colloid, the particles were found almost exclusively in large aggregates as shown in **Figure 91b**. Where individual particles could be discerned at their edges they were found to be spherical, with an average particle size of 4.09 nm. Comparatively, the maximum average particle size observed in the polymer-protected palladium colloids was 4.93 nm in the Pd/PAA system, representing an increase in particle size over the unprotected colloid.

Generalising across all systems studied, it may be said that the use of a protective polymer therefore had several effects on particle size and morphology. Firstly, it dramatically reduced the size of the aggregates present in the Rh and Pd particles, This is presumably the cause of the observed stabilising effects of the colloids, since the sedimentation rate is proportional to the particle size, as described by the Mason-Weaver equation [432]. Conversely, it had no effect on the degree of aggregation in the platinum colloids.

Secondly, the sizes of the particles were inversely proportional to the amount of polymer used, though this effect was significant in some systems and not in other. A similar effect was observed by Teranishi and Miyake, who grew PVP-protected Pd nanoparticles in aqueous alcohols and found the particle size to drop as the PVP concentration was increased [399]. This was presumably a result of the polymers modifying the growth of the particles in solution by affecting the reduction rate, as suggested by Hirai, Chawanya, and Naoki [433]

Thirdly, the morphology of the particles was dramatically impacted by the polymer. At low concentrations the particles were fused together, while at moderate concentrations they were approximately spherical, and at high concentrations they were tethered together into strings of small aggregates. This morphological dependence is illustrated schematically in **Figure 92**. Multiple mechanisms may be operating to give these morphological changes; at low polymer concentrations the poorly-protected nascent nanoparticles may aggregate with one another, leading to the fused morphologies as observed by TEM. At high concentrations, there may be too much polymer present in solution, leading to enhanced aggregation rates *via* depletion mechanisms [434]. Conversely, at moderate polymer concentrations a

'*goldilocks zone*' may be obtained where the ratio of polymer to nanoparticles is sufficient to stabilise the suspension, and not induce additional aggregation.

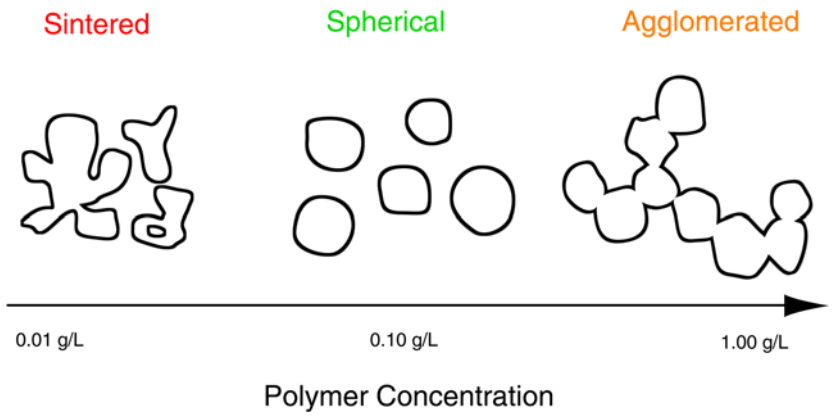

Figure 92: Schematic of the morphological properties of metal nanoparticles as a function of polymer concentration.

6.3.1.3 Spectrophotometric Turbidity Measurements

The UV/vis measurements of the colloids showed their A_{450} values varied significantly depending on the protective polymer used. The greatest value observed was 2.81 for the Pt/ARG colloid, while the lowest value observed was 0.000 for the unprotected Rh and Pd colloids. The full list of values is given in **Table 22**.

Interpretation of these values can be made in terms of the level of aggregation in the colloids. Metal nanoparticles have been shown to scatter light with an intensity directly proportional to their diameters [435, 436], and therefore aggregation of an ensemble of particles at constant concentration should produce an increase in the turbidity, and therefore the absorbance, of the medium in which they are suspended. Counterintuitively, however, a low turbidity does not *necessarily* mean a low level of aggregation; low turbidities can exist *either* because there is a low level of aggregation, *or* because the level of aggregation is so high that the incident beam can pass through the suspension unimpeded. In the majority of cases it is obvious which of these situations is correct though, as very large aggregates are visible to the naked eye.

Using this interpretive framework, a number of conclusions can be drawn regarding the effectiveness of the five polymers tested as stabilising agents. Firstly, the Pd and Rh colloids prepared in the presence of a protective polymer were all more stable than their unprotected counterparts. While the unprotected colloids aggregated rapidly and settled out of suspension, their polymer-protected

Table 22: A_{450} values (turbidities) for some polymer-protected metal colloids as a function of polymer concentration. Errors, though not reported here, are ± 5.4% with a certainty of 1σ. Dashed entries are duplicate systems not measured.

Polymer	Metal	Polymer solution volume, v [mL]					
		1.000	0.500	0.250	0.125	0.060	0.000
PVP	Rh	2.064	1.890	1.941	1.808	1.928	0.000
	Pd	1.223	1.289	1.364	1.431	1.346	0.000
	Pt	1.796	1.722	1.821	1.863	1.871	1.752
PVA	Rh	1.490	1.307	1.560	1.695	1.340	-
	Pd	1.349	1.494	1.365	1.345	1.313	-
	Pt	1.030	1.103	0.913	1.252	1.119	-
PAA	Rh	0.264	0.355	0.751	0.780	0.799	-
	Pd	1.416	1.552	1.799	1.526	1.921	-
	Pt	0.666	0.776	0.988	1.597	1.584	-
ARG	Rh	2.022	2.169	2.281	2.328	2.401	-
	Pd	1.567	1.596	1.627	1.639	1.714	-
	Pt	2.813	2.014	1.955	1.733	1.597	-
PAM	Rh	1.806	2.043	1.953	1.602	0.242	-
	Pd	0.102	0.100	0.100	0.115	0.113	-
	Pt	1.152	0.806	0.720	0.892	1.121	-

counterparts were colloidally stable and dark brown to black in colour. This is evident in the A_{450} values, which were 0.000 for the unprotected colloids, but ranged from 2.401 for one of the Rh/ARG colloids to 0.100 for the Pd/PAM colloids. The Pt colloids, conversely, were generally completely insensitive to the choice of polymer used, exhibiting A_{450} values of around 1.75 regardless of whether a polymer was present or not. This suggests that presence of a purportedly protective polymer confers no extra stability to the Pt colloids over the naturally-occurring electrostatic stabilisation mechanism.

Secondly, the polymer concentration was shown to significantly affect the turbidity of some systems. In many systems the A_{450} values were inversely proportional to the polymer concentration, for example the Rh/PAA system where a three-fold difference in the turbidities was observed. Some systems however, notably those including Pt, were insensitive to the polymer concentration, probably for the reasons described in the preceding paragraph. These results generally suggest that the

stability of a colloid is proportional to the amount of protective polymer used, given the caveats of the framework described earlier. To corroborate these results, photon correlation spectroscopy was performed, described in the following section.

6.3.1.4 Photon Correlation Spectroscopy

The photon correlation spectroscopy results generally supported those made by UV/vis, elucidating the same trends in stability with respect to polymer concentration. Using the z-average as a metric to assess the state of aggregation, it becomes clear that there are some systems which are very sensitive to the amount of polymer used, while there are others upon which this variable has almost no effect. The data is given in **Table 23**.

For the polymer-protected rhodium colloids the smallest average particle sizes were observed in the Rh/ARG system, ranging from 81 nm to 125 nm depending

Table 23: Z-averages [nm] of selected polymer-protected metal colloids as a function of polymer concentration.

Polymer	Metal	Z-averages [nm]					
		Polymer solution volume, v [mL]					
		1.000	0.500	0.250	0.125	0.060	0.000
PVP	Rh	-	-	-	-	-	-
	Pd	272	253	246	243	246	-
	Pt	289	262	266	266	262	-
PVA	Rh	314	332	289	328	527	
	Pd	-	-	-	-	-	
	Pt	258	254	270	263	263	
PAA	Rh	1210	1690	1090	1020	949	
	Pd	942	781	195	170	146	
	Pt	603	845	133	45.0	113	
ARG	Rh	81.0	96.0	86.0	103	125	
	Pd	392	861	225	149	126	
	Pt	-	-	-	-	-	
PAM	Rh	269	292	310	456	522	-
	Pd	-	-	-	-	-	
	Pt	496	456	779	214	182	

inversely on the concentration. All other polymers displayed the same trend but exhibited greater particle sizes, with the exception of the Rh/PAA system, where the particle size peaked at intermediate polymer concentrations. For the polymer-protected palladium colloids the smallest average particle size was observed in the Rh/PVP system, ranging from 272 nm to 246 nm, once again depending inversely on the PVP concentration. Both the Rh/ARG and Rh/PAA systems showed increasing stability with decreasing polymer concentration, however. The platinum colloids were insensitive to PVP or PVA concentration, but showed particle size maxima with PAA and PAM at 25 mg and 12 mg of polymer respectively.

On the surface these results seem somewhat contradictory, as different systems appear to respond differently, even oppositely, to changes in polymer concentration. All can be explained however by the notion that the stability of the colloids does not depend linearly on the polymer concentration, but rather follows a bell-curve type profile. In this case there would exist an optimal polymer concentration within these systems where the stability is greatest, with decreases at either higher or lower polymer concentration, caused by either a lack of protective polymer, or depletion flocculation from too much polymer, as described in the preceding TEM section.

For polymers where the optimal concentration range is higher than the experimentally studied range, the measured particle size would thus appear to increase with decreasing polymer concentration. Conversely, for polymers where the optimal concentration range is lower than the experimentally studied range, the particle size would appear to decrease with decreasing polymer concentration, as in the Pt/PAA system. If the optimal concentration range is broad then the particle size would be insensitive, as observed in the Pd/PVP system, while if the optimal concentration range is narrow and falls within the experimentally studied range then a minimum particle size would be observed, as with the Rh/PVA system.

6.3.2 Immobilisation Methods

6.3.2.1 General Observations

Mixed degrees of success were achieved with the three immobilisation methods trialled. While each method produced materials which clearly contained metal nanoparticles, the intimacy with which they were associated with the surface of the

support varied significantly. This was reflected in their appearances, representative photos of which are shown in **Figure 93**.

The rotary evaporation technique was shown to be a versatile method for catalyst synthesis, producing powders of moderate homogeneity regardless of the combination of polymer and support. The major problem with the technique was that often a significant portion of the colloidal material became immobilised on the inside walls of the flask rather than on the support material, or that the polymer would 'glue' the support particles to the walls of the flask making them difficult to remove. When the materials were dried they could be scraped free, but the resulting grey powders were intermixed with flexible dark black flakes, as shown in **Figure 93a**, which were later shown to be thin flakes of polymer containing high concentration of nanoparticles. When the materials were calcined the flakes were destroyed, and the materials generally lost the toughness imparted by the presence of the polymers.

The acetone precipitation method worked effectively for only three of the four polymers, with PAA unable to be precipitated by acetone. The remaining three polymers, PVP, PVA, and PAM, progressively precipitated during the acetone addition over a period of *ca.* 50 mL. This process removed all suspended matter from

Figure 93: Photographs of four catalysts materials prepared by three different immobilisation methods. The four pictures correspond to: a) Rh-PVA/HAp prepared by rotary evaporation, b) Rh-PVA/MCC prepared by acetone precipitation, c) Rh-PVA/Al_2O_3 prepared by adsorption, and d) Rh-PVP/Al_2O_3 prepared by adsorption.

the solutions, including the nanoparticles and the powdered support materials, producing a nebulous composite material composed of all three. Unlike the rotary evaporation method none of the material adhered strongly to the walls of the vessel, so the material could be recovered quantitatively by simple filtration. Drying the materials produced a series of dark and fluffy powders, shown in **Figure 93b**, the calcination of which brought about a significant reduction in their volumes and their colour.

The adsorption method was shown to be effective for selected systems, but impractical for others. Colloids protected by all four of the polymers adsorbed spontaneously and quantitatively to the HAp powders within a few hours, as assessed by the complete lack of any suspended matter evident in the supernatants after this period. Adsorption to the MCC powders also occurred spontaneously, but took significantly longer and did not occur to the same extent. Adsorption to SiO_2 and Al_2O_3 could not be clearly detected by changes in the supernatant colours, suggesting their adsorption capacities are lower than the other two supports tested under the same conditions. When the powders were filtered, however, all were varying shades of grey, suggesting that some amount of adsorption occurred in all cases. This is illustrated in **Figure 93c** and **d**, where the Rh-PVA/Al_2O_3 system is significantly darker than the Rh-PVP/Al_2O_3 system, suggesting a greater degree of adsorption in these systems.

All three of the methods trialled represent situations in which a range of different adsorption methods may be in operation. In the acetone-precipitation method the interaction between the colloid and the support is presumably predominantly mechanical, in that the support particles are simply ensconced in a polymer matrix. Conversely, the adsorption method relies solely on physisorption (or chemisorption) of the colloids to the supports, and no external 'force' is applied to induce this interaction. The rotary evaporation method represents an intermediate case where both mechanical and sorptive mechanisms can operate, since the powdered support material is heated for an hour with the colloid before the solvent is completely removed and the colloid precipitated onto the surface of the support.

The rapid and total adsorption of all four colloids to HAp is particularly interesting, since it has been shown that while PAA [437-439] and PAM [440] are adsorbed strongly on HAp surfaces, PVP is not [441, 442]. Given that unprotected

nanoparticles are shown to adsorb spontaneously on HAp surfaces in the previous chapter, this suggests that the immobilisation of the current polymer-protected nanoparticles onto the HAp surfaces may arise due to a NP-HAp interaction in addition to a possible polymer-HAp interaction, as hypothesised in the introduction to the current chapter.

Similarly, the adsorption of unprotected nanoparticles to MCC surfaces has been shown in the previous chapter to spontaneously produce materials with a metal loadings of at least 1.0 wt%, while in the current study the degree of adsorption is significantly less. The adsorption of PVP and PVA on cellulose surfaces has been shown to be sensitive to the type of cellulose used [443], with some types of cellulose having a high affinity for these polymers and other types very little affinity. The observation that the adsorbed fraction of metal is less when using polymer-protected colloids than naked colloids suggests that the polymer actually *inhibits* adsorption, even though the colloids are more stable and have a lower degree of agglomeration.

The adsorption of the four colloids to silica is also an interesting set of phenomena, since the adsorption of unprotected metal colloids did not occur to any significant proportion. Conversely, adsorption of PVA-protected colloids produced a dark black powder, while adsorption of PAA-protected colloids produced a dark grey powder, and adsorption of PAM or PVP-protected colloids produced light grey powders. The colours of these materials suggests that since they are not white, as the pristine support material is, the presence of the polymers *enhanced* adsorption in these systems. All four of the polymers are known to interact with silica surfaces to varying extents; PVA is shown to bind significantly to surface silanols and siloxane bridges [428], while the binding of PVP is significantly affected by the surface chemistry [426, 444], but can occur *via* hydrogen bonding between the surface silanols and the ketone moiety [445, 446]. Binding of PAM also occurs through silanols [447] but depends significantly on the electrolyte content of the dispersion medium [448-450], while binding of PAA also occurs, though to a lesser extent, and depends strongly on pH [451]. It could be the case, therefore, that the immobilisation of polymer-protected colloids on silica surfaces is facilitated by an interaction between the polymer and the silica, though it may also be possible that the polymers modify the

surface properties of the nanoparticles, for example their charge, making them more amenable to adsorption.

The adsorption of polymers to the alumina surface is also interesting. The adsorption of PAA-protected colloids produced black powders, PVA-protected colloids produced dark grey powders, PAM-protected colloids produce light grey powders, and PVP-protected colloids produce white powders with no obvious darkening at all. This suggests that the adsorption of the polymers *is* significant, with the exception of PVP, though probably does not occur through hydrogen bonding with surface hydroxyls as with silica. These observations generally support previously reported studies on polymer adsorption, which have shown that adsorption of PAA on alumina is strong while PVP is weak [452-454], while the adsorption of PAM and PVA are of lower affinity [427, 455]. Though some adsorption of unprotected metal particles occurs on the alumina surfaces, the adsorption is clearly *enhanced* by the presence of these polymers.

6.3.2.2 Transmission Electron Microscopy

Qualitative analysis of transmission electron micrographs of the samples showed there were substantial differences between the three preparative methods, both in terms of the sizes of the supported metal particles, and the homogeneity of their distribution across the surfaces of the support materials. Some example micrographs are shown in **Figure 94**. Generally speaking, the samples prepared by the adsorption method tended to have small nanoparticles dispersed evenly across all surfaces of the support materials, but with a relatively low loading. The samples prepared by acetone precipitation, on the other hand, appeared to have moderate loadings, but the particles were unevenly dispersed across the surface of the supports, many had become sintered together and grown during the calcination process, and many were in the form of large aggregates. The samples prepared by rotary evaporation showed properties intermediate of these two, with moderate loadings, moderate particle sizes, and only some small aggregates present. These characteristics are summarised in **Table 24**. It was also shown by analysis of the precursor colloids prior to immobilisation that their properties *in situ* were preserved on immobilisation to the support materials, so the colloids which had aggregated in colloidal suspension remained aggregated when immobilised on a support material, while colloids which had little to no aggregation in colloidal suspension produced catalysts with little to no

aggregates assuming that a preparative method was used which did not *induce* aggregation.

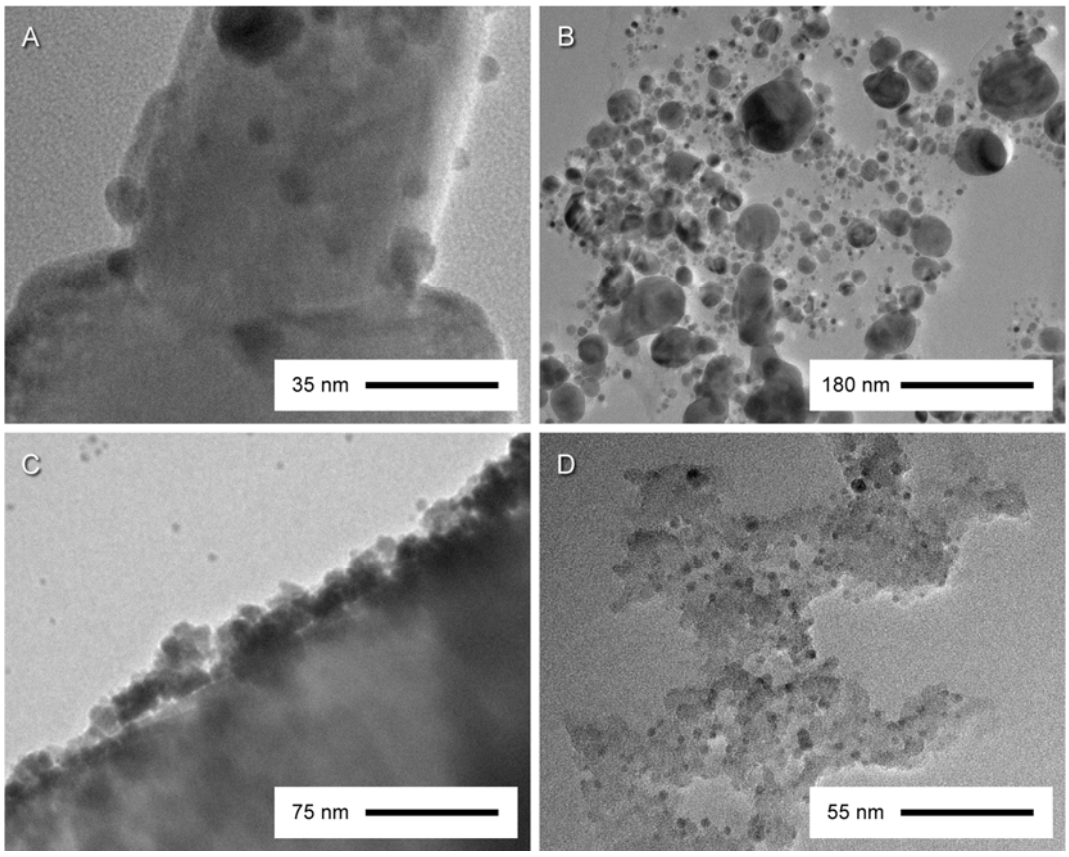

Figure 94: TEM micrographs of various catalysts prepared using polymer-protected colloids, illustrating the manifestly different properties evident between different synthesis conditions. Samples are a) PVP-Rh/HAp prepared by adsorption, b) PVP-Rh/MCC prepared by rotary evaporation, c) PVA-Rh/Al_2O_3 prepared by acetone precipitation, and d) PVP-Rh/SiO_2 prepared by adsorption. All micrographs are of samples after calcination at 500 °C in air for 3 hours.

Table 24: Characteristics of catalysts prepared from polymer-protected metal colloids by three different methods as assessed by transmission electron microscopy.

Catalyst Property	**Preparative Method**		
	Adsorption	**Rotary Evaporation**	**Precipitation**
Loading	Poor	Moderate	Moderate
Particle Size	Small	Moderate	Large
Particle Dispersion	Homogeneous	Some aggregates	Large aggregates

Hydroxyapatite supported catalysts usually had the most homogeneous coating of particles regardless of the preparative method as shown in **Figure 94a**, although this is consistent with the observations made in the previous chapter that apatite scavenges particles from solution spontaneously. No aggregates were observed in any instances. Cellulose supported catalysts also had good surface coverages of particles, but when they were calcined the supports disintegrated leaving a black ash composed predominantly of large fused nanoparticles as shown in **Figure 94b**, making cellulose an inappropriate support when calcination is required to remove a capping agent. The alumina supported catalysts generally had textural properties similar to those produced in the previous chapter: the surfaces were highly covered with small but irregularly shaped and polydisperse particles as shown in **Figure 94c**, though also with a large portion of 'free-floating' aggregates not associated with the alumina surfaces. The silica supported catalysts generally benefited from a greater degree of surface coverage using all the methods investigated here compared to the previous chapter, in many instances producing catalysts with a homogeneous covering of particles and relatively fewer unattached aggregates as shown in **Figure 94d**.

6.3.2.3 Transmission X-Ray Powder Diffraction

The transmission x-ray powder diffraction (referred to herein as WAXS) patterns of the catalysts typically showed little difference in their profiles compared to their relevant precursor support materials, regardless of the experimental treatment. This includes the calcination step, indicating there is no significant phase transformations induced in the support materials from this step. The obvious exception to this rule was for the cellulose-supported materials, as there was insufficient sample left after calcination to collect a powder pattern due to combustion. Reflections originating from the supported metals were not observable in the patterns, however this was presumably because of their low concentration and the relatively poor signal to noise in the patterns. Example patterns focused on the low-angle differences are shown in **Figure 95**.

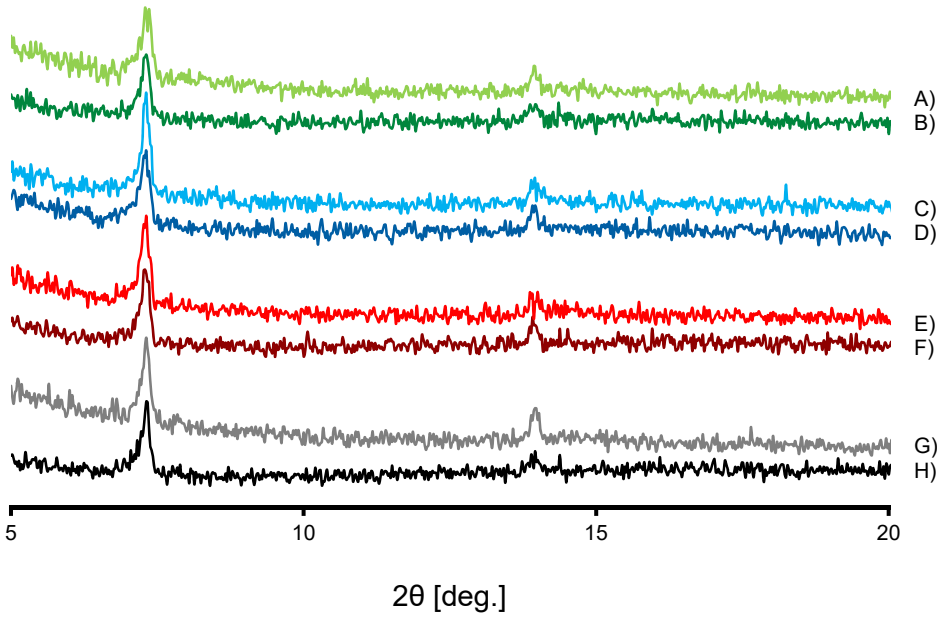

Figure 95: WAXS patterns of alumina catalysts prepared by adsorbing polymer-protected colloidal rhodium onto alumina. The eight traces correspond to PAM-Rh/Al_2O_3 post-calcination (a) and pre calcination (b), PAA-Rh/Al_2O_3 post calcination (c) and pre-calcination (d), PVA-Rh/Al_2O_3 post calcination (e) and pre-calcination (f), and PVP-Rh/Al_2O_3 post calcination (g) and pre-calcination (h).

6.3.2.4 Solid-State NMR

To investigate the nature of the adsorbed polymers in the current materials, ^{1}H solid-state NMR was performed. Firstly, spectra of the pure polymers were recorded to determine what chemical environments could be observed, their relative intensities, and their chemical shifts. These are shown in **Figure 96**. The PVA spectrum exhibited a relatively narrow resonance at 4.6 ppm, with a broad shoulder at *ca.* 2 ppm. Based on the assignments of Masuda, Kaji, and Horii, the first of these resonances was proposed to originate from the hydroxyl environments in the sample, while the latter resonance was thought to arise from the methylene and methine protons [456-458]. A similar spectrum was obtained for polyacrylamide, but with the addition of a weak shoulder at *ca.* 8 ppm, presumably originating from the $–NH_2$ protons. Similarly, the polyacrylic acid spectrum contained a strong resonance at 8.00 ppm corresponding to the –COOH protons, and a broader resonance at *ca.* 1.5 ppm corresponding to the chain protons [459]. The spectrum for PVP was dissimilar to the other three polymers, exhibiting only a single sharp resonance at 4.25 ppm. This presumably originated from strongly-bound water, as its assignment to the PVP

chain protons would be accompanied by the presence of other resonances in the spectrum.

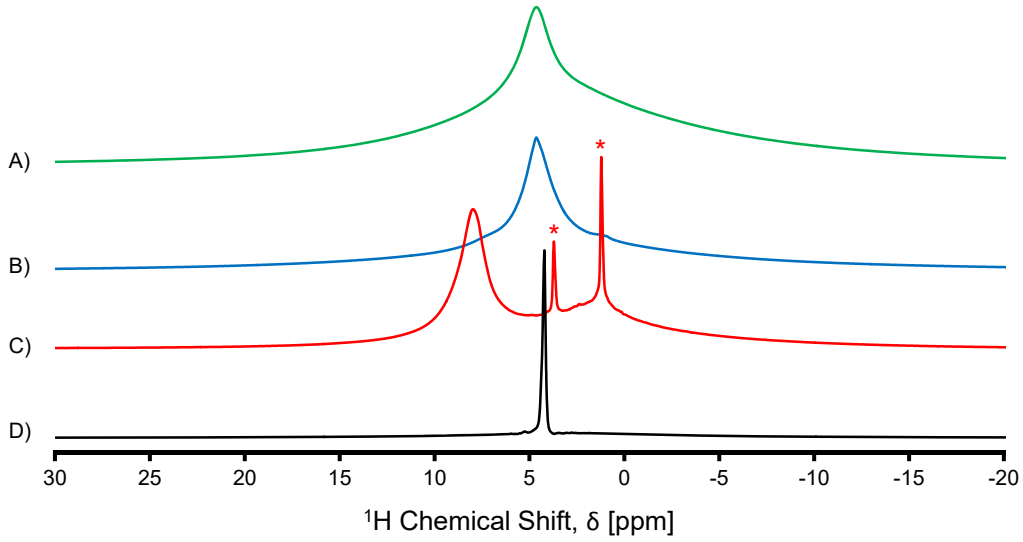

Figure 96: ^{1}H DPMAS NMR spectra of pure polymers. Samples are a) PVA, b) PAM, c) PAA, and d) PVP. The two resonance marked with asterisks originate from residual ethanol in the rotor used for cleaning.

When colloids prepared using these colloids were immobilised onto the various supported materials by adsorption from solution there were generally no detectable changes in the ^{1}H spectra compared to the pristine support materials. The exception to this generalisation were the spectra of the materials prepared using SiO_2, where the central hydroxyl resonance split into two environments as seen in the previous chapter. This was assigned as a difference in the hydration of the sample, however, and is not intrinsically associated with the polymers. These observations (or lack thereof) are consistent with the relatively little spontaneous adsorption observed to occur from solution, and so the lack of observable resonances was simply assigned as due to an insufficient concentration of protons.

Similarly few differences were observed in systems prepared by acetone precipitation of the polymers. In all cases the ^{1}H spectra were generally the same as the parent support, regardless of the choice of polymer. The notable exception was a weak doublet of peaks appearing at 0.82 ppm and 1.27 ppm in selected samples, putatively assigned as originating from adsorbed acetone.

A greater number of changes were observed in the ^{1}H spectra of samples prepared by rotary evaporation. These depended not only on the nature of the support, but also the polymer from which the materials were prepared. For materials with support materials which produced strong proton spectra prior to immobilisation of the colloids, the only changes were observed in hydration of the samples, manifesting as changes to the hydroxyl peaks at *ca.* 5 ppm. For the alumina-supported samples, however, the resonances in the proton spectra could be assigned as probably originating purely from the polymer, as the pristine alumina had no detectable hydroxyls. Examples are shown in **Figure 97**. These spectra show some resemblance to the corresponding pure polymers, but suggest there is significant structural rearrangement occurring in the materials upon their immobilisation onto the support materials.

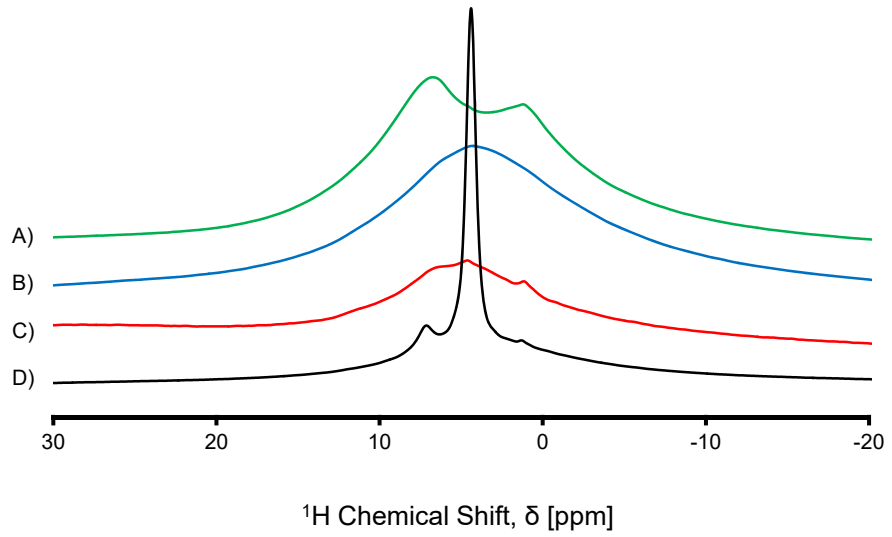

Figure 97: ^{1}H DPMAS NMR spectra of catalysts prepared by immobilisation of polymer-protected rhodium colloids onto Al_2O_3 by rotary evaporation. The four polymers are a) PAA, b) PVA, c) PAM, d) PVP.

6.3.2.5 X-Ray Photoelectron Spectroscopy

Though the previous instrumental methods gave some detail regarding the effects occurring with the support materials and the polymers, none gave any indication of the chemistry of the supported nanoparticles themselves. For this purpose x-ray photoelectron spectroscopy was undertaken on a series of HAp-supported catalysts, specifically with the intent of identifying changes in oxidation state within the precursor metal salts during reduction, and subsequently during calcination.

Survey scans of the hydroxyapatite-supported catalysts produced fairly predictable spectra, as shown in **Figure 98**. In all of the spectra, peaks were observed originating from the support material, the metals, and on occasion, the underlying indium substrate. In the unreduced samples, Cl 2s and 2p peaks were also evident, as is expected from the use of metal chloride salts. These peaks were absent from the reduced and calcined samples, suggesting that there is no residual chloride present at the surface of the catalysts. The gross binding energies of each element studied in each sample are given in **Table 25**, with deconvolution discussed sample by sample in the subsequent paragraphs.

The narrow scans of the core levels revealed a much greater level of chemical detail than the survey scans, with some spectral regions exhibiting clear differences between the different samples. The Ca 2p region was *not* one of these, showing two peaks originating from the $2p_{3/2}$ and $2p_{1/2}$ spin-orbit components, with peak shapes and positions identical between the nine samples, and equivalent to previously

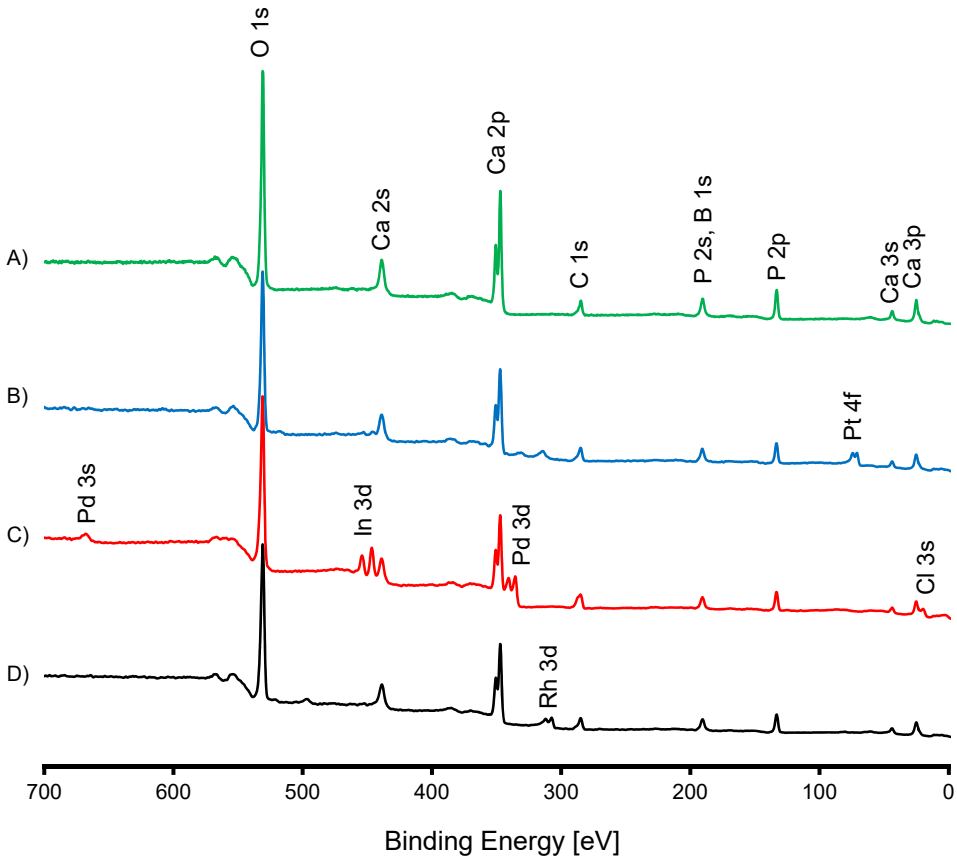

Figure 98: XPS survey spectra of metal nanoparticles on hydroxyapatite. The four traces correspond to a) pristine HAp, b) Pt/HAp, c) Pd/HAp, and d) Rh/HAp.

Table 25: Core level binding energy maxima for the measured catalysts.

Core-Level Binding Energy Maxima [eV]										
Sample	**O 1s**	**Ca $2p_{1/2}$**	**Ca $2p_{3/2}$**	**C 1s**	**Rh $3d_{3/2}$**	**Rh $3d_{5/2}$**	**Pd $3d_{3/2}$**	**Pd $3d_{5/2}$**	**Pt $4f_{5/2}$**	**Pt $4f_{7/2}$**
Rh/HAp pre-reduction	531.2	350.9	347.3	284.8	314.7	310	-	-	-	-
Pd/HAp pre-reduction	531.1	350.9	347.3	284.8	-	-	342.9	337.6	-	-
Pt/HAp pre-reduction	531.1	350.8	347.2	284.8	-	-	-	-	78.8	73.0
Rh/HAp post-reduction	531.1	350.8	347.3	284.8	311.9	307.1	-	-	-	-
Pd/HAp post-reduction	531.0	350.8	347.3	284.8	-	-	340.5	335.2	-	-
Pt/HAp post-reduction	531.0	350.7	347.1	284.8	-	-	-	-	74.3	70.9
Rh/HAp post-calcination	531.1	350.8	347.3	284.8	313	308.1	-	-	-	-
PdO/HAp post-calcination	531.1	350.8	347.3	284.8	-	-	342	336.8	-	-
PtO/HAp post-calcination	531.0	350.8	247.2	284	-	-	-	-	74.2	70.8
HAp (pristine)	531.1	350.8	347.2	284.8	-	-	-	-	-	-

reported hydroxyapatite samples [460, 461]. Conversely, the core level spectra the three metals varied significantly between samples, showing shifts in position and shape between the reduction and calcination steps.

The core level spectra of the Rh/HAp catalysts showed significant changes between the three samples studied, with shifts in the binding energies evident between the reduction and calcination step. The first sample, $RhCl_3$/HAp, showed two peaks corresponding to the $3d_{5/2}$ and $3d_{3/2}$ spin-orbit components with intensities of approximately 2:1 respectively. This is unexpected from the multiplicity of 3d electrons which dictates the ratio should be 3:2, although it is a well-known effect in Rh 3d core level spectra due to a Coster-Kronig transition between the two spin orbit components [431]. Because of this the peak areas weren't constrained during fitting, as no appropriate peak model could be otherwise formed. The simplest viable peak model resulting from this was a set of two doublets of approximately equal area, however a better fit was obtained using two components. Since the survey scans showed evidence of peaks in both the Cl 2s, 2p, and 3p regions it seems likely that at least one of these species is related to the 'free' $RhCl_3$ precursor. The second component may be surface-bound or otherwise substituted $RhCl_x$ species [462], though the exact nature of this component is not entirely clear. The deconvoluted data are shown in **Figure 99**.

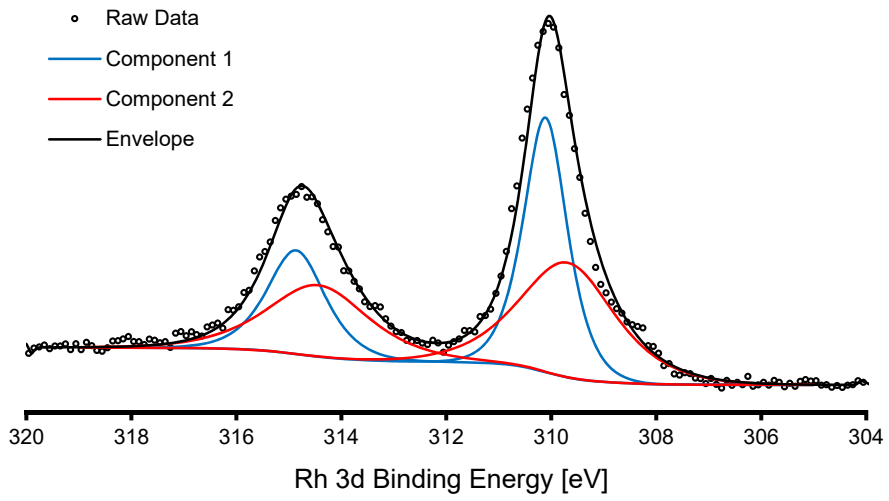

Figure 99: XPS Rh 3d core-level spectrum of the $RhCl_3$/HAp catalyst precursor.

When the sample was reduced there were significant shifts in the binding energies and peak shapes evident, with new maxima at 311.9 eV and 307.1 eV. The peaks additionally displayed significant asymmetry, both of which are characteristic of metallic rhodium [463]. No Cl peaks were found in the survey scans. This suggests that all Rh species in the sample were metallic rhodium, with no surface oxidation and no adsorbed chloride species. This does not, however, indicate that all of the precursor was completely reduced to metallic rhodium; after the reduction the sample was washed with water to remove chloride, however this could have also removed any unreduced (and water-soluble) $RhCl_3$ still present. The deconvoluted data are shown in **Figure 100**.

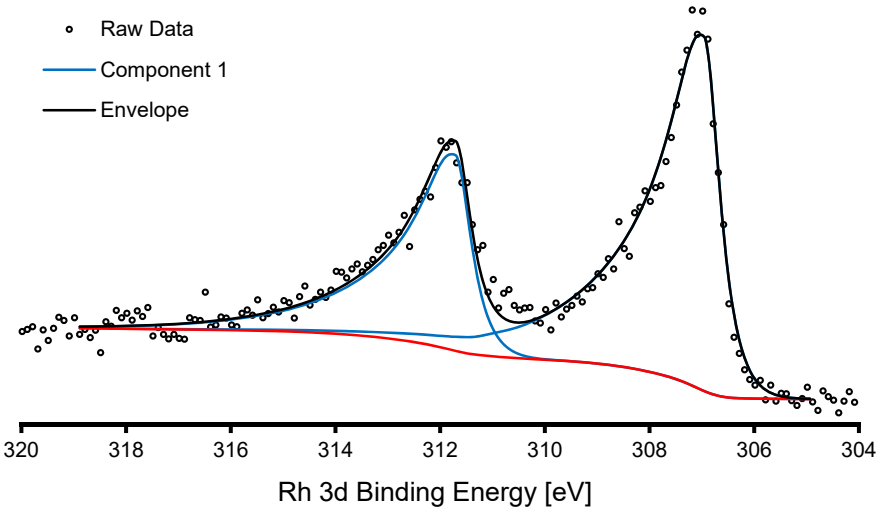

Figure 100: XPS Rh 3d core level spectrum of the reduced Rh/HAp catalyst.

The calcined sample showed further peak shifts from the reduced sample, and could be fitted with two sets of doublets with the $3d_{5/2}$ peak of the major component centred at 308.15 eV, and a second broader set of approximately half the area and twice the width at 310.65 eV. The first of these components corresponds in energy to Rh_2O_3 [463], which is expected from the high-temperature calcination treatment. The presence of RhO_2 was ruled out as the O 1s spectra were not consistent with the presence of this phase [463]. The exact nature of the second component is unclear, but the broad half widths and specific binding energies suggest it may a secondary rhodium oxide phase of unknown type, or perhaps even a range of minor oxide species. The deconvoluted data are shown in **Figure 101**.

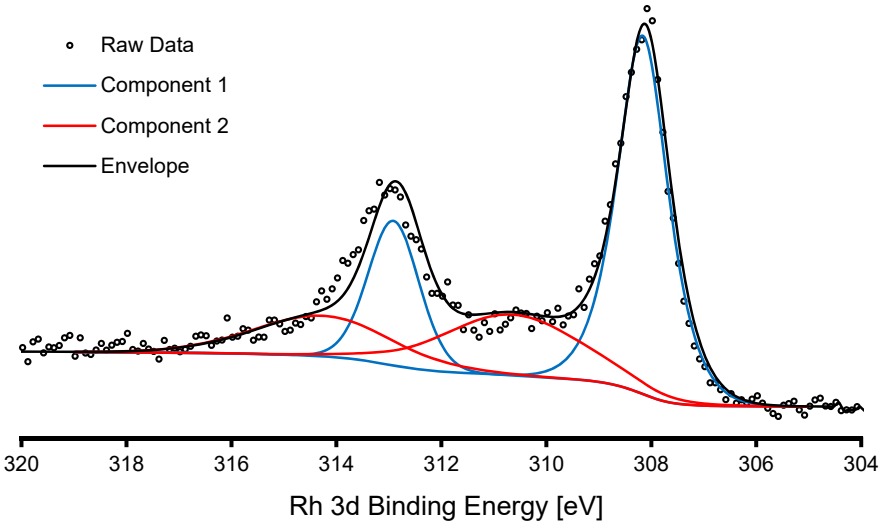

Figure 101: XPS core level spectrum of the calcined Rh/HAp catalyst.

The palladium samples were by far the most complicated to deconvolute, primarily because of the partial overlap between the Pd 3d shakeup peaks and the directly adjacent Ca 2p peaks. In all cases the Ca 2p peaks could be well fitted using a Shirley background and a spin-orbit doublet with a 1:2 area ratio, corresponding to the Ca $2p_{1/2}$ and $2p_{3/2}$ components at 350.9 eV and 347.4 eV respectively. This is shown in **Figure 102**. No features were observed in the pristine HAp sample in the region over which the Pd 3d peaks occur.

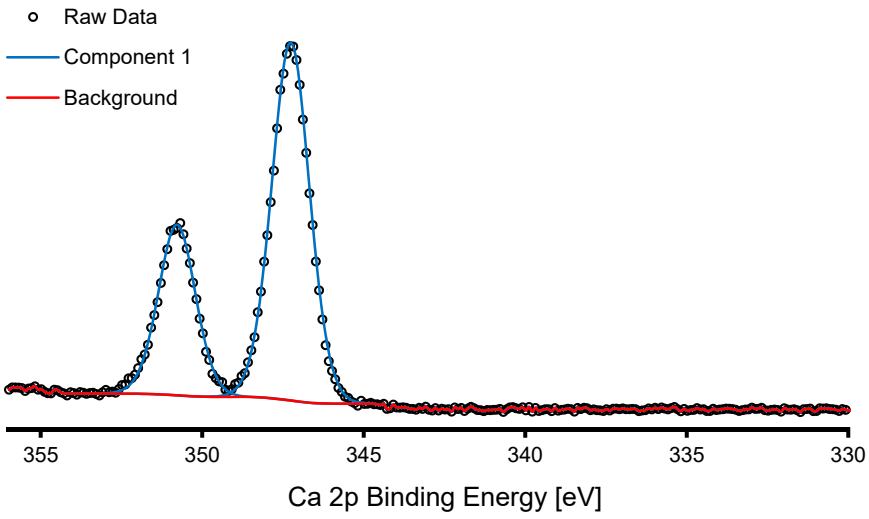

Figure 102: XPS core level spectrum of pristine HAp.

Fitting of the Na_2PdCl_4/HAp was the most complicated. The data was fitted with a spin-orbit double in the Ca 2p region as per the pristine HAp sample, and the remaining unfitted area assumed to be composed of various Pd 3d peaks. The bulk of this area could be accounted for by fitting a second doublet corresponding to the Pd $3d_{3/2}$ and $3d_{5/2}$ peaks, with binding energies of 342.9 eV and 337.6 eV and an area ratio of 3:4 respectively. This matches the reported binding energies of free Na_2PdCl_4 [464], but not $PdCl_2$ [465]. Two shoulders evident on the low-energy sides of these peaks suggested the sample contained a second component which was fitted with a third doublet with binding energies of 335.9 eV for the $3d_{3/2}$ component and 341.0 eV for the $3d_{5/2}$ component. It is suggested that this component may be chemisorbed Pd(II), since the sorption of Na_2PdCl_4 by HAp was clearly observable in the current study. Even with these three components fitted, the model still underestimated the photoelectron yield between the Pd component 1 $3d_{5/2}$ and Pd component 2 $3d_{3/2}$ peaks, as well as between the Pd component 1 $3d_{3/2}$ and Ca $2p_{3/2}$ peaks. A fourth set of peaks added in these regions adequately fitted the data, and are assigned as shake-up peaks originating from Pd component 1, since these were observed for species like $PdCl_2$ [465]. The fully deconvoluted peak model is shown in **Figure 103**.

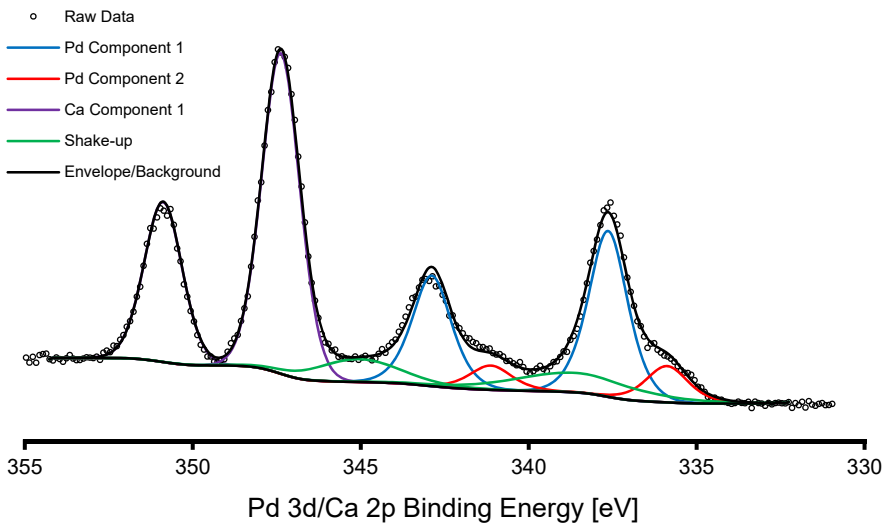

Figure 103: XPS Pd 3d core level spectrum of Na_2PdCl_4/HAp

The reduced sample, formally, Pd/HAp was easier to fit. Using a Shirley baseline the Ca 2p components were once again fitted with a doublet, and the major Pd 3d components, were fitted with a doublet of asymmetric Voight peaks, the binding energies for which were consistent with metallic Pd [466]. The fit was improved, however, by using a splined Shirley background, with iterative fitting of the background and the two Ca and Pd components. This iterative fitting procedure could not converge on an acceptable model with structureless residuals, however, suggesting the presence of a secondary Pd component. The addition of a third spin-orbit doublet therefore, with peak positions of 342.9 eV for the $3d_{3/2}$ component and 337.8 eV for the $3d_{5/2}$ component, solved this problem. The binding energies of this secondary component suggests it represents a small fraction of PdO [467], which is unsurprising given the exposure of the sample to the atmosphere. The deconvoluted data are shown in **Figure 104**.

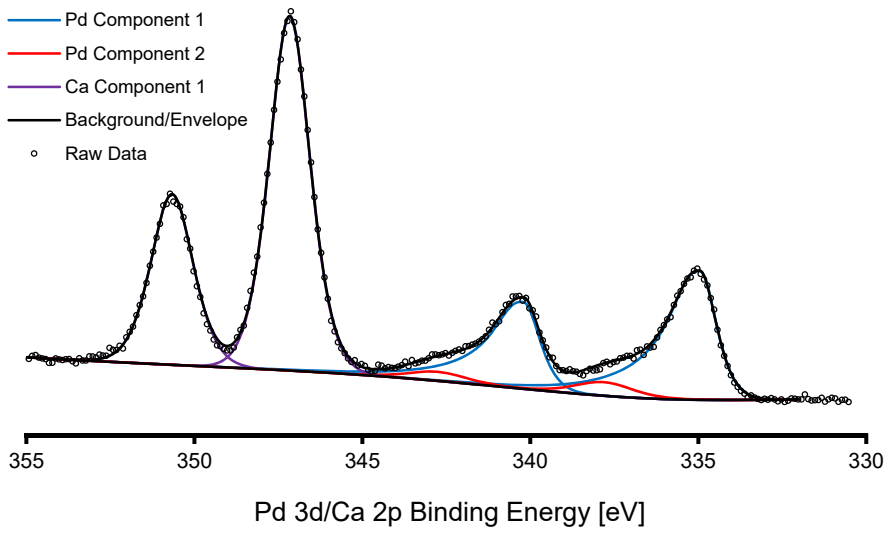

Figure 104: XPS Pd 3d core-level spectrum of Pd/HAp.

The calcined sample, assumed *a priori* to be PdO/HAp, could be deconvoluted in several different ways depending on the choice of background. As per the previous samples the Ca region was fit with a 1:2 spin-orbit doublet, and then the remaining peaks fitted as Pd species. The major component of these peaks was fitted accurately using another doublet, with binding energies of 342.0 eV for the $3d_{3/2}$ component and 336.7 eV for the $3d_{5/2}$ component. These correspond in energy to PdO [467], as

expected from the high-temperature calcination. The exact binding energy indicates the oxide may contain dissolved oxygen, characteristic of metallic palladium having been heated at high temperature for an extended period [468]. Using a splined Shirley background as per the previous sample, the peak model was improved further by the addition of *two* extra spin-orbit doublets, one with the $3d_{3/2}$ component at 344.9 eV and the $3d_{5/2}$ component at 339.9 eV, and the second with the $3d_{3/2}$ component at 343.6 eV and the $3d_{5/2}$ component at 338.2 eV. Assignment of these doublets was not pursued, since a simpler model of similar fit could be constructed using a regular Shirley background, as per the first sample, with only a single extra doublet present. The binding energies of this second Pd environment are 344.6 eV for the $3d_{3/2}$ component and 338.8 eV for the $3d_{5/2}$ component. Since PdO does not produce shake-up or plasmon peaks, this high binding energy component may represent some higher oxide of palladium. The final deconvoluted peak model is shown in **Figure 105**.

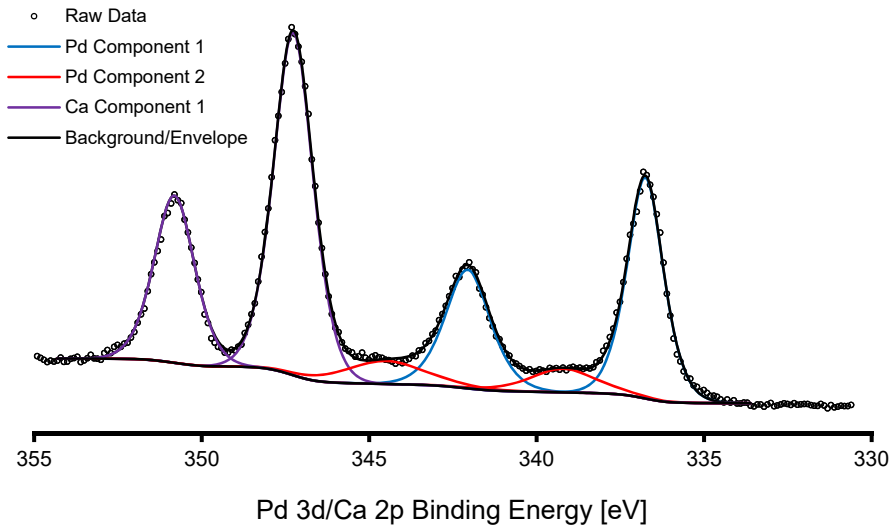

Figure 105: XPS Pd 3d core-level spectrum of calcined Pd/HAp.

The Pt/HAp samples presented a number of complications which made data analysis difficult. It would be expected *a priori* that there are multiple Pt environments in the sample, given that chloroplatinic acid is acidic and can attack the apatite surface, which could release calcium and phosphate ions into solution, and which may be coprecipitated with the platinum on drying, and may or may not substitute

into the lattice. Additional to these possibilities, pelletisation of the sample caused it to partially darken in colour, suggesting pressure-induced reduction of the Pt species. The Ca 2p spectra of the three platinum-containing samples were all identical, suggesting that the former of these issues was unlikely to have occurred to any significant extent, as reprecipitation of the dissolved HAp would presumably produce a different CaP phase with different binding energies.

The first of the samples, formally H_2PtCl_6/HAp, appeared to be composed of one major Pt environment and one minor environment, as evidenced by the presence of a high-binding-energy shoulder on the Pt $4f_{5/2}$ component. Fitting of two spin-orbit doublets to the data produced a good fit when using a Shirley baseline, with the $4f_{5/2}$ component of the major environment at 76.3 eV and the $4f_{7/2}$ component at 73.0 eV. The binding energies of the two spin-orbit components of the minor environment occurred at 78.4 eV and 75.1 eV for the $4f_{5/2}$ and $4f_{7/2}$ components respectively. While the fit was good with only the two environments, it was dramatically improved by the addition of a third set of doublets, with binding energies of 74.7 eV for the $4f_{5/2}$ component and 71.3 eV for the $4f_{7/2}$ component. The binding energies of this environment strongly suggest it originates from metallic Pt [469-471], which is consistent with the observed sample darkening during pelletisation. This raises the question of the origin of the other two environments, since it would be expected that at least one originates from a Pt(IV) species *ex* chloroplatinic acid. No literature is available on the binding energies of free chloroplatinic acid; however, binding energies for other Pt(IV) species are known, notably K_2PtCl_6. Pt $4f_{5/2}$ peaks for these species are usually observed around 75.5 eV [470, 472], and so if H_2PtCl_6 is observed at similar binding energies, this may be the origin of the minor component. The major component in the sample, however, was observed at a binding energy closer to a Pt(II) species [473]. Assuming the precursor, formally chloroplatinic acid, is entirely in the form of Pt(IV) species, it may be the case that the pelletisation of the sample induces a transition from Pt(IV) to Pt(II) to Pt(0). The deconvoluted peak model illustrating the species observed in the sample is shown in **Figure 106**.

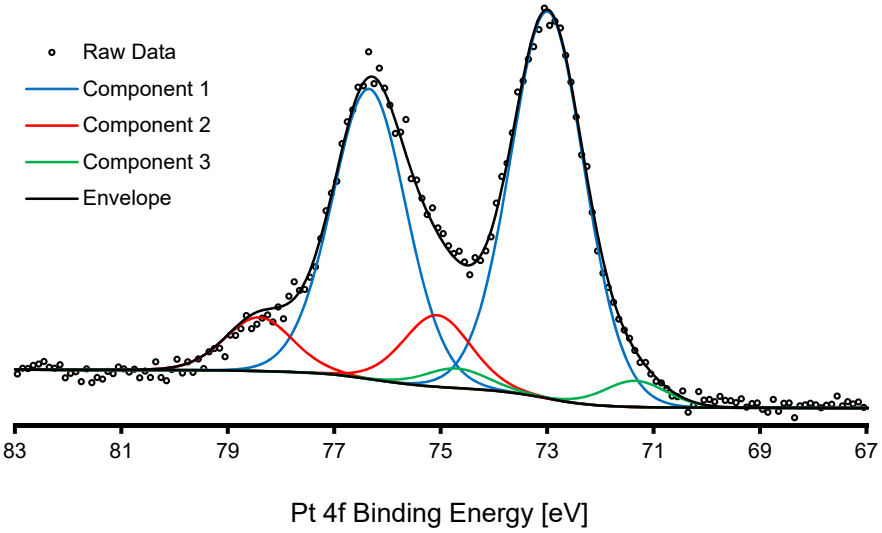

Figure 106: XPS Pt 4f spectrum of H_2PtCl_6/HAp.

The Pt 4f core-level spectrum of the reduced sample, formally Pt/HAp, showed significant differences compared to the unreduced samples. Two major peaks were observed, which were fitted with a spin-orbit doublet with binding energies of 74.1 eV for the $4f_{5/2}$ component and 70.1 eV for the $4f_{7/2}$ component. These correspond closely to the binding energies for Pt metal [469-471], as would be expected for a reduced sample. Introduction of an asymmetry parameter into the peak model increased the goodness of fit, which again is expected for metallic Pt. The data could not be accurately modelled with only this single environment however, and so a second spin-orbit doublet of significantly smaller area was added at higher binding energy, with the $4f_{5/2}$ component at 81.3 eV and the $4f_{7/2}$ component at 78.0 eV. These binding energies are remarkably high, and since they correspond to no common oxides [470, 474] or chlorides [472, 473, 475] of platinum, they are most likely satellite peaks of some type. The deconvoluted data are shown in **Figure 107**.

When the sample was calcined no changes to the Pt 4f core-level spectrum were observed. This suggests that it is heat-stable, at least at 500 °C for 3 hours, without becoming oxidised to PtO or PtO_2. The data was similar to **Figure 107**, so is not shown here.

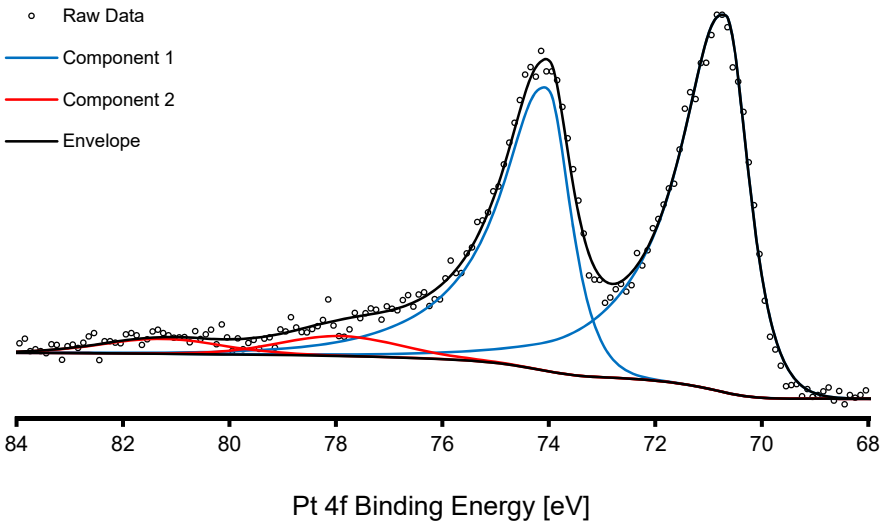

Figure 107: XPS Pt 4f core-level spectrum of Pt/HAp.

6.3.3 Catalyst Characterisation

This section of the chapter provides details on the characterisation of a set of catalysts produced using the optimised synthetic methods described in the previous sections, using pre-formed colloidal dispersions of metal nanoparticles stabilised using one of three polymers, immobilised onto the support materials described earlier. Three polymers were used, PVP, PVA, and PVP, at significantly lower concentrations than those used during the development work.

6.3.3.1 General Observations

The synthesis of the precursor colloids proceeded in much the same as described previously. Addition of sodium borohydride solution to the orange-coloured dilute metal salt solutions caused them to darken to dark brown or black, indicating the formation of nano-sized metal particles. The three systems prepared, comprising colloids of either rhodium, palladium, or platinum, protected by either PVP, PVA, or PAM, were all stable over the period over their preparation and subsequent immobilisation onto the relevant support materials, as indicated by the fact that none precipitated metal from suspension onto the walls and floor of the vessel. Rotary evaporation of the colloids onto the support materials (nine colloids x six support materials) yielded a set of 54 catalysts, the macroscopic textural properties of which were markedly different from those prepared in the earlier trial experiments due to the decrease polymer concentration. The resulting powders tended to adhere much

less strongly to the walls of the flasks, were more free-flowing, and generally less 'flaky' than the materials described earlier. Additionally, the homogeneity of the materials was significantly better than those prepared in the previous chapter, with all samples being equally coloured throughout, not speckled with individual light or dark grains. This was taken to be indicative of a much better dispersion of metal across the surface of the supports compared to the previous generation of catalysts, a fact which was later confirmed by electron microscopy.

6.3.3.2 Photomicroscopy

Photomicroscopic analysis of the catalysts confirmed the inferences made visually regarding the distribution of metal on their surfaces. As the pristine support materials were all white and metal nanoparticles appear black, their distributions could be easily visualised within the catalysts up to magnifications of *ca.* 50x. At higher magnification chromatic aberrations appeared in the micrographs, most commonly in the form of blurry blue and purple fringes within the vicinity of the areas rich in nanoparticles. Large aggregates of nanoparticles, which therefore appear at low magnification as black flecks, were generally absent from most of the catalysts studied.

For catalysts prepared using optically transparent support materials like silica and perlite, the analyses could be performed in transmitted light mode. In this configuration, regions of the catalysts containing high concentrations of metal particles could be discerned from those with low concentrations based on the intensity of the transmitted light, analogous to transmission electron micrographs. Though most surfaces of these particular catalysts appeared to be lightly coated with metal nanoparticles, some regions were obviously more heavily coated than others. This is illustrated in **Figure 108a**. When oblique illumination was used instead of transmitted illumination, these effects were more difficult to observe, as shown in **Figure 108b**.

Those which were not optically transparent like alumina were best viewed in reflectance mode. The metal distribution in these systems was less clear, but could be discerned based on subtle darkening of the surface of the support materials. As with the silica-based systems discussed in the previous paragraph, the surfaces of most

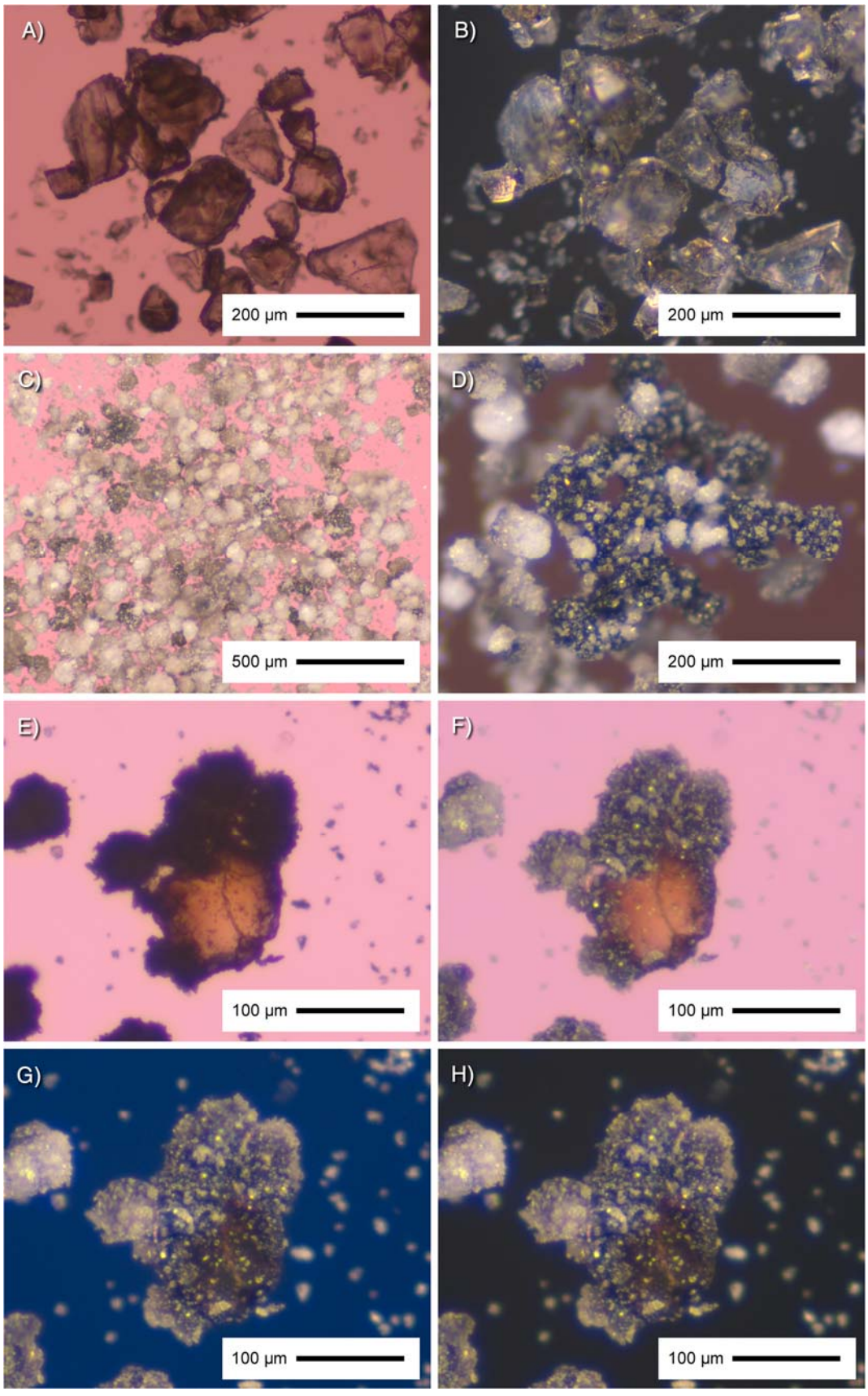

Figure 108: Photomicrographs of supported palladium catalysts prepared from polymer-protected colloids. Shown are PVP-Pd/SiO_2 (A,B) and PVP-Pd/Al_2O_3 (C-H) using various combinations of transmitted and oblique illumination.

particles appeared to be lightly covered with metal nanoparticles, though the distributions were not totally homogeneous. Examples of the alumina-supported catalysts illuminated in different ways are shown in **Figure 108c-h**.

Different textural properties were also observed between different catalysts, depending predominantly on which combination of polymer and support was used, but on the choice of metal. In some cases the catalyst particles were well-separated from one another as in a free-flowing powder, which tended to be the case for systems prepared using support materials with high surface areas, such as silica. In other systems, however, the catalyst particles appeared to be embedded in a malleable matrix, presumably the unadsorbed polymer. In selected cases the free polymer was observed to form flat black flakes in which the support particles were embedded, or to which they were attached. This tended to occur in systems based on support materials with low surface areas, for example alumina. The origin of these flakes was presumed to be unadsorbed polymer, which was later proven by infrared microspectroscopy.

The systems prepared using novel support materials generally exhibited similar properties to equivalent systems prepared using the model support materials. The metal distribution and textural properties of the silica or perlite supported catalysts were therefore similar, as were the hydroxyapatite and bioapatite supported catalysts. The halloysite supported catalysts, though chemically similar to both alumina and silica, exhibited properties that were intermediate of the two.

6.3.3.3 Transmission Electron Microscopy

Electron microscopic analysis of the supported palladium catalysts showed that there were a range of particle sizes present within the different catalysts, ranging from 2.3 nm for the PVA-Pd/BAp catalyst, up to 22 nm for the PVP-Pd/SiO_2 catalyst. The average particle sizes for the palladium catalysts are given in **Table 26**.

The particle sizes measured in the current catalysts span a significantly greater range than those observed in Chapter 5, for which there could be multiple reasons. As the polymer-protected colloids had particle sizes which were significantly smaller, this suggests that the increase in crystallite size is brought about after immobilisation, probably during the 500 °C calcination step. The primary mechanism is presumably particle sintering, whereby metal particles migrate and coalesce, producing an

increase in average particle size. The second possibility is that the calcination step induces oxidation of the nanoparticles, which was shown conclusively by XPS in the case of the Pd/HAp system. It may be expected that the transition from Pd to PdO is accompanied by an increase in lattice parameter, with subsequent swelling of the particles; however, it has been shown by Giorgio *et al.* that magnesia-supported palladium particles change lattice parameter by only a few percent when annealed under hydrogen or oxygen [476]. Assuming that the supported particles in the current study behave similarly, this effect is likely to contribute negligibly to the particle size increase.

The distribution of the metal nanoparticles across the surfaces of the supports was dramatically improved in many cases by using the current polymer-protected colloid immobilisation method, especially when compared with the catalysts

Table 26: Particle sizes measured by TEM of palladium catalysts prepared from polymer stabilised colloids.

Support	**Polymer**	**Measured Size [nm]**		**Dispersion [%]**
		Average	SD	
Al_2O_3	PVA	5.8	2.0	9.6
	PAA	3.5	1.1	16
	PVP	5.2	2.0	10
SiO_2	PVA	10	7.2	3.1
	PAA	4.7	1.2	13
	PVP	22	19	1.0
HAp	PVA	3.4	1.2	16
	PAA	4.4	2.2	9.3
	PVP	6.5	2.5	8.3
HNC	PVA	4.8	1.5	12
	PAA	5.5	2.6	7.9
	PVP	7.4	2.7	7.3
PRL	PVA	4.0	2.4	10
	PAA	-	-	-
	PVP	3.9	2.4	9.5
BAp	PVA	2.3	0.6	24
	PAA	3.9	1.0	16
	PVP	5.7	1.7	10

described in the previous chapter. This effect was most profound in the perlite-supported catalysts, where the metal nanoparticles were dispersed discretely and uniformly with almost no observable aggregation. Similarly, the level of aggregation was slightly reduced in the silica-supported catalysts, where the average aggregate size decreased approximately two orders of magnitude from microns to nanometres. The corollary though, since the samples had to be calcined, was that the average particle size in the aggregates increased dramatically.

The metal distribution in the halloysite-supported catalysts was also improved slightly, with few aggregates observable. The halloysite catalysts did, however, show some mild structural changes – the tubules evident in previous studies were altered, with no hollow interiors visible, and appearing flaky and fractured longitudinally, presumably due to a high-temperature phase transition brought about by their calcination. In spite of this, their surfaces remained homogeneously coated in nanoparticles in almost all cases. Conversely, the metal distributions in the alumina-supported catalysts were not improved at all, appearing identical to those described in the previous chapter. Similarly, marginal gains in homogeneity were observed in the hydroxyapatite or bioapatite supported catalysts. Even when catalysts were prepared from these materials in the absence of a polymer their metal distributions were fairly homogeneous, suggesting their distributions have little room for improvement. Example micrographs of selected systems are shown in **Figure 109**.

6.3.3.4 Laser Induced Breakdown Spectroscopy

Laser induced breakdown spectroscopy was successfully applied to the analysis of the current set of catalysts using the method laid out in Chapter 4. Emission spectra of the pristine supports used as blanks only showed peaks originated from elements in the supports, while the spectra of the catalysts contained the same peaks plus those resulting from the presence of the metal nanoparticles. The relative intensities of the peaks were sufficiently similar between the catalysts and the standards to indicate their ablation properties were similar, allowing quantification of the metal in the catalysts by comparison of the two.

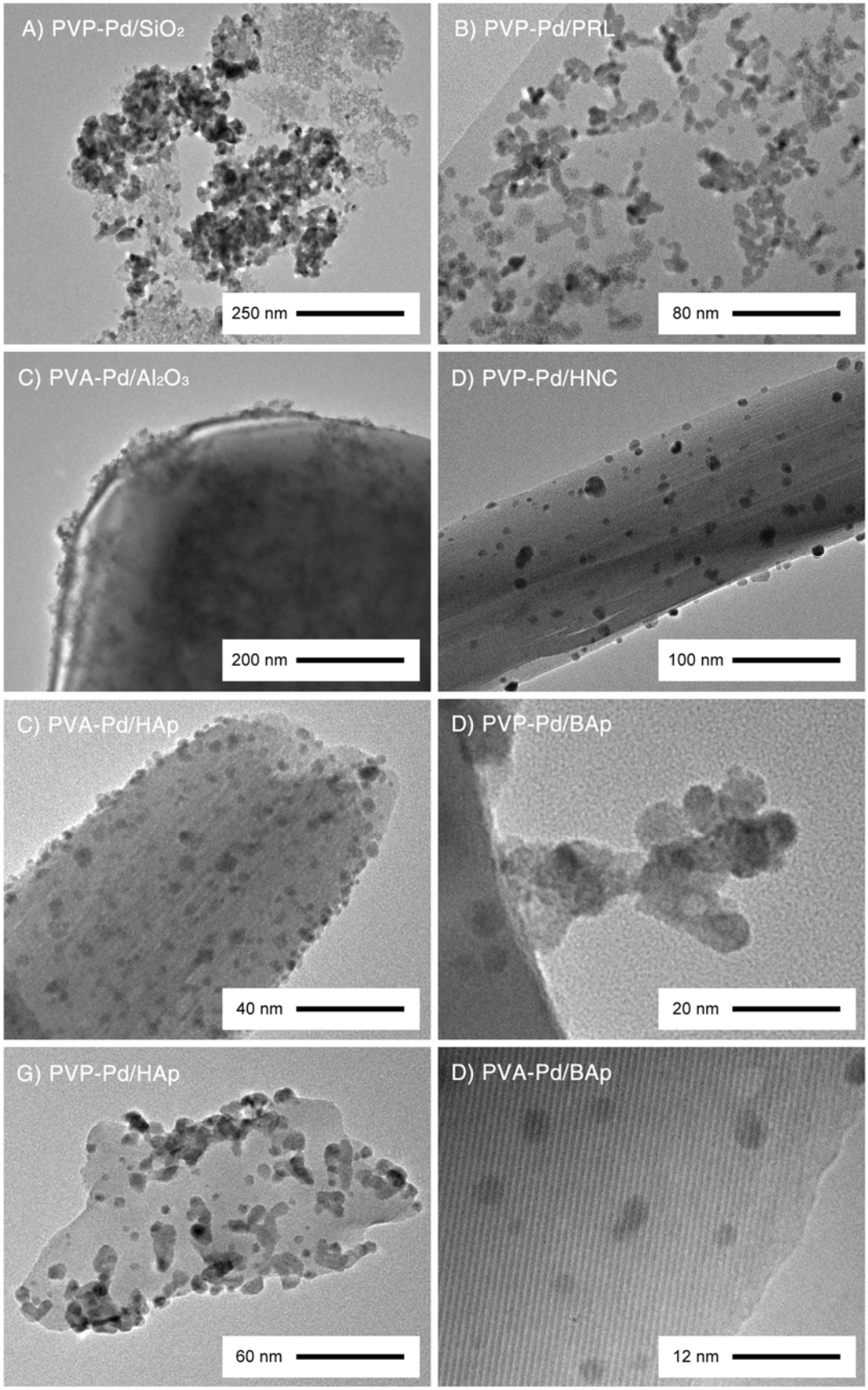

Figure 109: TEM micrographs of catalysts prepared from polymer-protected palladium colloids, after calcination. Metal distribution clearly varies from system to system, but is better than observed in the previous chapter.

The concentrations obtained by this method indicate that the loadings depended significantly on the nature of the support, but were almost independent of the nature of the polymer. The full list of concentrations is given in **Table 27**. The silica supported catalysts for example showed the greatest loadings, averaging 1.55%, while the perlite-supported catalysts had an average loading of only 0.46%, a difference of over three-fold between relatively similar materials. The spread in the loadings for the two groups of catalysts was much less, however, being 0.42% for the former and 0.093% for the latter. This is consistent with the observed properties of the support as detailed in Chapter 2, since the silica used has not only a higher surface area than the perlite, but also has greater surface functionality with which polymers could potentially bind. This suggests that the polymer coating is more 'mechanical' in nature than chemical; that is, it may not arise predominantly from any specific chemical interaction with the support, although it may be enhanced by it in cases where this may exist.

Similar trends to those described above were observed for catalysts prepared using the other support materials. The alumina supported catalysts generally had slightly higher loadings than the halloysite catalysts, despite having a lower surface area and being nearly devoid of any surface functionality. This supports the hypothesis above that the coating is not a chemical one. The opposite trend was observed with the apatite supported catalysts, with the bioapatite catalysts having higher loadings than the hydroxyapatite catalysts, despite having a lower surface area.

The most important issue to arise from the analysis related to the halloysite catalysts; quantification of their Pd content using the Si method gave results approximately three fold lower than using the Al method. This was done using a numerically mixed standard; that is, using the average response from individual alumina and silica standards, since halloysite is essentially a mixture of the two. It would be of interest to repeat the analyses using a single mechanically mixed standard, that is, one created by combining equal masses of silica and alumina standards in a single pellet.

Table 27: Loadings of palladium in catalysts prepared from polymer-protected colloids as measured by LIBS. All values given to 2 sf. All uncertainties given to a significance of 2σ.

Support	Polymer	Concentrations [wt%]	
		Loading	**Error**
Al_2O_3	PVA	1.3	0.11
	PAA	1.1	0.097
	PVP	1.1	0.096
SiO_2	PVA	1.4	0.16
	PAA	1.5	0.156
	PVP	1.8	0.19
HAp	PVA	0.75	0.071
	PAA	0.72	0.069
	PVP	1.2	0.12
HNC	PVA	0.95	0.095
	PAA	0.80	0.076
	PVP	0.71	0.073
PRL	PVA	0.44	0.044
	PAA	0.42	0.042
	PVP	0.51	0.051
BAp	PVA	0.73	0.072
	PAA	1.6	0.16
	PVP	1.5	0.15

Regardless of the differences in metal loading between different polymers and different support materials, the amount of metal in the catalysts was generally less than expected based on the amount of precursor used. This shows that the catalyst preparation method used, *viz.*, rotary evaporation, is a lossy method, where the uptake of metal is not quantitative. Although it is clear that a portion of the metal is lost during the process, it is not entirely clear how much metal is lost at which stage, since it is a multi-step synthesis. Most likely is that evaporation of the colloid onto the support material could also immobilise metal onto the inside of the flask in which the catalyst is prepared, a phenomenon which was observed unambiguously during the preparation of the materials. It could be the case that this film of colloidal particles immobilised on the flask walls also contains support material particles, in

which case the loading may not be decreased, but the total mass of catalyst yielded would be. It may also be the case that metal particles are lost during the calcination step, as the rising heat carries away nanoparticles which become freed from their polymer matrix as it is pyrolysed.

Another point which warrants discussion is what effect the calcination step may have on the instrumental response. Since most of the supports are shown to be thermally stable by analyses detailed later in this chapter, the chemical and physical properties of the bulk of the material are not expected to change significantly. Since it is the major components of the matrix which contribute to a sample's ablation properties, it is therefore not expected the ablation will be altered significantly either.

6.3.3.5 Power Diffraction

Analysis of the catalysts by x-ray powder diffraction revealed a range of structural alterations had occurred during their preparation. The majority of these changes appeared to be brought about by the calcination step, and thus the powder patterns between calcined and non-calcined catalysts exhibited the greatest differences. More subtle differences were observed between systems prepared using different polymers, associated particularly with reflections originating from the supported metals. These changes are discussed further in the following paragraphs.

Reflections from the supported palladium particles were visible in all of the systems studied. Where crystalline support materials were used the reflections were less obvious and were 'buried' amongst the reflections originating from the support, however where amorphous support materials like silica were used these signals were more clearly evident. In the case of samples which had not undergone calcination, the positions of these reflections indicated they originated from metallic palladium, which is consistent with the XPS analysis described in section 6.3.2.5. Their wide half-widths and weak intensities further suggest the particles are quite small, estimated at 3-4 nm based on the work described in Chapter 5. After the samples were calcined, the peaks narrowed and their positions dramatically shifted, suggesting they are oxidised to PdO and that some degree of particle sintering occurs. Example diffractograms for the PVP-Pd/SiO_2 system are shown in **Figure 110**.

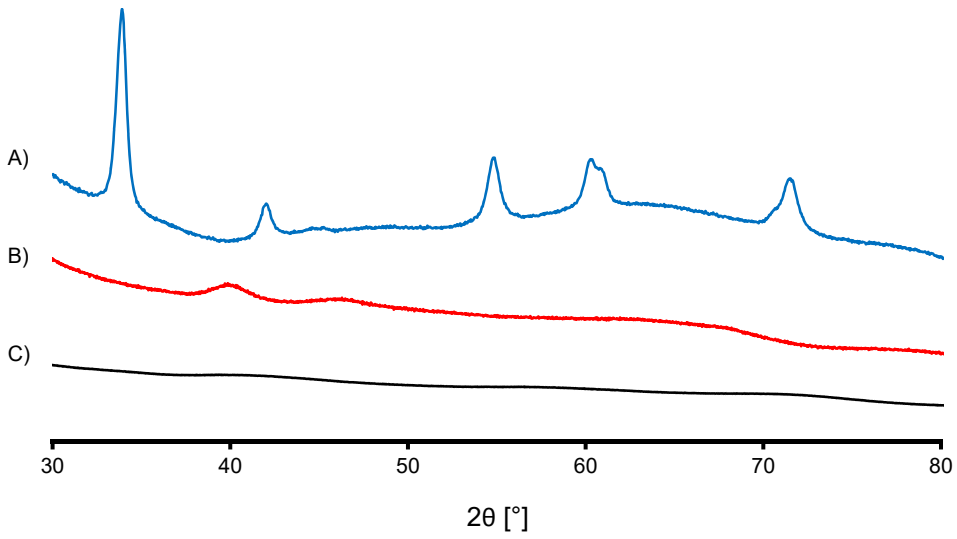

Figure 110: XRD patterns of the PVP-Pd/SiO_2 catalyst. The three traces correspond to a) calcined Pd/SiO_2, b) non-calcined PVP-Pd/SiO_2, c) pristine SiO_2.

While all of the supported metal particles clearly produced different diffraction patterns for different systems, the changes evident in the diffraction patterns of the support materials were less characteristic. In all of the systems using alumina, hydroxyapatite, or bioapatite as a support material there were no detectable changes in the reflections originating from the support materials, either in terms of their peak positions, their breadths, or their shapes. This is perhaps unsurprising given that all three of these materials are refractory to various degrees. Conversely, the halloysite-supported catalysts showed significant structural changes on calcination. While the majority of the reflections remained in the same positions and with the same intensities, the clay-like features in the patterns collapsed, concomitant with the formation of a number of new, broad, reflections. This suggests that the high temperatures to which the samples were exposed during calcination bring about some type of minor phase transition, which was confirmed in later sections by NMR and FTIR. Example patterns for some of the catalysts are shown in **Figure 111**.

Additional to the changes observed in the sharp diffraction peaks of the samples, differences were observed in the background intensities between different systems. Most significantly, the backgrounds were higher in the non-calcined samples, and lower in the calcined samples. Since the background intensity arises from disordered or amorphous components of the sample, this suggests that the calcination either brings about a crystallisation of amorphous components of the samples, or removes an amorphous surface layer of some type. The former of these seems unlikely, since

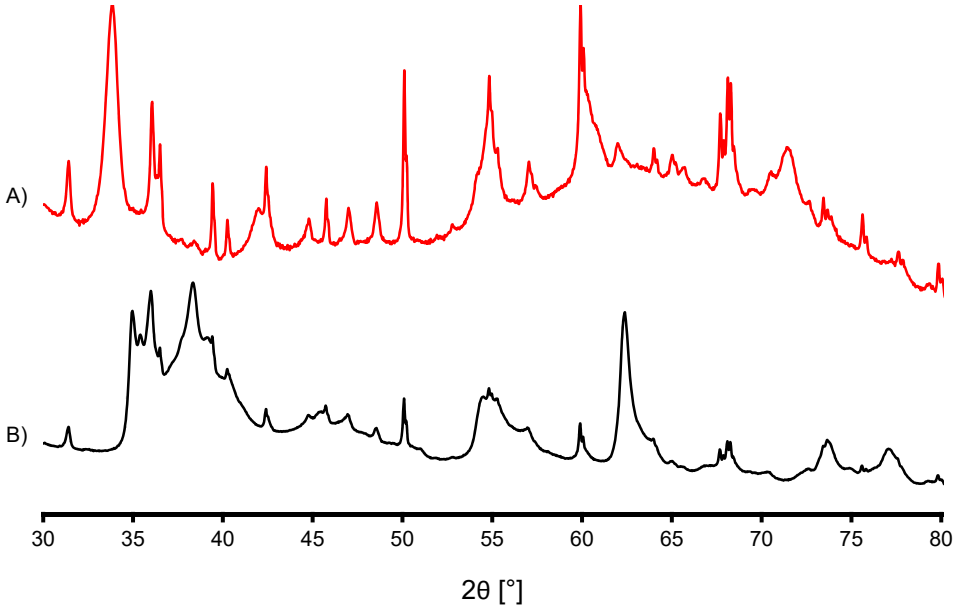

Figure 111: XRD patterns of PAA-Pd/HNC catalysts. The two traces represent the sample post-calcination (A) and pre-calcination (B).

this should manifest as a decrease in the widths of some of the reflections, however this was not observed in any instance. The latter of the two options therefore seems most probable, and is discussed further in the following paragraph.

Prior to calcination the samples can be described as a collection of particles of support material with a polymer coating around their exterior, as shown in **Figure 112**. When x-rays impinge on such a sample they first encounter the surface polymer layer throughout which nanoparticles are distributed in some unknown fashion, and their intensities immediately begin to be attenuated. The fewer the proportion of photons which penetrate the polymer layer the greater the contribution of the polymer to the diffraction pattern, and consequently the lesser the contribution of the support material. The ratio of the background intensity to the diffraction peak intensity thus gives an indication of the thickness of the polymer layer, and since the background intensities are much lower in the calcined sample, suggests strongly that the background signal arises from the polymer coatings, and that it is wholly removed by calcination. This effect is somewhat difficult to observe in the case of catalysts with crystalline support materials since the diffraction intensity from the crystalline components is much stronger than the amorphous components, however in catalysts with amorphous supports, such as those using silica or perlite, the effects were immediately obvious from even a cursory glance at the diffraction patterns.

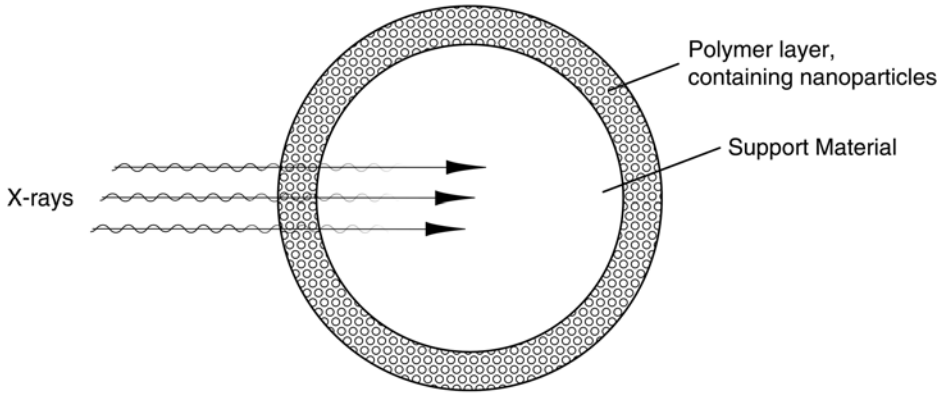

Figure 112: Schematic of x-rays impinging on a catalyst particle.

6.3.3.6 Infrared Spectroscopy

Infrared microspectroscopy was shown to be a powerful tool for characterising the catalysts. Generally speaking, the spectra of the calcined catalysts were similar to the pristine support materials, while the same samples prior to calcination showed a superposition of bands originating from the support materials and the adsorbed polymers. Specific differences for each group of catalysts are discussed below.

The spectra of the polymers showed various bands characteristic of their structures. Spectra of the polymers as-received are shown in **Figure 113**. The high-energy ends of the spectra were dominated by broad hydroxyl stretching bands arising from either sorbed water, or structural hydroxyls as in the case of PVA and PAA. Strong bands in the region 2900 cm^{-1} to 3000 cm^{-1} corresponding to methylene bending modes were observed in PAA, but were much weaker in PVA, and not observed in PVP. The two carbonyl-containing polymers exhibited strong bands in the region 1700 cm^{-1} to 1800 cm^{-1} corresponding to the C=O stretching mode, and all three exhibited a variety of weak C-C and C-H associated vibrational features in the 'fingerprint region', which are difficult to use diagnostically because they are not well resolved from one another due to the nature of the sampling method.

Alumina supported catalysts could be distinguished from one another pre-calcination on the basis of their infrared spectra, with obvious differences in the region 1300 cm^{-1} – 1800 cm^{-1} and at *ca.* 2900 cm^{-1}. Of note were the carbonyl vibrations, which appeared shifted to lower energies relative to the polymer on its own (from 1768 cm^{-1} to 1676 cm^{-1} for the PVP-Pd/Al_2O_3 catalyst; 1702 cm^{-1} to 1636

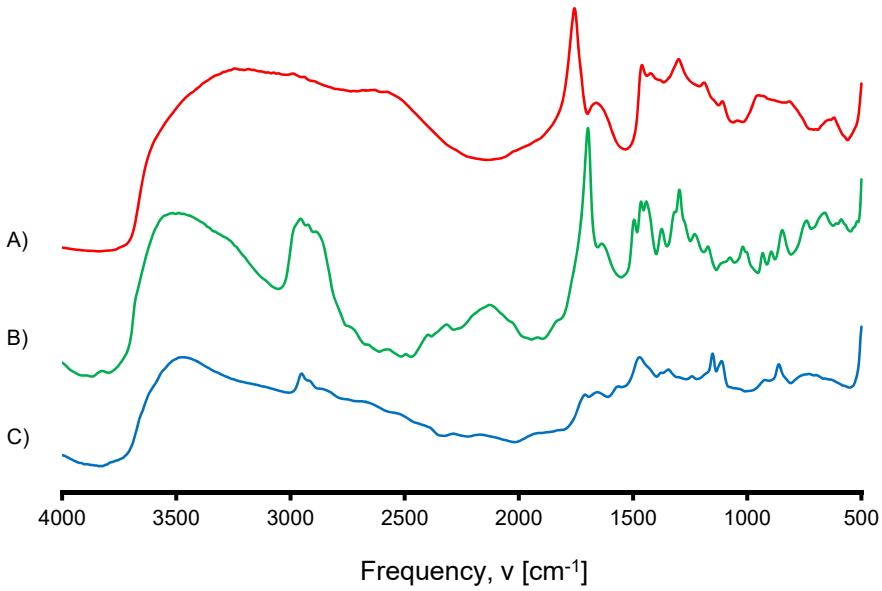

Figure 113: FTIR spectra of poly(vinylpyrrolidone), poly(acrylic acid), and poly(vinyl alcohol). Samples are A) PVP, B) PVA, C) PAA.

cm^{-1} for the PAA-Pd/Al_2O_3 catalyst). These both represent significant shifts from the pure polymer powders, and thus suggest that the carbonyl is implicated in bonding the polymer to either the metal particles or to the surface of the alumina itself. Upon calcination the bands belonging to the polymers are removed, and the spectra become similar to the native support. Examples are shown in **Figure 114**.

The silica-supported catalysts showed considerably greater variation than the alumina-supported catalysts, with band shapes and background slopes significantly different between – and even *within* – different catalysts. Example spectra are given in **Figure 115**. The high energy ends of the spectra were all similar to one another, with few differences between the different catalysts, the only significant difference being weak methylene bends observed in the PVA catalyst. At the low energy end of the spectra the shapes are predominantly that of silica, with weak superimposed bands corresponding to the polymers observed in different cases. The major difference was PVP, which shows various medium-strength bands including a strong carbonyl vibration at 1698 cm^{-1}. The calcined catalysts once again gave spectra fairly similar to the native support prior to calcination.

The differences within catalysts may be ascribed to the inhomogeneous coating of the silica particles, which is clearly observable in the photomicrographs. This would alter the optical properties of some particles over others, leading to differences in the

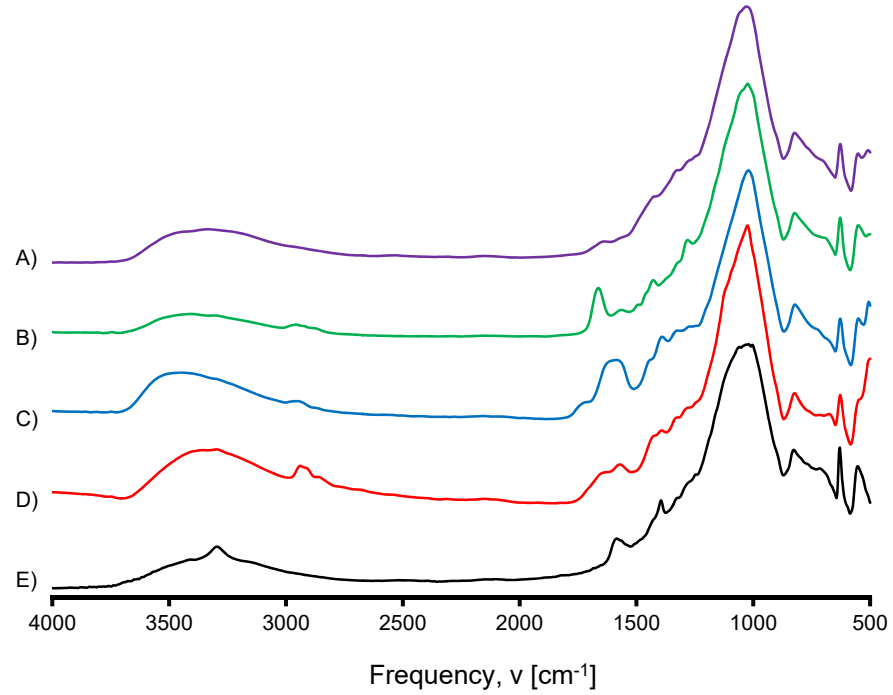

Figure 114: FTIR spectra of alumina-supported catalysts prepared from polymer-stabilised colloids. Samples are A) Calcined PAA-Pd/Al_2O_3, B) PVP-Pd/Al_2O_3, C) PAA-Pd/Al_2O_3, D) PVA-Pd/Al_2O_3, E) pristine Al_2O_3.

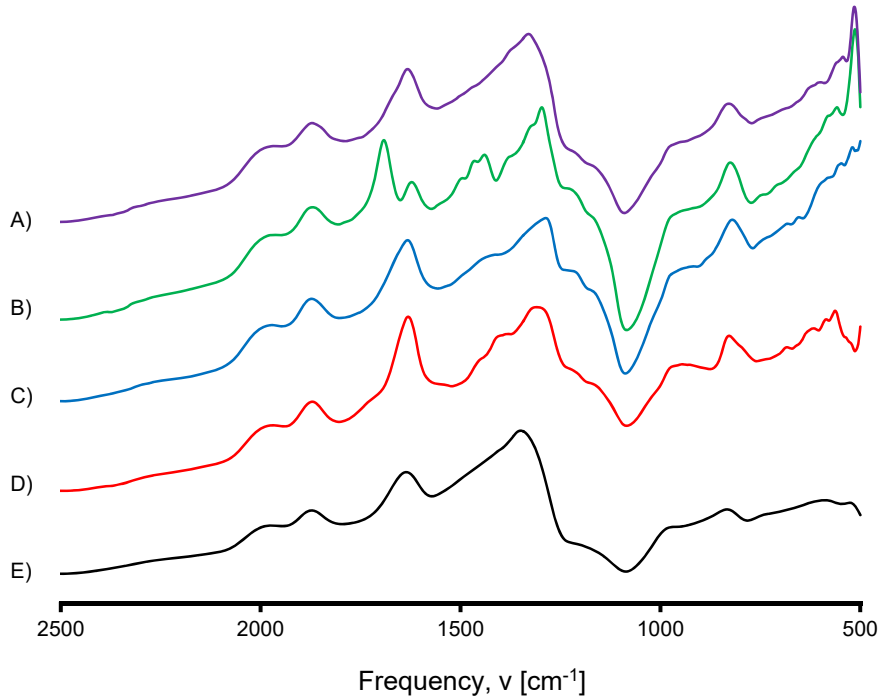

Figure 115: FTIR spectra of silica-supported catalysts prepared from polymer-stabilised colloids. Samples are A) Calcined PAA-Pd/SiO_2, B) PVP-Pd/SiO_2, C) PVA-Pd/SiO_2, D) PAA-Pd/SiO_2, E) pristine SiO_2.

IR spectra of different silica particles within a single catalyst. Furthermore, the relative lack of strong polymer bands in the particles may be because of the high surface area of the silica which would generally lead to a thin covering of polymer, except in the case of PVP where its high viscosity may inhibit its penetration into the silica pores, leaving it coating predominantly the outside of the particles.

The spectra for perlite supported catalysts, shown in **Figure 116**, were dramatically different to their parent support material, and to one another. The PAA and PVP protected catalysts exhibited the greatest difference to the native support materials, while the PVA protected catalyst showed almost no difference at all. The 'subsided' looking peak at 1300 cm^{-1} in the PAA protected catalyst was a spectral feature unique to catalysts prepared using that particular polymer, however, and was observed in the pre- and post-calcined samples.

The halloysite-supported catalysts showed by far the most dramatic changes in their infrared spectra between different samples. Examples are shown in **Figure 117**. When the polymer-protected colloids were immobilised onto the perlite, the resulting spectra were once again a superposition of the spectrum of pristine perlite with the major bands from the polymers superimposed on top. There were subtle differences observable between the spectra of catalysts prepared from different polymers, especially PVP and PAA, suggesting the ketone moieties may play some role in binding to the halloysite surface. On calcination, however, the spectra changed completely, losing all polymer-associated bands and any semblance to the original support material, and began to resemble the silica spectra described earlier. The pattern of silanols in the OH region was nearly completely lost, replaced by a broad featureless hump. This suggests that the material is thermally dehydroxylated, which presumably happens concurrent with a rearrangement of the structure. This is consistent with a thermal transformation as suggested by the powder diffraction data, and the changes in morphology observed by electron microscopy.

The hydroxyapatite supported catalysts showed similar types of differences to the other catalysts, in that the spectra are generally dominated by apatite bands, but with weak to moderate strength polymer bands superimposed on the top. This is especially evident in the 1200 cm^{-1} to 1800 cm^{-1} region and the 2900 cm^{-1} regions, where the catalysts are clearly distinguishable from one another. The hydroxyl stretching region at 3450 cm^{-1} to 3700 cm^{-1} is especially interesting, since there are a

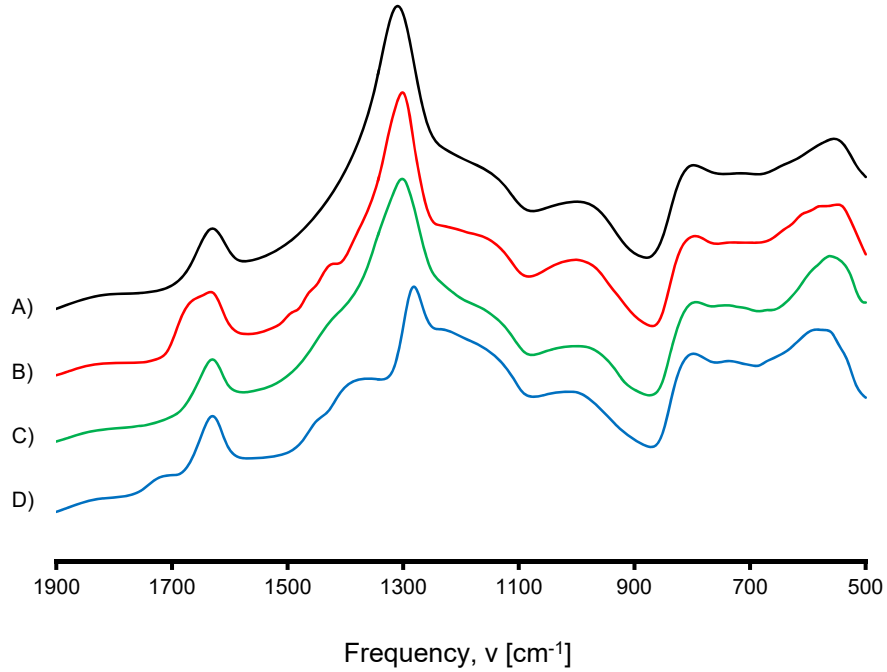

Figure 116: FTIR spectra of perlite-supported catalysts prepared from polymer-stabilised colloids. The four traces correspond to: a) pristine perlite, b) PVP-Pd/PRL, c) PVA-Pd/PRL, and d) PAA-Pd/PRL.

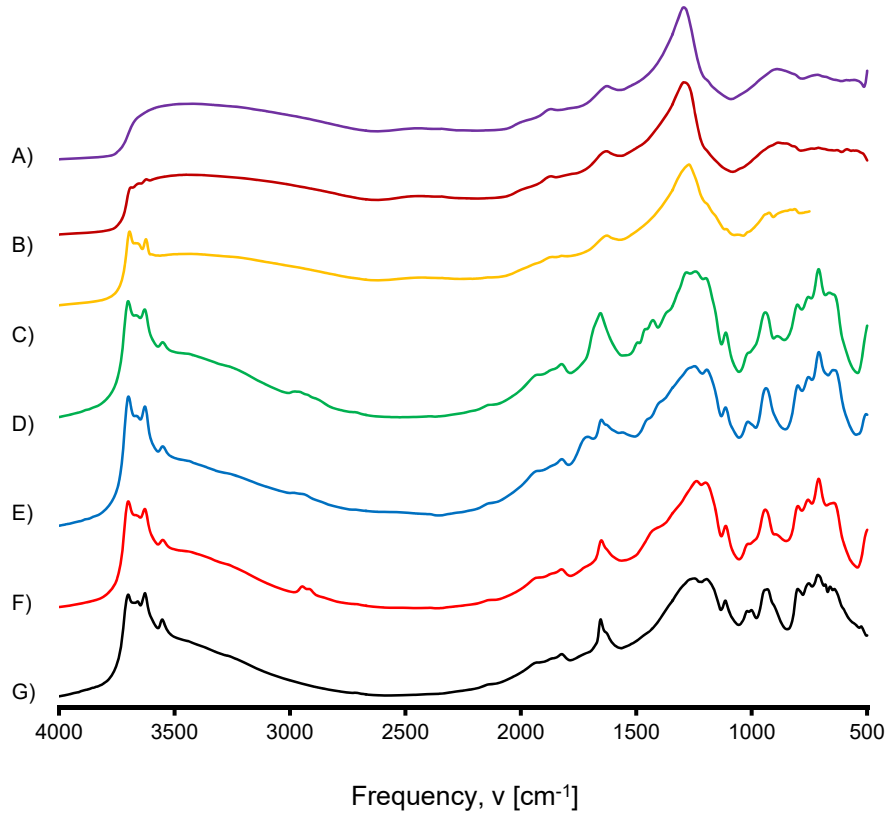

Figure 117: FTIR spectra of halloysite-supported catalysts prepared from polymer-stabilised colloids. The seven traces correspond to: a) calcined PVP-Pd/HNC, b) calcined PAA-Pd/HNC, c) calcined PVA-Pd/HNC, d) PVP-Pd/HNC, e) PAA-Pd/HNC, f) PAA-Pd/HNC, g) pristine HNC.

variety of subtle changes evident in the spectra, namely the appearance of two weak bands on calcination which appear at 3490 cm^{-1} and 3655 cm^{-1}. These almost certainly represent the formation of extra hydroxyl environments, probably due to thermal transformation of the apatite structure, producing species such as $Ca(OH)_2$. Example spectra are shown in **Figure 118**.

The bioapatite supported catalysts showed similar spectral changes to the hydroxyapatite-supported materials, exhibiting high-energy C-H modes, as well as changes in the C=O region. Example spectra are given in **Figure 119**. Compared to the hydroxyapatite supported catalysts which show addition of hydroxyl bands on calcination, the bioapatite supported catalysts show a complete *loss* of the second hydroxyl band at 3695 cm^{-1}. If this band originates from $Mg(OH)_2$ produced by hydrolysis of MgO, then it may be that the calcination step decomposes the $Mg(OH)_2$ back to MgO and H_2O [477].

6.3.3.7 Solid-State NMR

Solid state NMR was shown to be a powerful tool for characterising the catalysts, especially in combination with infrared spectroscopy and x-ray diffraction. The spectra of the catalysts exhibited numerous differences throughout their preparation, both between systems prepared using different polymers, and between systems which had or had not undergone calcination. For some systems the spectral changes were profound, while in others they were more subtle. In conjunction with data obtained from other techniques many of these changes could be rationalised in terms of known structural alterations, which are discussed on a per-system basis in the following paragraphs.

A cursory analysis of the ^{27}Al spectra of the alumina-supported catalysts showed no obvious differences between any of the samples studied. Highly zoomed spectra, however, showed some subtle differences between the different systems, as illustrated in **Figure 120**. Compared to the pristine alumina, the samples with immobilised colloids arguably exhibit a small decrease in the portion of Al(IV), suggesting it is a surface-related species. The weak peak at 25 ppm was also decreased significantly in intensity, though its origin is unknown. The ^{1}H spectra displayed a broad resonance at ca. 4.7 ppm which is removed on calcination, possibly corresponding to adsorbed water or some minor surface hydroxyl formation. Regardless, the changes observed

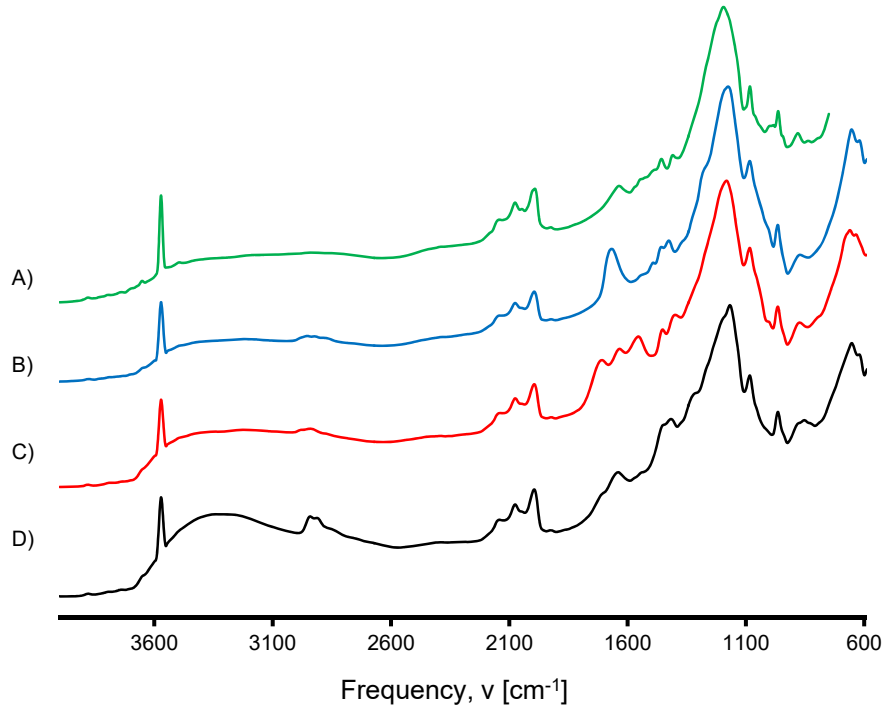

Figure 118: FTIR spectra of hydroxyapatite-supported catalysts prepared from polymer-protected colloids. The four traces correspond to: a) calcined PVA-Pd/HAp, b) PVP-Pd/HNC, c) PAA-Pd/HNC, d) PVA-Pd/HAp.

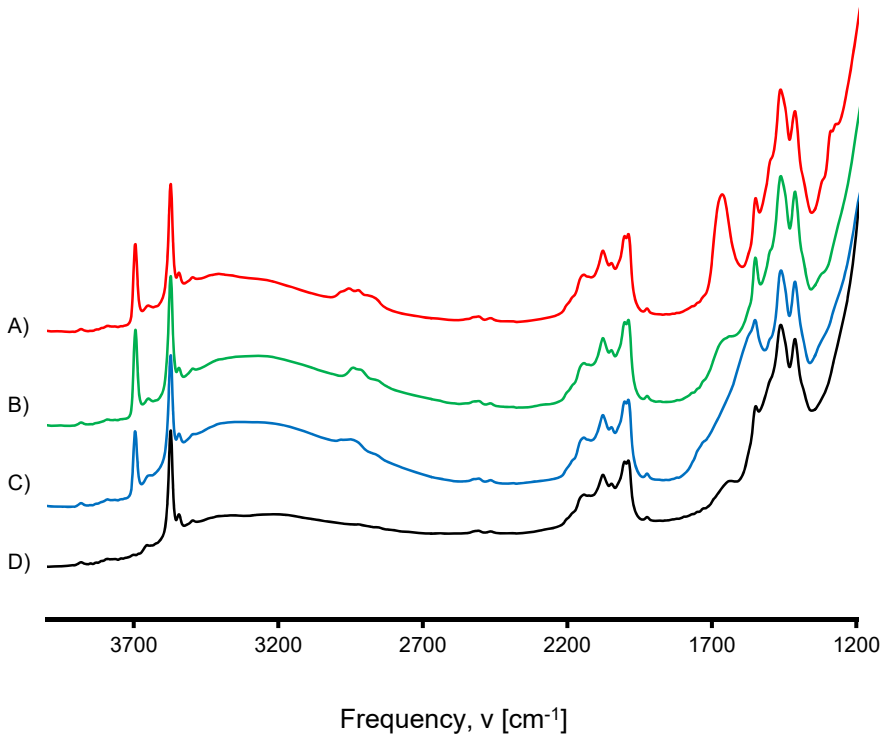

Figure 119: FTIR spectra of bioapatite-supported catalysts prepared from polymer-protected colloids. The four plots correspond to A) PVP-Pd/BAp, B) PVA-Pd/BAp, C) PAA-Pd/BAp, and D) calcined PVA-Pd/BAp.

were relatively subtle, indicating the material is stable throughout the synthetic process.

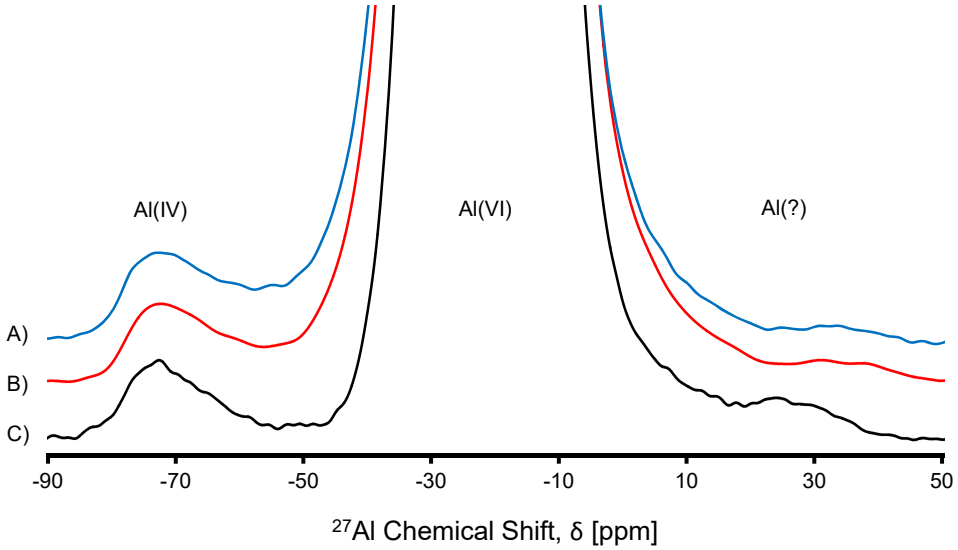

Figure 120: ^{27}Al DPMAS NMR spectra of PVA-Pd/Al_2O_3 catalysts. The three traces correspond to the non-calcined sample (A), the calcined sample (B), and pristine alumina (C).

The silica supported catalysts also showed relatively few differences in their NMR spectra. The most significant changes were observed in the ^{1}H spectra of the samples, which showed greatly decreased water peaks in the calcined samples, similar to the ^{1}H spectra for the catalysts described in the previous chapter. Different intensity ratios between the water peaks and the silanol resonances were observed between different polymers, also, which is consistent with their differing degrees of hygroscopicity, as seen in the ^{1}H spectra shown earlier in **Figure 96**. Any potential differences in the ^{29}Si spectra were difficult to confirm with certainty because of the poor signal to noise.

The halloysite-supported catalysts showed significant changes to their ^{27}Al spectra, and to a lesser extent their ^{1}H and ^{29}Si spectra. Upon immobilisation of the nanoparticles the silanol resonance decreased in intensity relative to the aluminol resonance, and on calcination the two further merged into a single broad-topped peak. The ^{27}Al spectra showed that on immobilisation there is a very small increase in the relative amounts of the Al(V) and Al(IV), in the order of 1%, while on calcination the two increase dramatically in intensity. The ^{29}Si resonance broadens

simultaneously, suggesting minor phase changes at the surface on immobilisation, but dramatic structural rearrangement when the samples are calcined. Similar changes were observed by Smith *et al.*, [478] who attribute the changes to dehydroxylation resulting in changes to the coordination number, which occurs during the thermal transition from halloysite to meta-halloysite and then to the mullite-cristobalite mixtures formed at higher temperatures. Curiously, the extent to which the spectra changed in this study depended on which polymer was used – the PVP-Pd/HNC catalysts (**Figure 121**) showed the greatest degree of change, and the PAA-Pd/HNC catalysts the least. This is consistent with the powder diffraction data which shows bulk phase changes, and the infrared data which shows significant changes to the vibrational bands present, and the morphological changes observed by TEM.

Several changes were evident in the NMR spectra of the hydroxyapatite catalysts which were generally the same regardless of the polymer. In the ^{1}H spectra a progressive narrowing of the structural OH peak was evident, progressing from a width of 0.48 ppm in the pristine support to 0.41 ppm on colloid immobilisation and 0.39 ppm on calcination. The broad water peak at *ca.* 5 ppm also changed, beginning at 2.3 ppm FWHM in the pristine support, increasing to 13.4 ppm on colloid immobilisation, and then then returning to 2.4 ppm upon calcination, but with a much greater intensity. In the ^{31}P spectra a progressive reduction in the intensity and complexity of the low-intensity peaks at the base of the phosphate peak were observed, as well a progressive increase in the phosphate peak width from 0.64 ppm in the native support, to 0.68 ppm on immobilisation, to 0.74 ppm on calcination.

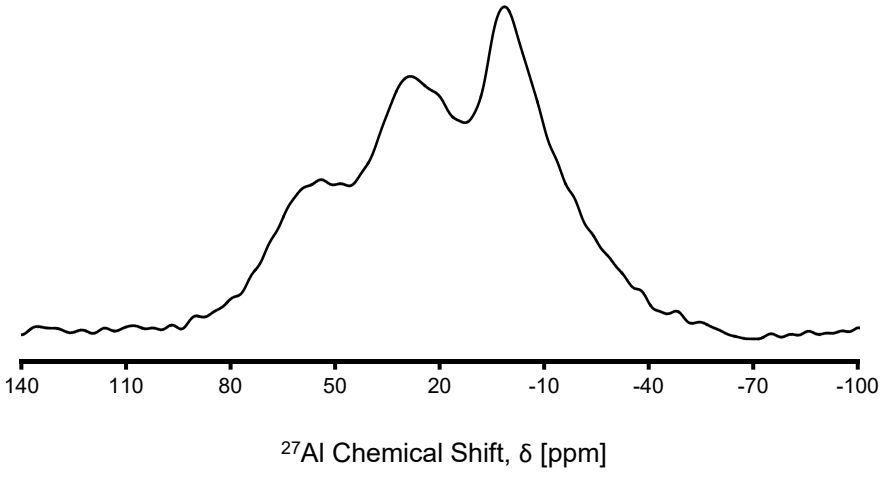

Figure 121: ^{27}Al DPMAS NMR spectrum of calcined PVP-Pd/HNC.

The change in adsorbed water content is consistent with the presence of the polymer coatings, which are hygroscopic and thus produce typical 'adsorbed water' features. The changes in the structural OH width, however, may initially suggest either an increase in the overall crystallinity of the sample, or a removal of less crystalline apatitic species, likely associated with the surface. The increase in width of the phosphate peak, however, precludes a bulk crystallinity increase, since this should narrow both the phosphate and hydroxyl peaks. Combined with the obvious loss of the non-apatitic phosphate environments evident in these spectra, shown in **Figure 122**, the alteration of surface species thus seems more likely, especially combined with the lack of observable changes to the powder diffraction patterns., which suggest no bulk composition changes. The infrared spectra, however, show two additional but weak hydroxyl bands suggesting the formation of extra species, possibly due to thermal transformation of the non-apatitic surface species. These would not be expected to change with temperature were they HAp, because both HAp and carbonated HAp are thermally stable until around 800 °C to 1200 °C [479, 480].

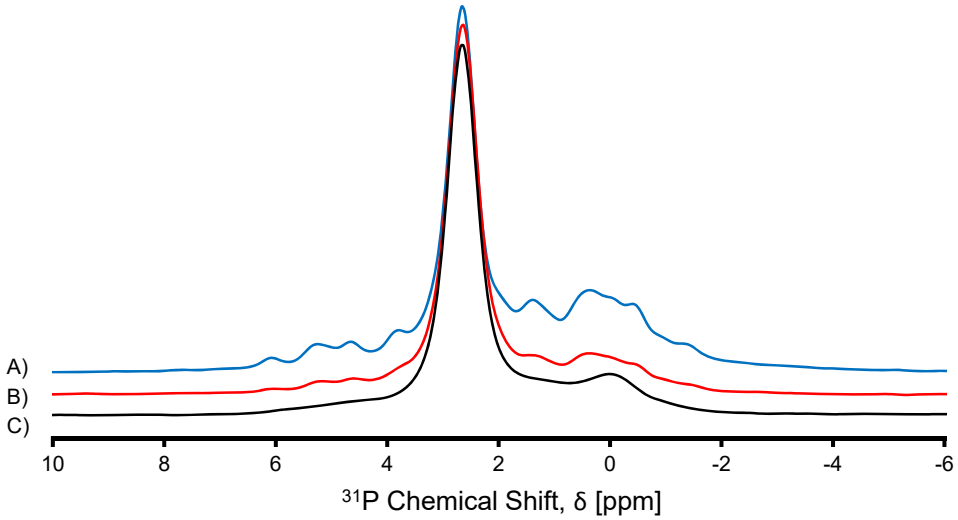

Figure 122: ^{31}P DPMAS NMR spectra of the PVA-Pd/HAp catalysts. The three traces correspond to a) pristine HAp, b) non-calcined PVA-Pd/HAp, c) calcined PVA-Pd/HAp.

The bioapatite supported catalysts showed relatively few changes to their NMR spectra compared to the hydroxyapatite supported catalysts. The ^{31}P spectra showed no obvious changes to their spectra throughout the preparation of the materials, regardless of whether cross polarisation or direct polarisation was used. No clear

changes to either the number or position of peaks present were observed, nor their widths or intensities. The ^{1}H spectra showed the same changes in the water peak as the hydroxyapatite catalysts, but no changes to the structural OH peak. Two extra protons environments were observed in the calcined catalysts, however, in the form of two weak but sharp peaks at 1.32 ppm and 4.80 ppm. This is interesting since it shows the opposite trend to the infrared data, which indicates that the hydroxyl (and thus proton) environments are dramatically reduced on calcination in these samples. The lack of appearance of these new environments in the infrared could simply be due to a lack of sensitivity, however the lack of any discernible disappearance of a proton environment in the ^{1}H NMR spectra is otherwise difficult to explain.

Perlite catalysts showed the fewest changes to their spectra of all, with no differences evident in either the ^{29}Si or ^{27}Al spectra. The width of the 4.5 ppm water peak was observed to increase on colloid immobilisation, as with those catalysts described previously, but was reduced again on calcination.

6.3.3.8 Catalytic Activity

Varying levels of activity were exhibited by the catalysts tested. The supported palladium catalysts, though highly active, required a significant induction period after introduction to the reactor before hydrogenation commenced. During the first thirty minutes they remained the brown colour associated with the calcined (and oxidised, according to the XPS and XRD results) PdO species, but changed rapidly to a dark grey or black colour at around 45 minutes. After addition of the cyclohexene its hydrogenation proceeded rapidly as assessed by GC-MS. This behaviour is consistent with an *in-situ* reduction from PdO to metallic Pd, since PdO itself is not catalytically active but Pd is. As with the previously tested catalysts the reactions produced cyclohexane only, with no side products detected by GC or NMR. Reaction rates were linear in all instances, with a drop in activity toward 90% conversion, presumably due to the decrease in substrate conversion brining about a mass transfer limit.

As contrast to the Pd catalysts, the Rh and Pt catalysts tested displayed no detectable activity at all. Even with an extended induction period of 2 hours at an elevated temperature of 40 °C no substrate conversion was observed in any instances. In the case of the rhodium catalysts this may simply be ascribed to an

inability to reduce the surface sesquioxide into the catalytically active metallic Rh, but for Pt the XPS results indicated no detectable increase in oxidation on calcination. It could be the case therefore that the platinum surfaces are either poisoned during the calcination step, or at least made more sensitive to poisoning by the same step. It is unclear from the XPS results what the nature of the poison may be if the former case is true, since there is relatively little change to either the C 1s or O 1s core level spectra, and therefore the latter may be more likely to be true. It could be of interest in the future to record XPS spectra of the B 1s region, since borane reagents are shown to passivate metal surfaces against catalytic activity [481].

Amongst the Pd catalysts a wide range of activities were observed, which are given in **Table 28**. The bioapatite supported catalysts showed no detectable activity whatsoever, while the alumina supported catalysts showed mild activity of *ca.* 1000 hr^{-1}, and all other catalysts displayed impressive levels of activity up to nearly 42,000 hr^{-1} as seen with the PVP-Pd/SiO_2 catalyst. The results indicate that not only is the choice of support material is important in producing a highly active catalyst, but the polymer choice has a significant effect also. This can be assessed by looking at the variation in activities between catalysts with the same support but prepared using different polymers; this is evident with the alumina and silica supported catalysts, both of which show relatively poor activity when PAA is used as the preparative polymer, compared to PVA or PVP. It should be noted that the same trends are not observed with the specific rate, which is not area-normalised like the turnover frequency. In terms of moles per hour of substrate turned over, the trend is much less clear.

Compared to other reported studies involving cyclohexene hydrogenation the activities reported herein are in many cases significantly higher. Comparison may be made between these and the values given in **Table 15** (Chapter 5), which are shown side-by-side in Appendix 4. Considering the reactions are performed at standard temperature and pressure, these results represent some of the fastest reported catalysts for cyclohexene hydrogenation yet, based on the absence of any more active catalyst reported in the literature. Substantial increases could be gained by replacing the calcination step with some other method of removing the capping polymer layer; specifically one which will not cause particle growth. Possibilities include an oxidising wash, for example with weakly acidic H_2O_2, or a low-temperature heating in an

Table 28: Activity of palladium catalysts prepared from polymer-protected colloids in the hydrogenation of cyclohexene.

Support	Polymer	Specific Rate [mmol g^{-1} hr^{-1}]	Turnover Frequency [hr^{-1}]
Al_2O_3	PVA	1,310	1,450
	PAA	296	200
	PVP	1,210	1,230
SiO_2	PVA	9,290	31,400
	PAA	4,670	3,890
	PVP	4,130	41,900
HAp	PVA	23,100	15,600
	PAA	12,720	14,600
	PVP	5,710	7,320
HNC	PVA	25,900	23,000
	PAA	7,230	9,690
	PVP	20,700	30,000
PRL	PVA	19,800	21,000
	PAA	8,790	10,300
	PVP	13,600	12,300
BAp	PVA	0.00	0.00
	PAA	0.00	0.00
	PVP	-	-

oxygen-rich environment to catalytically oxidise the polymer layer and convert it to CO_2.

In spite of the high activities described hitherto, the total lack of activity of the bioapatite-supported catalysts was considered unusual, especially given the remarkable activity of the hydroxyapatite-supported catalysts. The two materials are spectroscopically very similar, at least in terms of their bulk structure, which rules out some kind of bulk chemical effect as the reason for the activity differences. The bioapatite also has better wetting properties than the hydroxyapatite as shown by the results presented in Chapter 3, which rules out an inability for the solvent to wet the catalyst. No coatings were evident on the supported nanoparticles by TEM, which means at least that if the particles are enshrouded in something it is a very thin layer. The zeta potentials of the pristine supports, however, are slightly different from one

another, which suggests it could be a surface chemical effect. This may be due to some residual surface Brønsted basicity from the preparation of the material. Calcination of bone produces CaO which could be the species responsible, but CaO is not necessarily a total catalyst poison, since Au/CaO catalysts have been reported as active in epoxidation reactions [482], though since these are oxidative in nature, their behaviour may be opposite under reducing conditions.

Also of interest for further investigation is the anomalously low turnover frequencies of the alumina and silica-supported catalysts prepared from polyacrylic acid-stabilised colloids. Since their particle sizes are similar to the other catalysts it is not simply a case of an insufficient area of metal upon which the reaction may take place, nor is it a case of an insufficient amount of metal, since it shown by LIBS to be similar to the other two catalysts. Polyacrylic acid itself does not inhibit the activity of palladium, either, since it has been shown to be an effective grafting agent in previously reported catalysts [483]. Furthermore, it cannot be the case that polyacrylic acid poisons the palladium surface somehow, since when the same colloid is immobilised on other support materials the resulting catalyst is highly active.

6.4 Summary

The work detailed in this chapter shows conclusively that pre-generated colloidal dispersions of polymer-stabilised metal nanoparticles are appropriate precursors for the synthesis of support metal catalysts. It has been shown by a combination of UV/Vis, PCS, and TEM that the choice of polymer as a protecting agent for these colloids heavily influences the nature of the colloidal particles, specifically their state of aggregation, and that these characteristics are generally preserved when the colloids are immobilised onto support materials. Different immobilisation methods were further shown to produce catalysts with different textural properties, and thus this is a critical step in obtaining catalysts with homogeneous metal distributions and high loadings.

Air calcination was shown to be efficient at removing the polymer layer to reveal the metal particles, although it was also shown by XPS and XRD that this significantly oxidised the supported particles, the extent depending on the nature of the metal itself. Introduction of the catalysts to the hydrogen-rich environment of the reactor allowed re-reduction of the palladium catalysts to their active form after a

significant induction period, but not the rhodium or platinum catalysts. The majority of the palladium catalysts were shown to be highly active for the hydrogenation of cyclohexene, with turnover frequencies usually in excess of 10,000 hr^{-1} and up to 40,000 hr^{-1} in select instances. Not only do these results compare favourably to previously reported accounts of cyclohexene hydrogenation, but the activity of the catalysts using novel support materials compare favourably to those using traditional alumina or silica. The exception to this rule was the bioapatite supported catalysts, which showed no detectable activity.

Characterisation of the catalysts was performed using a combination of x-ray powder diffraction, solid-state NMR, infrared spectroscopy, TEM, and for the first time, LIBS. These instrumental methods showed that the immobilisation and calcination steps affected the physical and chemical properties of the support materials to various extents; for example alumina was shown to be stable throughout the entire process, while halloysite was found to decompose into meta-halloysite during the calcination step.

6.5 Recommendations for Further Research

There are several branches of further investigation which may be pursued following the research presented in this chapter. The greatest question is why the Rh and Pt catalysts were inactive, while their counterparts from the previous chapter are. It may be that the calcination step induces unfavourable changes to the surface chemistry of the particles, in which case further XPS analysis may be valuable. Alternately the use of probe molecules may be of some utility, for example absorption of CO and its detection by either NMR or FTIR. The same catalysts could also be re-created using alternative reducing agents to check whether the borohydride is providing a passivating coating. Different methods for removing the polymer coating may also be investigated, for example H_2O_2 treatment.

As the Pd catalysts were found to be highly active, extending studies on these particular catalytic systems would be of value. Improvements could be made to the textural properties of the catalysts, for example by improving the distribution of metal and reducing the size of the metal particles. This could be achieved by investing other protective polymers, for example the non-cyclic amide polyoxazoline. The aggregation behaviour of the colloid precursors and their sorption properties

may also be altered by investigating alternative solvent systems, which are known to affect properties such as the radius of gyration of the polymers. Once again, the data from Chapter 3 should be considered to maximise the wettability of the solvent system chosen. It is also of interest, of course, to investigate what other reactions the catalysts may be active for – alcohol oxidations, or carbon-carbon coupling reactions, for example. Alternative immobilisation methods could also be pursued, especially to avoid binding of the polymer to the inside of the preparative flasks, as encountered in this research.

Several other methods of characterisation may also be of interest, specifically to probe the interaction between the polymer and the support surfaces. Various methods such as grazing incidence x-ray diffraction, x-ray reflectivity, or ellipsometry methods could be of use. Infrared spectroscopic measurements could also be extended, for example by studying the specular reflectance spectra as a function of incidence angle. High resolution solid-state NMR could also be considered, using spectral enhancement methods and long acquisition times. It could also be of interest to correlate the metal loadings obtained by LIBS to those from an alternate method for the purposes of further method validation. Infrared mapping of the samples could additionally be used to map the intensity of the C=O stretches in the samples, which may give some further insight into the nature of the polymer coatings and their homogeneity within the samples. Raman spectroscopy could also be used to directly observe metal oxide vibrational modes, for example in PdO and Rh_2O_3, further backing up the evidence obtained by XPS and XRD that the calcination induces oxidation of the metal particles.

Chapter 7: Catalysts Prepared from Solvent-Stabilised Colloids

7.1 Introduction

In Chapter 6 of this thesis, the possibility was explored of using colloidal dispersions of polymer-stabilised metal nanoparticles to produce supported metal catalysts. Although this was shown to be a feasible synthetic route, subsequent removal of the polymer layer by calcination was shown to be problematic. Critically, this step was shown to oxidise the catalytically active palladium particles to inactive palladium oxide, induce crystallite growth, and cause phase transitions in selected support materials. It was clear, therefore, that there was a need to develop a synthetic route which conferred all the advantages of the previously studied colloidal route, but did not suffer from the same drawbacks. If metal colloids could be produced using a more labile and easily removable stabilising agent, this would present a viable solution to the problem.

A class of metal colloids which may satisfy these criteria are those stabilised by solvent molecules. A small number of reports have shown metal nanoparticles to be anomalously colloidally stable in selected polar organic solvents, even without the addition of extra protecting agents. For example, Pd colloids are stable in propylene carbonate [484], while Pt, Rh, and Ru are stable in alkaline ethylene glycol [485], Au is stable in DMF [486], and in previous work by the Author Rh and Pd were shown to be stable in DMF and DMSO [364]. If nanoparticles stabilised by organic solvents could be immobilised onto appropriate support materials, it may be that the solvent molecules could subsequently be removed by the application of gentle heat, a vacuum, or even the flow of dry air. This could produce catalysts of similar activity to those described in the previous chapter, but without any of the same drawbacks. No previous reports describe such a process, however, making this an interesting avenue of research to pursue.

In many of the previously described examples, the exact mechanistic nature of the stabilisation is unknown. Since there are only two general methods of stabilising colloidal particles, the options are somewhat limited. The first is that the solvents modify the surface properties of the particles, increasing the surface charge and

therefore the repulsive force between particles. This seems unlikely, however, as the solvents have dielectric constants less than water, and thus cannot support an electrical double layer to the same extent. The second option is that the solvent molecules bind to the surface of the metal particles, providing a thin but adequate layer of steric protection. In this sense they may be considered like ligand-stabilised nanoparticles, which is a well-developed field [487-489]. Solvent molecules may bind in similar ways as polymers with analogous structures; for example, PVP is shown to bind to the surface of platinum nanoparticles by coordination through the lone electron pairs on the amide nitrogen or carbonyl oxygen atoms [490], and so it may be imagined that molecules of DMF or similar amides may behave analogously. The polarity of the solvent is therefore important, as polar solvents tend to be better ligands, and should therefore provide greater protective ability. This has been confirmed in a study by Esumi *et al.,* who reported the synthesis of palladium nanoparticles in organic media, and found the stability to be proportional to the dielectric constant of the solvent [491].

Though the mechanism by which the solvents stabilise the particles against aggregation may be hypothesised, the exact combinations of which solvents should be used with which metals are unclear, and needs to be explored further. In the current research, a systematic investigation was therefore undertaken to assess the efficacy of a series of organic solvents to stabilise rhodium, palladium, and platinum nanoparticles. Selected systems were explored in greater depth, and different methods were trialled for immobilising them onto support materials. The resulting catalysts were tested using cyclohexene hydrogenation as a probe reaction, and were characterised by a combination of transmission electron microscopy (TEM), x-ray powder diffraction (XRD), Fourier transform infrared microscopy (FTIR), and laser induced breakdown spectroscopy (LIBS).

7.2 Experimental

7.2.1 Experimental Methods

As a first experiment, an initial set of 'screening trials' were conducted to determine which solvent systems would be suitable for the stabilisation of which colloidal metals. A total of 29 different solvents were tested for their ability to stabilise rhodium, palladium, and platinum colloids, generated using one of two

different reducing agents, giving a total of 174 colloids (29 solvents x 3 metals x 2 reducing agents). The solvents chosen are listed in **Table 29**, along with relevant physical properties expected to affect their ability to act as stabilising agents. As the reducing agents and metal salts required for these experiments are only soluble in selected solvents, the decision was made to prepare them as aqueous solutions, but undertake the reductions in mixed-media composed of part water and part organic cosolvent. Without knowing *a priori* what ratio would be most appropriate, the cosolvent fraction (referred to herein as φ) of 0.5 was selected, representing equal volume fractions of water and organic solvent.

To make each colloid, a 50 mL beaker was charged with 7.00 mL of Type 1 water, 8.00 mL of an organic solvent, 300 μL of a 0.03 mol L^{-1} metal stock (either $RhCl_3$, Na_2PdCl_4, or K_2PtCl_4), and a magnetic stirring flea. While stirring, 700 μL of a 0.03 mol L^{-1} reducing agent (either $NaBH_4$ or N_2H_4) was added dropwise, and the resulting colloids were stored at 4 °C indefinitely. Qualitative observations were made visually on the rate of aggregation, as assessed by changes in turbidity, as well as the amount of particulate matter settled from the colloids after fixed time periods. This work was conducted by an intern under instruction and supervision of the author[2].

After assessment of the stability of the colloids, a small number of the most stable systems were selected for further analysis. Two main factors were anticipated to affect the stability of these colloids: the concentration of metal they contained, c, and the proportion of the cosolvent, φ. If the solvent molecules are truly playing a protective role, then it was considered a greater cosolvent concentration may bring about a greater protective ability. Similarly, the greater the number of metal particles in solution the more frequent inter-particle collisions would be, and the greater the aggregation rate [492]. Optimisation of the synthetic conditions by control of these parameters was considered essential in order to subsequently produce catalysts with the maximum activity, and so two sets of experiments – the second and third experiments of this chapter – were undertaken to investigate their effects.

In the second experiment, Pd colloids of equal concentration were prepared in mixtures of water and N-methyl-2-pyrrolidone (NMP) of varying proportions ($0 \leq \varphi \leq 80$). Effects of the cosolvent concentration, φ, were then studied instrumentally

[2] Work undertaken by Gwenaelle LeBlanc, ESCOM (Ecole Supérieure de Chimie Organique et Minérale)

Table 29: Selected properties of organic solvents used in the preparation of solvent-protected colloidal palladium. All data taken from the CRC Handbook [493] unless otherwise specified. *a* taken from [494], *b* taken from [495], *c* taken from [297], *d* taken from [298], *e* taken from [496], *f* taken from [497].

Solvent Name	Relative Permittivity, ε	DN [kcal mol^{-1}]*	Predicted Molar Volume, V_m† [cm^3 mol^{-1}]
Water	80.10	18.0	18.0
N-methyl-2-pyrrolidone	32.17[a]	27.3[c]	96.3
N,N-dimethylformamide	38.25	26.6[c]	82.6
Dimethylsulfoxide	47.24	29.8[c]	71.1
Sulfolane	43.26	14.8[c]	95.3
Acetonitrile	36.64	14.1[c]	54.9
Hexamethylphosphoramide	31.30	38.8[c]	173.5
N,N-dimethylpropyleneurea	36.12[b]	29.6	125.1
3-Amino-1-propanol	-	-	79.2
Glyme	7.30	20.0[d]	107.3
Digylme	7.23	-	146.7
Tetrahydropyran	5.66	22.0[d]	97.5
o-Hydroxyacetophenone	-	-	119.4
Trimethyl phosphate	20.60	23.0[c]	121.3
Hexane-2,5-dione	-	-	121.8
Tetrahydrothiophene	2.28[f]	-	88.2
Oleic acid	2.34	-	313.9
Dimethyl phthalate	8.66	-	-
Diethyl carbonate	2.82	16.0[c]	120.9
Dimethyl carbonate	3.09	17.2[d]	87.9
Butanone	18.56	17.4[c]	91.7
Nitroethane	29.11	5.0[c]	74.3
Pyridine	13.26	33.1[c]	82.7
Morpholine	7.42	17.5[d]	93.5
Propionitrile	29.7	16.1[d]	71.4
Triethanolamine	29.36	-	127.3
Piperidine	4.33	25.4[c]	102.5
Decyl alcohol	7.93	-	191.1
Tetrahydrofuran	7.52	20.0[c]	79.8

* Donor number is a quantitative measure of Lewis basicity [498], representing the absolute value of the heat of formation between the solvent and $SbCl_5$ in CH_2Cl_2, given in kcal mol^{-1}. Formulated by Viktor Gutmann in 1976 [499] † Taken from ChemSpider, as predicted by ACD/Labs Percepta Physchem Module.

to determine whether or not they affected the particle size, or the state of aggregation. This served the primary purpose of finding the NMP concentration at which the aggregation was least, as immobilisation of an aggregated colloid onto support materials was shown in the preceding chapters to produce catalysts with poor activity. Secondly, it served to find how little NMP could be used without the colloids aggregating, which was considered desirable due to the increased price of NMP as a reaction medium over pure water. To prepare the colloids, a 100 mL beaker was charged with 1.00 mL of 0.05 mol L^{-1} Na_2PdCl_4 and sufficient volumes of water and NMP to produce solutions with NMP concentrations of 0%, 20%, 40%, 60%, or 80%. 2.0 mL of 0.05 mol L^{-1} $NaBH_4$ in water was added dropwise with stirring, followed by a 30 minute wait period. The colloids were then analysed instrumentally by UV/Vis and PCS, and TEM.

In the third experiment the effects of the concentration of Pd, *c*, were investigated. Pd colloids were prepared in 80 vv% aqueous NMP in the same way as above, but using $PdCl_2$ in NMP as the Pd source, in final concentrations ranging from 0 up to 0.01 mol L^{-1}. These were also characterised by UV/Vis and PCS in order to determine how much metal could be loaded into a single colloid without incurring significant amounts of aggregation.

As NMP-stabilised colloids are hitherto unreported, it was considered desirable to compare their properties to a similar, more conventional system. For this reason, a fourth experiment was undertaken, preparing a 'control sample' of PVP-stabilised palladium. This system was chosen as similar types of colloids are widely known [399, 500, 501], and moreover, PVP is structurally similar to NMP. A beaker was charged with 100 mL of an aqueous 0.009 mol L^{-1} $NaPdCl_4$ solution containing 50 mg of PVP, and 10 mL of 0.05 mol L^{-1} $NaBH_4$ solution added while stirring. The resulting colloid was then immediately analysed by UV/Vis spectrophotometry to determine its turbidity, in order to determine whether it was more or less aggregated than the equivalent NMP-stabilised colloid.

Once the optimum conditions for generating the colloids were determined, a fifth experiment was undertaken, investigating the optimum way to immobilise the solvent-protected colloids onto appropriate support materials. NMP-stabilised Pd colloids were chosen for this purpose, and immobilised by three methods onto the

four model support materials, SiO_2, Al_2O_3, HAp, and MCC. The three methods chosen were:

- **Adsorption from Excess Solution.** A 50 mL round bottom flask was charged with 0.66 g of support material, 19 mL of 0.0033 mol L^{-1} solution of NMP-stabilised Pd NPs. The solutions were stirred for 24 hours before filtering through Whatman 540 filter paper, and washing with 60 mL of Type-I water.

- **Evaporation.** A 50 mL round bottom flask was charged with the same materials as above, but was connected to a rotary evaporator. The sample was initially heated at 50°C for 1 hour, before raising the temperature to 80 °C and applying vacuum to remove the solvent.

- **Pore-Volume Impregnation.** A 100 mL porcelain crucible was charged with 0.66 g of support material and placed into a sandbath heated to 180 °C. 19 mL of the NMP-stabilised Pd NPs were added dropwise to the support material with stirring, allowing the solvent to evaporate between each addition.

Once the most appropriate catalyst preparation method was chosen, a sixth set of experiments were undertaken using this method to prepare a full suite of catalysts. A total of 24 systems were produced, using all eight of the support materials described in chapter 2, in combination with palladium nanoparticles stabilised by one of the three amide solvents, either DMF, NMP, or DMPU (3 solvents x 8 supports). Three large-scale metal colloids were prepared as the metal sources, as follows: A 1 L beaker was charged with 45 mL of 0.05 $PdCl_2$ dissolved in the appropriate amide, a further aliquot of 310 mL of the relevant organic solvent, and a large magnetic following flea. The solutions were stirred rapidly and chilled in an icebath to 5 °C before the dropwise addition of 200 mL of 0.05 mol L^{-1} $NaBH_4$ to reduce the $PdCl_2$ to its metallic state. The colloids were then used to impregnate the support materials to generate the resulting catalysts.

The catalysts were anticipated to contain a significant concentration of salt, and so a washing step was deemed necessary to remove it. In the interests of studying the properties of the catalysts before and after this step they were split in half, separating

the 3 g of each catalyst into two separate 1.5 g portions. One portion was subjected to a washing procedure (the 'washed' catalysts), and the other portion left unaltered (the 'unwashed' catalysts). The washing procedure involved adding the catalyst to a 15 mL polypropylene Falcon tube with 10 mL of distilled water, vortexing for 20 seconds, centrifuging at 3000 x *g* for 5 minutes, decanting the supernatant, and repeating four more times. The tubes and their contents were dried at 100 °C in a standard laboratory oven, and once dried the powders were transferred to polypropylene vials for storage at room temperature. The washed and unwashed catalysts were then subjected to instrumental analysis, and the washed catalysts tested for their catalytic activity.

7.2.2 Instrumental Methods

Instrumental analysis was generally similar to that described in Chapter 6, with some minor alterations to the parameters for specific instruments depending on their application.

To investigate the optical properties of the colloids, their UV/Vis absorption spectra were recorded. All analyses were performed using either a Cary 1 or Cary 100 spectrophotometer in double-beam mode, with the samples in 5 mm quartz cells using the blank dispersion medium of the colloid as the reference. The absorbance at 450 nm was used as an indirect indicator of the turbidity of the colloids, which has previously been shown to be a reliable index of the state of aggregation of colloidal particles [396]. The PVP-protected palladium colloid used as a reference was too dense to be measured in standard cuvettes, and so a novel sampling configuration was used. Rather than significantly dilute the colloid and risk changing the state of aggregation, it was analysed pressed between two CaF_2 windows in a SpectraTech Presslok holder carefully placed into the beampath of the spectrophotometer. As this was not a fixed-pathlength cell, a method was devised to calculate the pathlength based on the absorbance of the cell in the infrared region. It was placed into a PerkinElmer Spectrum 400 FTIR spectrometer, and the absorbance at 2127 cm^{-1} measured. As the molar absorptivity of water is well known [502], this was used to back-calculate the pathlength using Beer's law.

To collect more direct information on the size of the colloidal particles they were analysed by PCS. All analyses were performed using a Malvern ZetaSizer 3000 HS_A

using glass fluorescence cuvettes, as the recommended disposable polystyrene cuvettes were attacked by polar aprotic solvents like DMF and NMP. Viscosities and refractive indices required for the data analysis were interpolated from the data of Garcia-Abuín *et al.* [503]

The sizes of the colloidal particles, either in suspension or when immobilised onto a support, were measured by TEM. All analyses were performed using a Philips CM-30 operated at 250 kV. Sample preparation was as described in the previous chapters.

The physical structures of the catalysts were investigated by XRD to determine if there were any differences between the washed and unwashed catalysts, and between catalysts prepared from different solvents. All analyses were performed on a PANalytical Empyrean diffractometer as described in Chapter 6.

The catalysts were also investigated by infrared microscopy to determine whether there were any changes to their structures after immobilisation of the nanoparticles. All analyses were performed using a PerkinElmer Spectrum Spotlight 200 FT-IR microscope as described in Chapter 6.

Cyclohexene hydrogenations were also performed as described in Chapter 5, but at 1 atm H_2 and 25 °C. Analysis of the reaction mixtures was performed using an Agilent 7890A GC system equipped with an HP-5 column and coupled to a 5975C MSD, also described in Chapter 6.

Analysis of solvent purities was performed on the GC-MS system described in Chapter 5. To optimise the analysis programme, a composite sample was made composed of 1 drop of each solvent in 100 mL of acetone. The sample was placed in a silanised vial with a PTFE/silicon septum, and 1 μL was injected onto a Zebron ZB-5 column using an autoinjector. The analysis was repeated multiple times, adjusting the parameters between each run in order to observe as many peaks as possible. The final optimised programme had an initial oven temperature of 50 °C, ramped to 300 °C over a period of 10 minutes. Helium was used as the carrier gas at a flow rate of 5 mL min^{-1}. The MSD was operated in total ion mode, but set to scan the m/z range 40 – 200, thus suppressing background noise originating from low-mass ions. Each solvent was then run individually, and the purity calculated as the percentage of the solvent peak to the sum of all observable peaks.

7.2.3 Materials

Metal Salts: Palladium(II) chloride (laboratory reagent, 99%), and rhodium(III) chloride hydrate (laboratory reagent) were obtained from Aldrich Chemical Co., Inc. Potassium(II) tetrachloroplatinate (laboratory reagent, 99%) was obtained from BDH Chemicals Ltd or Precious Metals Online, Monash University LPO, Melbourne.

Reducing Agents: Sodium borohydride (laboratory chemical) was obtained from Asia Pacific Specialty Chemicals Ltd. Hydrazinium hydrate (laboratory reagent, >98%) was obtained from Ajax Chemicals.

Solvents: Dimethyl sulfoxide (synthesis grade, >99.5%) was obtained from Scharlau. N,N-Dimethylformamide (>99.5%) was obtained from Merck Chemicals. Acetonitrile (analytical reagent, >99.5%), and tetrahydrofuran (laboratory reagent, >99.9%) were obtained from Ajax Finechem. 1-Methyl-2-pyrrolidone (anhydrous, 99.5%), hexamethylphosphoramide (99%), 1,3-dimethyl-3,4,5,6-tetrahydro-2(1H)-pyrimidinone (98%), 3-amino-1-propanol (99%), dimethoxyethane (reagent plus grade, ≥99%), bis(2-methoxyethyl) ether (99%), tetrahydropyran (98%) and o-hydroxyacetophenone (97%) were obtained from Aldrich Chemical Co., Inc. Sulfolane (laboratory reagent), trimethyl phosphate (laboratory reagent), triethanolamine (analytical reagent, >98%), piperidine (GPR, >98%), hexane-2,5-dione (laboratory reagent), tetrahydrothiophene (laboratory reagent), tetrahydropyran (laboratory reagent), oleic acid (laboratory reagent, >98%), dimethyl phthalate (laboratory reagent, >99%), diethyl carbonate (laboratory reagent, >99%), dimethyl carbonate (laboratory reagent, >98%), butanone (laboratory reagent, >99%), and nitroethane (laboratory reagent) were obtained from BDH Chemicals Ltd. Pyridine (analytical reagent, >99.5%) was obtained from Ajax Chemicals. Morpholine was obtained from Prolabo. Propionitrile (purum, >97%), and decylalcohol (pract.) were obtained from Fluka Analytical.

7.3 Results and Discussion

7.3.1 Solvent Screening

Attempts at reducing the metal salts in mixed media were met with varying degrees of success. In all cases, the addition of the aqueous reducing agent to the

solutions caused one of three phenomena: either no change was observed, or they became green, blue, or purple, or the solutions became black.

In instances where no changes in colour were observed, it seemed clear that that the presence of the cosolvent inhibited the formation of nanoparticles. Though it was considered outside the scope of the research to determine the exact reason for the inhibition, several theories may be postulated. Firstly, it may be the case that the reduction potential of the reducing agent is insufficient in these solvents to reduce the $PdCl_2$, as the activity of both sodium borohydride [504] and hydrazine [505] are shown to be solvent-dependent. Whether this is an effect of the interaction between the solvent and the reducing agent itself, or whether the solvent increases the reduction potential of the $PdCl_2$ (*viz.*, makes it more negative) is unknown, however. Secondly, it could be that in these systems the reduction proceeds, but the nascent metal nuclei are stabilised against growth by strong adsorption of the solvent molecules, and thus the solution does not blacken. Thirdly, it may be that the cosolvent molecules are preferentially reduced by the reducing agent, leaving the metal salts in their +II, +II, or +IV oxidation states.

In instances where the solutions changed to blue, green, or purple, it is clear that the reducing agent was active, but the formation of nanoparticles was still inhibited. This occurred most notably when $PdCl_2$ was reduced in the presence of acetonitrile. The strong colours of these solutions were reminiscent of charge-transfer bands in coordination complexes, suggesting a similar effect may be responsible for the presently reported phenomenon. Moreover, the observation that the colour change only occurred on addition of the reducing agent suggests the palladium is in a lower oxidation state than Pd(II), for example Pd(0). As hydrazine reduction of $PdCl_2$ in the presence of coordinating ligands is shown to produce Pd(0) coordination complexes [506], it could be that a complex of the type $PdCl_x(MeCN)_y$ is formed, where x is probably 0, and y is probably 4 or 6.

Solutions which turned black, indicating the formation of palladium nanoparticles, exhibited a wide range of stabilities. Some aggregated within minutes, suggesting the solvent confers no extra stability to the dispersions, while some remained colloidally suspended indefinitely (at least over 23 months). Additional discrepancies were observed in their stability when different reducing agents were

used, with some systems being more stable when reduced by hydrazine compared to borohydride, or true of the converse.

Rhodium colloids were generally unable to be produced by reduction of $RhCl_3$ with either borohydride or hydrazine. This is unsurprising for hydrazine since it does not reduce rhodium at room temperature, though the inactivity of the borohydride reducing agent suggests the presence of the cosolvent inhibits reduction somehow. This may occur by lowering the reduction potential, or perhaps by sterically shielding the palladium atoms against reaction with the borohydride. In the handful of cases where reduction took place, the stability of the resulting colloids were poor, showing that in these systems the cosolvent molecules did no confer any extra protective ability to the metal nanoparticles.

The palladium systems were generally much more amenable to reduction than the rhodium. Four solvents yielded colloids with long term stability when prepared by borohydride reduction: MeCN, NMP, DMPU, and morpholine. DMF stabilised palladium for only an hour or so, which is interesting given that the other two amide solvents produced colloids which were stable for several months. Several other combinations yielded moderate stability, while few entirely inhibited reduction. The NMP stabilised colloids were especially stable, being a light brown colour with no evidence of aggregation. Hydrazine reduction on the other hand generally produced less stable colloids.

The platinum systems behaved much like the rhodium solutions, with most solvent systems not conferring any extra level of stability over water alone. Borohydride-reduced colloids were stable in MeOH, DMSO, and morpholine, while none were stable when reduced using hydrazine. Those generated in MeCN, interestingly, formed homogeneous blue and purple solutions, presumably due to the formation of coordination complexes of the type described earlier.

From this initial screening experiment, it was clear that palladium was the only one of the metals worth pursuing for further development. Not only did it yield the greatest number of stable colloids, but palladium colloids were shown in previous chapters to produce the most active catalysts. The anomalously high stability of the amide-stabilised colloids (especially NMP and DMPU) further suggested that these types of solvents may be the most appropriate for stabilising palladium colloids

against aggregation, and would therefore produce catalysts with the most homogeneous dispersions of metal particles. DMF, conversely, exhibited a relatively poor capacity for stabilising the palladium colloids, which was interesting given the three solvents represent a nearly homologous series. Structures of the three are shown in **Table 30**. These were pursued for further method development, and the synthetic conditions optimised to make the most of their stabilising abilities.

Table 30: Names and structures of the three structurally analogous amides chosen for further investigation as reaction media for the synthesis of palladium colloids.

Structure	Abbreviation	Systematic Name
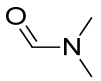	DMF	N,N-dimethylformamide
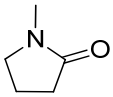	NMP	N-methyl-2-pyrrolidone
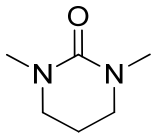	DMPU	1,3-dimethyl-3,4,5,6-tetrahydro-2(1H)-pyrimidinone*

* Alternately called dimethylpropyleneurea, as per the abbreviation.

At this point it was considered of interest to investigate the purity of the solvents in order to determine that it was not a impurity within them which may be responsible for stabilisation of the colloids. Gas chromatographic analysis of the solvents used showed that the majority were of high purity, usually better than reported on the bottle. None of the colloids with the most powerful protective ability exhibited purities of 100%, however, which does not rule out the possibility that the stabilisation is brought about by a minor species present in the solutions. The measured purities for each solvent tested are given in **Table 31**. It could be of interest, in the future, to repeat these experiments with solvents of a higher purity, for example after purification by the methods of Armarego and Chai [507].

7.3.2 Reduction Conditions

Of the three solvent systems chosen for further investigation, the NMP-stabilised colloids exhibited the greatest stability, and so this was chosen as a model system for further development. Though the interaction and stoichiometry of the reaction of borohydride with metal salts in aqueous solution is relatively well known [508, 509], the stoichiometry in NMP is not. It was therefore of interest to assess how much

borohydride was required to fully reduce aqueous NMP solutions of palladium chloride, so that the resulting colloids contained as much Pd(0) and as little Pd(II) as possible.

Table 31: Purities of the solvents used to stabilise metal colloids, as measured by GC-MS.

Solvent	Colour	Reported Purity	Measured Purity
Dimethylsulfoxide	None	>99.5	100
Dimethylformamide	None	>99.5	100
Acetonitrile	None	>99.9	n.d.
N-methylpyrrolidone	None	>99.5	95.0
Sulfolane	Light yellow	>98.0	100
Pyridine	None	>99.5	100
Trimethylphosphate	None	>98.0	100
Hexamethylphosphoramide	V. light yellow	>99.0	100
Triethanolamine	None	>98.0	100
Piperidine	Light yellow	>98.0	100
Dimethylpyrimidinone	None	>98.0	98.8
Aminopropanol	None	>99.0	100
Hexane-2,5-dione	Light yellow	-	49.3
Morpholine	None	-	99.4
Tetrahydrothiophene	Orange	-	94.0
Tetrahydropyran	None	>98.0	98.6
Tetrahydrofuran	None	>99.9	n.d.
Glyme	None	>99.0	n.d.
Diglyme	None	>99.0	n.d.
Propionitrile	V. light yellow	>97.0	96.5
Decanol	None	-	97.3
Oleic acid	Yellow	>98.0	n.d.
Dimethyl phthalate	None	>99.0	99.7
Hydroxyacetophenone	None	>97.0	94.2
Diethylcarbonate	None	>99.0	100
Dimethylcarbonate	None	>98.0	100
Butanone	None	>99.0	100
Nitroethane	None	-	100

Measurement of the A_{450} of the palladium colloids prepared in 50% NMP showed that the turbidity of the system reached a maximum at around 3 mL of reducing agent, as shown in **Figure 123**. This volume represents three mole equivalents of $NaBH_4$ relative to the Pd content, suggesting a 3:1 stoichiometry, assuming that the maximum turbidity represents complete reduction. Comparatively, other M(II) ions like Co(II) have a 2:1 stoichiometry [510]. This suggests the reaction between sodium borohydride and $PdCl_2$ in aqueous NMP is not stoichiometric, since this would require a sixth of the volume used. It may be, however, that the turbidity maximum doesn't necessarily signal complete reduction, but that the peak is a result of particle sintering of some of the suspended particles from the H_2 generated by the catalytic decomposition of the borohydride added [370]. Without information on the speciation of the palladium, however, this is only speculative. Quantitative information could be obtained from the dried colloids after analysis by XPS or similar. Regardless of the nature of the peak, three mole equivalents of $NaBH_4$ were used for all subsequent reductions in the current work.

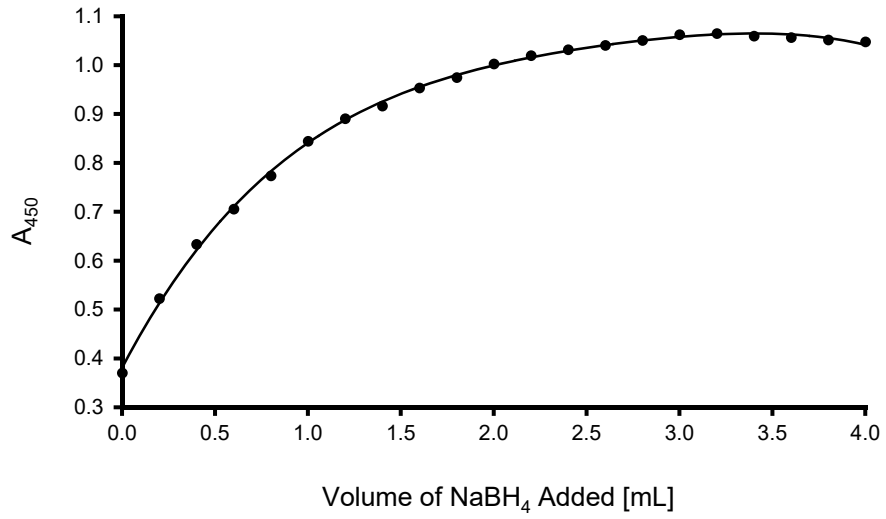

Figure 123: Absorbance at 450 nm of colloidal palladium prepared in 50% N-methyl-2-pyrrolidone as a function of the volume of 0.05 mol L^{-1} $NaBH_4$ added

In the next experiment, the turbidity of Pd colloids prepared in NMP was studied as a function of the NMP concentration, φ. As with the generation of many of the other colloids detailed in this thesis, addition of borohydride solution to the mixed aqueous-organic metal salt solution caused the solution to darken, indicating the formation of metal nanoparticles. The lower the cosolvent concentration the faster the samples appeared to turn dark, suggesting the presence of the cosolvent modifies the reduction kinetics in similar ways to traditional polymers. Allowing the colloids to

stand for 48 hours for their stabilities to 'develop' showed that the amount of metal precipitated was proportional to φ, providing strong evidence for increased stability at higher cosolvent concentrations and increased aggregation rates at lower concentrations.

Spectrophotometric measurements of the colloids showed their absorbance profiles all increased monotonically toward lower wavelengths, with weak shoulders at *ca.* 400 nm corresponding to electronic absorption by unreduced Pd(II) precursor. The optical absorbance at 450 nm therefore contained contributions from both the suspended particles and the Na_2PdCl_4, and so interpretation of these values was made with caution. **Figure 124** shows the absorbance of the colloids at these wavelengths dropped with increasing NMP concentration, suggesting either a continuous increase in stability with φ, or alternatively a continuous decrease in the amount of metal which was reduced. Analyses at higher wavelengths were therefore performed, as these were not 'contaminated' with contributions from the Pd(II) species. At 800 nm, for example, the absorbance initially increases toward *ca.* 50% NMP, before dropping again toward higher concentrations. While these show slightly different trends at low NMP concentrations, it is clear from the data that the lowest absorbances and therefore presumably the least aggregation is attained with the highest NMP concentration possible. As a consequence of this, the decision was

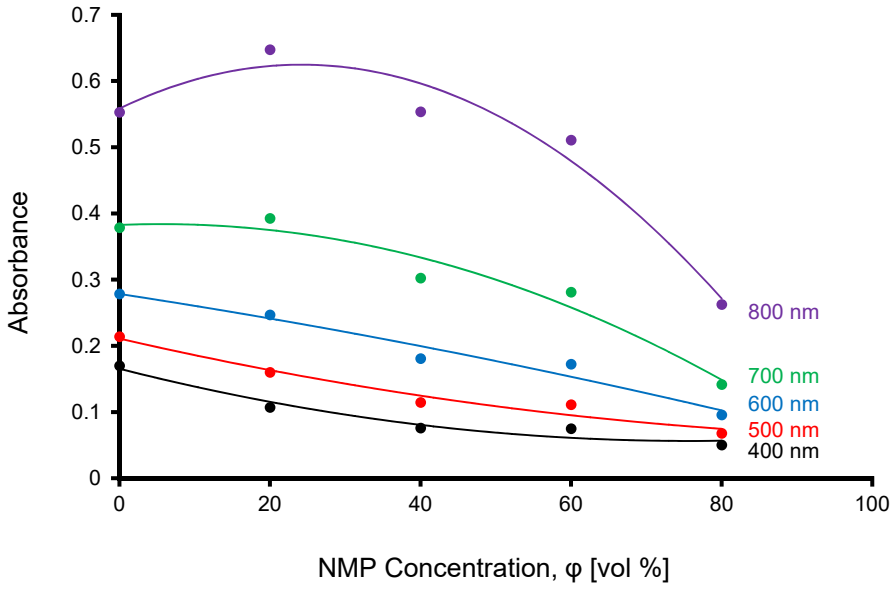

Figure 124: Absorbance at five different wavelengths of palladium colloids prepared in NMP as a function of NMP concentration.

made that all future colloids would be prepared in 80% aqueous NMP, or other amide solvents where appropriate.

In the next experiment, the stability of NMP-stabilised colloids was assessed as a function of metal concentration, *c*. All of the colloids prepared exhibited long-term stability, even those containing the greatest amount of palladium. Spectrophotometric analysis of the colloids showed the turbidity of the colloids depended significantly, but not quite linearly, on the metal concentration. This was considered unsurprising, as the turbidity of a colloidal suspension, other factors aside, is proportional to the number of particles in it [511].

The possibility was additionally considered that the data may carry information on the state of aggregation of the colloids which was being artificially suppressed by the much greater difference in turbidity produced by the variation in metal concentration. To expose this data, it was deemed necessary to normalise the A_{450} values to the metal concentration, by diving the former by the later. A second normalisation to the pathlength of the cell then yields values with units of L g^{-1} cm^{-1}, which may be recognised as similar to the molar absorptivity in L mol^{-1} cm^{-1} traditionally used for homogeneous species. A similar method of analysis was used by Liu *et al.*, who measured the 'extinction coefficients' of colloidal gold nanoparticles [435].

This method of data analysis pivots on the assumption that normalising the turbidity against concentration is a valid step, and that the absorbance increases linearly with concentration as per Beer's law. To check this assumption, the 'control colloid' composed of PVP-protected palladium was diluted several times and analysed by UV/vis to determine if the plot of A_{450} against palladium concentration was linear. The results were modelled well by a linear trend line, as shown in **Figure 125**. This suggests that this particular colloid followed Beer's law, insofar as the absorbances were proportional to concentration.

Though the absorbance was found to be linear with concentration, this does not necessarily indicate that the assumption is valid, as scattering and absorption of radiation by heterogeneous dispersions is non-trivial. For example, Evanoff and Chumanov measured the extinction, scattering, and absorption cross sections for silver nanoparticles of varying sizes using an integrating sphere. They found that though the extinction cross section increased linearly with particle diameter, the ratio

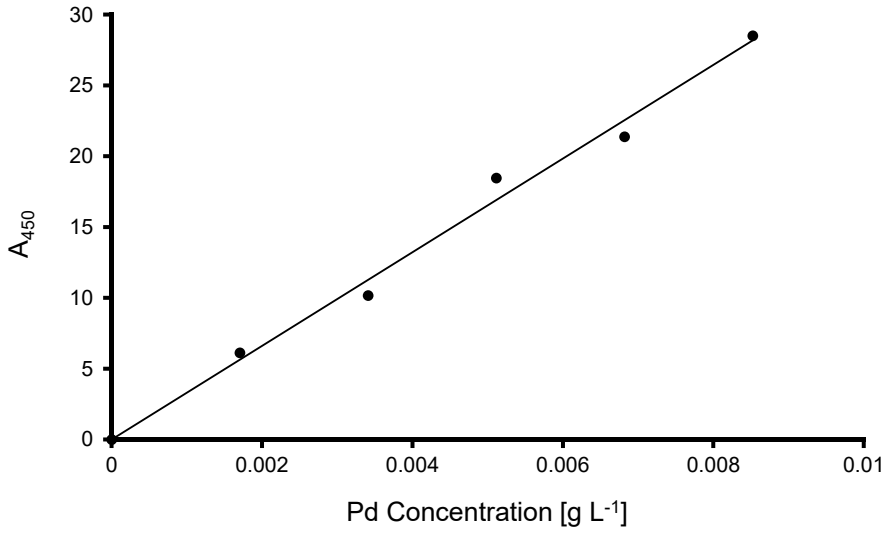

Figure 125: Plot of the absorbance at 450 nm of colloidal palladium as a function of concentration. Linearity is indicative that colloidal dispersions obey Beer's law, despite being non-molecular species to which the law is ordinarily applied.

of extinction to absorption varied significantly, with the optical properties of particles less than 30 nm in size dominated by absorption effects, and those larger dominated by scattering effects [512]. With this caveat in mind, the analysis was pursued regardless. A plot of the resulting values, herein referred to as the 'extinction coefficient', against palladium concentration is shown in **Figure 126**. A similar method of analysis was used by Liu *et al.*, who prepared colloidal gold nanoparticles which had an 'extinction coefficient' similar to that reported here [435].

Since the scattering power of a colloid is *generally* proportional to the particle size, and given the caveats described previously, these data suggest that the amount of

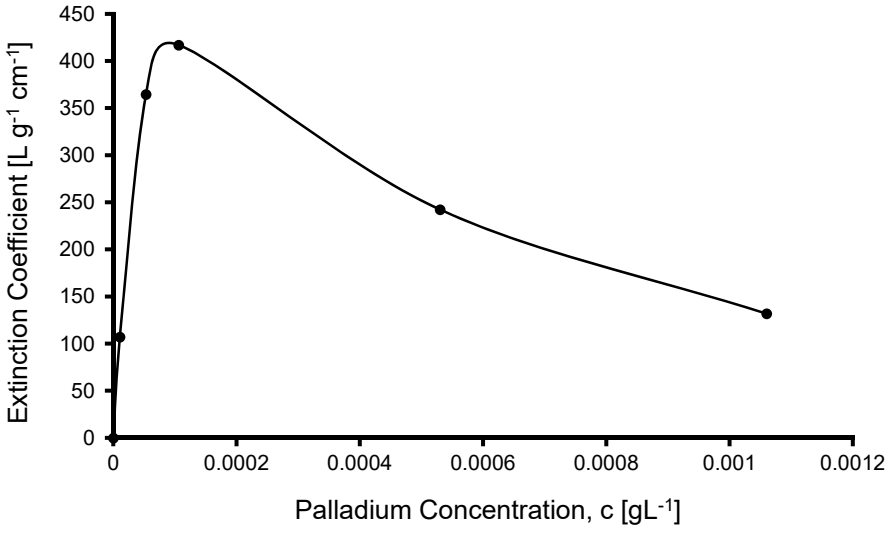

Figure 126: Extinction coefficient of NMP-stabilised palladium colloids as a function of Pd concentration.

aggregation in the colloids increases with concentration, up until it becomes too concentrated and begins to settle out. At this point only 'fines' remain in suspension, and so the extinction coefficient appears to drop again. Analysis of the same colloids by PCS showed the average particle size in suspension decreased with concentration as per the turbidity data. This is illustrated in **Figure 127**. Given the apparent increase in aggregation with metal concentration, the minimum practical metal concentration was used in all subsequent colloids.

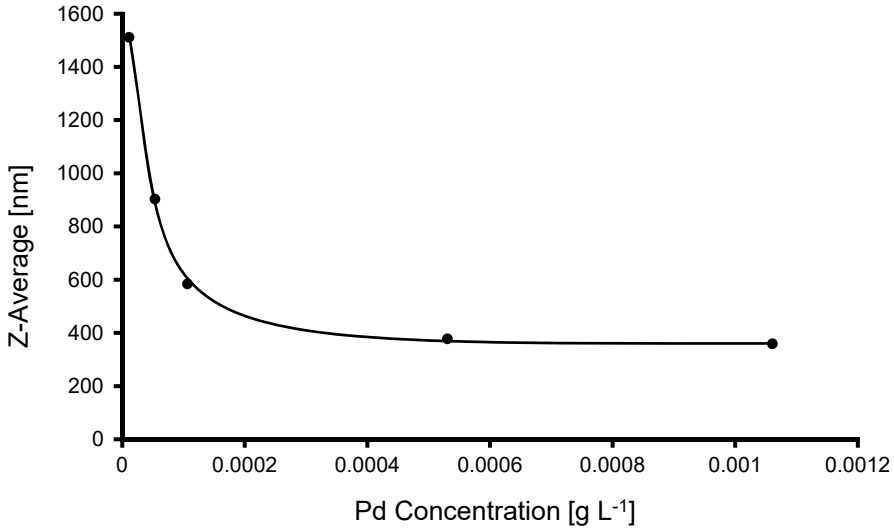

Figure 127: Hydrodynamic radius, expressed as the Z-average, for NMP-stabilised palladium colloids as a function of concentration.

7.3.3 Immobilisation Methods

Using the optimised conditions for generating the NMP-stabilised colloids, a large batch of NMP-stabilised colloidal nanoparticles was used to test various immobilisation methods. The three different methods each displayed mixed degrees of success, having issues either with a low affinity of the support materials for the nanoparticles, or with the high boiling point of NMP. The issues associated with each technique are discussed in the following paragraphs.

The adsorption method was shown to be somewhat effective, in that the NMP-protected palladium nanoparticles spontaneously adhered to the surfaces of the four model support materials with no additional heat or pressure required. The loadings, though not quantified, were estimated to be low based on the negligible lightening of the supernatants during adsorption, and the relatively light colour of the powders after their filtration. Additionally the lengths of time required for the adsorptions to

occur were significantly greater than observed with the catalysts prepared from electrostatically stabilised colloids in Chapter 5, or the catalysts prepared from polymer-protected colloids in Chapter 6, taking more than a week.

The rotary evaporation method was shown to be totally ineffective. Even at 100 °C sufficient vacuum could not be established using a water aspirator to remove more than 1 mL of liquid from the samples after 5 hours. This is perhaps unsurprising given the boiling point of NMP is approximately 200 °C at atmospheric pressure, placing it amongst a group of polar aprotic solvents such as DMSO (the boiling point of which is 'only' 180 °C), which are generally considered to be quite challenging to remove from reaction mixtures. Heating of the samples in an open beaker on a hot plate at *ca.* 150 °C was shown to effectively remove all of the solvent over a period of 5-10 hours, though it also lead to the majority of the colloidal metal becoming deposited in a thin layer on the topmost surfaces of the settled particles of support material.

The pore-volume impregnation was shown to be by far the most effective method trialled, though also the most tedious to implement. The support materials all appeared to be stable when heated to 160 °C, in that they did not significantly discolour or change in physical appearance over the course of several hours. Dropwise addition of the colloids to these materials resulted in immobilisation of the suspended nanoparticles onto their surfaces, indicating the support particles are effectively wetted by the colloids. This is consistent with the wetting data obtained in Chapter 3, which showed that amides like DMF had excellent wetting properties for a wide range of support materials. Because of the high boiling points of the solvents, a ten minute delay was required between each successive addition for the solvent to dry. Even after the colloid addition was complete and the powders were dried for a further hour they retained some degree of tackiness, suggesting they may contain a small portion of residual solvent, although all were generally a homogeneous grey or black colour. This method was therefore chosen to produce the full suite of catalysts, subjected to catalytic testing and full instrumental analysis as described in the following section.

7.3.4 Catalyst Synthesis and Characterisation

7.3.4.1 General Observations

In order to achieve maximum stability in the precursor colloids for the final batch of catalysts, they were generated in 80 vv% NMP. Because of the amount of metal required to be dissolved in the dispersion medium, and the resulting amount of sodium borohydride required to do it, this necessitated that the $PdCl_2$ be dissolved in the organic cosolvent rather than in pure water. This occurred easily in all three solvents, producing dark brown solutions containing species presumably of the type $PdCl_2L_2$, where L = DMF, NMP, or DMPU [513]. The solutions in DMF or NMP were stable over the period they were used, however the $PdCl_2$ in the DMPU solution gradually blackened and plated in the inside of the flask, indicating the reduction to metallic Pd. Though not tested, the DMPU may have acted as an oxidising agent in these cases, and may have produced species analogous to those produced by oxidation of NMP [514]. This could be tested by washing the catalysts with an organic solvent, and analysing the eluent by GC-MS, LC-MS, or NMR.

Addition of the sodium borohydride solution to these three solutions brought about their reduction to metallic palladium, as indicated by the change in colour from dark brown to black. The DMF colloid was stable for approximately an hour before aggregation was significant enough to be visually identifiable, while the DMPU colloid was stable for approximately 24 hours, and the NMP colloid was stable indefinitely.

Pore volume impregnation of the eight support materials with these colloids generally proceeded as per the immobilisation trial described in the previous section. The aggregates evident in the DMF and DMPU stabilised colloids were observed to break apart during the process, and became dispersed finely through the powdered support. The rate at which the solvents evaporated from the 24 different systems varied significantly, generally reflecting the trends in their boiling points. The DMPU evaporated the slowest (b.p 246 °C), the DMF evaporated the fastest (b.p. 152 °C), while the NMP evaporated at an intermediate rate (b.p. 202 °C). Once the colloids had been impregnated into the support materials, similar differences were observed in the tackiness of the materials; the DMF-impregnated catalysts appeared completely dry, while the NMP-impregnated catalysts were slightly tacky, and the

DMPU-impregnated catalysts were very tacky. This suggested there may be residual organic matter present in these systems, a fact which was later confirmed by infrared microscopy.

The colours of the catalysts varied significantly between the different systems, depending predominantly on the solvent used. Examples are shown in **Figure 128**. The catalysts impregnated with DMF-stabilised Pd nanoparticles were usually a light

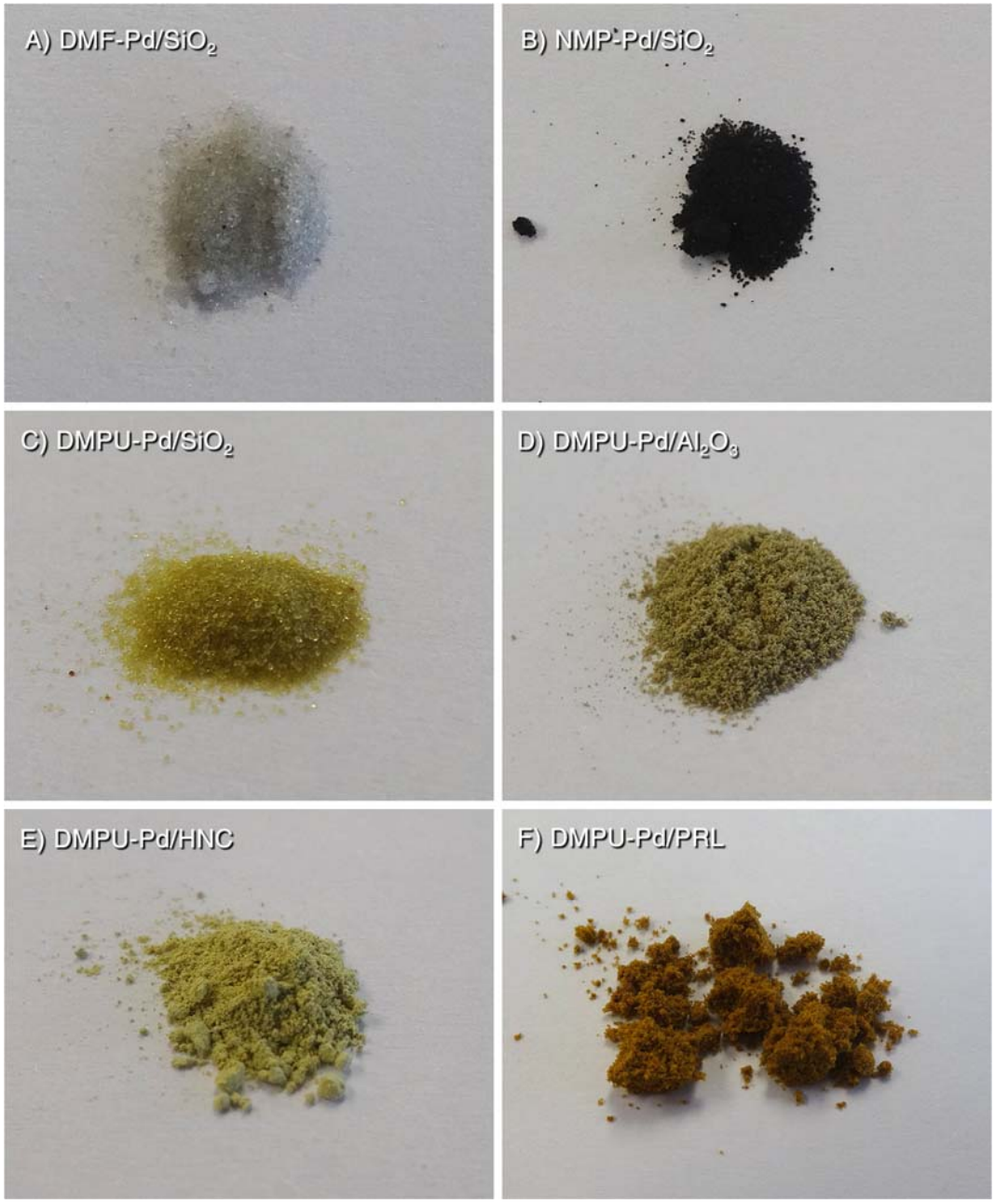

Figure 128: Photographs of supported palladium catalysts prepared by impregnation with solvent-stabilised colloids. The catalysts prepared by impregnation with DMF or NMP stabilised colloids were generally black or grey as in A and B, while those impregnated with DMPU stabilised colloids tended to be more yellow, as in C-F.

grey colour, while the catalysts impregnated with NMP-stabilised nanoparticles were dark black to brown, depending on the support material. The catalysts impregnated with DMPU-stabilised nanoparticles, however, were varying shades of yellow. This could be due to unreduced palladium in the samples; however, this does not explain why they were so light in colour, since the precursor colloids were black.

7.3.4.2 Transmission Electron Microscopy

Analysis of the catalysts post-washing by transmission electron microscopy revealed striking differences between the twenty-four different systems. Most notably, four different phenomena were observed. Firstly, the distribution of metal across the surfaces of the catalysts varied significantly depending on the choice of stabilising solvent. Systems prepared using DMF as a stabilising agent generally had the least homogeneous dispersion, with most of the metal presence as large aggregates up to 100 μm in size. Conversely, systems preparing using NMP as a stabilising agent generally exhibited excellent metal dispersion, with most of the metal dispersed uniformly as individual nanoparticles. Systems prepared using DMPU as a stabilising agent generally exhibited properties intermediate of the two. This is reflective of stability of the precursor colloids, suggesting that aggregates present in solution are maintained intact when immobilised onto the support materials. Examples of this are shown in **Figure 129a-f**.

Secondly, the metal distribution was shown to be strongly affected by the choice of support material. Systems prepared using silica or alumina generally had poor metal distributions regardless of the metal source, with most of the metal bound in large aggregates. Conversely, those prepared using apatitic or cellulosic support materials had much better dispersion. This trend is similar to that observed in Chapter 5 of this thesis, using electrostatically stabilised metal colloids as a metal source. Importantly, this suggests the attraction between the support and the nanoparticles occurs without any significant influence of the solvent, unlike in Chapter 6 where interaction often occurred through the polymer.

The third effect observed, and perhaps the most important for the catalytic activity of the materials, was that many of the nanoparticles in the systems analysed appeared to be coated with a layer of material 4 nm to 6 nm in thickness, with a low

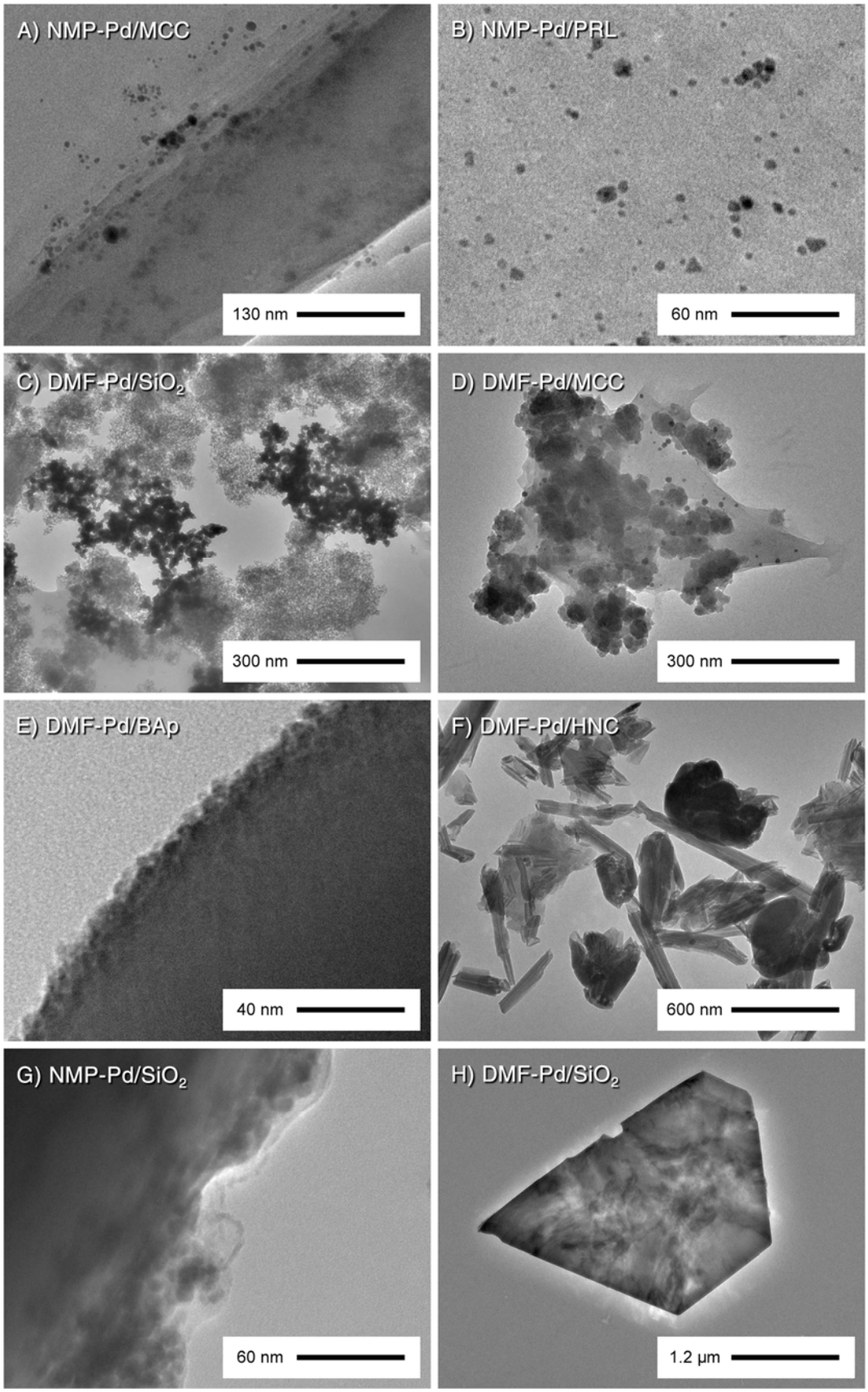

Figure 129: TEM micrographs of catalysts prepared from solvent-protected colloids. Clear differences are evident in the distribution of metal particles throughout the different systems studied.

atomic mass as judged by its transparency, and a low volatility as judged by the fact it did not evaporate under the intense electron beam. An example is shown in **Figure 129g**. This effect was predominantly observed in the systems prepared using NMP and DMPU-stabilised colloids. The origin of this coating layer is discussed later, in section 7.3.4.5.

The fourth observed effect was that many of the systems studied appeared to contain residual salt, even after being washed repeatedly with water. Salt crystals were identifiable on the TEM grids by their unique rhombohedral morphology as shown in **Figure 129h**, as well as their 'shimmery' appearance.

7.3.4.3 Laser Induced Breakdown Spectroscopy

Palladium loadings in the catalysts measured by LIBS showed the average metal content of the catalysts was 1.07 ± 0.15 wt%, which agrees well with the loading of 1.0% to which they were designed. The values for each catalyst along with associated errors are given in **Table 32**. The highest loading was observed for the DMPU-Pd/HNC catalyst at 1.81 wt%, while the lowest loading was observed for the DMF-Pd/PRL catalyst at 0.47 wt%.

The nature of the impregnating solvent appeared to have a significant effect on the final loading of the catalysts. This can be seen in the average loadings, where the NMP-impregnated catalysts have an average palladium content of just 0.87 wt%, while the DMF-impregnated catalysts have a Pd content of 1.10 wt%, and the DMPU-impregnated catalysts have a loading of 1.25%. The origin of this discrepancy may be related to the way in which the catalysts were prepared; if the catalysts were not completely dried during successive impregnations, then they may contain residual 'pockets' of liquid colloidal material, which would be rinsed away during the washing step, resulting in a decrease in the loading.

Secondly, the loadings may be reflective of the trend in the boiling points of the solvents. Given that the impregnations were performed at a fixed temperature of 160°, the closer the boiling point of the impregnating solvent to this temperature, the more rapidly (and violently) it will be evaporated from the surface. For lower-boiling solvents like DMF, this could be expected to eject droplets of nanoparticle-containing solvent from the system, which would be swept away by the fumehood in which the materials were prepared. This effect can be seen clearly by placing a colloid

near its boiling point in a beaker with a watch glass on top; gradual blackening of the watchglass indicates nanoparticles are being deposited on it. Without the watchglass in place the nanoparticle-containing vapour would be swept away into the atmosphere, resulting in a decrease in the loading of the catalysts.

Table 32: Palladium loadings measured by LIBS for catalysts prepared by impregnation with solvent-protected colloids. All concentrations are relative to the NAA-characterised standards described in Chapter 4.

Support	Solvent	Concentrations [wt%]	
		Loading	Error
Al_2O_3	DMF	0.59	0.06
	NMP	1.09	0.09
	DMPU	0.89	0.08
SiO_2	DMF	0.86	0.10
	NMP	1.15	0.13
	DMPU	1.80	0.21
HAp	DMF	1.26	0.13
	NMP	0.49	0.05
	DMPU	1.61	0.16
MCC	DMF	1.26	0.29
	NMP	1.61	0.39
	DMPU	0.92	0.22
HNC	DMF	1.19	0.13
	NMP	0.55	0.06
	DMPU	1.81	0.19
PRL	DMF	0.47	0.05
	NMP	0.50	0.06
	DMPU	0.50	0.05
BAp	DMF	1.92	0.19
	NMP	0.59	0.06
	DMPU	1.63	0.16
MFC	DMF	1.25	0.30
	NMP	0.95	0.22
	DMPU	0.87	0.20

7.3.4.4 X-Ray Powder Diffraction

Analysis of the samples by x-ray powder diffraction showed that the bulk structure of the materials remained intact throughout their preparation, as indicated by the similarity of the patterns for the pristine supports, the impregnated catalysts, and the washed catalysts. While this is expected for many of the thermally stable materials like alumina or silica, it is perhaps surprising that the bulk structure of the cellulosic materials retained their integrity, especially given the high temperatures to which they were heated. Any thermal decomposition may have been limited by the presence of the amide solvent being dripped onto the materials, which would presumably have absorbed the majority of the thermal energy.

A second effect which could be seen in the data was the presence of the reflections originating from the supported palladium particles. In many cases these were so broad and weak that they were difficult to observe, but once again could be seen easily in systems containing amorphous support materials like silica and perlite, since these do not produce sharp diffraction peaks which overlap with those of metallic palladium. Example diffractograms are shown in **Figure 130**. The positions of the palladium peaks indicated that they originated from metallic palladium rather than a palladium oxide, which importantly suggests they the catalysts would not require regeneration to convert them to their active forms, either *in-situ* in the reactor as in

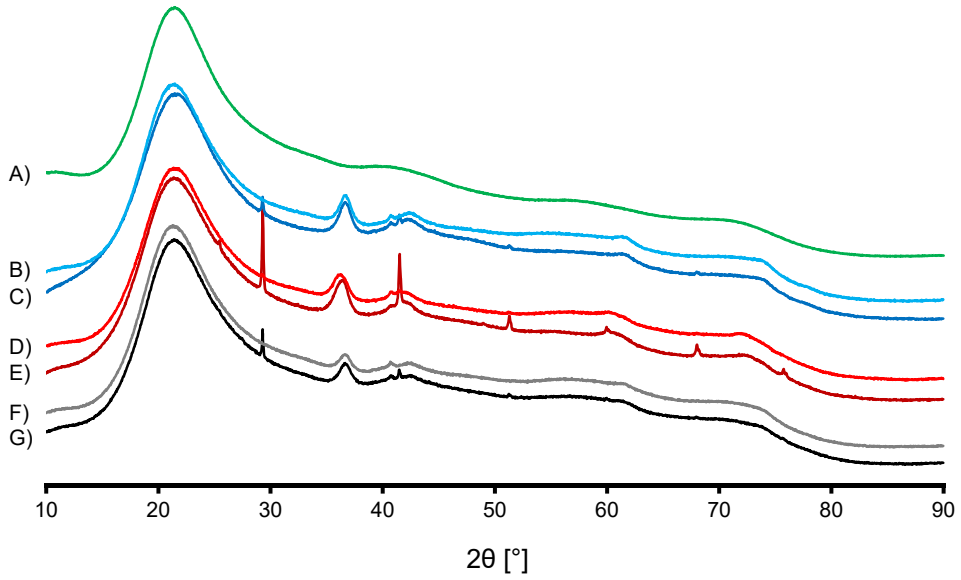

Figure 130: XRD patterns of silica-supported catalysts prepared by impregnation with solvent-stabilised palladium colloids. The six traces represent pristine SiO_2 (A), DMPU-Pd/SiO_2 post (B) and pre (C) washing, NMP-Pd/SiO_2 post (D) and pre (E) washing, and DMF-Pd/SiO_2 post (F) and pre (G) washing.

the previous chapter, or by some other reduction method on the bench. This was later confirmed in the activity tests, which showed the catalysts were active without any necessary regeneration. Additionally, the metallic Pd peaks were evident in all the samples, regardless of which solvent was used to stabilise the palladium colloid from which they were prepared, DMPU included. This importantly suggests that despite being yellow, these samples still contain metallic palladium.

A third effect which was observed in selected systems was the presence of additional peaks in the diffraction patterns of the unwashed catalysts, which were greatly diminished in intensity by the washing step. The positions of these peaks corresponded to NaCl (ICDD PDF 01-071-3741), which was presumably precipitated onto the samples from the precursor colloids, which were not ion-exchanged to remove residual ionic species. The origin of the sodium ions is presumably the sodium borohydride reducing agent, while the origin of the chloride is presumably the palladium chloride metal salt used. This supports the observation made by TEM that salt exists in these systems, though it also shows XRD is not sensitive enough, at least with the programme currently used, to detect the trace amounts of salt present even after washing.

7.3.4.5 Fourier Transform Infrared Microspectroscopy

Infrared microspectroscopy performed on the samples showed significant differences in the spectra between the pristine supports, the impregnated catalysts, and the washed catalysts. There were no gross differences evident in the bands associated with the support materials themselves, indicating that they remained structurally intact and largely unaltered by the impregnation process used, which supports the observations made by x-ray diffraction. Conversely, multiple differences were observed between systems in the C=O and C-H stretching regions, examples of which are discussed in subsequent paragraphs.

Generally speaking, the spectra of all of the systems contained additional bands which were not present in the pristine support materials at 1600 cm^{-1} to 1700 cm^{-1}, the region associated with carbonyl stretches, and various medium-strength bands at 2700 cm^{-1} to 3000 cm^{-1} corresponding to alkyl deformation modes. The alkyl bands were generally similar between the different systems regardless of the support or protecting solvent, although the carbonyl region showed significant differences

depending on both of these parameters. These bands were absent in the pristine supports, strong in the unwashed catalysts, but diminished in intensity in the washed catalysts. This suggests that the bands originated from a water-soluble species which was partially, but not completely, removed during the catalyst washing step. Further theories of their origin are discussed shortly.

The silica-supported catalysts showed these additional bands in all of their spectra, regardless of which colloid they were impregnated with. In the case of the DMF-impregnated catalyst a single band at 1678 cm^{-1} was observed, which agrees well with the carbonyl stretching frequency of neat DMF [515]. This band was completely removed during the washing step, which supports the idea that it originates from residual solvent which is not strongly bound to the catalysts.

Conversely, the NMP-impregnated catalyst exhibited at least three additional bands at 1676 cm^{-1}, 1725 cm^{-1} and 1771 cm^{-1}, despite its structure containing only a single carbonyl group. These bands were only diminished on washing and not completely removed, suggesting the species from which they originate are either strongly bound to the catalyst, or not water-soluble. Given that the carbonyl stretching frequency of neat NMP is 1735 cm^{-1} according to the NIST Webbook, this suggests that none of these species originate from residual solvent, but rather some alternate chemically transformed species.

The DMPU-impregnated catalysts had more complicated spectra than either of the two previously discussed samples. On impregnation a manifold of bands appeared in the carbonyl region, notably at 1717 cm^{-1}, 1674 cm^{-1}, and 1634 cm^{-1}. When the sample was washed only two bands remained, appearing at 1699 cm^{-1} and 1561 cm^{-1}. These are illustrated in **Figure 131**. As with the catalysts prepared from NMP-stabilised colloids, it appears that the species from which these bands originate are not from neat DMPU but rather a chemically transformed species which is either strongly surface-bound or not water-soluble.

With many of the samples there were clear differences at the high energy end of the infrared spectra, especially in the 2950 cm^{-1} region associated with C-H modes. In some cases these were difficult to observe due to the presence of much strong absorptions at similar frequencies, as in the case of the strong O-H vibration in silica.

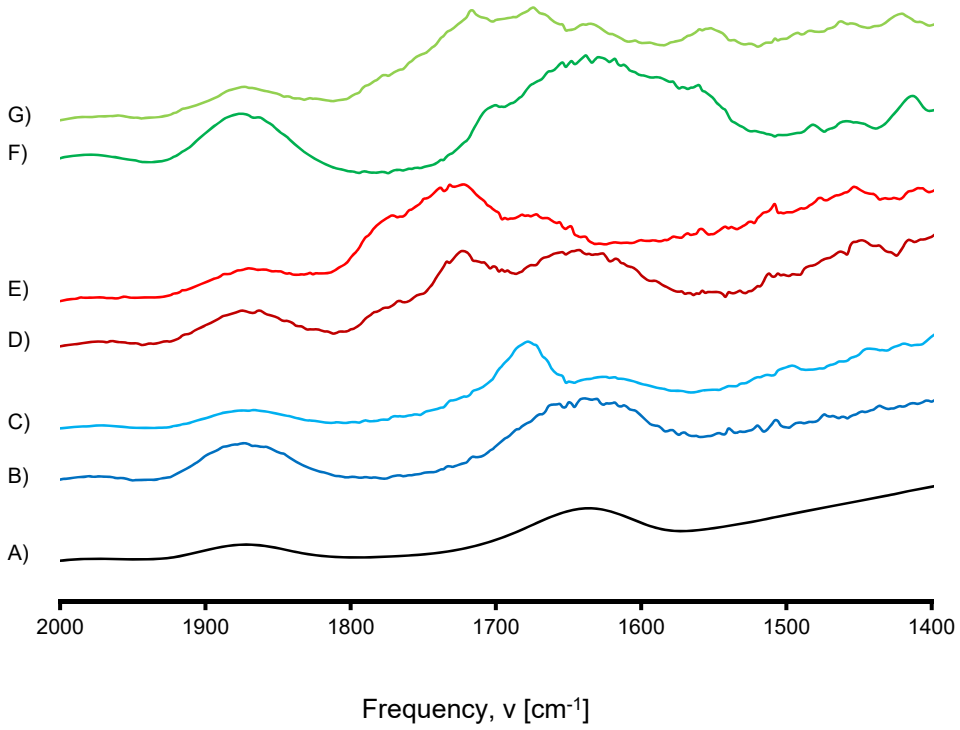

Figure 131: FTIR spectra of the silica-supported catalysts prepared from solvent-protected colloids, zoomed on the carbonyl stretching region The seven traces represent pristine silica (A), DMF-Pd/SiO_2 after (B) and before (C) washing, NMP-Pd/SiO_2 after (D) and before (E) washing, and DMPU-Pd/SiO_2 after (F) and before (G) washing.

The converse was true of the alumina-supported samples, since the alumina used has no strong vibrational modes in this region. The DMF-impregnated alumina-supported catalysts showed no obvious spectral differences to their pristine alumina counterpart, suggesting there was no residual DMF remaining in the catalyst. Conversely, the NMP-impregnated alumina-supported catalyst exhibited strong amide bands, and moderate CH bands at 2780 cm^{-1} to 3040 cm^{-1}. When the sample was washed, these bands shifted to lower frequency by *ca.* 10 cm^{-1} and changed in shape, presumably as a result of the weakly-bound NMP being washed away, and only the non-labile species remaining. The same changes were observed with the DMPU-impregnated catalysts as, shown in **Figure 132**.

Given the evidence that the additional bands in the spectra of the catalysts prepared from NMP and DMPU stabilised colloids were not removable by washing and did not correspond to the neat solvents, the possibility that they were some type of decomposition product of the two were investigated. While the decomposition of DMPU is not widely investigated, there are multiple pathways for NMP composition reported in the literature. Three major pathways were identified by Poulain, Monod

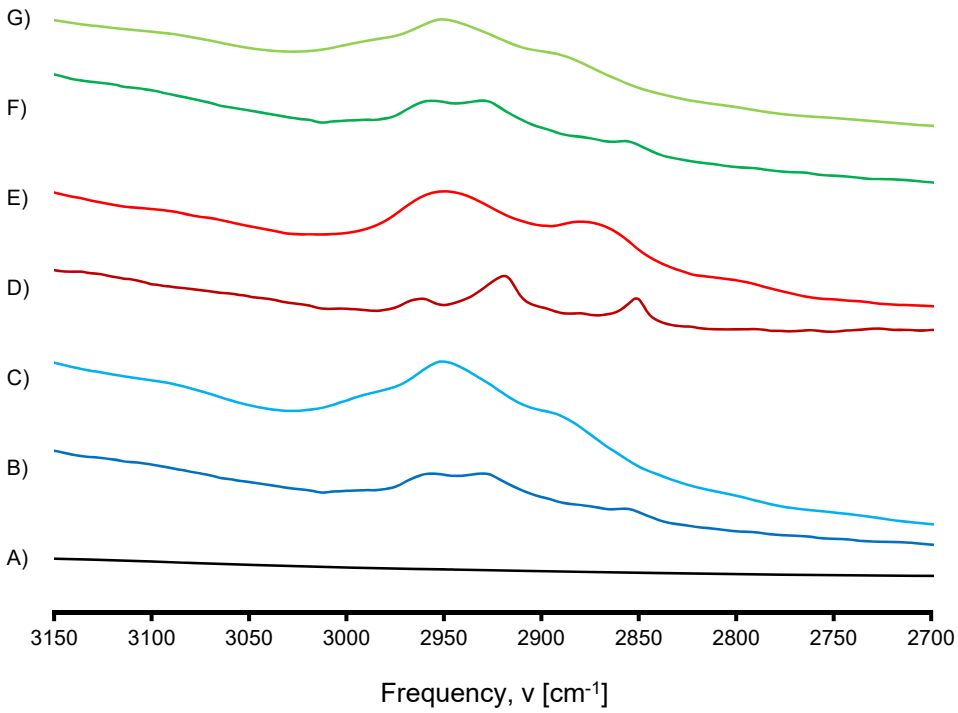

Figure 132: FTIR spectra of alumina-supported catalysts prepared by impregnation of solvent-stabilised colloids. The seven traces correspond to Al_2O_3 when impregnated with: a) nothing, b) DMF/Pd after washing, c) DMF/Pd before washing, d) DMPU/Pd after washing, e) DMPU/Pd before washing, f) NMP/Pd after washing, g) NMP/Pd before washing.

and Wortham, initiated by either: H-abstraction from the α-carbon, attack by OH radicals, or a ring-opening mechanism which occurs on solid particles to generate linear amine-containing carboxylic acids [516]. Similarly, Berrueco *et al.* described the observation by size exclusion chromatography of a wide range of polymers formed simply by heating neat NMP in an atmosphere of air, with molecular weights up to 7,000 [517]. Campbell and Striebig also describe a number of oxidation products of NMP which contain varying carbonyl groups, including 2-pyrrolidone, methylsuccinimide, succinimide, various acetamides, formamides, amines, and aldehydes [514].

It may be the case with the current samples, therefore, that "removable bands" observed in the infrared originate from these small molecule decomposition products, while the "permanent bands" originate from polymerised decomposition products. Similar chemistry may be occurring with the DMPU-containing systems, though it is likely that different decomposition products would be observed given its slightly different structure. Moreover to the IR evidence, the presence of polymerised

species explains the coatings observed on the particles by TEM, as well as the unusual yellow colour of the catalysts, and the residual 'tackiness' observed in the supposedly dry final materials.

7.3.4.6 Catalytic Activity

All of the catalysts exhibited modest activity in the hydrogenation of cyclohexene. Each generated cyclohexane as the only detectable product by either GC-MS or NMR, the rate of generation of which was linear and began immediately once hydrogen was admitted into the reactor. Processing of the data revealed the greatest activity was observed with the NMP-Pd/HNC catalyst which had a turnover frequency of 8750 hr^{-1}, while the lowest activity was observed with the DMF-Pd/HAp catalyst of 78.0 hr^{-1}. The activities are given in full in **Table 33**, and summarised in Appendix 4 side-by-side with the activities for previously described catalysts.

Once again, there were some clear trends which emerged from the activity data. There were obvious differences in the activity of catalysts prepared with different support materials; alumina-supported catalysts exhibit low activity (*ca.* 200 hr^{-1}), while the activity of the halloysite-supported catalysts was more than an order of magnitude greater, which is similar to trends observed in the previous two chapters. The cellulose-supported catalysts exhibited modest activities (*ca.* 2000 hr^{-1}), but only for those impregnated with DMPU or DMF, not NMP. This is explained by the presence of polymerised NMP in these materials, which would have the effect of blocking the active sites of the catalysts and therefore reducing their activity. This may further be related to the surface areas of the materials, as those support materials with low surface areas like alumina could be anticipate to acquire thicker coatings than those with higher surface areas.

These data shows conclusively that though the activity of the currently reported catalysts is modest, it is not zero. The use of solvent-protected colloids can be used therefore to produce catalytically active materials, though significant extra work would be required to optimise the synthetic conditions to allow the 'full potential' of these systems to be exposed. Additional experiments which could be performed for these purposes are described in Section 7.5.

Table 33: Activity of palladium catalysts prepared by pore volume impregnation with solvent-protected colloids in the hydrogenation of cyclohexene.

Support	Solvent	Specific Rate [mmol g^{-1} hr^{-1}]	Turnover Frequency [hr^{-1}]
Al_2O_3	DMF	770	815
	NMP	91.3	97.0
	DMPU	203	215
SiO_2	DMF	2010	2140
	NMP	1140	1210
	DMPU	1750	1850
HAp	DMF	73.4	78.0
	NMP	665	704
	DMPU	2310	2550
MCC	DMF	876	929
	NMP	141	150
	DMPU	4480	4750
HNC	DMF	4030	4280
	NMP	8260	8750
	DMPU	1840	1950
PRL	DMF	7640	8100
	NMP	91.4	97.0
	DMPU	5590	5930
BAp	DMF	520	491
	NMP	1160	1230
	DMPU	138	146
MFC	DMF	2190	2316
	NMP	152	161
	DMPU	1960	2080

7.4 Summary

A variety of solvents were tested for their ability to stabilise colloidal dispersions of rhodium, palladium, and platinum nanoparticles. Palladium was found to be the easiest metal to stabilise, and exhibited the least aggregation when in solutions of

NMP and DMPU. Only modest stability was gained from DMF, and since the three solvents are structurally similar, the three were investigated further.

Analysis of the reduction conditions showed the reduction of $PdCl_2$ with $NaBH_4$ in 50 vol% NMP had a stoichiometry of approximately 3:1, which indicated that a significant portion of the $NaBH_4$ was consumed in side-reactions, most probably catalytic decomposition. As the proportion of NMP in the reaction mixtures was increased, the amount of aggregation in the colloids was shown to decrease. Conversely, as the amount of metal in the colloids was increased, so too did the amount of aggregation.

Immobilisation of the resulting metal particles onto the surface of the support materials was significantly more difficult than with the electrostatically or polymer-protected colloids. Adsorption of the nanoparticles, though spontaneous, was too slow to be of use, while the high boiling points of the three amide solvents made removal of the solvent from the catalysts difficult. A pore-volume impregnation method was used for the preparation of the catalysts, since it was shown to be the most versatile and produce the most desirable textural characteristics within the resulting catalysts.

Impregnation of the eight support materials with the solvent-stabilised colloids produced a series of twenty four catalysts, each with properties dependent on which solvent was used. The catalysts prepared by impregnation with DMF tended to be highly aggregated, while those prepared by impregnation with NMP tended to have less aggregation, while those prepared by impregnation with DMPU were an unusual shade of yellow. Analysis of the catalysts by LIBS showed that they all contained palladium, with an average of 1.07 wt%. Furthermore, analysis by XRD showed they all contained metallic palladium, although this does not necessarily mean that all the palladium contained in the catalysts is metallic. Analysis by FTIR showed they contained significant portions of residual organic material, most likely decomposition products of the protecting solvents. All of the catalysts displayed some degree of activity in the hydrogenation of cyclohexene, though more modest than those reported in previous chapters.

7.5 Suggestions for Further Research

There are several directions for future research which may be of interest to pursue, pertaining either to characterisation of the existing catalysts, or their further development and refinement.

Firstly, it could be of interest to trial additional solvent systems which may be capable of stabilising metal colloids. Given the success observed in the use of amide solvents, there are several others which could be of utility, especially substituted ureas and imidazole derivatives. Some examples are given in **Table 34**. These should be investigated along with alternative reducing agents for the colloids, with possible reactions between the two monitored.

Table 34: Alternative amide solvents which could be used to stabilise metal colloids.

Structure	Name
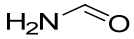	Formamide
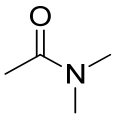	N,N-dimethylacetamide
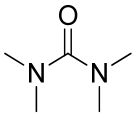	N,N,N,N-tetramethylurea
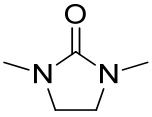	1,3-dimethyl-2-imidazolidinone
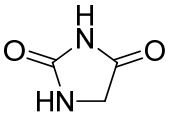	2,4-imidazolidinedione

Similarly it may be of interest to investigate different metal precursors and investigate their ability to be stabilised by various systems. It could be interesting, for example, to examine the differences between species in different oxidation states, such as K_2PtCl_4 compared to K_2PtCl_6, as they are likely to interact with the solvent molecules in different ways.

For the most stable precursor colloids, a number of methods could be used to probe their structure. Time-resolved UV/vis measurements could be used for example to determine the rate at which the samples aggregate, since this would

impact on their ability to be used as precursors for preparing catalysts. Of special interest is the nature of the stabilisation, and how the solvent molecules inhibit the aggregation of the metal particles. If the protection is brought about by adsorption of the solvent molecules to the particle's surfaces, then a co-adsorption study using carbon monoxide and FTIR could be performed to probe this [396, 431, 518-522]. Conversely, if the protection is brought about simply by increases in the viscosity of the dispersion medium, then the addition of a non-bonding polymer such as polyethylene glycol could be used to investigate this effect.

Size tuning effects in the precursor colloids would also be of interest to investigate. A method using multiple successive reduction cycles could be used to produce larger particles; for example, a solution of $PdCl_2$ in NMP could be reduced, then a second aliquot of $PdCl_2$ added and reduced. The particles from the first aliquot may act as seeds upon which the remaining metal may be condensed, resulting in a larger average particle size [523].

Perhaps most importantly, it would be of interest to investigate alternate methods for immobilising these colloids onto support materials that does not produce the growth of a polymer overlayer. The experiments could be repeated under a blanket of nitrogen, for example, or alternative and more effective methods for solution-phase adsorption of the particles could be investigated. It would be of interest to investigate the amount of residual solvent-based material in these systems by thermogravimetric analysis, as well as solid-state NMR to help identify the nature of the species, and chromatographic analyses of solvent washed from the catalysts to help identify the decomposition products.

Chapter 8: Conclusion

This thesis describes work undertaken to investigate the synthesis, characterisation, and activity of a range of novel supported metal catalysts. In order to control the textural properties of the catalysts, it was considered of interest to investigate using pre-formed colloidal metal nanoparticles as a metal source, and to immobilise these particles onto a range of support materials with different physicochemical properties.

A series of support materials for the catalysts were obtained or otherwise produced, and subsequently characterised by a suite of instrumental methods in Chapter 2. Four 'model' commercially available support materials were chosen, as well as four novel analogues. Their macrostructures and microstructures were analysed by scanning electron microscopy (SEM), transmission electron microscopy (TEM), and laser diffraction analysis (LDA). Elemental compositions of the materials were measured by x-ray fluorescence spectroscopy (XRF), and used to guide subsequent analyses on the chemical structures of the materials as assessed by x-ray powder diffraction (XRD), Fourier transform infrared microspectroscopy (μFTIR), and solid-state nuclear magnetic resonance spectroscopy (SS-NMR). The surface chemical properties were also investigated using zeta potential measurements.

Results from the analysis of these materials illustrated that they had a diverse range of properties. The model support materials tested were generally shown to be similar to previously reported systems. The silica gel had an amorphous mesoporous structure, a high degree of surface hydroxylation, and a negative surface charge in aqueous suspension. The alumina tested was shown to be composed predominantly of the α polymorph, but with a small amount of other transitional aluminas present. It had a low surface area and no porosity, with a low degree of surface hydration and a surface charge depending strongly on pH. The hydroxyapatite tested was shown to be highly crystalline with a fine particle size, but contained a significant portion of a secondary calcium phosphate phase, probably β-TCP. It dispersed readily in water, and had a negative surface charge at most pHs. The microcrystalline cellulose used was shown to be highly crystalline, composed predominantly of the cellulose I polymorph, but with no significant surface charge.

The novel support materials tested generally had similar properties to the model supports, with some notable exceptions. The halloysite nanoclay was shown to be composed predominantly of unsubstituted halloysite, with a small contaminant portion of quartz nanoparticles. The halloysite particles were a mixture of tubules and platelets, dispersed easily in water, and had electrokinetic properties similar to the silica gel tested. The perlite was shown to be composed of thin sheets with no significant porosity, and significantly less hydrated than the silica gel. The bioapatite extracted from bovine bones was shown to be more pure and more crystalline than the commercial hydroxyapatite, but had a greater degree of substitution and a larger crystallite size. The macrofibrillar cellulose had similar properties to the microcrystalline cellulose, but a much larger particle size and a greater degree of crystallinity.

In order for catalysts prepared from these materials to be used effectively in subsequent catalytic reactions, it was considered necessary to investigate their wettability with a range of organic solvents so that rational solvent selection could be made. For this purpose the Washburn capillary rise method was used in Chapter 3, which showed significant differences in the wetting properties of the different materials. Several effects related to the wetting properties of heterogeneous surfaces arose from these analyses and were discussed. These results are anticipated to be a useful reference for those working with biphasic catalytic systems, for which there is little information in the literature regarding the compatibility of catalytically-relevant solvents and supports.

To quantitatively measure the amount of metal in the catalysts produced using these materials, and investigation was undertaken into the use of laser-ablation based analytical techniques. A series of matrix-matched standards were prepared and analysed by laser ablation-inductively coupled plasma-mass spectrometry (LA-ICP-MS) and the experimental parameters systematically investigated. Analysis of a series of laboratory reference materials by neutron activation analysis (NAA) was used to validate these standards, so that they could be used comparatively (and quantitatively) for the analysis of catalysts prepared later in the work. Decommissioning of the laser unit and subsequent acquisition of a laser induced breakdown spectrometer (LIBS) meant further method development was switched to this technique. The reference materials investigated by NAA were systematically investigated using this new

method, which proved to be highly precise with excellent linearity, but also susceptible to variations in the sample matrix. Careful control of these parameters therefore allowed the method to be used in subsequent chapters for accurate measurement of catalyst loadings. This represents a significant and novel contribution to the list of analytical tools suitable for studies on heterogeneous catalysts.

A range of catalysts were then prepared by supporting rhodium, palladium, and platinum nanoparticles on the aforementioned support materials. These metals were prepared as colloidal dispersions, and subsequently immobilised onto the surface of the supports. As these metals were not intrinsically stable in colloidal suspension, three different methods of stabilising them were investigated. In Chapter 5, colloids stabilised by natural electrostatic forces were produced and immobilised *in-situ* onto the support materials. Instrumental characterisation of the materials showed there were no significant changes to the bulk structures of the supports during this immobilisation, though some disruption to the surface structures were observed, especially in terms of the state of hydration of the catalysts. Analysis by electron microscopy showed that the distribution of metal across the catalysts depended significantly on the nature of the support. Catalysts prepared using alumina or silica as a support material generally exhibited a poor distribution of metal, while those using hydroxyapatite or cellulose contained nanoparticles distributed evenly across their surfaces. All of the materials tested exhibited good catalytic activity in the hydrogenation of cyclohexene, 1-octene, and 1,5-cyclooctadiene, with turnover frequencies up to 64,000 hr^{-1} observed in selected systems. In many cases, the catalysts prepared using novel support materials exhibited superior catalytic activity to those using the traditional supports like alumina or silica.

A second series of catalysts was then produced in Chapter 6 using polymer-protected colloidal metal nanoparticles. A series of trial experiments were undertaken investigating ten different polymers and their ability to stabilise colloidal rhodium, palladium, and platinum nanoparticles. A range of colloids were produced using these polymers, and subsequently analysed using UV/Vis spectrophotometry and photon correlation spectroscopy (PCS). Results from this trial indicated that six of the ten polymers produced stable colloids, while the other four polymers conferred no extra stability. *Ex-situ* analysis of the colloids by TEM showed they contained

aggregates of varying sizes, and generally supported the results obtained by the previous techniques. Three of the polymers, PVA, PVP, and PAA, were then selected for further development. The effects of polymer concentration were measured, which clearly showed there was a minimum concentration required to stabilise the colloids.

Three different methods were then investigated for immobilising these colloids onto the support materials, with a rotary evaporation-based technique producing the best results. Removal of the polymer layer from these catalyst materials by calcination was shown to induce significant phase changes in selected materials, and analysis by x-ray photoelectron spectroscopy (XPS) also showed it oxidised the supported metal particles. The activities of the catalysts were then tested in cyclohexene hydrogenation, which showed that the platinum and rhodium catalysts were totally inactive, while the palladium-based catalysts had greater activities than those observed in the previous chapter, with turnover frequencies up to 41,900 hr^{-1}.

A third generation of catalysts was then prepared in Chapter 7, using novel "solvent stabilised" colloids as a metal source. A screening programme was undertaken to investigate which solvents were capable of stabilising colloidal rhodium, palladium, and platinum, using a total of 30 different solvents and two reducing agents. Polar aprotic solvents, especially amides, were shown to be the most effective stabilising solvents, and especially for palladium. The three solvents N,N-dimethylformamide (DMF), N-methyl-2-pyrrolidone (NMP), and dimethyl-pyrimidinone (DMPU) were selected for further development. Investigation of the reduction conditions showed that the stability of the NMP stabilised colloids was proportional to the concentration of NMP in the dispersion medium, and inversely proportional to the concentration of metal it contained. Immobilisation of palladium nanoparticles stabilised by these solvents onto the eight support materials was performed by multiple successive pore volume impregnations, which produced an array of materials with different properties. Instrumental characterisation showed that the bulk structures of the materials were not significantly degraded by this process, but that the impregnation produced an immobile coating over the catalysts which reduced their catalytic activity. Cyclohexene hydrogenations performed with materials showed they exhibited modest catalytic activity, up to 8750 hr^{-1}.

These experiments have shown conclusively that the immobilisation of colloidal metal nanoparticles onto solid support materials can produce highly active supported metal catalysts, but that the properties of the catalysts depend significantly on the nature of the colloid, the support material, and the immobilisation method used. This represents a substantial expansion on the currently published body of knowledge, both in terms of methods of catalyst preparation, and their subsequent analysis.

Appendix 1: Supplementary Information for Chapter 4

This appendix contains extra experimental details regarding the experiments undertaken in Chapter 4. The motivations and goals of performing these experiments are described earlier on in the thesis, and so only experimental details are given here. The methods are split into three major sections based on techniques used for their analysis, *viz.*, LA-ICP-MS, NAA, and LIBS.

A1.1 LA-ICP-MS Workflow

A1.1.1 Standard Preparation Methods

Method A: Alumina (2.97 g) was dispersed in 100 mL of a dilute metal salt solution (2.83×10^{-4} mol L^{-1} Na_2PdCl_4, 2.91 mol L^{-1} $RhCl_3$, 1.53×10^{-4} mol L^{-1} K_2PtCl_4) by magnetic stirring in a Pyrex beaker. Reducing agents were added, either as solutions (0.03 mol L^{-1} $NaBH_4$, 0.03 mol L^{-1} NH_2NH_2) or bubbled through (H_2 gas) until no further increase in turbidity was observed visually. The material was gravity filtered through Whatman 540 grade filter paper and oven dried in air at 100 °C for 24 hours.

Method B: The same as method A, but with Nalgene beakers, in an attempt to minimise the adsorption of metal particles to the walls of the beaker.

Method C: Same as A, but with 0.2 mL of saturated $Al_2(SO_4)_3$ added to suppress the electric double layers surrounding the particles [370]. Though this was predicted to accelerate the rate of aggregation, it was also predicated to accelerate the rate of adsorption of particles to the support materials. The reducing agents were added more slowly in this instance, so that the rate of generation of particles would be less than the rate of adsorption, thus providing necessary time for the particles to adsorb to the supports rather than aggregate with one another.

Method D: Same as C, but using $LaCl_3$ instead of $Al_2(SO_4)_3$, since $LaCl_3$ is a more powerful precipitating agent;

Method E: Same as A, but with the dispersion medium adjusted to either pH 2 or 12 using 1 mol L^{-1} HCl or NaOH.

Method F: Same as A, but using either aminopropyltrimethyoxysilane or mercaptopropyltrimethoxysilane-functionalised alumina, prepared by hydroxylating the alumina by stirring with 1 mol L^{-1} NaOH, followed by washing, then functionalization using a method from the literature [524].

Method G: Same as A, but with ultrasonic reduction. The dispersion medium was changed for 10 vol% aqueous MeOH rather than pure water, and the beakers were heated at 50 °C in an ultrasonic bath for 2 hours. The intent with this method was that the heating and slow reduction would induce better adherence to the support than the previous methods;

Method H: A metal colloid was generated using the same reduction method as Method A, but without the alumina present, and 1 mL of 5 wt% PVA added. The alumina was then added to the colloid, and the solvent removed by rotary evaporation at 80 °C and reduced pressure using an aspirator connected to a high-pressure water supply.

Method I: A metal colloid was generated as per method H, but was immobilised onto the Al_2O_3 by heating the dry Al_2O_3 to 80°C then adding the colloid dropwise, waiting for the solvent to evaporate before adding the next drop (a 'pore volume impregnation' method).

Method J: A metal salt solution of equivalent composition to that in method A was added to a Pyrex beaker and evaporated over a laboratory hot-plate at 60°C until dry. The precipitate was reconstituted in neat ethanol, alumina (2.97 g) and PVP (1 ml 5 wt%) were added, and the solvent evaporated off under the same conditions. Since alcohols are reducing agents for metal salts this process produced nanoparticles which adhered to the support.

Method K: The same as method J, but instead of reconstituting in ethanol, the powders were dispersed in water as per method A and immediately reduced using the same method.

A1.1.2 Linearity Testing

Five round-bottom flasks were each charged with 3.000 g of alumina and a magnetic stir bar. Various volumes of metal salt solutions were added as listed in **Table 35**, and the beakers topped to 100.0 mL with Type 1 water. The samples were reduced by dropwise addition of two mole equivalents of 0.03 mol L^{-1} $NaBH_4$ solution. The resulting suspensions were stirred for 1 hour, and 100 μL of 0.1 molL^{-1} $LaCl_3$ solution was added. After a further hour the samples were gravity-filtered using Whatman 540 filter paper and dried in air at 100 °C for 24 hours. Once dried, 50 mg of each standard was combined with 950 mg of microcrystalline cellulose as a binding agent and ground to optical homogeneity in standard porcelain mortar and pestle. The resulting powders were pelletised and stored in a desiccator until analysis.

Table 35: Solution volumes used to prepare the LA-ICP-MS standards.

Solution/ Volume	Concentration [wt%]				
	0.50	**1.00**	**1.50**	**2.00**	**2.50**
$RhCl_3$	2.90	5.80	8.75	11.65	14.60
Na_2PdCl_4	2.80	5.65	8.50	11.30	14.15
H_2PtCl_6	1.55	3.10	4.60	6.15	7.70

A1.1.3 Standard Doping

Method A: A small amount of alumina (0.100 g) was placed in a polypropylene cup and impregnated with a solution of $Co(acac)_3$ (100 μL at 0.18 mol L^{-1} in MeOH) resulting in a state of incipient wetness. The mixture was gently stirred under a flow of air to evaporate the solvent.

Method B: Prepared as per A, except an additional aliquot of PVP solution (100 μL, 5% w/v in MeOH) was added as a film-forming agent.

Method C: Prepared as per A, except an additional aliquot of PEG4000 solution (100 μL, 5% w/v in MeOH) was added as a film-forming agent.

Method D: The terminal bulb of a Büchi B-580 glass oven configured as a Kugelrohr was charged with alumina (0.100 g) and $Co(acac)_3$ (100 μL at 0.18 mol L^{-1} in MeOH), plus an additional aliquot of 10 mL of MeOH, and heated under vacuum at 120 °C to evaporate the solvent.

Method E: Prepared as per D except an additional aliquot of PVP solution (100 μL, 5% w/v in MeOH) was added to the bulb.

Method F: Prepared as per D except an additional aliquot of PEG4000 solution (100 μL, 5% w/v in MeOH) was added to the bulb.

Method G: A mortar and pestle was charged with alumina (0.95 g) and solid $Co(acac)_3$ (0.50 g) and ground until optically homogeneous.

Method H: Prepared as per B, except a single impregnation solution was used (100 μL, 0.18 M $Co(acac)_3$ and 5% w/v PVP in MeOH) rather than two separate solutions.

Method I: Prepared as per C, except a single impregnation solution was used (100 μL, 0.18 M $Co(acac)_3$ and 5% w/v PEG4000 in MeOH) rather than two separate solutions.

Method J: Prepared as per H, but dried in an oven at 30 °C for 20 minutes rather than with a flow of room-temperature air.

Method K: A beaker was charged with alumina (0.100 g), $Co(acac)_3$ solution (100 μL, 0.18 M in DCM), n-heptane (20 mL), DCM (10 mL), and a magnetic stir bar. Binary mixtures of DCM and n-heptane are nonazeotropic, so evaporation of the solvent results in a continuous enrichment of the higher-boiling component (n-heptane) until the lower-boiling component (dichloromethane) is gone. The solution was stirred and heated vigorously to evaporate the lower-boiling DCM in which the $Co(acac)_3$ is soluble, leaving only the n-heptane in which it is insoluble, causing the $Co(acac)_3$ to precipitate onto the surface of the alumina. The solution was then heated until dry.

Method L: A polyethylene cup was charged with alumina (0.100 g) impregnated with $Co(acac)_3$ solution (100 μL, 0.18 M in MeOH). The cup and its contents were cooled to -196 °C by immersing in liquid nitrogen, then placed into a glass desiccation chamber. The chamber was pumped down to draw away the solvent as it heated to room temperature using a vacuum (0.01 mbar) with a cold trap (liquid nitrogen/EtOH) in-line to collect the evaporated solvent.

Method M: A Schlenk tube was charged with alumina (0.100 g) and $Co(acac)_3$ solution (1 ml, 1.8 M in ^tBuOH) and frozen using an EtOH slush bash. The contents were freeze-dried by evacuating the tube under vacuum (0.01 mbar) with a cold trap (EtOH/liquid nitrogen) in-line.

A1.1.4 Data Processing

Method A: Raw data was not smoothed at all, and used as-received from the spectrometer. At each time interval the aluminium to cobalt ratio was calculated by dividing one by the other, and the average of the result was calculated.

Method B: The raw data was not smoothed, and at the aluminium to cobalt ratio calculated for each time interval. This was smoothed with a 5-point moving average, and the average of this calculated.

Method C: The raw data was smoothed with a 5-point moving average, the aluminium to cobalt ratios calculated for each time point, and the average calculated from this.

Method D: The raw data was smoothed, the aluminium to cobalt ratio calculated for each time point, then the ratio signal was smoothed again. The average was calculated from this 'doubly smoothed' data.

Method E: The aluminium signal was averaged, then the cobalt signal was averaged, then the two values divided by one another to obtain the final value.

Method F: The aluminium and cobalt signals were smoothed, each one was averaged, then the two were divided by one another to obtain the final value.

A1.1.5. Pulse Parameter Optimisation

The 1.00 wt% standard described in A1.1.2 was doped with cobalt using the method selected from the previous two experiments. Multiple line scans were performed on the sample, adjusting the laser parameters between scans to investigate their effects. The power/fluence was adjusted, followed by the spot size, scan speed, and repetition rate.

A1.1.6 Standard Testing

Once the technical variability was assessed a new generation of standards were prepared using higher concentrations, up to 2.5 wt%. Line scans of the sample were performed, Co to PGE ratios calculated, and calibration curves constructed. Results from this trial, as detailed later in the results section, indicated that a third generation of standards need be produced.

A1.2 NAA Workflow

For the third generation of standards the best methods from the initial development were re-investigated but prepared using linearly increasing amounts of metal, *viz.*, a series of standards. Method J from A1.1.1 was selected as the method showing the least amount of metal loss, and so these were created using the four support materials Al_2O_3, SiO_2, HAp, and MCC in the five different concentrations listed in **Table 35**. The samples were split in half, with one half kept, and the other half doped with cobalt. To measure the absolute concentration of metal in the resulting standards so that they could be used quantitatively as laboratory reference materials (LRMs), samples were sent for Neutron Activation Analysis. Samples were dried *in vacuo* at 100°C for 24 hours prior to bottling under nitrogen.

A1.3 LIBS Workflow

A1.3.1 Preliminary Optimisation

The first experiments performed were to investigate whether appropriate emission signals could be obtained from the samples. Approximately 200 mg of each of the 1 wt% standards for the four different materials was pelletised and analysed by LIBS using "timing mode", where the laser constantly rasters across the sample surface while its parameters can be altered on the fly and the spectrum quality inspected. The laser power, gate delay, and laser repeat rate were iteratively adjusted to obtain the lowest background and greatest peak intensities, and these settings were used for further developmental work. Emission lines chosen for study were Rh 343.49, Pd 340.6, and Pt 330.1. Parameters were then systematically altered to investigate their effects on the data.

A1.3.2 Dilution Testing

Samples were re-prepared by diluting each of the 1 wt% standards with microcrystalline cellulose in ratios of 1:0 (undiluted), 1:1, 1:2, 1:5, 1:10, 1:20, and 1:50. Each sample was analysed using an array of 10x10 spots covering a 10 mm x 10 mm area on the sample, and ablated five times sequentially. The quality of the data was inspected, and the effects of dilution assessed. The most appropriate level of dilution was then chosen for all subsequent experiments.

A1.3.3 Pulse Counting

A set of samples were re-prepared as per the previous section, and the same 10 x 10 array of spots was ablated on each sample (newly prepared), but repeated 20 times. The peak to background ratios were again calculated to assess whether the best sensitivity was obtained near the pristine surface, or deeper into the pellet.

A1.3.4 Grinding Effects

A set of samples were re-prepared as per the previous experiment, but hand-ground in an agate mortar and pestle for either 0s, 10s, 100s, or 1000s. The samples were ablated in a 10x10 array once again, and the effects on the quality of the data used to assess the most appropriate amount of grinding to use for subsequent analyses.

A1.3.5 Pulse Parameters

In the next set of experiments the effects of pulse parameters were investigated. The LIBS unit used in this study had only three adjustable parameters: laser repetition rate, laser power, and gate delay. Repetition rate was set at a fixed 1 Hz, and the other two parameters were systematically altered and their effects on the PBR investigated.

A1.3.6 Calibration Curves

The NAA-measured samples described in A1.2 were pelletised and analysed using the optimised parameters selected from the previous experiments, and calibration curves constructed. The effect of line choices was investigated, as well as different normalisation options.

Appendix 2: Reactor Design and Operation

The reactor used for all of the hydrogenations reported herein was based on the design on a number of microreactors reported in the literature for hydrogenation in organic synthesis. It is composed of three essential components. A general schematic is given in **Figure 133**.

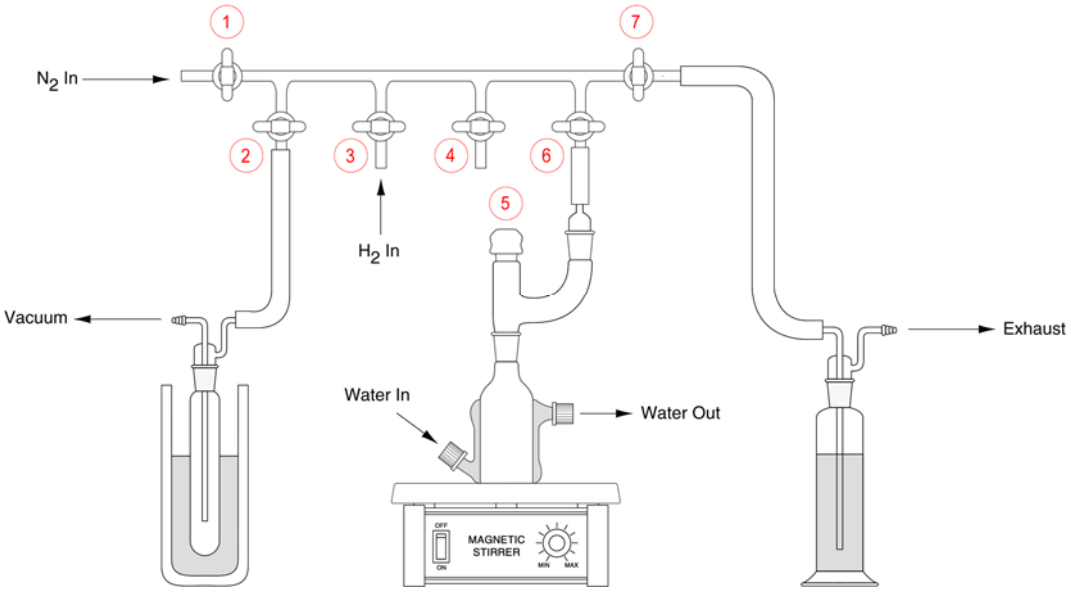

Figure 133: Schematic of the gas-liquid hydrogenation reactor used in the current study.

Beginning with all valves closed, operation of the reactor was performed as follows:

1. The reactor vessel was charged with *ca.* 200 mg of catalyst, 45 mL of n-heptane, and a magnetic stirring flea;
2. Valves 1 and 7 were opened to purge the manifold with nitrogen;
3. Valve 6 was opened to blanket the reactor with nitrogen;
4. Gentle stirring of the reactor was commenced, valve 7 was closed, and valve 2 was opened to evacuate its contents. Vacuum was applied until the solvent began to boil;
5. Valve 2 was closed, and valve 1 opened to replace the contents with nitrogen;
6. Valve 7 was opened to purge the contents to waste;

7. Steps 4, 5, and 6 were repeated twice more to reduce the oxygen content of the reactor to a minimum;

8. Valve 2 was opened to evacuate the reactor contents, and vacuum applied until the solvent boiled. Valve 2 was immediately closed, and valve 3 opened;

9. An aliquot of substrate was injected into the reactor through the rubber septum at port 5;

10. Stirring was increased to a maximum, allowing the hydrogenation to proceed;

11. Samples are withdrawn using a glass syringe through septum 5 at regular intervals for analysis by GC-MS. The pressure could be monitored, if necessary, *via* a manometer connected through Valve 4;

12. At the completion of the reaction, valve 3 was closed to isolate the hydrogen supply;

13. Valve 2 was opened to evacuate the residual hydrogen until the solvent began to boil. Valve 1 was opened to replace the atmosphere of the reactor with nitrogen. Valve 7 was opened for 10 seconds to vent the contents to atmosphere. Valves 1 then 7 were immediately closed.

14. Step 13 was repeated twice more to remove all residual hydrogen

15. Stirring was ceased. Valve 1 was opened, and septum 5 removed. The reactor was now open to the atmosphere, but blanketed under nitrogen.

16. The reactor was disconnected, the organic matter decanted, and the catalyst immediately washed with water.

17. The catalyst is filtered through celite with extra water, and then stored underwater for later disposal.

Extreme caution must be exercised during hydrogenations performed by this method, ensuring the reactions occur in an oxygen-free environment, that undue pressure is not built up inside the reactor, and that the spent catalysts do not contact oxygen, that there are no sources of sparks or flames nearby, and that the build-up of static electricity is kept to a minimum. Failure to observe these rules can result in solvent fires and explosions.

Appendix 3: Treatment and Calculation of Analytical Errors

Any kind of measurement is accompanied by some degree of uncertainty, and quantitative chemical analyses are no exception. The activity of a supported metal catalyst is a prime example of this, and one which is dealt with repeatedly in this body of research in Chapter 5, Chapter 6, and Chapter 7. This appendix details the treatment of the errors associated with these measurements.

There are three primary measurements which are needed to calculate a turnover frequency. One must know the rate at which a given mass of catalyst can convert a substrate into products, the amount of metal within this mass, and what portion of the metal is likely to be catalytically active. These tasks have respectively been accomplished using GC-MS, LIBS, and TEM, and the errors arising in each of these analyses are dealt with as follows.

A3.1 Error from GC-MS

There are multiple sources of variance in a chromatographic analysis, all of which contribute to the total analytical error of a method [525, 526]. In this work, conversion rates for the catalytic reactions were obtained by extracting aliquots of the reaction mixture at fixed time intervals and measuring the substrate concentration by GC-MS. Concentrations were obtained by creating a standard curve, then determining the concentration of unknown samples by interpolation, with the concentration change as a function of time representing the conversion rate. In this situation errors will obviously manifest in both the standard curve and the analysis of an unknown, and so the two must be considered with equal weight, as described below.

When the unknowns were analysed, data like those in **Figure 134** were obtained. For a reaction which proceeds at a constant rate, it is clear that any deviation from linearity in the data represents a manifestation of analytical error, and thus the size of the deviation carries information about the size of the error. In this data, the black points represent the calculated concentration of substrate in a sample at time t; it thus follows that the slope of the data represents the conversion rate. Linear regression analysis can be used to obtain the slope (in units of mmol min^{-1}), but this

says nothing about the slope's accuracy. For this purpose the standard deviation in the residuals is calculated, by using the regression equation to calculate the concentrations at each time point, then taking the difference between the real and calculated values (the residuals). Assuming the errors are normally distributed, their spread can be used to calculate the slope uncertainty. Addition and subtraction of 1σ to the first and last data points respectively gives the maximum slope, while the converse gives the minimum slope. 2σ thus gives the range of slopes within which the real conversion rate must fall with a certainty of *ca.* 95%.

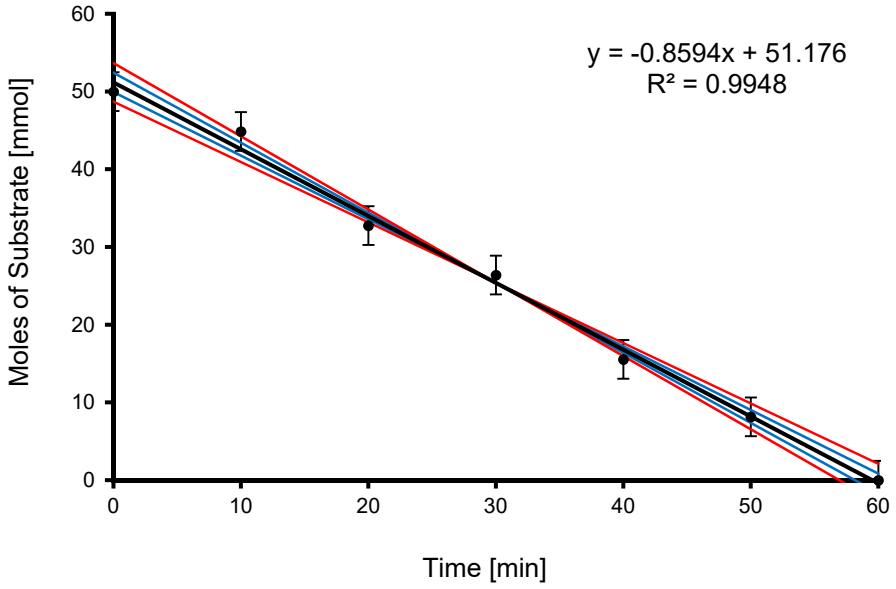

Figure 134: Hypothetical results of a GC analysis. Calculated concentrations are given by the black data points, a linear fit to these points given by the black line, the error bars representing the standard deviation in the residuals, the blue lines representing the maximum and minimum slopes to 1σ certainty, and the red lines representing the same but to 2σ.

A typical standard curve produced in this work is shown in **Figure 135**. Note that the coefficient of determination (the R^2 value) is significantly higher than that for the previous data, and consequently the error is significantly less. Regardless, it is still valuable to calculate and to delineate its various sources. Since these curves were prepared by weighing aliquots of cyclohexene on a four-figure balance the uncertainty in the x positions of the data points are very small, and thus only the error in the y dimension is considered here. Once again linear regression is used, followed by calculation of the standard deviation in the residuals, which are then used to generate the slope uncertainty at 2σ confidence. This error is then added to the values described in the previous section to obtain the total error in the assay.

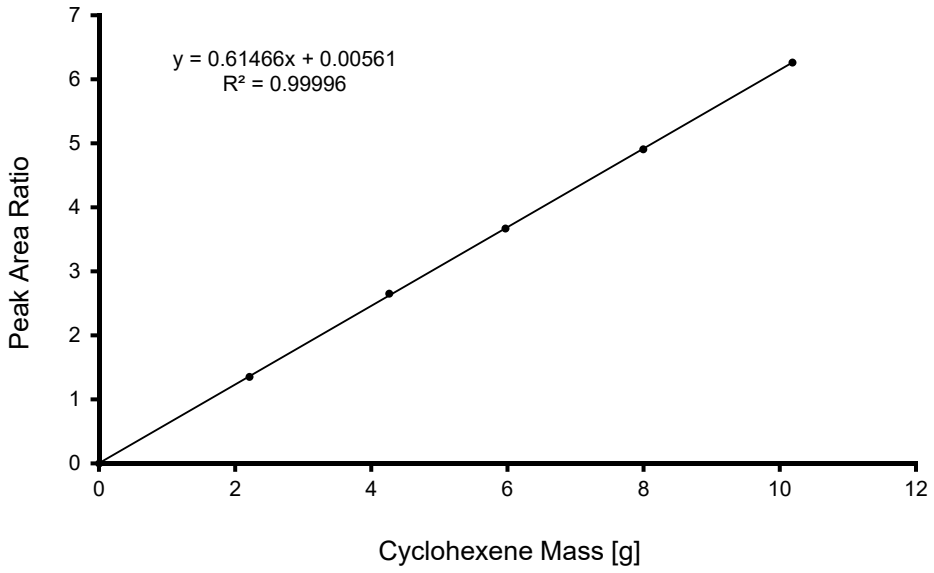

Figure 135: Typical GC-MS standard curve.

The error associated with the standard curve is approximately equal across all analyses, since the instrumental response does not drift significantly with time. The predominant contribution to the error is therefore the conversion rate, the actual values for which range from 2% to 10% depending on the nature of the data.

A3.2 Error from LIBS

Sources of error in LIBS analysis of supported metal catalysts, like any other assay, arise from many places. Being essentially a ratio method, comparing the instrumental response of a standard to that of an unknown, the source of error can be divided into two categories:

- Error in standard concentration. How accurately is the concentration of metal in the standard known?
- Error from sampling statistics. Given *n* number of ablations of the samples and standard, how accurately can their instrumental response be measured?

The former of these is too complicated to be dealt with in full, but the end result is that the elemental concentrations measured by NAA are given with an uncertainty of $\pm 2\sigma$. This encompasses many of the experimental uncertainties in the analysis process, including sample weights, irradiation fluxes and times, k-factors, peak areas, *etc.*

The error in sampling statistics, however, can be dealt with in full here. For each sample, the actual mass ratio of metal to support is estimated based on a fixed number of ablations. Because of fluctuation in laser intensity and intrinsic heterogeneity in the sample, the greater the number of ablations taken the greater the accuracy with which the mean can be known. Assuming the variation is normally distributed, the accuracy with which the mean is estimated can be calculated in the form of the standard error. Double the standard error is therefore equivalent to the error in the mean to an uncertainty of $\pm 2\sigma$. The relative SE is calculated for measurements taken on both the standard and the sample, and added together as percentages. This is summed with the error obtained from the elemental analysis by NAA to yield the total error in the assay, typically in the order of 10%. The greatest contributor in this regard is actually the concentration of the standard, as measured by NAA.

A3.3 Error from TEM

Transmission electron microscopes are subject to several effects which limit their accuracy. First and foremost the magnification must be accurately calibrated, since the values reported by an instrument are only nominal. This can be achieved by analysing a standard material whose dimensions are accurately known, then comparing the measured result with the actual values. In this work two types of standards were used; a monodisperse latex sphere particle size standard to cover the low magnifications, and bovine catalase crystals to cover higher magnifications. Latex spheres are produced by many manufacturers in many different sizes, although a 70 nm variety were used here. Catalase has unusually large lattice spacings of 8.75 nm and 6.85 nm, which are easily measurable and do not vary considerably [527].

A series of micrographs of the catalase crystals were collected at magnifications ranging from 20 kx to 350 kx, and the lattice spacings measured by counting the number of dark fringes visible in the micrographs, measuring the total distance between them, and dividing the latter by the former. The ratio between the observed lattice spacing and the literature lattice spacing gives the correction factor, which allows calculation of the 'true' magnification of the microscope. Some example micrographs are shown in **Figure 136**.

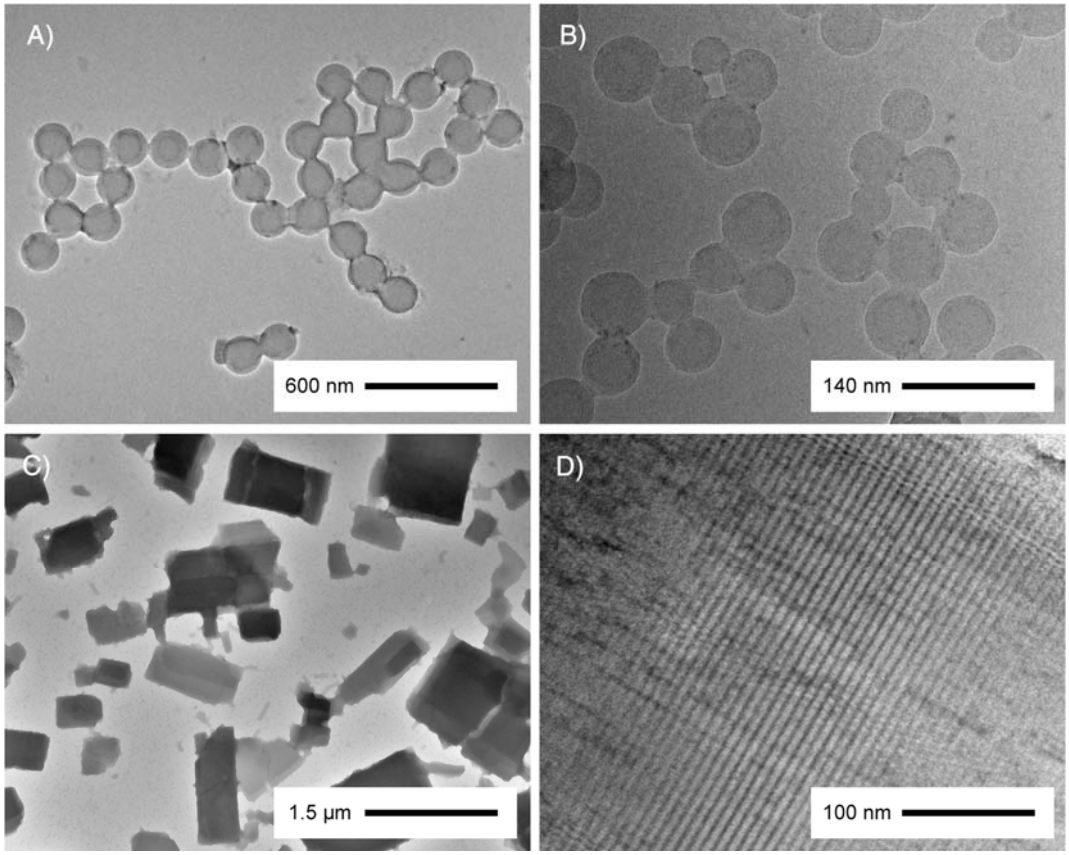

Figure 136: TEM micrographs of the magnification calibration standards used. Individual micrographs represent A) low magnification image of the latex sphere standard, B) higher magnification of the same, C) low magnification image of the catalyse crystals, D) higher magnification of the same, exhibiting clear phase contrast in the form of interference fringes from diffraction of the beam electrons through the crystal.

When the nominal magnifications are plotted against the calculated magnifications, as in **Figure 137**, a calibration curve is obtained. Fitting a straight line to the data *via* linear regression gives a slope of 0.8228, indicating that on average the actual magnification is 82.28% lower than what is reported by the instrument. Repeat measurements of the sample over different days produced a relative standard deviation in the calibration factors of 4.9% ($\pm 2\sigma$, n=5), which not only encompasses the ability to set the sample repeatedly at eucentric height, but also to correctly focus the electron beam, and reliably collect measurements from the resulting micrographs.

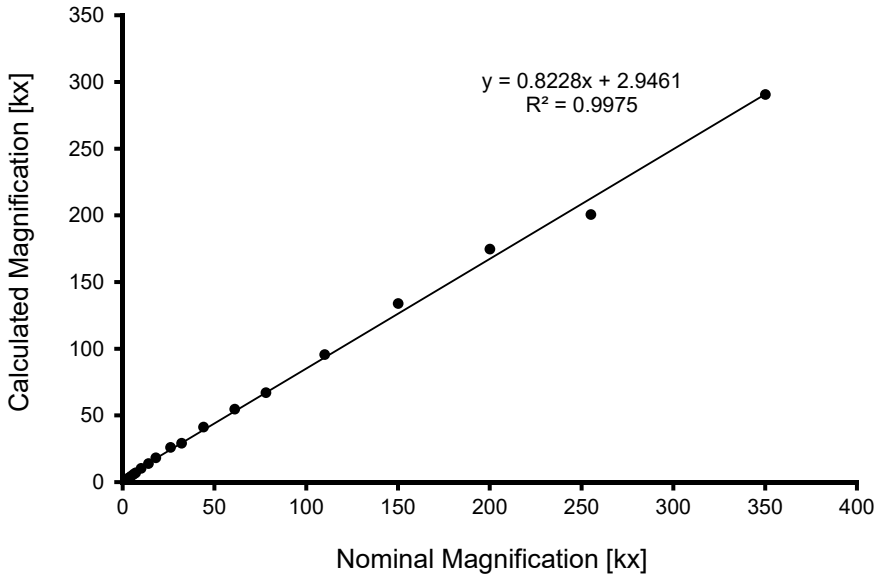

Figure 137: TEM magnification calibration curve.

Further to the errors described above, two additional sources of inaccuracy arise in estimating the average diameter of a collection of nanoparticles. It is not practical to measure every nanoparticle in a population of several million, and so a representative sub-sample must be selected. The mean and standard deviation will vary from subsample to subsample, however, and thus the means themselves have a standard deviation. The standard error in the mean therefore can be used to estimate the accuracy of a set of measurements, and is added to the error described above.

The last source of error in the measurements arises from the use of digital micrographs. Since digital micrographs comprise a two-dimensional array of pixels, it follows that the smallest measurement than can be made on such an image is between two adjacent pixels. If the size of an object is small relative to the size of a pixel then the resolution is insufficient to accurately measure it. It can be said therefore that the higher the magnification the greater the number of pixels a given particle will span, and the less important this effect becomes. If the number of nanometres represented by a pixel is plotted against magnification, as in **Figure 138**, it can be seen that the trend accurately follows a power law, and that the magnitude of the issue drops precipitously as the magnification is increased. Knowing the magnification at which micrographs were collected from which a particle size

distribution was measured, the percentage error of a pixel relative to the average particle size can then be calculated, and added to the total error.

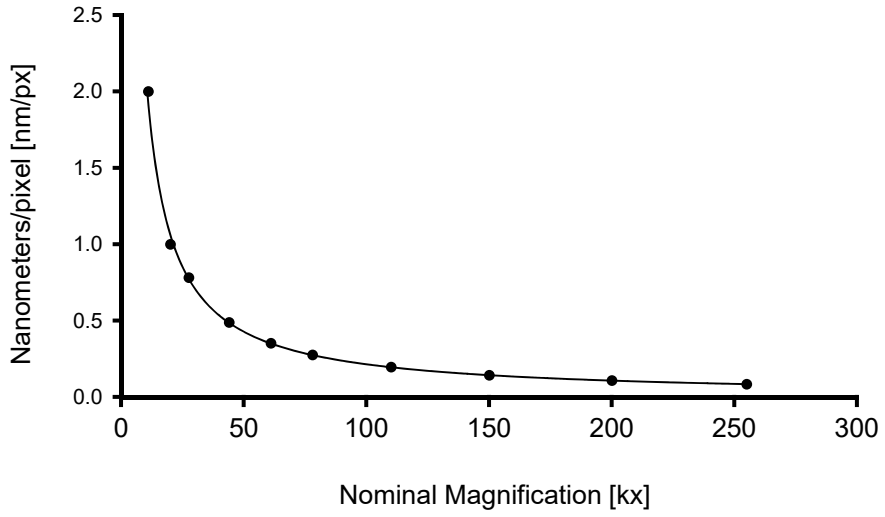

Figure 138: Pixel size in real space as a function of magnification.

All three of these sources of error are of approximately equal magnitude, and thus all are equally important. While the magnification error is more-or-less fixed between analyses, the other two vary dynamically from sample to sample. Typical standard errors in the particle size are in the order of 5-10%, while typical 'pixel size errors' are slightly less, especially at higher magnifications. The sum error in a particle size measurement therefore lies around 20%, but varies from sample to sample.

Appendix 4: Turnover Frequency Comparisons

Turnover frequencies for the cyclohexene hydrogenations described earlier in this thesis are repeated here for ease of comparison. The leftmost column of activities are taken verbatim from Chapter 5, the middle activities from Chapter 6, and the rightmost activities from Chapter 7. The abbreviation "*n.t.*" is used to indicate that a particular catalyst was not tested.

Catalyst	**Protecting Agent**	**Activity [hr^{-1}]**	**Protecting Agent**	**Activity [hr^{-1}]**	**Protecting Agent**	**Activity [hr^{-1}]**
Pd/Al_2O_3	None	5,380	PVA	1,450	DMF	815
			PVA	200	NMP	97.0
			PVP	1,230	DMPU	215
Pd/SiO_2	None	2,940	PVA	31,400	DMF	2140
			PVA	3,890	NMP	1210
			PVP	41,900	DMPU	1850
Pd/HAp	None	10,700	PVA	15,600	DMF	78.0
			PVA	14,600	NMP	704
			PVP	7,320	DMPU	2550
Pd/MCC	None	30,200	PVA	*n.t.*	DMF	929
			PVA	*n.t.*	NMP	150
			PVP	*n.t.*	DMPU	4750
Pd/HNC	None	15,700	PVA	23,000	DMF	4280
			PVA	9,690	NMP	8750
			PVP	30,000	DMPU	1950
Pd/PRL	None	9,070	PVA	21,000	DMF	8100
			PVA	10,300	NMP	97.0
			PVP	12,300	DMPU	5930
Pd/BAp	None	3,080	PVA	0.00	DMF	491
			PVA	0.00	NMP	1230
			PVP	0.00	DMPU	146
Pd/MFC	None	11,800	PVA	*n.t.*	DMF	2316
			PVA	*n.t.*	NMP	161
			PVP	*n.t.*	DMPU	2080

References

1. L. J. Thénard, *Ann. Chim.,* 85, **1813**, 61-64

2. H. Davy, *Phil. Trans. R. Soc. Lond.,* 106, **1816**, 1-22

3. H. Davy, *Phil. Trans. R. Soc. Lond.,* 107, **1817**, 77-85

4. H. Davy, *Phil. Trans. R. Soc. Lond,* 107, **1817**, 77-85

5. L. J. Thénard, *Ann. Chim. Phys.,* 8, **1818**, 306-312

6. E. Davy, *Phil. Trans. R. Soc. Lond.,* 110, **1820**, 108-125

7. J. W. Döbereiner, *J. für Chem. Phys.,* 34, **1822**, 91-92

8. J. W. Döbereiner, *J. für Chem. Phys.,* 38, **1823**, 321-326

9. M. M. Dulong, P. J. Thénard, *Ann. Phil.,* 6, **1823**, 376-378

10. J. J. Berzelius, *Årsberättelse om framstegen i fysik och kemi* (Royal Swedish Academy of Sciences, 1835)

11. M. W. Roberts, *Catal. Lett.,* 67(1), **2000**, 1-4

12. C. H. Bartholomew, R. J. Farrauto, *Fundamentals of Industrial Catalytic Processes (Second Edition)* (Wiley, Hoboken, 2006)

13. K. J. Laidler, *Pure Appl. Chem.,* 68(1), **1996**, 149-192

14. J. Heveling, *J. Chem. Educ.,* 89(12), **2012**, 1530-1536

15. L. Lloyd, *Handbook of Industrial Catalysts* (Springer, New York, 2011)

16. J. Hagen, *Industrial Catalysis: A Practical Approach* (Wiley, Weinheim, Germany, Second Edition, 2006)

17. C. T. Campbell, *Acc. Chem. Res.,* 46(8), **2013**, 1712-1719

18. C. T. Campbell, J. R. V. Sellers, *Faraday Discuss.,* 162, **2013**, 9-30

19. C. R. Henry, *Prog. Surf. Sci.,* 80(3–4), **2005**, 92-116

20. A. Y. Stakheev, L. M. Kustov, *Appl. Catal. A,* 188(1-2), **1999**, 3-35

21. S. E. Wanke, P. C. Flynn, *Catal. Rev.,* 12(1), **1975**, 93-135

22. P. Harris, *Int. Mater. Rev.,* 40(3), **1995**, 97-115

23. P. Wynblatt, *Acta. Metall.,* 24(12), **1976**, 1175-1182

24. P. Wynblatt, N. A. Gjostein, *Acta Metall.,* 24(12), **1976**, 1165-1174

25. Y. Takasu, T. Kawaguchi, W. Sugimoto, Y. Murakami, *Electrochim. Acta,* 48(25–26), **2003**, 3861-3868

26. W. A. Spieker, J. R. Regalbuto, *Chem. Eng. Sci.,* 56(11), **2001**, 3491-3504

27. C. H. Hu *et al.*, *J. Catal.,* 274(1), **2010**, 99-110

28. F. Pinna, *Catal. Today,* 41(1-3), **1998**, 129-137

29. J. Haber, J. Block, B. Delmon, *Pure Appl. Chem.,* 67(8-9), **1995**, 1257-1306

30. J. Haber, *Pure Appl. Chem.,* 63(9), **1991**, 1227-1246

31. A. J. van Dillen, R. J. A. M. Terörde, D. J. Lensveld, J. W. Geus, K. P. de Jong, *J. Catal.,* 216(1–2), **2003**, 257-264

32. T. A. Dorling, B. W. J. Lynch, R. L. Moss, *J. Catal.,* 20(2), **1971**, 190-201

33. H. A. Benesi, R. M. Curtis, H. P. Studer, *J. Catal.,* 10(4), **1968**, 328-335

34. M. Haruta *et al.*, *J. Catal.,* 144(1), **1993**, 175-192

35. H. Sakurai, M. Haruta, *Appl. Catal. A,* 127(1-2), **1995**, 93-105

36. P. Serp, R. Feurer, R. Morancho, P. Kalck, *J. Mol. Catal A Chem.,* 101(2), **1995**, L107-L110

37. M. Besson, P. Gallezot, *Catal. Today,* 57(1-2), **2000**, 127-141

38. K. Mori, T. Hara, T. Mizugaki, K. Ebitani, K. Kaneda, *J. Am. Chem. Soc.,* 126(34), **2004**, 10657-10666

39. D. L. Trimm, C.-W. Lam, *Chem. Eng. Sci.,* 35(6), **1980**, 1405-1413

40. S. Scirè, S. Minicò, C. Crisafulli, C. Satriano, A. Pistone, *Appl. Catal. B,* 40(1), **2003**, 43-49

41. D. Ciuparu, M. R. Lyubovsky, E. Altman, L. D. Pfefferle, A. Datye, *Catal. Rev.,* 44(4), **2002**, 593-649

42. C. Kul Ryu, M. Wong Ryoo, I. Soo Ryu, S. Kyu Kang, *Catal. Today,* 47(1–4), **1999**, 141-147

43. A. F. Ahlström-Silversand, C. U. I. Odenbrand, *Appl. Catal. A,* 153(1–2), **1997**, 157-175

44. A. Maeda, F. Yamakawa, K. Kunimori, T. Uchijima, *Catal. Lett.,* 4(2), **1990**, 107-112

45. L. Prati, M. Rossi, *Appl. Catal. B,* 23(2–3), **1999**, 135-142

46. M. Xu, D. W. Goodman, A. Bhattacharyya, *Appl. Catal. A,* 149(2), **1997**, 303-309

47. R. Burch, *J. Catal.,* 71(2), **1981**, 348-359

48. R. Burch, L. C. Garla, *J. Catal.,* 71(2), **1981**, 360-372

49. F. B. Passos, D. A. G. Aranda, M. Schmal, *J. Catal.,* 178(2), **1998**, 478-488

50. J. L. Carter, G. B. McVinker, W. Weissman, M. S. Kmak, J. H. Sinfelt, *Appl. Catal.,* 3(4), **1982**, 327-346

51. Yin, J. Liebscher, *Chem. Rev.,* 107(1), **2007**, 133-173

52. D. K. Liguras, D. I. Kondarides, X. E. Verykios, *Appl. Catal. B,* 43(4), **2003**, 345-354

53. P. N. Rylander, *Hydrogenation Methods* (Academic Press Inc. Ltd., London, 1985)

54. M. Bowker, *The Basis and Applications of Heterogeneous Catalysis* (Oxford University Press, New York, 1998)

55. R. J. Baxter, P. Hu, *J. Chem. Phys.,* 116(11), **2002**, 4379-4381

56. R. R. Allen, *J. Am. Oil. Chem. Soc.,* 58(3), **1981**, 166-169

57. G. P. Chiusoli, P. M. Maitlis, *Metal-catalysis in industrial organic processes* (Royal Society of Chemistry, 2008)

58. K. Weissermel, H.-J. Arpe, *Industrial Organic Chemistry* (Wiley, Weinheim, Fourth Edition, 2003)

59. M. Appl, in *Ullmann's Encyclopedia of Industrial Chemistry*. (Wiley-VCH Verlag GmbH & Co. KGaA, 2000).

60. R. A. Sheldon, *Pure Appl. Chem.,* 72(7), **2000**, 1233-1246

61. E. Crezee *et al.*, *Appl. Catal. A,* 251(1), **2003**, 1-17

62. I. Karamé, *Hydrogenation* (InTech, Published Online, 2012)

63. H. Conrad, G. Ertl, E. E. Latta, *Surf. Sci.,* 41(2), **1974**, 435-446

64. W. H. Weinberg, R. P. Merrill, *Surf. Sci.,* 33(3), **1972**, 493-515

65. V. G. Litovchenko, A. A. Efremov, *Condens. Mater. Phys.,* 2(3), **1999**, 561-576

66. N. Sheppard, *Annu. Rev. Phys. Chem.,* 39, **1988**, 589-644

67. J. Kua, W. A. Goddard, *J. Am. Chem. Soc.,* 121(47), **1999**, 10928-10941

68. F. Delbecq, P. Sautet, *Surf. Sci.,* 295(3), **1993**, 353-373

69. C. T. Campbell, S.-K. Shi, J. M. White, *Appl. Surf. Sci.,* 2(3), **1979**, 382-396

70. R. L. Palmer, J. N. Smith, *J. Chem. Phys.,* 60, **1974**, 1453-1463

71. H. Bonzel, R. Ku, *Surf. Sci.,* 33(1), **1972**, 91-106

72. B. Jenny, P. Pichat, *Langmuir,* 7(5), **1991**, 947-954

73. M. J. Vincent, R. D. Gonzalez, *Appl. Catal. A,* 217(1–2), **2001**, 143-156

74. G. D. Weatherbee, C. H. Bartholomew, *J. Catal.,* 77(2), **1982**, 460-472

75. P. A. Rautanen, J. R. Aittamaa, A. O. I. Krause, *Chem. Eng. Sci.,* 56(4), **2001**, 1247-1254

76. P. Chou, M. A. Vannice, *J. Catal.,* 107(1), **1987**, 140-153

77. U. K. Singh, M. Albert Vannice, *J. Catal.,* 191(1), **2000**, 165-180

78. I. Horiuti, M. Polanyi, *Trans. Faraday Soc.,* 30(0), **1934**, 1164-1172

79. M. Boudart, *Chem. Rev.,* 95(3), **1995**, 661-666

80. F. H. Ribeiro, A. E. Schach Von Wittenau, C. H. Bartholomew, G. A. Somorjai, *Catal. Rev.,* 39(1-2), **1997**, 49-76

81. A. P. Umpierre, E. de Jesús, J. Dupont, *ChemCatChem,* 3(9), **2011**, 1413-1418

82. R. M. Koros, E. J. Nowak, *Chem. Eng. Sci.,* 22(3), **1967**, 470

83. R. J. Madon, M. Boudart, *End. Eng. Chem. Fund.,* 21(4), **1982**, 438-447

84. F. Notheisz, A. g. Zsigmond, M. l. Barto´k, Z. Szegletes, G. V. Smith, *Appl. Catal. A,* 120(1), **1994**, 105-114

85. H. S. Taylor, *P. R. Soc. Lond. A-Conta.,* 108(745), **1925**, 105-111

86. T. Zambelli, J. Wintterlin, J. Trost, G. Ertl, *Science,* 273(5282), **1996**, 1688-1690

87. C. Mohr, H. Hofmeister, J. Radnik, P. Claus, *J. Am. Chem. Soc.,* 125(7), **2003**, 1905-1911

88. M. L. Helm, M. P. Stewart, R. M. Bullock, M. R. DuBois, D. L. DuBois, *Science,* 333(6044), **2011**, 863-866

89. M. M. Schubert *et al.*, *J. Catal.,* 197(1), **2001**, 113-122

90. A. M. Venezia *et al.*, *Appl. Catal. A,* 211(2), **2001**, 167-174

91. F. Deganello, L. F. Liotta, A. Macaluso, A. M. Venezia, G. Deganello, *Appl. Catal. B,* 24(3–4), **2000**, 265-273

92. A. M. Venezia, D. Duca, M. A. Floriano, G. Deganello, A. Rossi, *Surf. Interf. Anal.,* 18(8), **1992**, 619-622

93. M. Gruttadauria, R. Noto, G. Deganello, L. F. Liotta, *Tetrahedron Lett.,* 40(14), **1999**, 2857-2858

94. D. Duca, F. Arena, A. Parmaliana, G. Deganello, *Appl. Catal. A,* 172(2), **1998**, 207-216

95. L. F. Liotta, G. A. Martin, G. Deganello, *J. Catal.,* 164(2), **1996**, 322-333

96. D. Duca, G. La Manna, G. Deganello, *Catal. Lett.,* 52(1), **1998**, 73-79

97. D. Duca, L. F. Liotta, G. Deganello, *Catal. Today,* 24(1–2), **1995**, 15-21

98. L. F. Liotta *et al.*, *Catal. Today,* 66(2–4), **2001**, 271-276

99. L. Guczi *et al.*, *J. Catal.,* 182(2), **1999**, 456-462

100. G. Deganello, D. Duca, A. Martorana, G. Fagherazzi, A. Benedetti, *J. Catal.,* 150(1), **1994**, 117-126

101. G. Deganello, D. Duca, A. Martorana, G. Fagherazzi, A. Benedetti, *J. Catal.,* 150(1), **1994**, 127-134

102. G. Deganello *et al.*, *J. Catal.,* 151(1), **1995**, 125-134

103. D. Duca, L. F. Liotta, G. Deganello, *J. Catal.,* 154(1), **1995**, 69-79

104. G. Fagherazzi *et al.*, *Catal. Lett.,* 6(3), **1990**, 263-269

105. A. M. Venezia, D. Duca, M. A. Floriano, G. Deganello, A. Rossi, *Surf. Interf. Anal.,* 19(1-12), **1992**, 543-547

106. A. M. Venezia, R. Bertoncello, G. Deganello, *Surf. Interf. Anal.,* 23(4), **1995**, 239-247

107. J. B. d. E. de la Caillerie, J. J. Fripiat, *Catal. Today,* 14(2), **1992**, 125-140

108. J.-B. d'Espinose de la Caillerie, J. J. Fripiat, *Clay. Clay Miner.,* 39(3), **1991**, 270-280

109. G. Kovalenko *et al.*, *Kinet. Catal.,* 48(5), **2007**, 757-764

110. D. Divakar *et al.*, *J. Chem. Technol. Biotechnol.,* 82(3), **2007**, 253-258

111. B. M. Choudary, G. V. M. Sharma, P. Bharathi, *Angew. Chem. Int. Edit.,* 28(4), **1989**, 465-466

112. A. Louloudi, N. Papayannakos, *Appl. Catal. A,* 204(1), **2000**, 167-176

113. Á. Mastalir, Z. Király, F. Berger, *Appl. Catal. A,* 269(1–2), **2004**, 161-168

114. H. Lu, H. Yin, Y. Liu, T. Jiang, L. Yu, *Catal. Commun.,* 10(3), **2008**, 313-316

115. S. M. Echeverria, V. M. o. Andres, *Appl. Catal.,* 66(1), **1990**, 73-90

116. T. S. Ahmadi, Z. L. Wang, T. C. Green, A. Henglein, M. A. El-Sayed, *Science,* 272(5270), **1996**, 1924-1925

117. K. R. Brown, D. G. Walter, M. J. Natan, *Chem. Mater.,* 12(2), **2000**, 306-313

118. A. R. Tao, S. Habas, P. Yang, *Small,* 4(3), **2008**, 310-325

119. R. M. Rioux, H. Song, J. D. Hoefelmeyer, P. Yang, G. A. Somorjai, *J. Phys. Chem. B,* 109(6), **2005**, 2192-2202

120. P. Burtin, J. P. Brunelle, M. Pijolat, M. Soustelle, *Appl. Catal.,* 34(0), **1987**, 225-238

121. P. Burtin, J. P. Brunelle, M. Pijolat, M. Soustelle, *Appl. Catal.,* 34(0), **1987**, 239-254

122. J. A. Farmer, C. T. Campbell, *Science,* 329(5994), **2010**, 933-936

123. M. G. Mason, *Phys. Rev. B,* 27(2), **1983**, 748-762

124. M. H. Lee, C.-F. Cheng, V. Heine, J. Klinowski, *Chem. Phys. Lett.,* 265(6), **1997**, 673-676

125. D. S. Maciver, H. H. Tobin, R. T. Barth, *J. Catal.,* 2(6), **1963**, 485-497

126. H. Pines, W. O. Haag, *J. Am. Chem. Soc.,* 82(10), **1960**, 2471-2483

127. H. Pines, C. T. Goetschel, *J. Catal.,* 6(3), **1966**, 380-384

128. J. Chisem, I. C. Chisem, J. S. Rafelt, J. H. Clark, *Chem. Commun.,* (22), **1997**, 2203-2204

129. E. F. Vansant, P. V. D. Voort, K. C. Vrancken, *Characterization and Chemical Modification of the Silica Surface* (Elsevier, 1995)

130. G. C. Bond, P. B. Wells, *Appl. Catal.,* 18(2), **1985**, 221-224

131. G. C. Bond, P. B. Wells, *Appl. Catal.,* 18(2), **1985**, 225-230

132. J. W. Geus, P. B. Wells, *Appl. Catal.,* 18(2), **1985**, 231-242

133. A. Frennet, P. B. Wells, *Appl. Catal.,* 18(2), **1985**, 243-257

134. P. B. Wells, *Appl. Catal.,* 18(2), **1985**, 259-272

135. G. C. Bond, F. Garin, G. Maire, *Appl. Catal.,* 41, **1988**, 313-335

136. H. H. Murray, C. Harvey, J. M. Smith, *Clay. Clay Miner.,* 25(1), **1977**, 1-5

137. G. J. Churchman, *Clays Clay Miner.,* 38(6), **1990**, 591-599

138. G. J. Churchman, J. S. Whitton, G. G. C. Claridge, B. K. G. Theng, *Clays Clay Miner.,* 32(4), **1984**, 241-248

139. B. K. G. Theng, G. J. Churchman, J. S. Whitton, G. G. C. Claridge, *Clays Clay Miner.,* 32(4), **1984**, 249-258

140. M. Soma, G. J. Churchman, B. K. G. Theng, *Clay Miner.,* 27(4), **1992**, 413-421

141. G. J. Churchman, T. J. Davy, L. A. G. Aylmore, R. J. Gilkes, P. G. Self, *Clay Miner.,* 30(2), **1995**, 89-98

142. S. R. Levis, P. B. Deasy, *Int. J. Pharm.,* 243(1–2), **2002**, 125-134

143. D. G. Shchukin, G. B. Sukhorukov, R. R. Price, Y. M. Lvov, *Small,* 1(5), **2005**, 510-513

144. M. Du, B. Guo, D. Jia, *Eur. Polym. J,* 42(6), **2006**, 1362-1369

145. W. Jing *et al.*, *Shiyou Huagong,* 40(9), **2011**, 949-953

146. Z.-Y. Cai *et al.*, *Adv. Chem. Eng. Sci.,* 1, **2011**, 15-19

147. P. Liu, M. Zhao, *Appl. Surf. Sci.,* 255(7), **2009**, 3989-3993

148. I. Friedman, R. L. Smith, W. D. Long, *Geol. Soc. Am. Bull.,* 77(3), **1966**, 323-328

149. M. Roulia, K. Chassapis, J. A. Kapoutsis, E. I. Kamitsos, T. Savvidis, *J. Mater. Sci.,* 41(18), **2006**, 5870-5881

150. M. Doğan, M. Alkan, Ü. Çakir, *J. Colloid Interface Sci.,* 192(1), **1997**, 114-118

151. M. Alkan, M. Doğan, *J. Colloid Interface Sci.,* 207(1), **1998**, 90-96

152. M. Alkan, Ö. Demirbaş, M. Doğan, *Micropor. Mesopor. Mat.,* 84(1–3), **2005**, 192-200

153. M. Doğan, M. Alkan, *J. Colloid Interface Sci.,* 267(1), **2003**, 32-41

154. M. Doğan, M. Alkan, *Chemosphere,* 50(4), **2003**, 517-528

155. M. Doğan, M. Alkan, A. Türkyilmaz, Y. Özdemir, *J. Hazard. Mater.,* 109(1–3), **2004**, 141-148

156. M. Doğan, M. Alkan, Y. Onganer, *Water Air Soil Poll.,* 120(3), **2000**, 229-248

157. T. Mathialagan, T. Viraraghavan, *J. Hazard. Mater.,* 94(3), **2002**, 291-303

158. M. Alkan, M. Doğan, *J. Colloid Interface Sci.,* 243(2), **2001**, 280-291

159. A. Sarı, M. Tuzen, D. Cıtak, M. Soylak, *J. Hazard. Mater.,* 148(1–2), **2007**, 387-394

160. S. N. Hosseini, S. M. Borghei, M. Vossoughi, N. Taghavinia, *Appl. Catal. B,* 74(1–2), **2007**, 53-62

161. J. C. Elliott, P. E. Mackie, R. A. Young, *Science,* 180(4090), **1973**, 1055-1057

162. D. Haverty, S. A. M. Tofail, K. T. Stanton, J. B. McMonagle, *Phys. Rev. B,* 71(9), **2005**, 094103

163. Y. Z. Wan *et al.*, *Mat. Sci. Eng. C,* 27(4), **2007**, 855-864

164. M. R. Mucalo, D. L. Foster, *Croat. Chem. Acta,* 77(3), **2004**, 509-517

165. D. Bartle, M. Mucalo, *J. Bone Joint Surg. Br.,* 91-B, **2009**, 343

166. M. R. Mucalo *et al.*, *J. Appl. Biomater. Biom.,* 2, **2004**, 96-104

167. N. Ignjatović *et al.*, *Biomaterials,* 20(9), **1999**, 809-816

168. M. R. Mucalo, *Hydroxyapatite (HAp) for Biomedical Applications* (Elsevier, Cambridge, 2015)

169. C. C. Fuller, J. R. Bargar, J. A. Davis, M. J. Piana, *Environ. Sci. Technol.,* 36(2), **2001**, 158-165

170. D. P. Uskokovic, S. K. Milonjic, D. I. Rakovic, *Mater. Sci. Forum,* 494(405), **2005**, 405-410

171. J. Boisson, A. Ruttens, M. Mench, J. Vangronsveld, *Environ. Pollut.,* 104(2), **1999**, 225-233

172. C. N. Mulligan, R. N. Yong, B. F. Gibbs, *Eng. Geol.,* 60(1–4), **2001**, 193-207

173. N. Jamwal, M. Gupta, S. Paul, *Green Chem.,* 10(9), **2008**, 999-1003

174. J. Qiao, W. Zhu, G. Zhuo, H. Zhou, X. Jiang, *Chin. J. Catal.,* 29(3), **2008**, 209-211

175. B. C. Ranu, L. Adak, K. Chattopadhyay, *J. Org. Chem.,* 73(14), **2008**, 5609-5612

176. K. Mori, T. Hara, T. Mizugaki, K. Ebitani, K. Kaneda, *J. Am. Chem. Soc.,* 125(38), **2003**, 11460-11461

177. K. Kaneda, K. Mori, T. Hara, T. Mizgaki, K. Ebitani, *Catal. Surv. Asia,* 7(4), **2004**, 231-239

178. T. Hara *et al.*, *Green Chem.,* 6(10), **2004**, 507-509

179. N. Hashimoto *et al.*, *Chem. Lett.,* 39(1), **2010**, 49-51

180. K. Kim, S. Lee, K. Yoon, *Korean J. Chem. Eng.,* 23(3), **2006**, 356-361

181. J. H. Jun, T. H. Lim, S.-W. Nam, S.-A. Hong, K. J. Yoon, *Appl. Catal. A,* 312(0), **2006**, 27-34

182. J. Ashok, S. Kumar, M. Subrahmanyam, A. Venugopal, *Catal. Lett.,* 121(3), **2008**, 283-290

183. T. Mitsudome, A. Noujima, T. Mizugaki, K. Jitsukawa, K. Kaneda, *Chem. Commun.,* (35), **2009**, 5302-5304

184. T. Mitsudome *et al.*, *Angew. Chem. Int. Edit.,* 47(41), **2008**, 7938-7940

185. M. I. Domínguez, F. Romero-Sarria, M. A. Centeno, J. A. Odriozola, *Appl. Catal. B,* 87(3-4), **2009**, 245-251

186. G. Raju, P. S. Reddy, J. Ashok, B. M. Reddy, A. Venugopal, *J. Nat. Gas. Chem.,* 17(3), **2008**, 293-297

187. W. Fang, J. Chen, Q. Zhang, W. Deng, Y. Wang, *Chem. Eur. J.,* 17(4), **2011**, 1247-1256

188. C.-M. Ho, W.-Y. Yu, C.-M. Che, *Angew. Chem. Int. Edit.,* 43(25), **2004**, 3303-3307

189. H. Sun *et al.*, *Angew. Chem. Int. Edit.,* 48(24), **2009**, 4390-4393

190. K. Mori *et al.*, *Chem. Mater.,* 19(6), **2007**, 1249-1256

191. Y. Zhang *et al.*, *J. Phys. Chem. C,* 114(39), **2010**, 16443-16450

192. A. Abad, C. Almela, A. Corma, H. García, *Tetrahedron,* 62(28), **2006**, 6666-6672

193. Y. Pérez, M. Fajardo, A. Corma, *Catal. Commun.,* 12(12), **2011**, 1071-1074

194. Y.-P. Sun *et al.*, *Catal. Commun.,* 12(3), **2010**, 188-192

195. T. Leventouri, *Biomaterials,* 27(18), **2006**, 3339-3342

196. G. Cho, Y. Wu, J. L. Ackerman, *Science,* 300(5622), **2003**, 1123-1127

197. A. O'Sullivan, *Cellulose,* 4(3), **1997**, 173-207

198. J. Cai, S. Kimura, M. Wada, S. Kuga, *Biomacromolecules,* 10(1), **2009**, 87-94

199. J. He, T. Kunitake, A. Nakao, *Chem. Mater.,* 15(23), **2003**, 4401-4406

200. K. R. Reddy, N. S. Kumar, P. S. Reddy, B. Sreedhar, M. L. Kantam, *J. Mol. Catal A Chem.,* 252(1–2), **2006**, 12-16

201. C. M. Cirtiu, A. F. Dunlop-Briere, A. Moores, *Green Chem.,* 13(2), **2011**, 288-291

202. K. R. Reddy, N. S. Kumar, *Synlett,* 2006(14), **2006**, 2246-2250

203. L. Wu, M. Shamsuzzoha, S. M. C. Ritchie, *J. Nanopart. Res.,* 7(4-5), **2005**, 469-476

204. D. L. Foster, PhD Thesis (University of Waikato, 2001).

205. D. F. Laird, PhD Thesis (University of Waikato, 2010).

206. S. Ek, A. Root, M. Peussa, L. Niinistö, *Thermochim. Acta,* 379(1–2), **2001**, 201-212

207. B. L. Newalkar, S. Komarneni, *J. Sol-Gel Sci. Techn.,* 18(3), **2000**, 191-198

208. K. J. D. MacKenzie, M. E. Smith, *Multinuclear Solid-State NMR of Inorganic Materials* (Elsevier Science Ltd., Oxford, 2002)

209. C. E. Bronnimann, R. C. Zeigler, G. E. Maciel, *J. Am. Chem. Soc.,* 110(7), **1988**, 2023-2026

210. J. Trébosc, J. W. Wiench, S. Huh, V. S. Y. Lin, M. Pruski, *J. Am. Ceram. Soc.,* 127(9), **2005**, 3057-3068

211. H. A. Benesi, A. C. Jones, *J. Phys. Chem.,* 63(2), **1959**, 179-182

212. R. S. McDonald, *J. Phys. Chem.,* 62(10), **1958**, 1168-1178

213. P. Innocenzi, *J. Non-Cryst. Solids,* 316(2–3), **2003**, 309-319

214. E. I. Kamitsos, A. P. Patsis, G. Kordas, *Phys. Rev. B,* 48(17), **1993**, 12499-12505

215. A. J. Van Roosmalen, J. C. Mol, *J. Phys. Chem.,* 83(19), **1979**, 2485-2488

216. B. Himmel, T. Gerber, H. Bürger, *J. Non-Cryst. Solids,* 91(1), **1987**, 122-136

217. B. Himmel, T. Gerber, H. Bürger, *J. Non-Cryst. Solids,* 119(1), **1990**, 1-13

218. K. Kamiya *et al.*, *J. Non-Cryst. Solids,* 240(1–3), **1998**, 202-211

219. J. P. O'Reilly, C. P. Butts, I. A. I'Anso, A. M. Shaw, *J. Am. Ceram. Soc.,* 127(6), **2005**, 1632-1633

220. C. Schwer, E. Kenndler, *Anal. Chem.,* 63(17), **1991**, 1801-1807

221. G. Xu, J. Zhang, G. Song, *Powder Technol.,* 134(3), **2003**, 218-222

222. T. Suhara, H. Fukui, M. Yamaguchi, *Colloids Surf. A,* 101(1), **1995**, 29-37

223. T. Jesionowski, *Colloids Surf. A,* 222(1–3), **2003**, 87-94

224. S. Schwarz *et al.*, *Colloids Surf. A,* 163(1), **2000**, 17-27

225. M. L. Fisher, M. Colic, M. P. Rao, F. F. Lange, *J. Am. Ceram. Soc.,* 84(4), **2001**, 713-718

226. S. M. Olhero, J. M. F. Ferreira, *Powder Technol.,* 139(1), **2004**, 69-75

227. G. A. Parks, *Chem. Rev.,* 65(2), **1965**, 177-198

228. M. McMillan, J. S. Brinen, G. L. Haller, *J. Catal.*, **1986**, 243-247

229. G. Piedra, J. J. Fitzgerald, N. Dando, S. F. Dec, G. E. Maciel, *Inorg. Chem.,* 35(12), **1996**, 3474-3478

230. C. Pecharroman, I. Sobrados, J. Iglesias, T. Gonzalez-Carreno, J. Sanz, *J. Phys. Chem. B.,* 103(30), **1999**, 6160-6170

231. L. Favaro *et al.*, *J. Solid State Chem.,* 183(4), **2010**, 901-908

232. M. R. Hill, T. J. Bastow, S. Celotto, A. J. Hill, *Chem. Mater.,* 19(11), **2007**, 2877-2883

233. A. Boumaza *et al.*, *J. Solid State Chem.,* 182(5), **2009**, 1171-1176

234. C. M. Koretsky, D. A. Sverjensky, J. W. Salisbury, D. M. D'Aria, *Geochim. Cosmochim. Ac.,* 61(11), **1997**, 2193-2210

235. T. H. Ballinger, J. T. Yates, *Langmuir,* 7(12), **1991**, 3041-3045

236. J. B. Peri, R. B. Hannan, *J. Phys. Chem.,* 64(10), **1960**, 1526-1530

237. G. V. Franks, L. Meagher, *Colloids Surf. A,* 214(1–3), **2003**, 99-110

238. A. López Valdivieso, J. L. Reyes Bahena, S. Song, R. Herrera Urbina, *J. Colloid Interface Sci.,* 298(1), **2006**, 1-5

239. B. P. Singh, R. Menchavez, C. Takai, M. Fuji, M. Takahashi, *J. Colloid Interface Sci.,* 291(1), **2005**, 181-186

240. J. A. Yopps, D. W. Fuerstenau, *J. Colloid Sci.,* 19(1), **1964**, 61-71

241. Q. Yang, T. Troczynski, *J. Am. Ceram. Soc.,* 82(7), **1999**, 1928-1930

242. J. F. Mustard, J. E. Hays, *Icarus,* 125(1), **1997**, 145-163

243. N. Pleshko, A. Boskey, R. Mendelsohn, *Biophys. J.,* 60(4), **1991**, 786-793

244. I. Rehman, W. Bonfield, *J. Mater. Sci.-Mater. M.,* 8(1), **1997**, 1-4

245. M. C. Chang, J. Tanaka, *Biomaterials,* 23(24), **2002**, 4811-4818

246. C. Jäger, T. Welzel, W. Meyer-Zaika, M. Epple, *Magn. Reson. Chem.,* 44(6), **2006**, 573-580

247. W. P. Rothwell, J. S. Waugh, J. P. Yesinowski, *J. Am. Ceram. Soc.,* 102(8), **1980**, 2637-2643

248. G. Yin, Z. Liu, J. Zhan, F. Ding, N. Yuan, *Chem. Eng. J,* 87(2), **2002**, 181-186

249. R. G. Zhbankov *et al.*, *J. Mol. Struct.,* 614(1–3), **2002**, 117-125

250. J. J. Cael, K. H. Gardner, J. L. Koenig, J. Blackwell, *J. Chem. Phys.,* 62(3), **1975**, 1145-1153

251. M. Tsuboi, *J. Polym. Sci.,* 25(109), **1957**, 159-171

252. M. L. Nelson, R. T. O'Connor, *J. Appl. Polym. Sci.,* 8(3), **1964**, 1311-1324

253. S. Barsberg, *J. Phys. Chem. B,* 114(36), **2010**, 11703-11708

254. A. Isogai, M. Usuda, T. Kato, T. Uryu, R. H. Atalla, *Macromolecules,* 22(7), **1989**, 3168-3172

255. R. H. Atalla, J. Gast, D. Sindorf, V. Bartuska, G. Maciel, *J. Am. Chem. Soc.,* 102(9), **1980**, 3249-3251

256. H. Kono, T. Erata, M. Takai, *Macromolecules,* 36(10), **2003**, 3589-3592

257. H. Kono *et al.*, *J. Am. Chem. Soc.,* 124(25), **2002**, 7506-7511

258. M. Österbeg, P. M. Claesson, *J. Adhes. Sci. Technol.,* 14(5), **2000**, 603-618

259. E. Joussein *et al.*, *Clay Miner.,* 40(4), **2005**, 383-426

260. R. L. Frost, A. M. Vassallo, *Clay. Clay Miner.,* 44(5), **1996**, 635-651

261. R. Newman, C. Childs, G. Churchman, *Clay Miner.,* 29(3), **1994**, 305-312

262. R. Oestrike *et al.*, *Geochim. Cosmochim. Ac.,* 51(8), **1987**, 2199-2209

263. S. K. Lee, S. B. Lee, S. Y. Park, Y. S. Yi, C. W. Ahn, *Phys. Rev. Lett.,* 103(9), **2009**, 095501

264. Q. Zeng, H. Nekvasil, C. P. Grey, *J. Phys. Chem. B,* 103(35), **1999**, 7406-7415

265. H. Maekawa, T. Saito, T. Yokokawa, *J. Phys. Chem. B,* 102(39), **1998**, 7523-7529

266. X. Xue, M. Kanzaki, *J. Phys. Chem. B,* 105(17), **2001**, 3422-3434

267. M. E. Fleet, X. Liu, *Biomaterials,* 28(6), **2007**, 916-926

268. I. R. Gibson, W. Bonfield, *J. Biomed. Mater. Res.,* 59(4), **2002**, 697-708

269. S. A. Redey *et al.*, *J. Biomed. Mater. Res.,* 50(3), **2000**, 353-364

270. C. Rey, J. L. Miquel, L. Facchini, A. P. Legrand, M. J. Glimcher, *Bone,* 16(5), **1995**, 583-586

271. A. Doostmohammadi *et al.*, *Mater. Chem. Phys.,* 132(2–3), **2012**, 446-452

272. E. de Morais Teixeira *et al.*, *Cellulose,* 17(3), **2010**, 595-606

273. L. Gilbert, C. Mercier, in *Stud. Surf. Sci. Catal.,* M. Guisnet *et al.*, Eds. (Elsevier, 1993), vol. Volume 78, pp. 51-66.

274. R. A. Rajadhyaksha, S. L. Karwa, *Chem. Eng. Sci.,* 41(7), **1986**, 1765-1770

275. S. Mukherjee, M. A. Vannice, *J. Catal.,* 243(1), **2006**, 108-130

276. E. W. Washburn, *Phys. Rev.,* 17(3), **1921**, 273-283

277. L. Galet, S. Patry, J. Dodds, *J. Colloid Interface Sci.,* 346(2), **2010**, 470-475

278. A. Siebold, A. Walliser, M. Nardin, M. Oppliger, J. Schultz, *J. Colloid Interface Sci.,* 186(1), **1997**, 60-70

279. J. Shang, M. Flury, J. B. Harsh, R. L. Zollars, *J. Colloid Interface Sci.,* 328(2), **2008**, 299-307

280. R. Crawford, L. K. Koopal, J. Ralston, *Colloids Surf.,* 27(4), **1987**, 57-64

281. M. E. P. Wålinder, D. J. Gardner, *J. Adhes. Sci. Tehnol.,* 13(12), **1999**, 1363-1374

282. E. Chibowski, L. Holysz, *J. Adhes. Sci. Technol.,* 11(10), **1997**, 1289-1301

283. E. Chibowski, L. Holysz, *Langmuir,* 8(2), **1992**, 710-716

284. G. Liu, M. Zhang, C. Ridgway, P. Gane, *Colloids Surf. A,* 443(0), **2014**, 286-295

285. A. Siebold, M. Nardin, J. Schultz, A. Walliser, M. Oppliger, *Colloids Surf. A,* 161(1), **2000**, 81-87

286. J. M. McHale, A. Auroux, A. J. Perrotta, A. Navrotsky, *Science,* 277(5327), **1997**, 788-791

287. H. J. Busscher, H. P. de Jong, J. Arends, *Mater. Chem. Phys.,* 17(6), **1987**, 553-558

288. F. Dourado, F. M. Gama, E. Chibowski, M. Mota, *J. Adhes. Sci. Technol.,* 12(10), **1998**, 1081-1090

289. B. Biliński, L. Holysz, *Powder Technol.,* 102(2), **1999**, 120-126

290. W. A. Zisman, *Relation of the Equilibrium Contact Angle to Liquid and Solid Constitution* (1964)

291. A. Mihranyan, A. P. Llagostera, R. Karmhag, M. Strømme, R. Ek, *Int. J. Pharm.,* 269(2), **2004**, 433-442

292. C. Verlhac, J. Dedier, H. Chanzy, *J. Polym. Sci. Part A Polym. Chem.,* 28(5), **1990**, 1171-1177

293. L. Borum-Nicholas, O. C. Wilson Jr, *Biomaterials,* 24(21), **2003**, 3671-3679

294. R. Redón *et al.*, *J. Colloid Interface Sci.,* 287(2), **2005**, 664-670

295. E. C. DeCanio, V. P. Nero, J. W. Bruno, *J. Catal.,* 135(2), **1992**, 444-457

296. H. Jeziorowski, H. Knozinger, W. Meye, H. D. Muller, *J. Chem. Soc. Faraday Trans.,* 69(0), **1973**, 1744-1758

297. Y. Marcus, *J. Solution Chem.,* 13(9), **1984**, 599-624

298. Y. Marcus, *Chem. Soc. Rev.,* 22(6), **1993**, 409-416

299. G. Vazquez, E. Alvarez, J. M. Navaza, *J. Chem. Eng. Data,* 40(3), **1995**, 611-614

300. M. Korn, E. Killmann, J. Eisenlauer, *J. Colloid Interface Sci.,* 76(1), **1980**, 7-18

301. B. Fubini, V. Bolis, A. Cavenago, E. Garrone, P. Ugliengo, *Langmuir,* 9(10), **1993**, 2712-2720

302. J. Catalán, C. Díaz, F. García-Blanco, *J. Org. Chem.,* 66(17), **2001**, 5846-5852

303. K. Miyai, M. Nakamura, K. Tamura, S. Murakami, *J. Solution Chem.,* 26(10), **1997**, 973-988

304. A. Wakisaka, H. Abdoul-Carime, Y. Yamamoto, Y. Kiyozumi, *J. Chem. Soc. Faraday Trans.,* 94(3), **1998**, 369-374

305. R. G. LeBel, D. A. I. Goring, *J. Chem. Eng. Data,* 7(1), **1962**, 100-101

306. D. B. G. Williams, M. Lawton, *J. Org. Chem.,* 75(24), **2010**, 8351-8354

307. H. An, G. Liu, V. S. J. Craig, *Adv. Colloid Interface Sci.,* (0),

308. N. Gemo, P. Biasi, T. O. Salmi, P. Canu, *J. Chem. Thermodyn.,* 54(0), **2012**, 1-9

309. A. C. D. International Union of Pure and Applied Chemistry, Comission on Solubility Data, *Hydrogen and Deuterium* (Pergamon, Oxford, 1981)

310. Purwanto, R. M. Deshpande, R. V. Chaudhari, H. Delmas, *J. Chem. Eng. Data,* 41(6), **1996**, 1414-1417

311. J. Pardo, M. C. López, J. Santafé, F. M. Royo, J. S. Urieta, *Fluid Phase Equilibr.,* 109(1), **1995**, 29-37

312. E. Brunner, *J. Chem. Eng. Data,* 30(3), **1985**, 269-273

313. S. K. Lachowicz, D. M. Newitt, K. E. Weale, *Trans. Faraday Soc.,* 51(0), **1955**, 1198-1205

314. M. Balcerzak, *Anal. Sci.,* 18(7), **2002**, 737-750

315. R. Djingova, H. Heidenreich, P. Kovacheva, B. Markert, *Anal. Chim. Acta,* 489(2), **2003**, 245-251

316. M. M. Todand, I. JarviS, K. E. Jarvis, *Chem. Geol.,* 124(1–2), **1995**, 21-36

317. J. P. Singh, S. N. Thakur, *Laser-Induced Breakdown Spectroscopy* (Elsevier, Amsterdam, 2007)

318. R. Noll, *Laser Induced Breakdown Spectroscopy: Fundamentals and Applications* (Springer, New York, 2012)

319. D. A. Cremers, L. J. Radziemski, *Handbook of Laser-Induced Breakdown Spectroscopy* (Wiley, West Sussex, 2013)

320. D. A. Rusak, B. C. Castle, B. W. Smith, J. D. Winefordner, *Crit. Rev. Anal. Chem.,* 27(4), **1997**, 257-290

321. F. J. Fortes, J. Moros, P. Lucena, L. M. Cabalín, J. J. Laserna, *Anal. Chem.,* 85(2), **2013**, 640-669

322. R. Fantoni *et al.*, *Spectrochim. Acta. B,* 63(10), **2008**, 1097-1108

323. D. W. Hahn, N. Omenetto, *Appl. Spectrosc.,* 66(4), **2012**, 347-419

324. A. P. M. Michel, *Spectrochim. Acta. B,* 65(3), **2010**, 185-191

325. G. Asimellis, N. Michos, I. Fasaki, M. Kompitsas, *Spectrochim. Acta. B,* 63(11), **2008**, 1338-1343

326. P. Lucena, J. J. Laserna, *Spectrochim. Acta. B,* 56(2), **2001**, 177-185

327. P. Lucena, J. M. Vadillo, J. J. Laserna, *Anal. Chem.,* 71(19), **1999**, 4385-4391

328. M. A. Palacios *et al.*, *Sci. Total Environ.,* 257(1), **2000**, 1-15

329. E. K. Shibuya, J. E. S. Sarkis, J. Enzweiler, A. P. S. Jorge, A. M. G. Figueiredo, *J. Anal. Atom. Spectrom.,* 13(9), **1998**, 941-944

330. K. E. Jarvis, J. G. Williams, S. J. Parry, E. Bertalan, *Chem. Geol.,* 124(1–2), **1995**, 37-46

331. S. F. Boulyga, K. G. Heumann, *Anal. Bioanal. Chem.,* 383(3), **2005**, 442-447

332. M. Resano *et al.*, *J. Anal. Atom. Spectrom.,* 21(9), **2006**, 899-909

333. P. Sylvester *et al.*, in *10th International Platinum Symposium: Oulu, Geological Survey of Finland, Extended Abstracts*. (2005), pp. 16-20.

334. J.-P. Lorand, O. Alard, *Geochim. Cosmochim. Ac.,* 65(16), **2001**, 2789-2806

335. P. Sattari, J. M. Brenan, I. Horn, W. F. McDonough, *Econ. Geol.,* 97(2), **2002**, 385-398

336. K. Oguri, G. Shimoda, Y. Tatsumi, *Chem. Geol.,* 157(3), **1999**, 189-197

337. M. Gros, J. P. Lorand, A. Luguet, *Chem. Geol.,* 185(3), **2002**, 179-190

338. J. E. Mungall, D. R. A. Andrews, L. J. Cabri, P. J. Sylvester, M. Tubrett, *Geochim. Cosmochim. Ac.,* 69(17), **2005**, 4349-4360

339. A. Luguet *et al.*, *Earth Planet. Sci. Lett.,* 189(3–4), **2001**, 285-294

340. S. Rauch, G. M. Morrison, M. Moldovan, *Sci. Total Environ.,* 286(1–3), **2002**, 243-251

341. S. Rauch, M. Lu, G. M. Morrison, *Environ. Sci. Technol.,* 35(3), **2000**, 595-599

342. D. Hutchinson, I. McDonald, *Miner. Deposita,* 43(6), **2008**, 695-711

343. M. Motelica-Heino, S. Rauch, G. M. Morrison, O. F. X. Donard, *Anal. Chim. Acta,* 436(2), **2001**, 233-244

344. B. Gómez *et al.*, *Sci. Total Environ.,* 299(1–3), **2002**, 1-19

345. A. P. d. S. Jorge, J. Enzweiler, E. K. Shibuya, J. E. S. Sarkis, A. M. G. Figueiredo, *Geostandard. Newslett.,* 22(1), **1998**, 47-55

346. A. Figueiredo, J. Enzweiler, J. Sarkis, A. Jorge, E. Shibuya, *J. Radioanal. Nucl. Chem.,* 244(3), **2000**, 623-625

347. P. J. Sylvester, S. M. Eggins, *Geostandard. Newslett.,* 21(2), **2007**, 215-229

348. A. Campbell, M. Humayun, in *Lunar and Planetary Institute Science Conference Abstracts*. (1999), vol. 30, pp. 1974.

349. A. J. Campbell, M. Humayun, *Anal. Chem.,* 71(5), **1999**, 939-946

350. S. A. Junk, *Nucl. Instrum. Methods Phys. Res. Sect. A,* 181(1–4), **2001**, 723-727

351. K. H. Jensen, S. Rauch, G. Morrison, P. Lindberg, *Arc. Environ. Contam. Toxicol.,* 42(3), **2002**, 338-347

352. R. Strobel, W. J. Stark, L. Mädler, S. E. Pratsinis, A. Baiker, *J. Catal.,* 213(2), **2003**, 296-304

353. E. F. Murphy *et al.*, *Chem. Mater.,* 13(4), **2001**, 1296-1304

354. V. Zuzaniuk, R. Prins, *J. Catal.,* 219(1), **2003**, 85-96

355. S. Hannemann *et al.*, *Appl. Catal. A,* 316(2), **2007**, 226-239

356. S. Lestari *et al.*, *Energy Fuels,* 23(8), **2009**, 3842-3845

357. G. Alloncle, N. Gilon, C.-P. Lienemann, S. Morin, *C. R. Chim.,* 12(6–7), **2009**, 637-646

358. C. Beck, T. Mallat, A. Baiker, *Catal. Lett.,* 75(3-4), **2001**, 131-136

359. M. Guillong, D. Gunther, *J. Anal. At. Spectrom.,* 17(8), **2002**, 831-837

360. I. Kroslakova, D. Gunther, *J. Anal. At. Spectrom.,* 22(1), **2007**, 51-62

361. A. V. Delgado, F. González-Caballer, R. J. Hunter, L. K. Koopal, J. Lykelma, *Pure Appl. Chem.,* 77(10), **2005**, 1753-1805

362. D. H. Everett, *Basic Principles of Colloid Science* (Royal Society of Chemistry Paperbacks, London, 1988)

363. R. J. Hunter, *Foundations of Colloid Science* (Oxford University Press, Oxford, 2001)

364. J. E. Jaine, MSc Thesis (University of Waikato, 2011).

365. H. C. Brown, C. A. Brown, *J. Am. Chem. Soc.,* 84(14), **1962**, 2827-2827

366. D. B. Williams, C. B. Carter, *Transmission Electron Microscopy: A Textbook for Materials Science* (Springer, 2009)

367. D. Balzar *et al.*, *J. Appl. Crystallogr.,* 37(6), **2004**, 1-14

368. A. Borodziński, M. Bonarowska, *Langmuir,* 13(21), **1997**, 5613-5620

369. A. E. Schweizer, G. T. Kerr, *Inorg. Chem.,* 17(8), **1978**, 2326-2327

370. D. N. Furlong, A. Launikonis, W. H. F. Sasse, J. V. Sanders, *J. Chem. Soc. Faraday Trans.,* 80(3), **1984**, 571-588

371. E. Benguerel, G. P. Demopoulos, G. B. Harris, *Hydrometallurgy,* 40(1-2), **1996**, 135-152

372. J. M. Sánchez, M. Hidalgo, J. Havel, V. Salvadó, *Talanta,* 56(6), **2002**, 1061-1071

373. C. Drew Tait, D. R. Janecky, P. S. Z. Rogers, *Ceochim. Cosmochim. Ac.,* 55(5), **1991**, 1253-1264

374. J.-F. Boily, T. M. Seward, *Geochim. Cosmochim. Ac.,* 69(15), **2005**, 3773-3789

375. D. Nachtigall, S. Artelt, G. Wünsch, *J. Chromatogr. A,* 775(1-2), **1997**, 197-210

376. C. H. Gammons, *Geochim. Cosmochim. Ac.,* 60(10), **1996**, 1683-1694

377. H. Borchert *et al.*, *Langmuir,* 21(5), **2005**, 1931-1936

378. E. E. Gonzo, M. Boudart, *J. Catal.,* 52(3), **1978**, 462-471

379. E. Segal, R. J. Madon, M. Boudart, *J. Catal.,* 52(1), **1978**, 45-49

380. S. M. Davis, G. A. Somorjai, *J. Catal.,* 65(1), **1980**, 78-83

381. O. Domínguez-Quintero *et al.*, *J. Mol. Catal A Chem.,* 197(1-2), **2003**, 185-191

382. L. M. Rossi *et al.*, *Green Chem.,* 9(4), **2007**, 379-385

383. Z. Xu, B. C. Gates, *J. Catal.,* 154(2), **1995**, 335-344

384. M. Boudart, D. J. Sajkowski, *Faraday Discuss.,* 92(0), **1991**, 57-67

385. M. Adlim, M. Abu Bakar, K. Y. Liew, J. Ismail, *J. Mol. Catal A Chem.,* 212(1–2), **2004**, 141-149

386. C. Liu, Y. Xu, S. Liao, D. Yu, *J. Mol. Catal A Chem.,* 149(1–2), **1999**, 119-123

387. J. Allen *et al.*, *Appl. Organomet. Chem.,* 25(4), **2011**, 245-254

388. Z. Király, I. Dékány, Á. Mastalir, M. Bartók, *J. Catal.,* 161(1), **1996**, 401-408

389. B. P. M. Holbrook, R. Rajagopalan, K. Dronvajjala, Y. K. Choudhary, H. C. Foley, *J. Mol. Catal A Chem.,* 367(0), **2013**, 61-68

390. K. Mori, T. Urata, S. Okada, H. Yamashita, *Top. Catal.,* 57(10-13), **2014**, 1026-1031

391. X.-Y. Quek, Y. Guan, E. J. M. Hensen, *Catal. Today,* 183(1), **2012**, 72-78

392. F. Boccuzzi, A. Chiorino, M. Gargano, N. Ravasio, *J. Catal.,* 165(2), **1997**, 140-149

393. T. S. Huang, Y. H. Wang, J. Y. Jiang, Z. L. Jin, *Chin. Chem. Lett.,* 19(1), **2008**, 102-104

394. V. Chechik, R. M. Crooks, *J. Am. Chem. Soc.,* 122(6), **2000**, 1243-1244

395. Y.-M. Chung, H.-K. Rhee, *Catal. Lett.,* 85(3-4), **2003**, 159-164

396. J. E. Jaine, M. R. Mucalo, *J. Colloid Interface Sci.,* 375(1), **2012**, 12-22

397. M. Chen, J. P. Liu, S. Sun, *J. Am. Chem. Soc.,* 126(27), **2004**, 8394-8395

398. M. Koebel, L. Jones, G. Somorjai, *J. Nanopart. Res.,* 10(6), **2008**, 1063-1069

399. T. Teranishi, M. Miyake, *Chem. Mater.,* 10(2), **1998**, 594-600

400. M. Miyake, K. Miyabayashi, *Catal. Surv. Asia,* 16(1), **2012**, 1-13

401. R. Narayanan, M. A. El-Sayed, *J. Phys. Chem. B,* 109(26), **2005**, 12663-12676

402. C.-J. Jia, F. Schuth, *Phys. Chem. Chem. Phys.,* 13(7), **2011**, 2457-2487

403. G. A. Somorjai, F. Tao, J. Y. Park, *Top. Catal.,* 47(1), **2008**, 1-14

404. A. T. Bell, *Science,* 299(5613), **2003**, 1688-1691

405. Q. Wang, H. Liu, H. Wang, *J. Colloid Interface Sci.,* 190(2), **1997**, 380-386

406. W. Yu *et al.*, *J. Mol. Catal A Chem.,* 142(2), **1999**, 201-211

407. J.-D. Grunwaldt, C. Kiener, C. Wögerbauer, A. Baiker, *J. Catal.,* 181(2), **1999**, 223-232

408. C.-W. Chen, T. Serizawa, M. Akashi, *Chem. Mater.,* 11(5), **1999**, 1381-1389

409. G. A. Somorjai, J. Y. Park, *Top. Catal.,* 49(3-4), **2008**, 126-135

410. G. A. Somorjai, S. K. Beaumont, *Top. Catal.*, **2015**, 1-13

411. J. N. Kuhn, C.-K. Tsung, W. Huang, G. A. Somorjai, *J. Catal.,* 265(2), **2009**, 209-215

412. L. R. Baker *et al.*, *Catal. Lett.,* 142(11), **2012**, 1286-1294

413. V. V. Pushkarev, K. An, S. Alayoglu, S. K. Beaumont, G. A. Somorjai, *J. Catal.,* 292, **2012**, 64-72

414. R. Rioux, B. Hsu, M. Grass, H. Song, G. Somorjai, *Catal. Lett.,* 126(1), **2008**, 10-19

415. C. J. Kliewer *et al.*, *J. Am. Chem. Soc.,* 132(37), **2010**, 13088-13095

416. J. N. Kuhn, W. Huang, C.-K. Tsung, Y. Zhang, G. A. Somorjai, *J. Am. Chem. Soc.,* 130(43), **2008**, 14026-14027

417. M. Grass, R. Rioux, G. Somorjai, *Catal. Lett.,* 128(1-2), **2009**, 1-8

418. V. V. Pushkarev, N. Musselwhite, K. An, S. Alayoglu, G. A. Somorjai, *Nano Lett.,* 12(10), **2012**, 5196-5201

419. S. Alayoglu, C. Aliaga, C. Sprung, G. A. Somorjai, *Catal. Lett.,* 141(7), **2011**, 914-924

420. W. D. Michalak, J. M. Krier, K. Komvopoulos, G. A. Somorjai, *J. Phys. Chem. C,* 117(4), **2013**, 1809-1817

421. K. An *et al.*, *J. Am. Chem. Soc.,* 135(44), **2013**, 16689-16696

422. M. E. Grass *et al.*, *Angew. Chem. Int. Edit.,* 47(46), **2008**, 8893-8896

423. H. Wang *et al.*, *Nano Lett.,* 13(6), **2013**, 2976-2979

424. Z. Kónya *et al.*, *Catal. Lett.,* 81(3-4), **2002**, 137-140

425. M. Pattanaik, S. K. Bhaumik, *Mater. Lett.,* 44(6), **2000**, 352-360

426. K. Esumi, M. Oyama, *Langmuir,* 9(8), **1993**, 2020-2023

427. D. Santhiya, S. Subramanian, K. A. Natarajan, S. G. Malghan, *J. Colloid Interface Sci.,* 216(1), **1999**, 143-153

428. T. F. Tadros, *J. Colloid Interface Sci.,* 64(1), **1978**, 36-47

429. D. Li *et al.*, *ACS Catal.,* 2(7), **2012**, 1358-1362

430. I. Száraz, W. Forsling, *Polymer,* 41(13), **2000**, 4831-4839

431. M. R. Mucalo, R. P. Cooney, *Chem. Mater.,* 3, **1991**, 1081

432. C. M. Alexander, J. C. Dabrowiak, J. Goodisman, *J. Colloid Interface Sci.,* 396, **2013**, 53-62

433. H. Hirai, H. Chawanya, N. Toshima, *React. Polym.,* 3(2), **1985**, 127-141

434. M. J. Snowden, S. M. Clegg, P. A. Williams, I. D. Robb, *J. Chem. Soc. Faraday Trans.,* 87(14), **1991**, 2201-2207

435. X. Liu, M. Atwater, J. Wang, Q. Huo, *Colloids Surf. B,* 58(1), **2007**, 3-7

436. Y. Q. He, S. P. Liu, L. Kong, Z. F. Liu, *Spectrochim. Acta. Mol. Biomol. Spectrosc.,* 61(13–14), **2005**, 2861-2866

437. J. Zhang *et al.*, *Mater. Chem. Phys.,* 99(2–3), **2006**, 398-404

438. D. N. Misra, *Langmuir,* 7(11), **1991**, 2422-2424

439. D. N. Misra, *J. Colloid Interface Sci.,* 181(1), **1996**, 289-296

440. Pradip, Y. A. Attia, D. W. Fuerstenau, *Colloid Polym. Sci.,* 258(12), **1980**, 1343-1353

441. S. Shimabayashi, Y. Yoshida, K. Arima, T. Uno, *Phosphorus Res. Bull.,* 4, **1994**, 89-94

442. I. S. Elashmawi, H. E. Abdel Baieth, *Curr. Appl. Phys.,* 12(1), **2012**, 141-146

443. Y. Ishimaru, T. Lindström, *J. Appl. Polym. Sci.,* 29(5), **1984**, 1675-1691

444. R. S. Parnas, M. Chaimberg, V. Taepaisitphongse, Y. Cohen, *J. Colloid Interface Sci.,* 129(2), **1989**, 441-450

445. M. Toki, T. Chow, T. Ohnaka, H. Samura, T. Saegusa, *Polym. Bull.,* 29(6), **1992**, 653-660

446. M. A. Cohen Stuart, G. J. Fleer, B. H. Bijsterbosch, *J. Colloid Interface Sci.,* 90(2), **1982**, 310-320

447. O. Griot, J. A. Kitchener, *Trans. Faraday Soc.,* 61(0), **1965**, 1026-1031

448. V. Shubin, P. Linse, *J. Phys. Chem.,* 99(4), **1995**, 1285-1291

449. V. Shubin, *J. Colloid Interface Sci.,* 191(2), **1997**, 372-377

450. D. Solberg, L. Wågberg, *Colloids Surf. A,* 219(1–3), **2003**, 161-172

451. M. Wiśniewska, *J. Therm. Anal. Calorim.,* 101(2), **2010**, 753-760

452. K. Ishiduki, K. Esumi, *Langmuir,* 13(6), **1997**, 1587-1591

453. I. Száraz, W. Forsling, *Langmuir,* 17(13), **2001**, 3987-3996

454. K. Esumi, M. Iitaka, K. Torigoe, *J. Colloid Interface Sci.,* 232(1), **2000**, 71-75

455. E. Ringenbach, G. Chauveteau, E. Pefferkorn, *Colloids Surf. A,* 99(2–3), **1995**, 161-173

456. K. Masuda, H. Kaji, F. Horii, *Polym. J.,* 33(4), **2001**, 356-363

457. K. Masuda, H. Kaji, F. Horii, *Polym. J.,* 31(1), **1999**, 105-107

458. K. Masuda, H. Kaji, F. Horii, *Polym. J.,* 33(2), **2001**, 190-198

459. B. Li *et al.*, *Macromolecules,* 40(16), **2007**, 5776-5786

460. G. N. Raikar, J. L. Ong, L. C. Lucas, *Surf. Sci. Spectra,* 4(1), **1996**, 9-13

461. T. T. Eighmy, A. E. Kinner, E. L. Shaw, J. D. Eusden, C. A. Francis, *Surf. Sci. Spectra,* 6(3), **1999**, 193-201

462. H. J. Borg, L. C. A. van den Oetelaar, L. J. van Ijzendoorn, J. W. Niemantsverdriet, *J. Vac. Sci. Technol. A,* 10(4), **1992**, 2737-2741

463. Y. Abe, K. Kato, M. Kawamura, K. Sasaki, *Surf. Sci. Spectra,* 8(2), **2001**, 117-125

464. M. Senō, S. Tsuchiya, *J. Electron. Spectrosc. Relat. Phenom.,* 8(2), **1976**, 165-168

465. M. C. Militello, S. J. Simko, *Surf. Sci. Spectra,* 3(4), **1994**, 402-409

466. M. C. Militello, S. J. Simko, *Surf. Sci. Spectra,* 3(4), **1994**, 387-394

467. M. C. Militello, S. J. Simko, *Surf. Sci. Spectra,* 3(4), **1994**, 395-401

468. K. Noack, H. Zbinden, R. Schlögl, *Catal. Lett.,* 4(2), **1990**, 145-155

469. Z. Paál, M. Muhler, R. Schlögl, *Surf. Sci. Spectra,* 4(2), **1996**, 119-124

470. J. L. G. Fierro, J. M. Palacios, F. Tomas, *Surf. Interf. Anal.,* 13(1), **1988**, 25-32

471. M. Engelhard, D. Baer, *Surf. Sci. Spectra,* 7(1), **2000**, 1-68

472. G. J. Leigh, W. Bremser, *J. Chem. Soc. Dalton Trans.,* (12), **1972**, 1216-1219

473. S. D. Jackson *et al.*, *J. Catal.,* 139(1), **1993**, 191-206

474. M. Hecq, A. Hecq, J. P. Delrue, T. Robert, *J. Less Common Met.,* 64(2), **1979**, P25-P37

475. J. P. Contour, G. Mouvier, M. Hoogewys, C. Leclere, *J. Catal.,* 48(1–3), **1977**, 217-228

476. S. Giorgio, C. R. Henry, C. Chapon, C. Roucau, *J. Catal.,* 148(2), **1994**, 534-539

477. P. J. Anderson, R. F. Horlock, *Trans. Faraday Soc.,* 58(0), **1962**, 1993-2004

478. M. E. Smith, G. Neal, M. B. Trigg, J. Drennan, *Appl. Magn. Reson.,* 4(1-2), **1993**, 157-170

479. C.-J. Liao, F.-H. Lin, K.-S. Chen, J.-S. Sun, *Biomaterials,* 20(19), **1999**, 1807-1813

480. J. Barralet, J. C. Knowles, S. Best, W. Bonfield, *J. Mater. Sci. Mater. Med.,* 13(6), **2002**, 529-533

481. C. A. Jaska *et al.*, *J. Am. Chem. Soc.,* 127(14), **2005**, 5116-5124

482. D. K. Dumbre, V. R. Choudhary, N. S. Patil, B. S. Uphade, S. K. Bhargava, *J. Colloid Interface Sci.,* 415(0), **2014**, 111-116

483. D. E. Bergbreiter, A. Kippenberger, Z. Zhong, *Can. J. Chem.,* 84(10), **2006**, 1343-1350

484. M. T. Reetz, G. Lohmer, *Chem. Commun.,* (16), **1996**, 1921-1922

485. Y. Wang, J. Ren, K. Deng, L. Gui, Y. Tang, *Chem. Mater.,* 12(6), **2000**, 1622-1627

486. H. Yamamoto *et al.*, *Nanoscale,* 4(14), **2012**, 4148-4154

487. W. W. Weare, S. M. Reed, M. G. Warner, J. E. Hutchison, *J. Am. Chem. Soc.,* 122(51), **2000**, 12890-12891

488. C. Pan *et al.*, *J. Am. Chem. Soc.,* 123(31), **2001**, 7584-7593

489. T. Yonezawa, T. Kunitake, *Colloids Surf. A,* 149(1–3), **1999**, 193-199

490. Y. Borodko, S. M. Humphrey, T. D. Tilley, H. Frei, G. A. Somorjai, *J. Phys. Chem. C,* 111(17), **2007**, 6288-6295

491. K. Esumi, M. Suzuki, T. Tano, K. Torigoe, K. Meguro, *Colloids Surf.,* 55, **1991**, 9-14

492. F. J. M. Ruiz-Cabello *et al.*, *J. Phys. Chem. B,* 117(39), **2013**, 11853-11862

493. *CRC Handbook of Chemistry and Physics (Digital Edition)* (CRC Press, LLC., 2008)

494. J. George, N. V. Sastry, *J. Chem. Eng. Data,* 49(2), **2004**, 235-242

495. J. Rosenfarb, H. L. Huffman, J. A. Caruso, *J. Chem. Eng. Data,* 21(2), **1976**, 150-153

496. M. H. H. van Dam, A. S. Lamine, D. Roizard, P. Lochon, C. Roizard, *Ind. Eng. Chem. Res.,* 36(11), **1997**, 4628-4637

497. R. Ruoff, D. S. Tse, R. Malhotra, D. C. Lorents, *J. Phys. Chem.,* 97(13), **1993**, 3379-3383

498. P. Muller, *Pure Appl. Chem.,* 66(5), **1994**, 1077-1184

499. V. Gutmann, *Coord. Chem. Rev.,* 18(2), **1976**, 225-255

500. H. Hirai, N. Yakura, Y. Seta, S. Hodoshima, *React. Func. Polym.,* 37(1–3), **1998**, 121-131

501. N. Toshima, T. Yonezawa, K. Kushihashi, *J. Chem. Soc. Faraday Trans.,* 89(14), **1993**, 2537-2543

502. S. Y. Venyaminov, F. G. Prendergast, *Anal. Biochem.,* 248(2), **1997**, 234-245

503. A. García-Abuín, D. Gómez-Díaz, M. D. La Rubia, J. M. Navaza, *J. Chem. Eng. Data,* 56(3), **2011**, 646-651

504. H. C. Brown, E. J. Mead, B. C. Subba Rao, *J. Am. Chem. Soc.,* 77(23), **1955**, 6209-6213

505. A. Furst, R. C. Berlo, S. Hooton, *Chem. Rev.,* 65(1), **1965**, 51-68

506. L. Malatesia, M. Angoletta, *J. Chem. Soc.,* (0), **1957**, 1186-1188

507. W. L. F. Armarego, C. L. L. Chai, *Purification of Laboratory Chemicals* (Elsevier, Oxford, 2008)

508. S. W. Heinzman, B. Ganem, *J. Am. Chem. Soc.,* 104(24), **1982**, 6801-6802

509. J. Shen, Z. Li, Q. Yan, Y. Chen, *J. Phys. Chem.,* 97(32), **1993**, 8504-8511

510. G. N. Glavee, K. J. Klabunde, C. M. Sorensen, G. C. Hadjipanayis, *Langmuir,* 9(1), **1993**, 162-169

511. G. Mie, *Ann. Phys.,* 24(3), **1908**, 377-445

512. D. D. Evanoff, G. Chumanov, *J. Phys. Chem. B,* 108(37), **2004**, 13957-13962

513. I. I. Volchenskova, K. B. Yatsimirskii, *Theor. Exp. Chem.,* 13(2), **1977**, 146-151

514. H. L. Campbell, B. A. Striebig, *Environ. Sci. Tech.,* 33(11), **1999**, 1926-1930

515. G. Durgaprasad, D. N. Sathyanarayana, C. C. Patel, *Bull. Chem. Soc. Jpn.,* 44(2), **1971**, 316-322

516. L. Poulain, A. Monod, H. Wortham, *J. Photochem. Photobiol. A,* 187(1), **2007**, 10-23

517. C. Berrueco *et al.*, *Energy Fuels,* 23(6), **2009**, 3008-3015

518. M. R. Mucalo, R. P. Cooney, *J. Chem. Soc. Chem. Commun.,* (2), **1989**, 94-95

519. M. R. Mucalo, R. P. Cooney, *J. Chem. Soc. Faraday Trans.,* 87, **1991**, 3779

520. M. R. Mucalo, R. P. Cooney, *J. Chem. Soc. Faraday Trans.,* 87(23), **1991**, 3779-3785

521. M. R. Mucalo, R. P. Cooney, *J. Chem. Soc. Faraday Trans.,* 87(8), **1991**, 1221-1227

522. M. R. Mucalo, R. P. Cooney, *J. Colloid Interface Sci.,* 150(2), **1992**, 486-491

523. J. P. Wilcoxon, P. P. Provencio, *J. Am. Chem. Soc.,* 126(20), **2004**, 6402-6408

524. S. L. Westcott, S. J. Oldenburg, T. R. Lee, N. J. Halas, *Langmuir,* 14(19), **1998**, 5396-5401

525. V. J. Barwick, *J. Chromatogr. A,* 849(1), **1999**, 13-33

526. D. R. Deans, *Chromatographia,* 1(5-6), **1968**, 187-194

527. N. G. Wrigley, *J. Ultrastruct. Res.,* 24(5–6), **1968**, 454-464

List of Publications

Some of the results from this research have been published in, or submitted to, scientific journals under the following names:

1. "Measurements of the wettability of catalyst support materials using the Washburn capillary rise technique", *Pow. Technol.*, 276 **2015** 123-128

2. "Halloysite-supported precious metal nanoparticles as olefin hydrogenation catalysts", submitted to *Colloids Surf. A,* ***2016***.

Some of the results from this research are yet to be published, but are to be submitted as follows:

3. "Quantification of the metal content in supported catalysts using laser induced breakdown spectroscopy", to submit to *J. Atom. Anal. Spectrom.*

4. "Preparation of supported catalysts from polymer-protected colloidal metal nanoparticles", to submit to *Appl. Cat. A.*

5. "Supported catalysts prepared from amide-stabilised colloidal palladium nanoparticles", to submit to *J. Nanopart. Res.*